Revista Brasileira de Ciências Mecânicas

Journal of the Brazilian Society of Mechanical Sciences

2

PUBLICAÇÃO DA ABCM - ASSOCIAÇÃO BRASILEIRA DE CIÊNCIAS MECÂNICAS

VOL. XXI - No.2 - JUNE 1999

ISSN 0100-7386

JOURNAL OF THE BRAZILIAN SOCIETY OF MECHANICAL SCIENCES
REVISTA BRASILEIRA DE CIÊNCIAS MECÂNICAS

REVISTA BRASILEIRA DE CIÊNCIAS MECÂNICAS
JOURNAL OF THE BRAZILIAN SOCIETY OF
MECHANICAL SCIENCES
Vol. 1. Nº 1 (1979)-
Rio de Janeiro: Associação Brasileira de Ciências
Mecânicas
Trimestral
Inclui referências bibliográficas.
1. Mecânica
ISSN-0100-7386

A REVISTA BRASILEIRA DE CIÊNCIAS MECÂNICAS publica trabalhos que cobrem os vários aspectos da ciência e da tecnologia em Engenharia Mecânica, incluindo interfaces com as Engenharias Civil, Elétrica, Química, Naval, Nuclear, Aeroespacial, Alimentos, Agrícola, Petróleo, Materiais, etc., bem como aplicações da Física e da Matemática à Mecânica.

INDEXED by Applied Mechanics Reviews
and Engineering Information, Inc..

Publicação da / Published by
ASSOCIAÇÃO BRASILEIRA DE CIÊNCIAS MECÂNICAS
THE BRAZILIAN SOCIETY OF MECHANICAL SCIENCES

Secretária da ABCM : Ana Lúcia Fróes de Souza
Avenida Rio Branco, 124 18º Andar
20040-001 Rio de Janeiro RJ
Tel.: (021) 221-0438/Fax: (021) 509-7128
www.puc-rio.br/parcerias/abcm
abcm@domain.com.br

Presidente: Carlos Alberto de Almeida
Vice-Presidente: Hans Ingo Weber
Secretário: Paulo Batista Gonçalves
Diretor de Patrimônio: Felipe Bastos de F. Rachid
Secretário Geral: Nestor Alberto Z. Pereira

Secretária da RBCM: Maria de Fátima Alonso de Sousa
UNICAMP - FEM - C.P. 6122
13083-970 Campinas SP
Tel.: (019) 788-3205/Fax: (019) 289-3722
E-Mail: abcm@fem.unicamp.br

EDITOR
Leonardo Goldstein Jr.
UNICAMP - FEM - DETF - C.P. 6122
13083-970 Campinas SP
Tel.: (019) 289-3006 Fax: (019) 289-3722
E-Mail: abcm@fem.unicamp.br

EDITORES ASSOCIADOS
Agenor de Toledo Fleury
IPT - Instituto de Pesquisas Tecnológicas
Divisão de Mecânica e Eletricidade - Agrupamento de Sistemas de Controle
Cidade Universitária - C.P. 7141
01064-970 São Paulo SP
Tel.: (011) 268-2211 Ramal 504 Fax: (011) 869-3353
E-Mail: agfleury@ipt.br

Alisson Rocha Machado
Universidade Federal de Uberlândia
Departamento de Engenharia Mecânica - Campus Santa Mônica
38400-206 Uberlândia MG
Tel.: (034) 239-4149 Fax: (034) 235-0382
E-Mail: alissonm@ufu.br

Angela Ourivio Nieckele
Pontifícia Universidade Católica do Rio de Janeiro
Departamento de Engenharia Mecânica
Rua Marquês de São Vicente, 225 Gávea
22453-900 Rio de Janeiro RJ
Tel.: (021) 239-0719 Fax: (021) 294-9148
E-Mail: nieckele@mec.puc-rio.br

Hans Ingo Weber
Pontifícia Universidade Católica do Rio de Janeiro
Departamento de Engenharia Mecânica
Rua Marquês de São Vicente, 225 Gávea
22453-900 Rio de Janeiro RJ
Tel.: (021) 529-9323 Fax: (021) 294-9148
E-Mail: hans@mec.puc-rio.br

Paulo Eigi Miyagi
Universidade de São Paulo - Escola Politécnica
Departamento de Engenharia Mecânica - Mecatrônica
Avenida Prof. Mello Moraes, 2231
05508-900 São Paulo SP
Tel.: (011) 818-5580 Fax: (011) 818-5471/813-1886
E-Mail: pemiyagi@usp.br

Seyyed Said Dana
Universidade Federal da Paraíba
Centro de Tecnologia-Campus I
Departamento de Tecnologia Mecânica
58059-900 João Pessoa PB
Tel.: (083) 216-7356 Fax: (083) 216-7179
E-Mail: dana@dtm.ct.ufpb.br

CORPO EDITORIAL:

Alcir de Faro Orlando (PUC-RJ)
Antonio Francisco Fortes (UnB)
Armando Albertazzi Jr. (UFSC)
Atair Rios Neto (UNIVAP)
Benedito Moraes Purqueiro (EESC-USP)
Carlos Alberto de Almeida (PUC-RJ)
Carlos Alberto Martin (UFSC)
Clovis Raimundo Maliska (UFSC)
Emanuel Rocha Woiski (UNESP-FEIS)
Francisco Emilio Baccaro Nigro (IPT-SP)
Francisco José Simões (UFPb)
Genesio José Menon (EFEI)
Henrique Rozenfeld (EESC USP)
Jair Carlos Dutra (UFSC)
João Alziro Herz de Jornada (UFRGS)
José João de Espindola (UFSC)
Jurandir Itizo Yanagihara (EP USP)
Lirio Schaefer (UFRGS)
Lourival Boehs (UFSC)
Luis Carlos Sandoval Goes (ITA)
Marcio Ziviani (UFMG)
Mario Ussyr (EMBRACO)
Moyses Zindeluk (COPPE-UFRJ)
Nisio de Carvalho Lobo Brum (COPPE-UFRJ)
Nivaldo Lemos Coppini (UNICAMP)
Paulo Afonso de Oliveira Soviero (ITA)
Rogério Martins Saldanha da Gama (LNCC)
Valder Steffen Jr. (UFU)

REVISTA FINANCIADA COM RECURSOS DO

Programa de Apoio a Publicações Científicas

MCT ***CNPq*** FINEP

RBCM - J. of the Braz. Soc. Mechanical Sciences
Vol. XXI - No.2 - 1999 - pp. 164-174

ISSN 0100-7386
Printed in Brazil

Interdisciplinary Control Design for a Solar Car Implementation

Marcelo Godoy Simões
Nilson Noris Franceschetti
Julio Cesar Adamowski
Universidade de São Paulo
Escola Politécnica
Departamento de Engenharia Mecânica - Mecatrônica
05508-900 São Paulo, SP Brazil
mgs@usp.br

Abstract

The paper describes an advanced drive system control for a solar powered vehicle. The drive system control extracts the maximum electrical power from a distributed solar array that covers the surface of the vehicle, with distributed RISC based peak power tracker controllers for each individual solar panel. The vehicle propulsion has two steering wheels and one propulsion wheel based on a brushless dc machine drive control. The system is capable to sequence from start-up to shutdown, it is torque or speed controlled and a on-board computer for system monitoring and communication for energy management in the race strategy which optimizes the energy management. The drive system has been fully implemented in a two seat carbon fiber prototype with satisfactory performance and can be easily translated to other types of electrical vehicles.

Keywords:*Solar Car, Electric Vehicle, Control Drive.*

Introduction

Alternative energy solutions are getting a lot of attention on the last few years due to the requirements of clean and safe renewable energy sources. Solar photovoltaic and thermal energy, wind power, and biomass generation are gaining more acceptance because of environmental and safety problems of conventional power plants and advancement of technology. Electric vehicles are also focus of intense research due to the necessity of pollution control and decrease of oil importation. In addition, the need for more energy to supply the overwhelming industrial growth usually requires cost-competitive solutions with local energy production or co-generation (de Haan, 1996).

Several countries have initiated policies aimed at the development of alternative energy resources. In Brazil, the Polytechnic School of the University of São Paulo (EPUSP) has taken steps to include new undergraduate and graduate training programs in alternative energy related education. The World Solar Challenge (WSC), a solar race across the Australian outback, has been adopted as an unique way to bring together and motivate students to get involved in university projects and studies in solar energy technology and electric vehicle construction (Roche et al., 1997; Godoy Simões et al., 1997). The race regulations allowed only sun-derived propulsion energy, with battery storage of the same. The race rules specified that the maximum vehicle dimensions should be 19.7 ft long, 6.6 ft wide, and 5.3 ft high. Therefore, the solar cell arrangement was fit into a box having the dimensions of a two-seated car. The vehicle required the capability to pass an articulated truck traveling in the opposite direction at 50 mph, on a narrow two-lane highway, without losing control. To race in the WSC, a car was to be designed to optimize (1) aerodynamic performance, since the highway used as the course was straight with only small elevations, (2) the solar energy utilization, which must be the only source of electrical energy, and (3) the vehicle stability, to cross the 3,000 km from Darwin to Adelaide, with articulated trucks on both sides. The car was named Poli-Solar, shown in Fig. 1 with the characteristics given in Table 1.

Drive Control System

The complete drive control system is shown on Fig. 2 and the characteristics are given in Table 1. There are eight solar panels distributed on the vehicle surface, four panels are constructed with 16 % ASE cells (ASE, 1996), and the remaining four panels with 15.5 % ASE cells. The solar cells are connected in strings, forming a zigzag pattern across the surface. The back of the cell is prepared to receive SN-CU leads with a silver based sold and each cell is adhered to the vehicle carbon fiber surface with a two-side coating tape. Every group of 20 cells has a parallel diode rectifier to keep

Manuscript received: September 1998, Technical Editor: Paulo Eigi Miyagi.

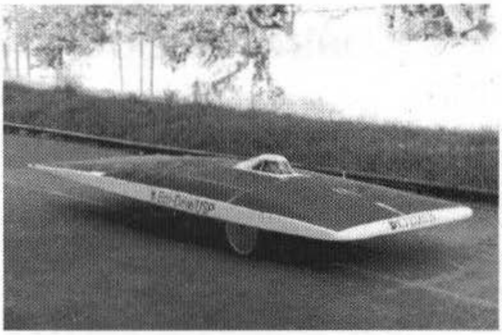

Fig. 1 Photograph of the solar powered vehicle

Table 1 **Solar vehicle characteristics**

Dimensions	6 m x 2 m x 1.6 m
Total solar surface area	12 m^2
Occupants	2
Front suspension	Double A
Back suspension	Pro-link
Steering	Steel cable driven
Solar power rating	1,800 w
Battery capacity	200 Ah
Maximum speed	56 mph
Solar array control	RISC PIC16C74 based
Machine drive control	Analog control based
On-board computer	68HC11 based
Energy management	Based on captured energy

the string operating in case of cell damages. Each solar panel is connected to a Maximum Peak Power Tracker (MPPT) system for maximum energy transference, by matching the panel impedance to the drive system (Bose et al., 1984), as explained latter. The total solar energy is either stored in the battery or flows to the machine according to the demand (Patterson, 1990). Energy monitoring and management is also explained latter.

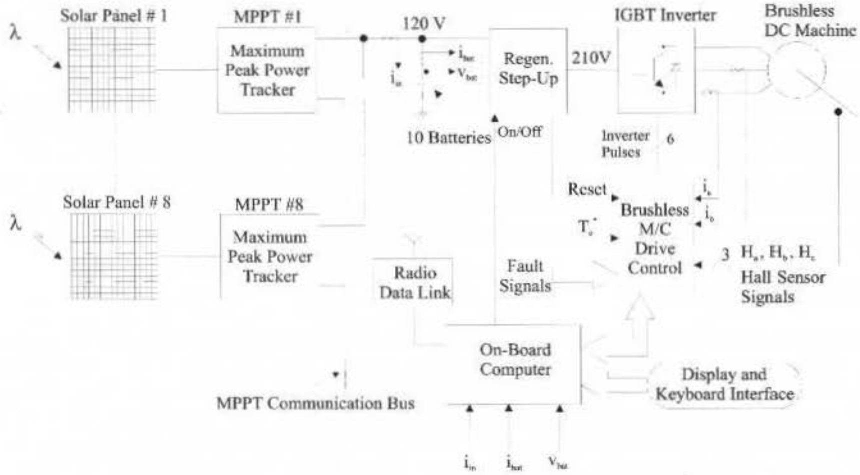

Fig. 2 Block diagram of solar powered vehicle drive control system

The battery bus is composed by two parallel sets of ten batteries, with a total voltage of 120 V. This voltage is further increased to 210 V by a step-up switching regulator with regeneration capability, as shown in Fig. 3. The trade-off study of total battery weight versus physical step-up size yielded an inverter bus voltage of 210 V for a given weight as the optimum configuration (Magliaro, 1987). There are two controlled switches (Insulated Gate Bipolar Transistor - IGBT) with free-wheeling diodes, the IGBT T_1 controls the input-output ratio by PWM, while the IGBT T_2 operates during regeneration, i.e., when the inverter bus voltage increases, the regenerative logic turns T_1 off and T_2 on with a hysteresis control, allowing the power to flow back to the batteries as seen in the experimental data of Fig. 4, where the machine torque was reversed with constant speed. The bus voltage has a LC ringing response, as the current flows back as indicated by a higher inductor ripple skewed non-symmetrically to the negative rate. In order to reduce transients superimposed on the inverter bus, a dynamic brake set for 400 V, and high-voltage zener diodes for spikes have been provided.

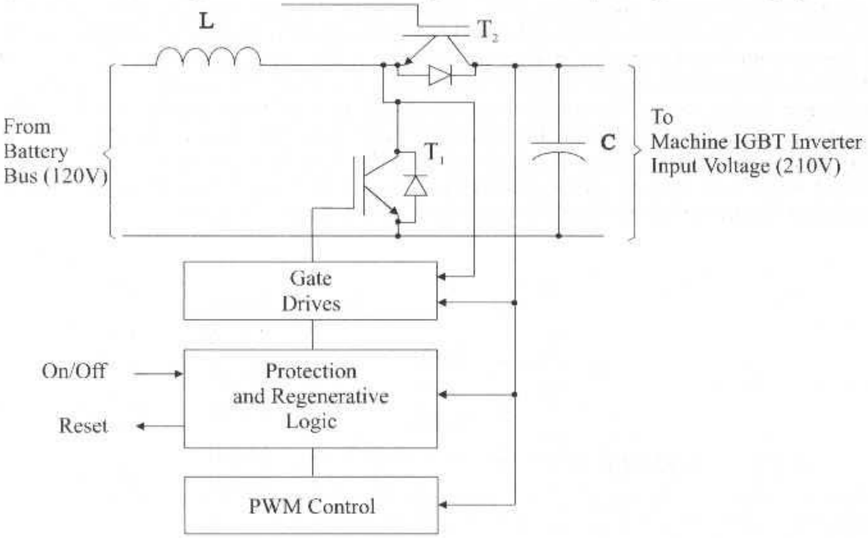

Fig. 3 Regenerative voltage step-up diagram

Fig. 4 Regeneration results for machine torque inversion showing: step-up machine bus voltage, IGBT T_1 voltage and the inductor current

The step-up system can be turned off by the on-board computer which during the system start-up resets the brushless machine drive control as indicated in Fig. 2. The IGBT inverter was constructed with Semikron leg modules and gate-drives, commanded by the inverter pulses of the brushless machine drive control system (Sakmann, 1987). Figure 5 depicts the machine drive control system, the torque level (T_e^*) is either a manual command given by a potentiometer on the driver's dash, or it is a signal from the on-board computer during cruise-control. The reference torque (T_e^*) is compared to the estimated torque. The estimated torque is reconstructed from the instantaneous machine currents i_a and i_b with one analog switch based circuit commanded by the look up table which addresses the inversions and additions necessaries to build the torque current I_T. The PI control output is pulse-width-modulated with a triangular carrier frequency of 20 kHz. The Hall sensor signals (H_a, H_b and H_c) addresses the ROM look up table of the machine phase sequence to generate the inverter pulses which are separated for the up and down devices with a dead-time circuit (5 μsec).

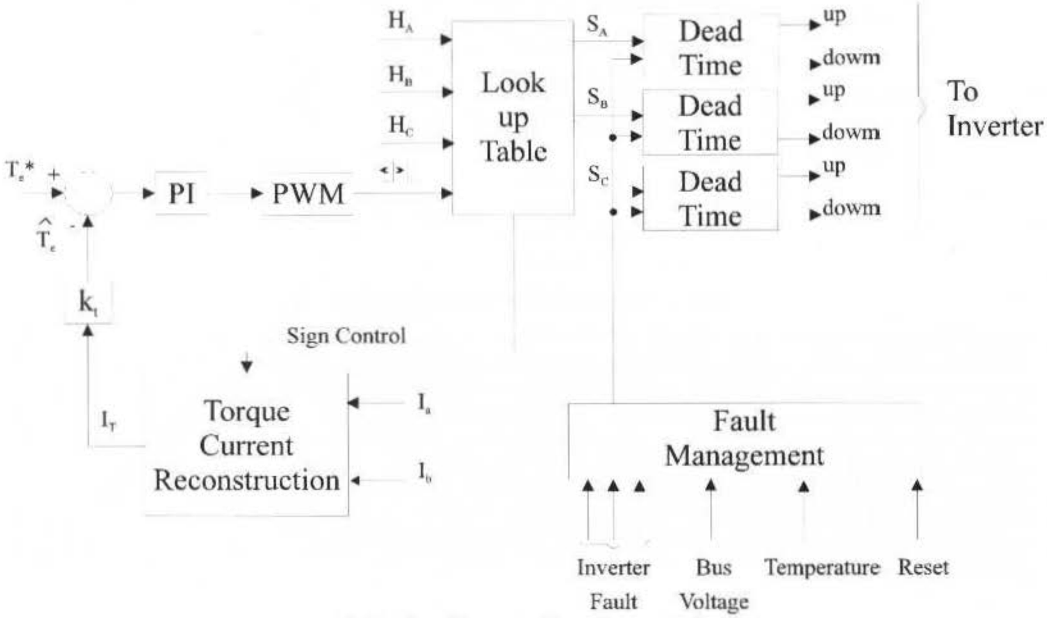

Fig. 5 Brushless machine drive control

The fault management circuit receives the inverter, bus-voltage, temperature and reset signals, in order to turn-off the inverter pulses in case of any fault. Figure 2 shows the on-board computer which receives the total solar panel current (i_{in}), the battery current (i_{bat}), and the battery voltage (v_{bat}) with DAC channels and the individual solar panel data with a point-to-point serial MPPT communication bus. The information is sent for the support car by a radio data link for energy management as explained latter. There is a LCD display and keyboard interface with the driver, who can also observe the generated energy, the vehicle speed, and command the drive control system to stay either in torque or in speed loop control. Figure 6 shows the drive system control sequencing diagram. During the start-up the batteries are connected (manually) and after the bus capacitors are charged (sensed with analog comparators), the Maximum Peak Power Trackers (MPPT) are connected with internal relays. There is a soft-start procedure, which is performed by gradually increasing of the MPPT duty-cycle, and the search algorithm is started. When the solar panels are ready and providing energy to the batteries, the on-board computer is booted and several checks and tests are performed. Thereafter the pilot can either operate the vehicle with a manual set-point in torque control mode, or vary the speed set-point in cruise control mode. When the brake is depressed, the torque control loop is always activated and the driver should command the torque level manually. The shutdown can either be initiated by the driver or automatically by any fault signal.

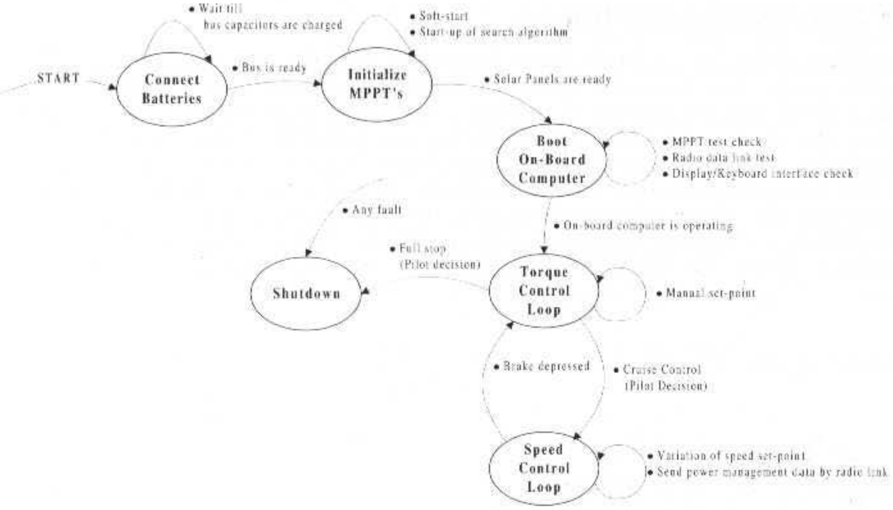

Fig. 6 Drive system control sequencing diagram

The drive system control was tested in laboratory, with the complete set of wheel and gear connected to the machine shaft, in both torque loop and speed loop control modes. The drive system performance is shown in Fig. 7. A positive and negative torque responses are depicted in Fig. 7(a) and 7(b) for set-point commands of ± 15 Nm, (during the torque transient the machine was kept in constant speed of 650 RPM). The speed loop response, with the cruise-control mode activated, is displayed in Fig. 7(c), which shows the correspondent instantaneous machine torque and speed, for a speed step reference of 250 RPM. The steady-state terminal machine voltage and current signals can be observed in Fig. 7(d). The drive system was intensively tested in the solar vehicle, in order to build-up the air-drag efficiency curves, but the responses are not shown here

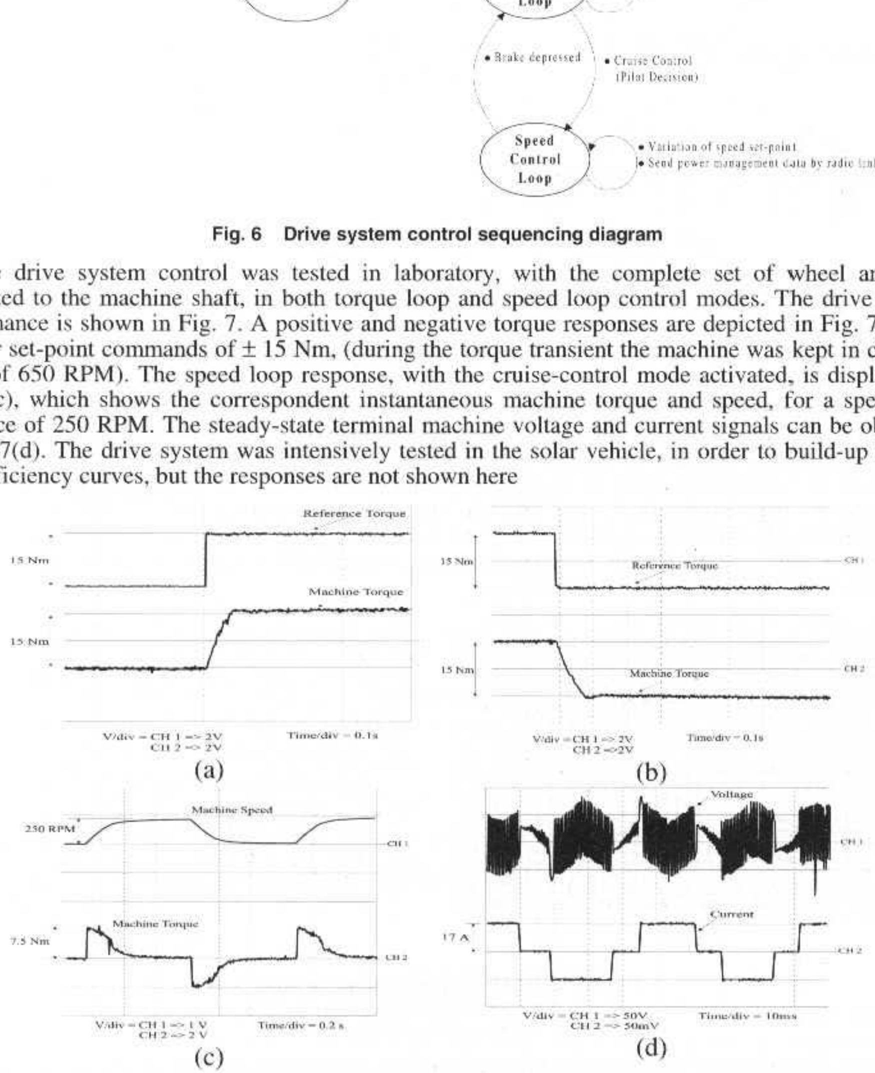

Fig. 7 Drive system performance, (a) Positive torque command (+15 Nm), constant speed (650 RPM), (b) Negative torque command (–15 Nm), constant speed (650 RPM), (c) Constant speed command (+ 250 RPM) and actual machine torque response, (d) Steady-state terminal machine voltage and current.

Solar Array System Control

The design, construction and operation of the vehicle solar array as the source of all electric power, required the greatest care, because of the fragility and high cost of solar cells. A detailed description of solar array design requirements falls outside the scope of this paper which has been focused on the description of controls aspects. Each panel delivers power subjected to different levels of sunlight due to the car's surface curvature, and also to the temperature. Figure 8 shows the electrical characteristics for the 16% solar cells used in the back of the vehicle, the front cells are similar ones but have 15.5% rated efficiency. The current produced by the solar cell is proportional to the solar intensity normal to the cell surface, whereas the voltage-temperature characteristics are symmetrical diode-like curves (Raushenback, 1986). The mathematical modeling for the solar array is given by the following equations:

$$J = k1 \cdot \lambda - k2 \cdot e^{\alpha V - \beta T - \gamma} \tag{1}$$

$$v = \frac{1}{\alpha}\left[ln\left(\frac{\lambda}{k} - \frac{i_p}{Acel} \right) + \beta T + \gamma \right] \tag{2}$$

$$v_p = \sum_{j=1}^{Ncel} v_j - Ncel \cdot R_s \cdot i_p \tag{3}$$

where J is the current density (mA/cm^2), v is the single voltage cell (V), v_p is the total voltage (V) in the array, i_p is the array current (A), λ is the solar intensity (mW/cm^2) and T is the temperature (°C). The parameters $k1$ (non-dimensional), $k2$ (mA/cm^2), α (voltage coefficient V^{-1}), β (temperature coefficient °C^{-1}) and γ (non-dimensional) are adjusted from the manufacturer curves with a multi-linear regression algorithm (Rawlings, 1988), where the parameters are calculated to minimize the quadratic error, N_{cel} is the number of cells in a series-string connection that makes the array, and R_s is the individual contact resistance between the cells.

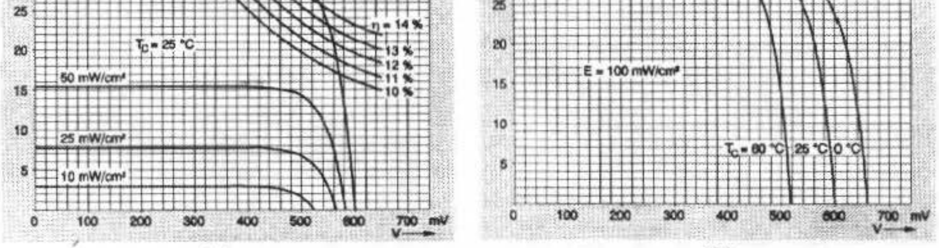

(a) (b)

Fig. 8 Electrical characteristics for solar cells, V x I dependence on solar intensity, V x I dependence on temperature.

The maximum power occurs at the intersection of the voltage-current curve and the hyperbole of the correspondent power as show on Fig. 9. Of course, such maximum power point changes as the solar intensity and the temperature vary (Rawlings et al., 1993; Salameh and Taylor, 1990; Sullivan and Powers, 1993). It is therefore necessary to use a converter capable to locate and operate at the voltage that maximizes the output power, as shown in Fig. 9. Such maximum-power-point-tracking can be performed by a boost type switching regulator indicated in Fig. 10. The boost regulator is driven by the RISC PIC16C74 microcontroller which calculates the instantaneous power and searches step-by-step the optimum duty-cycle so as to maximize the power drawn from the panel and delivered to the battery/machine inverter system (Microchip, 1994).

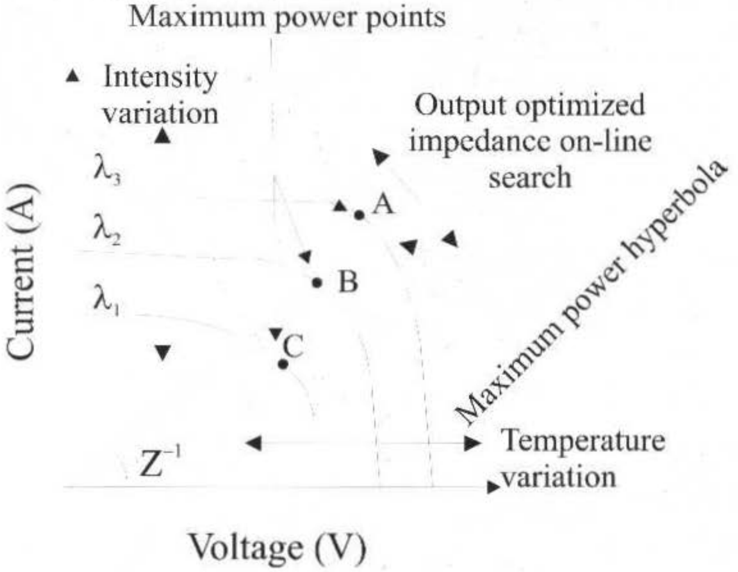

Fig. 9 Search method of maximum power at solar array with duty cycle programming

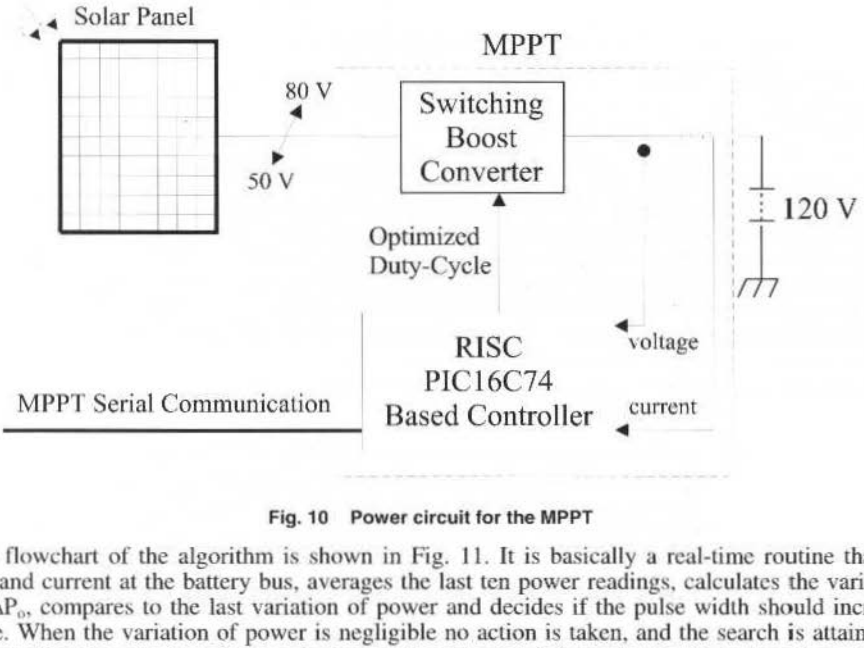

Fig. 10 Power circuit for the MPPT

The flowchart of the algorithm is shown in Fig. 11. It is basically a real-time routine that reads voltage and current at the battery bus, averages the last ten power readings, calculates the variation of power ΔP_o, compares to the last variation of power and decides if the pulse width should increase or decrease. When the variation of power is negligible no action is taken, and the search is attained. The microcontroller also monitors the panel power and sends such information to the on-board computer via serial communication and detects open output by sensing the battery voltage, shutting down the search for voltage protection.

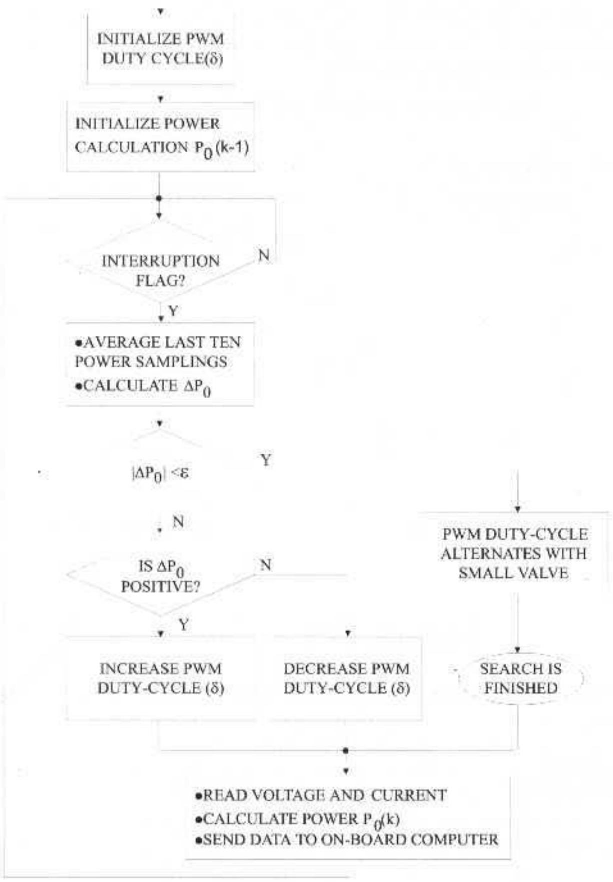

Fig. 11 Flowchart diagram for duty-cycle search procedure

The PWM switching waveform of the boost transistor is shown in Fig. 12, the solar cell current and the battery current tracking for two levels of intensity. In both cases the machine torque load was kept constant; therefore, any increase in the solar level results in the corresponding increasing of current flowing to the battery. As the solar level increases, the PWM settles down to a new pulse width, as showed in figure, indicating the solar cell current, PWM switching and battery current waveform, the high frequency current ripple is filtered out at the battery. MPPT efficiency was always better than 96%.

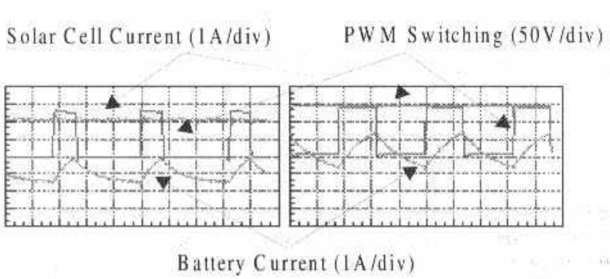

Fig. 12 PWM switching, solar cell current and battery current tracking, (a) Results for solar intensity at 55 mW/cm^2, (b) Results for solar intensity at 90 mW/cm^2

Energy Monitoring and Management

The ultimate goal in a solar powered vehicle is the achievement of the maximum average efficiency at the minimum weight. The average efficiency is a combination of system components integration, which take into account road gradients and surfaces, predicted meteorological conditions and race strategies. For a given amount of collected energy, there is an optimum average speed which should be kept constant. The vehicle must undergo road tests in order to build a look-up table of vehicle efficiency in terms of speed. There are several forces opposing motion: rolling resistance, aerodynamic drag and gravity when climbing hills. For a given stored energy in the batteries and the prediction for a certain amount to be collected in the next period of hours, the driver should keep the speed as close as possible to the optimum value. Several variables on the car are monitored by an on-board computer based on the microprocessor 68HC11 shown in the block diagram of Fig. 13. Such variables were sent via a radio link to a computer for a team-support car (Motorola, 1991).

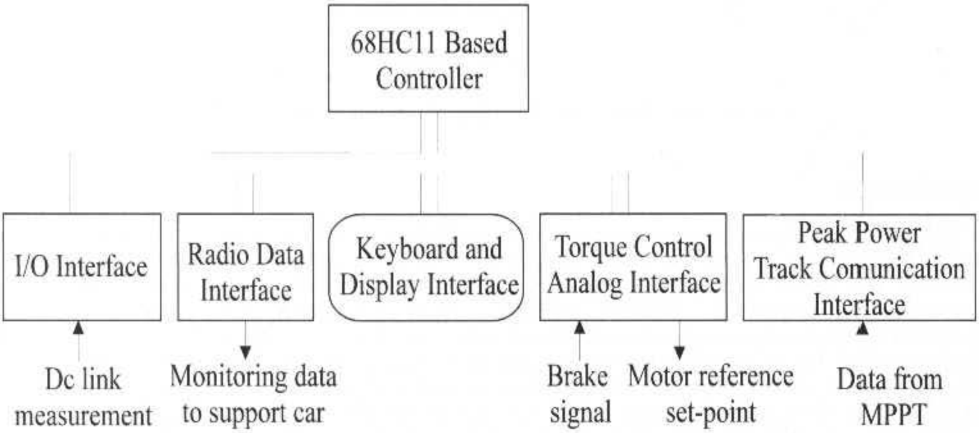

Fig. 13 Block diagram of on-board computer

The measurements of power on each solar panel, vehicle speed, brushless machine torque and battery current are monitored by a management software. The on-board computer can also perform speed control loop as dictated by the race strategy. In a competition like the World Solar Challenge, the race starts at 8:00 AM and stops daily at 5:00 PM. The sunlight at the end of the day can still be collected. The portable computer on the support car must calculate how much charge is in the battery, with the integration of the battery current on a sampling basis; in order to predict the collected power, a model based on the celestial sphere (Walraven, 1978) was implemented in a portable computer, which could communicate with the on-board computer through a radio link to predict the amount of power that each panel was delivering. This model was fine tuned with trial-and-error experimentation, with the help of a reference cell measuring the solar intensity. The collected energy changes drastically in shiny, cloudy or rainy days, as depicted by two typical day insolation curves on Fig. 14. The calculation of the optimum average speed is valid for periods of stable weather conditions, which is evaluated by the team experience. For a given period of time, the following procedure must be done to estimate the amount of available energy:

- Get geographical position coordinates
- Get local solar incidence reference
- Calculate the power on each panel
- Estimate the total energy captured for the route
- Estimate the stored battery energy
- Calculate the optimum speed for the route
- Keep track of the average speed

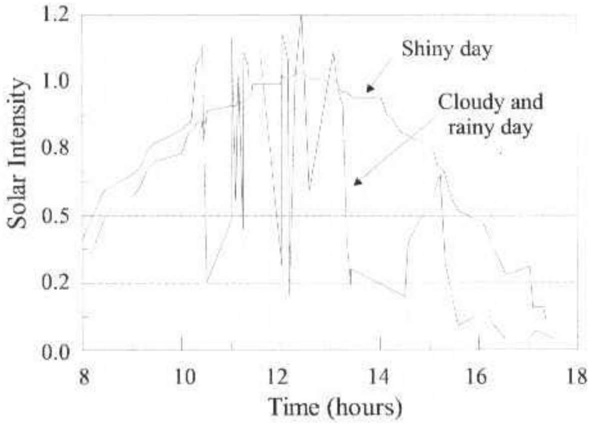

Fig. 14 Typical actual day sunlight data on two Australian routes

Conclusion

This paper described an advanced drive system control for a solar powered vehicle. The system has been fully implemented in the university car called Poli-Solar, completely designed by students for a solar race. The nature of this project has given motivation for other investigations on solar energy systems and electric vehicles technology. The drive system operates with full performance, extracting the maximum electrical power from a distributed solar array that covers the surface of the vehicle, by distributed RISC based controllers with individual solar panel peak power tracking capabilities. Such energy is used to drive a four quadrant brushless dc machine based vehicle propulsion with battery surplus storage. The control functions include start-up and shutdown sequencing, feedback with torque or speed loop, system monitoring, communication for energy management, and calculation of speed for race strategy aiming the optimum energy management. Further studies on the drive performance are still in progress and new advancements will be reported.

Acknowledgment

Several people and institutions made this project possible. The most sincere thanks are to the academic spirit and off-hours dedication from the undergraduate student team, leaded during two years by Rogério K. Makita, Carlos A. B. Gonçalves, Daniel M. M. S. Santos, Marcelo de M. Sampaio, Felipe Canhoto and Andrei F. Monteiro. The tremendous help by Eng. Alan T. de Souza and Eng. Eduardo Bomeisel, who dedicated themselves in a very time-consuming work was very important. The grant given by FAPESP # 96/1485-0, and the internal support from the University of Sao Paulo, made possible all the importation, purchases and fabrication required. Citizen provided the trip and transportation funds for the vehicle and the team.

References

ASE GmbH, 1996, Solar cells datasheet, Germany.

Bose, B. K., Szczesny, P. M., Steigerwald, R. L., 1984, "Microcomputer control of a residential photovoltaic power conditioning system," IEEE Trans. Ind. Elec., vol. 21, pp. 852-859.

de Haan, S.W.H., 1996, "Power electronics for renewable energy systems: state of the art, trends and challenges," PEMC Invited Paper, Budapest, vol. 3, pp. 31-38.

Godoy Simões, M., Franceschetti, N. N., Adamowski, J.C., 1997, "A photovoltaic based electric vehicle drive system", 30th Int. Symp. on Automotive Technology and Automation - ISATA, Florence, Italy, pp. 307-314.

Microchip Technology, 1994, "Embedded Control Handbook".

Migliaro, M. W., 1987, "Considerations for selecting and sizing batteries," IEEE Transactions on Industry Applications, vol. 23 (1).

Motorola, 1991, "68HC11 Reference Manual", Raushenback, 1986, "Solar cell array design handbook," vol. I, II, Jet Propulsion Laboratory.

Rawlings, J. O., 1988, "Applied Regression Analysis", Belmont, CA., Wadsworth & Brooks/Cole.

Roche, D. M. et. al, 1997, "Speed of light - The 1996 World Solar Challenge", Photovoltaics Special Research Centre, Sydney, Australia.

Sakmann, W. H., 1987, "A brushless dc motor controlled by a microprocessor with examples for a three-phase motor" IEEE Trans. on Ind. Elec., vol. 34, no. 3, pp. 339-345.

Salameh, Z., Taylor, D., 1990, "Step-up maximum power point tracker for photovoltaic arrays," Solar Energy, vol. 44 (1) , pp. 57-61.

Sullivan, C. R., J. Powers, M. J., 1993, "A high efficiency maximum power point tracker for photovoltaic arrays in a solar-powered race vehicle," Power Elect. Spec. Conference, pp. 574-580.

Patterson, D. J., 1990, "Electrical system design for a solar powered vehicle," Power Elect. Spec. Conference, pp. 618-622.

Walraven, R., 1978, "Calculating the position of the sun," Solar Energy, vol. 20, pp. 393-397.

RBCM - J. of the Braz. Soc. Mechanical Sciences
Vol. XXI - No.2 - 1999 - pp. 175-184

ISSN 0100-7386
Printed in Brazil

Reaction Null Space Control of Free-Floating and Elastic Base Robots

D.N. Nenchev
Department of Intelligent Machine and System Engineering
Hirosaki University
3 Bunkyo-cho, Hirosaki 036-8561, Japan
nenchev@cc.hirosaki-u.ac.jp

K. Yoshida
M. Uchiyama
Department of Aeronautics and Space Engineering
Tohoku University
Aoba-yama 01, Sendai 980-8579 Japan
yoshida@astro.mech.tohoku.ac.jp
uchiyama@space.mech.tohoku.ac.jp

Abstract

The equations of motion of both free-flying and elastic base robots have a similar structure. Particularly, we show that a so-called inertia coupling matrix plays a significant role for the dynamics. We derive necessary conditions for the existence of the null space of this matrix. The null space aims in decoupling manipulator motions from base motion. Decoupling means that fast motions can be performed without disturbing the base. Also, efficient inertial coupling can be achieved, which is helpful for controlling base motion through manipulator-induced reactions.

Keywords: *Reaction Null Space Control, Robots*

Introduction

Spaceborne telerobots are characterized with a relatively low-mass movable base. Path planners and controllers must take care of the dynamic interaction between manipulator(s) and base, in addition to end-effector motion planning and control.

A typical example of a space telerobot is a free-floating robot (FFR) comprising a manipulator arm attached to a satellite base, such as the ETS VII (Oda,1996). During the last decade, a number of methods for motion planning and control of such systems have been developed (Xu et al., 1992). Another example is a system consisting of a dextrous manipulator attached to a large arm, such as the Special Purpose Dextrous Manipulator (SPDM) mounted on the Space Station Remote Manipulator System (SSRMS) (see Fig. 1), or the Small Fine Arm mounted on the large Japanese Experimental Module Remote Manipulator System (JEMRMS) (Xu et al., 1992). The large arm can be regarded as an elastic base with reference to the dextrous manipulator. Operation of the dextrous manipulator induces reaction forces at the base, and hence, vibrations of the large arm. Again, motion planning and control of the dextrous manipulator for reducing the disturbance on the elastic base is necessary (Book et al., 1989), (Torres et al., 1994). We shall further on refer to a system like the SPDM/SSRMS as a flexible structure mounted manipulator system (FSMS).

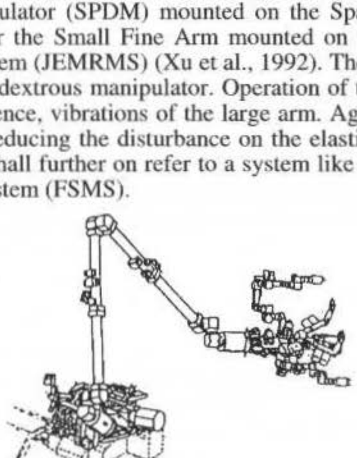

Fig. 1 SSRMS with SPDM

To tackle the dynamic interaction problem described above, we introduced recently the concept of reaction null space (Yoshida et al., 1995), (Yoshida et al., 1996). The idea originates from our previous

Presented at DINAME 97 – 7th International Conference on Dynamic Problems in Mechanics, 3 – 7 March 1997, Angra dos Reis, RJ, Brazil. Technical Editor: Agenor de Toledo Fleury.

work on free-flying robots, where the null space of a certain inertia-mass matrix was used to plan so called "fixed-attitude-restricted (FAR)" motions (Nenchev et al., 1990), (Nenchev et al., 1992). The aim of this paper is to show that the reaction null space concept is a suitable approach to the dynamic interaction problem in the sense that (1) full dynamic interaction decoupling is provided, and (2), the approach is general and can be applied to the various types of space-born telerobots.

Equation of Motion

We base our discussion on the general model of moving base robots as described in (Yoshida et al., 1996). The model comprises a moving base and a number of mechanisms attached to it, such that a tree-like structure is formed (Fig. 2). We distinguish the following three types of mechanisms: (1) manipulators; (2) compensators; (3) other mechanisms.

First, we note that manipulators comprise usually open kinematic chains; sometimes the structure can be tree-like (e.g. the structure of the SPDM/SSRMS system). Next, the term "compensator" has been introduced here to emphasize the role of mechanisms able to compensate fully or to some extent base reaction induced by the manipulators. A typical example of a compensator is an attitude control mechanism. Finally, the group of "other mechanisms" covers antenna pointing mechanisms, solar array pointing mechanisms etc. The first and the third group of mechanisms are considered to be "disturbance generators;" they induce some undesirable motion to the base. For convenience, we shall further on refer to the mechanisms in Fig. 2 as the generalized mechanism.

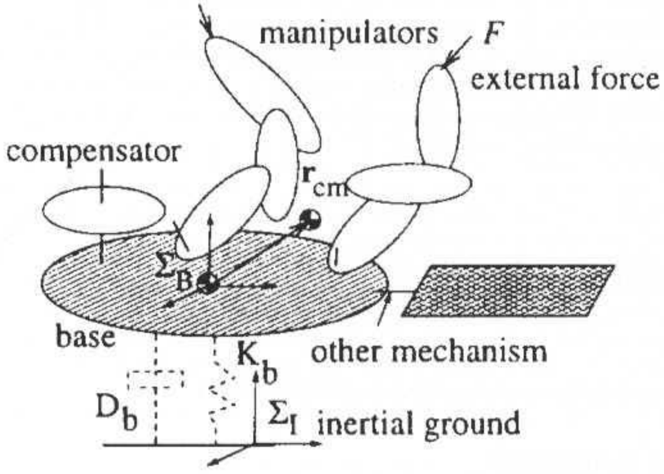

Fig. 2 General model of a space borne telerobot

Our main focus is in reducing/controlling the total base disturbance through inertial coupling with manipulator motions. At this point we can ignore the structure of the generalized mechanism, just focusing on the wrenches acting at the base. The wrenches of disturbance generators are dynamic ones. They can vary significantly in direction and magnitude, depending on the source. Manipulators, for example, induce typically low-frequency variations (between 0.01 Hz and 1 Hz) with point-to-point motions, and higher-frequency variations (between 10 Hz and 100 Hz) with smooth motions (Rohn et al., 1990). Other sources are flexible bodies which induce also quasi-periodic components, and impacts having quiet a different reaction characteristics. Obviously, the total disturbing wrench is of complex nature.

The system dynamics can be represented generally as

$$\begin{bmatrix} H_b & H_{bm} \\ H_{bm}^T & H_m \end{bmatrix}\begin{bmatrix} \ddot{x}_b \\ \ddot{\theta} \end{bmatrix}+\begin{bmatrix} D_b & 0 \\ 0 & D_m \end{bmatrix}\begin{bmatrix} \dot{x}_b \\ \boldsymbol{\theta} \end{bmatrix}+\begin{bmatrix} K_b & 0 \\ 0 & 0 \end{bmatrix}\begin{bmatrix} x_b \\ \boldsymbol{\theta} \end{bmatrix}+\begin{bmatrix} c_b \\ c_m \end{bmatrix}=\begin{bmatrix} 0 \\ \tau \end{bmatrix}, \tag{1}$$

where $\boldsymbol{x}_b \in \Re^m$ denotes the positional and orientational coordinates of the base with respect to the inertial frame[1], $\theta \in \Re^n$ stands for the generalized coordinates of the generalized mechanism, $\boldsymbol{H}_b, \boldsymbol{D}_b, \boldsymbol{K}_b \in \Re^{m \times m}$ denote inertia, damping and stiffness matrices of the base, respectively $\boldsymbol{H}_m, \boldsymbol{D}_m \in \Re^{n \times n}$ denote inertia and damping matrices, respectively, of the generalized mechanism, c_b and c_m denote velocity-dependent nonlinear terms, and $\tau \in \Re^n$ is the joint torque. $\boldsymbol{H}_{bm} \in \Re^{m \times n}$ will be called the inertia coupling matrix. The above equation is similar to that used in (Torres etal., 1994), (Book et al., 1989) for an FSMS. In the particular case of an FFR, the base damping and stiffness are set to zero: $\boldsymbol{D}_b = \boldsymbol{K}_b = 0$.

The inertia coupling matrix $\boldsymbol{H}_{bm}$ appears in both upper and lower parts of the dynamic equation. We will show that this matrix plays a key role in the dynamics of space-born telerobots, and can be useful in designing motion planning and control laws. First, note that the total base reaction wrench W can be represented as follows:

$$W=\begin{bmatrix} m\ddot{r}_{cm} \\ \dfrac{d}{dt}[\, mr_{cm}\times\dot{r}_{cm}+\sum_{j=1}^{n}(I_j\omega_j+m_jr_j\times\dot{r}_j) \end{bmatrix}, \tag{2}$$

where $\boldsymbol{r}_{cm}$ denotes the center of mass position of the generalized mechanism, $\boldsymbol{I}_j, \omega_j, \boldsymbol{m}_j, \boldsymbol{r}_j$ stand for the inertia matrix, angular velocity, mass and center-of-mass position, respectively, for body j, and $m = \Sigma\, m_j$. The expression $\sum_{j=1}^{n}(I_j\omega_j+m_jr_j\times\dot{r}_j)$ denotes angular momentum and imposes a nonholonomic constraint in case of an FFR. On the other hand, the upper part of Eq. (2) denoting the reaction force, represents a holonomic constraint. Under the assumption that the inertia coupling matrix $\boldsymbol{H}_{bm}$ is a function of the joint positions only, which is strictly true for FFR, Eq. (2) can be rewritten in terms of generalized coordinates, as follows:

$$W=H_{bm}\ddot{\theta}+\dot{H}_{bm}\dot{\theta} \tag{3}$$

The last equation can be integrated:

$$L=L_0+H_{bm}\dot{\theta} \tag{4}$$

We shall refer to $\boldsymbol{L}$ as the coupling momentum of an FSMS.

The Reaction Null Space

Reactionless Motion

Here we shall examine the special case of motions that do not induce any base reaction. It should be apparent that in this case the coupling momentum will be conserved.

It can be shown (Nenchev et al., 1996) that at a configuration $\tilde{\theta}$ of the generalized mechanism, such that rank $H_{bm}(\tilde{\theta}) = \max_{\theta} \operatorname{rank} H_{bm}(\theta)$:

1. Zero reaction is achieved with the joint acceleration

$$\ddot{\theta}_c=-H_{bm}^{+}\dot{H}_{bm}\dot{\theta}+(E-H_{bm}^{+}H_{bm})\zeta \tag{5}$$

---

[1] Generally, m=6 (n ≥ m)

where $H^{+}_{bm} \in \Re^{n \times m}$ denotes the Moore-Penrose generalized inverse of the inertia coupling matrix, $\boldsymbol{E} \in \Re^{n \times n}$ stands for the unit matrix, θ and $\zeta \in \Re^{n}$ are arbitrary;

2. Coupling momentum conservation is achieved with the joint velocity

$$\dot{\theta}_c = H^{+}_{bm}\overline{L} + (E - H^{+}_{bm} H_{bm})\zeta \qquad (6)$$

where ζ denotes again an arbitrary vector, and $\overline{L} = const$.

The condition for maximum rank of the inertia coupling matrix is in fact a controllability condition, as discussed by Spong with regard to passive-joint manipulators (Spong, 1994). Below we refer to the maximum rank case as well-conditioned inertial coupling; otherwise the configuration of the generalized mechanism will be characterized as ill-conditioned inertial coupling.

The expression $P_{RNS} \equiv (E - H^{+}_{bm} H_{bm})$ appearing in both Eqs. (5) and (6), stands for the projector onto the null space of the inertia coupling matrix. This null space we call the reaction null space of a space robot.

Existence of the Reaction Null Space

The reaction null space exists (i.e. dim $\aleph(\boldsymbol{H}_{bm}) > 0$), if the generalized mechanism has some redundancy with respect to the base variables: $n > m$. The redundancy can appear in various forms:

- Kinematic redundancy;
- Dynamic redundancy;
- Redundancy from the selective reaction null space;
- Redundancy due to singularity of the inertia coupling matrix.

First we note that kinematic redundancy is available when the DOF of the manipulators is larger than the DOF of the base. As an example we point out the SSRMS/SPDM system (Xu et al., 1992). Second, recall that the concept of dynamic redundancy was introduced by Arai et al. (Arai et al., 1992). Dynamic redundancy implies the existence of controllable dynamic parameters, which are not directly related to manipulability. One possible interpretation of such dynamic parameters would be in terms of the DOF of the compensators. Third, we point out some applications when the reactions in certain directions can be ignored. For an FFR, reactions yielding translational motion of the base are one example. For an FSMS, one could ignore reactions in those components which correspond to high-stiffness directions of the elastic base structure. To tackle such cases, we introduced the selective reaction null space (Nenchev et al., 1995). Denote by $\boldsymbol{S} = \mathrm{diag}\,(s_1, s_2, \ldots, s_6)$ a selection matrix, where $s_i = 1$ specifies a Cartesian-space direction requiring zero base reaction, while $s_i = 0$ otherwise. Then, we denote the selective reaction null space as $\aleph(\boldsymbol{SH}_{bm})$. Obviously, dim $\aleph(\boldsymbol{SH}_{bm}) \geq$. dim $\aleph(\boldsymbol{H}_{bm})$. Generally, a reaction null space of higher dimension is desirable since it yields a larger DOF when planning the reactionless motion.

Finally, the reaction null space will also exist when the inertia coupling matrix $\boldsymbol{H}_{bm}$ is singular. There will be, however, singular directions in which no inertial coupling/decoupling would be possible at all. Further analysis is needed, which goes beyond the scope of the present work.

Decoupled and Strongly Coupled Motions of Space Robots

The reaction null space projector $\boldsymbol{P}_{RNS}$ ensures total inertial decoupling between the base and the generalized mechanism, in case of an FFR. In case of an FSMS, some nonlinear coupling remains. On the other hand, for some tasks, such as correction of spacecraft attitude errors or changing the spacecraft attitude through manipulator motion (the so-called manipulator inversion task (Nenchev et al., 1992)), in case of an FFR, or suppressing structural vibrations of the base through a proper motion of the generalized mechanism, in case of an FSMS, a very efficient inertial coupling motion should be generated. Efficient coupling is related to efficient transfer of the generalized mechanism energy toward a specific base energy (i.e. FFR: kinetic energy, FSMS: strain energy), or vice versa. The most efficient inertial coupling in a least-squares sense is ensured through the projector $H^{T}_{bm} H_{bm}$ since it is orthogonal to the null space projector.

Note that the general solution of Eq. (3) is

$$\ddot{\theta} = H^{+}_{bm}(W - \dot{H}_{bm}\dot{\theta}) + (E - H^{+}_{bm} H_{bm})\zeta \qquad (7)$$

Note also that with well conditioned inertial coupling (i.e. nonsingular $\boldsymbol{H}_{bm}$), $H_{bm}^{+}=H_{bm}^{T}(H_{bm}H_{bm}^{T})^{-1}$, which clearly shows that the first term on the right-hand-side of Eq. (7) comes from the orthogonal complement of the reaction null space, and hence, ensures the most efficient inertial coupling in a least-squares sense.

Decoupling Control

From the system dynamics Eq. (1) we can eliminate the joint acceleration:

$$\tilde{H}\ddot{x}_b+\tilde{D}\dot{x}_b+\tilde{K}x_b+\tilde{c}+H_m n=\tau, \tag{8}$$

where

$$\tilde{H}=H_{bm}^{T}-H_m H_{bm}^{+}H_b,$$
$$\tilde{c}=c_m+D_m\dot{\theta}-H_m H_{bm}^{+}c_b$$
$$\tilde{D}=-H_m H_{bm}^{+}D_b,\tilde{K}=-H_m H_{bm}^{+}K_b$$

and $\boldsymbol{n}$ denotes an arbitrary vector from the reaction null space.

The structure of the last equation suggests the following decoupling control strategy: (1) design a control loop for exact feedback linearization with regard to the base control subtask, and (2), accomplish end-effector control within the reaction null space, by proper definition of vector $\boldsymbol{n}$. These two subtasks can be realized with the help of the following control law:

$$\tau=u_{ref}+\tilde{c}+H_m n \tag{9}$$

The closed-loop system is

$$\tilde{H}\ddot{x}_b+\tilde{D}\dot{x}_b+\tilde{K}x_b=u_{ref} \tag{10}$$

Base Reaction Control Subtask

$\boldsymbol{u}_{ref}$ is designed to achieve the specific base reaction control, depending on the particular type of space robot. In case of an FSMS, base vibration damping can be achieved with:

$$u_{ref}=-\tilde{G}_v\dot{x}_b, \tag{11}$$

where $\tilde{G}_v\overset{def}{=}H_m H_{bm}^{+}G_v,G_v$ denoting a constant vibration suppression gain. In case of an FFR, the following PD base motion control law would be appropriate:

$$u_{ref}=\tilde{H}\ddot{x}_{bd}+\tilde{G}_{bd}(\dot{x}_{bd}-\dot{x}_b)+\tilde{G}_{bd}(x_{bd}-x_b), \tag{12}$$

where $\boldsymbol{x}_{bd}$ denotes a desired value, $\tilde{G}_{**}\overset{def}{=}-H_m H_{bm}^{+}G_{**},G_{**}$ being a constant gain, and subscript ** indicating either '*bd*' (base-derivative) or '*bd*' (base-proportional). The crucial point with the above controls is the well-conditioning of the inertial coupling, such that matrix $\tilde{H}$ is of full rank *m*.

End-effector Path Tracking Control Subtask

In order to determine the null space vector $\boldsymbol{n}$, we shall make use of the general solution (8). The arbitrary vector ζ appearing there, is determined by substituting the joint acceleration into the end-effector kinematics:

$$\ddot{x}_e = J\ddot{\theta} + \dot{J}\dot{\theta}, \tag{13}$$

where $\boldsymbol{x}_e \in \Re^p$ denotes end-effector task coordinates and $\boldsymbol{J}(\theta) \in \Re^{p \times n}$ is the end-effector Jacobian. Note that the reference frame is at the base. After some formula manipulation, one obtains

$$\ddot{\theta} = H_{bm}^{+}(W - \dot{H}_{bm}\dot{\theta}) + \bar{J}^{+} [\ddot{x}_e - \dot{J}\dot{\theta} - JH_{bm}^{+}(W - \dot{H}_{bm}\dot{\theta})] \tag{14}$$

where $\bar{J} \overset{def}{=} JP_{RNS}$ is a restricted Jacobian matrix appearing typically in redundancy resolution schemes (Nenchev, 1993). It can be shown that $\bar{J}^{+} \in \aleph(H_{bm})$, and hence, the second term on the right hand side of the last equation is indeed a reaction null space vector.

Let the control law be given by (10) with

$$n = \bar{J}^{+} [\ddot{x}_{ed} + G_{ed}\dot{e}_e + G_{ep}e_e - \dot{J}\dot{\theta} - JH_{bm}^{+}(G_v\dot{x}_b - \dot{H}_{bm}\dot{\theta})] \tag{15}$$

where $\boldsymbol{x}_{ed}$ is the desired end-effector path, $\boldsymbol{e}_e = \boldsymbol{x}_{ed} - \boldsymbol{x}_e$ is the path tracking error and $\boldsymbol{G}_{ed}$ and $\boldsymbol{G}_{ep}$ denote proper gain matrices. Under well-conditioned inertial coupling *and* full rankness of the restricted Jacobian $\bar{J}$, as well as when $\boldsymbol{n} \geq \boldsymbol{m+p}$, the base subtask can be performed (vibration suppression or motion tracking), and simultaneously the end-effector error converges to zero asymptotically.

Examples

We illustrate the reaction null space based control by means of three examples of FSMS.

Kinematic Redundancy

First, we consider a planar 3R manipulator mounted on a base translating horizontally, which is attached to the inertial frame through a linear spring and a damper. The parameters of the base are: mass $m_b = 1$ kg, damping $d_b = 0.1$ Nsm^{-1}, stiffness $k_b = 100$ Nm^{-1}.

The parameters of the manipulator are: link length $\boldsymbol{l}_i = 1$ m, (i=1,2,3), link mass $m_i = 10$ kg lumped at the center of each link, link moments of inertia have been ignored.

The upper part of Fig. 3 shows the system, tracking with its end-point a path without inducing any disturbances to the base. Since the reaction null space is 2-dimensional, it is possible to track any path in task space which complies with well-conditioned inertial coupling and non-singularity of matrix $\bar{J}$. Because of the decoupling property of the reaction null space, the selection of the feedback gains is not critical: for example, for the end-point control high gains are used ($\boldsymbol{G}_{ep}$ = diag[400,400] s^{-2}, $\boldsymbol{G}_{ed}$ = diag[200,200] s^{-1}. The gain for base vibration suppression control was $g_v = 10$ rad^{-1}. The desired end-point path was planned through a fifth order spline. Other planning can be also used; there is no requirement for zero boundary conditions. From the results shown in Fig. 3 it is seen that the reference path is tracked perfectly, with practically zero base disturbance.

Herein "ref" denotes the reference path, while "act" stands for the actual one.

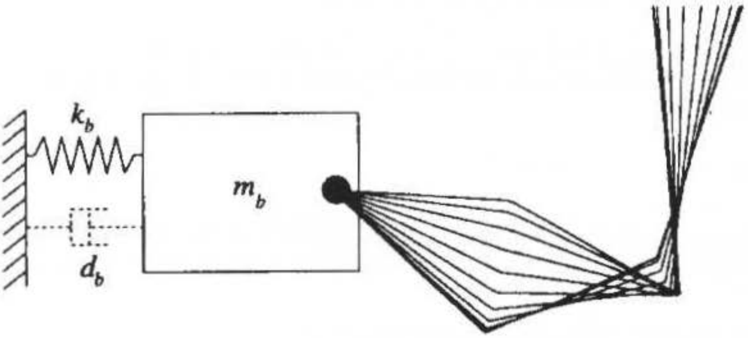

Fig. 3 A Redundant FSMS tracking a reactionless path

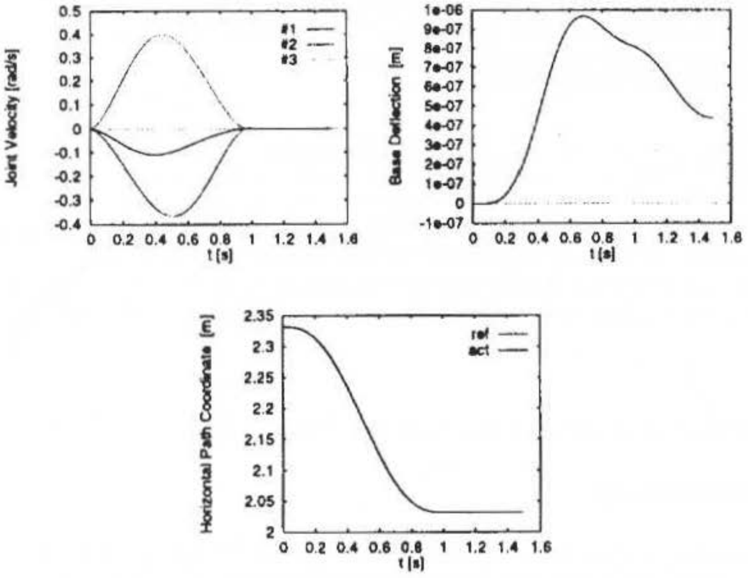

Fig. 4 Redundant FSMS end-point path track-ing

Selective Reaction Null Space

The experimental setup TREP, designed at Tohoku University, consists of a small 2R rigid link manipulator attached to the free end of a flexible double beam representing a flexible base. The TREP FSMS is modeled according to Fig. 5. The local coordinate frame, fixed at the point of attachment of the manipulator to the beam, is referred to as the flexible base coordinate frame. Since the flexible base has been designed as a double beam, the reaction torque can be neglected as a disturbance. This is also the case with the reaction force component along the longitudinal axis of the base. Thus, we shall consider just the reaction force along the so-called low stiffness direction, which coincides with the x axis of the flexible base coordinate frame. This means that $m=1$. Since the manipulator has two motors ($n=2$), there is a one-dimensional selective reaction null space.

The manipulator is driven by DC servomotors with velocity command input. There is no hardware limit for the rotation of the second joint. Joint positions are measured by optical encoders and are fed back for position control. Base deflections and base reactions are measured by the strain gauge and the force/torque sensor, respectively. Real-time feedback vibration suppression uses data from the strain gauge.

We demonstrate the efficiency of the control for both vibration suppression and reactionless path motion. Reactionless path motion is generated via the null space vector $\boldsymbol{n}$. Such motion can be performed in a cyclic manner since the second link has endless rotation capability. An external force is applied to the elastic base during the motion. Details on other experimental conditions can be found in (Nenchev et al., 1997). Figure 6a and Fig. 6b display the results in the case with and without vibration suppression control, respectively. In the first case, we see that base vibration is very effectively suppressed, and the joint motion continues to track the reactionless path. In the case without vibration suppression, it is interesting to note that the vibration of the base is not "disturbed" at all through the joint motion. This clearly demonstrates the dynamic decoupling ability of the control.

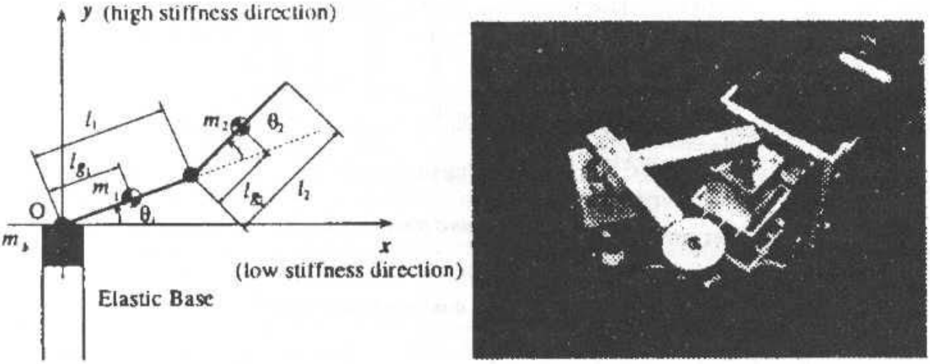

Fig. 5 Model and photo of TREP

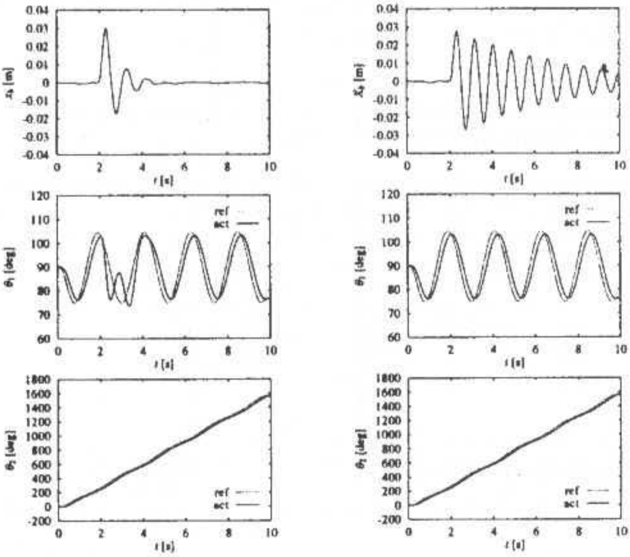

(a) (b)

Fig. 6 Reactionless motion and base vibration of TREP: (a) with vibration suppression; (b) without vibration suppression (experiment)

Dynamic Redundancy

We attached a second arm to our experimental FSMS TREP (Yoshida et al., 1997), as shown in Fig. 7. The upper arm task is defined as end-point control (keeping a fixed position in inertial space) in the presence of vibrations. Obviously, 2 DOF are needed for this task; therefore the same arm cannot be used for vibration suppression. We use the second, lower arm only for vibration suppression. This means that the dynamic redundancy condition will be met. Experimental data is shown in Fig. 8. It is seen that vibration is effectively suppressed by the lower arm. In the same time, the upper arm is able to keep the end-point fixed.

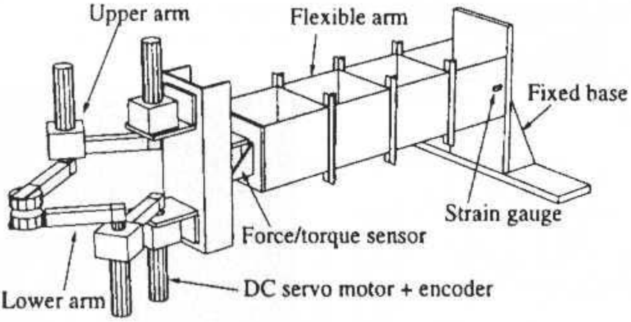

Fig. 7 Experimental dual-arm FSMS TREP-II

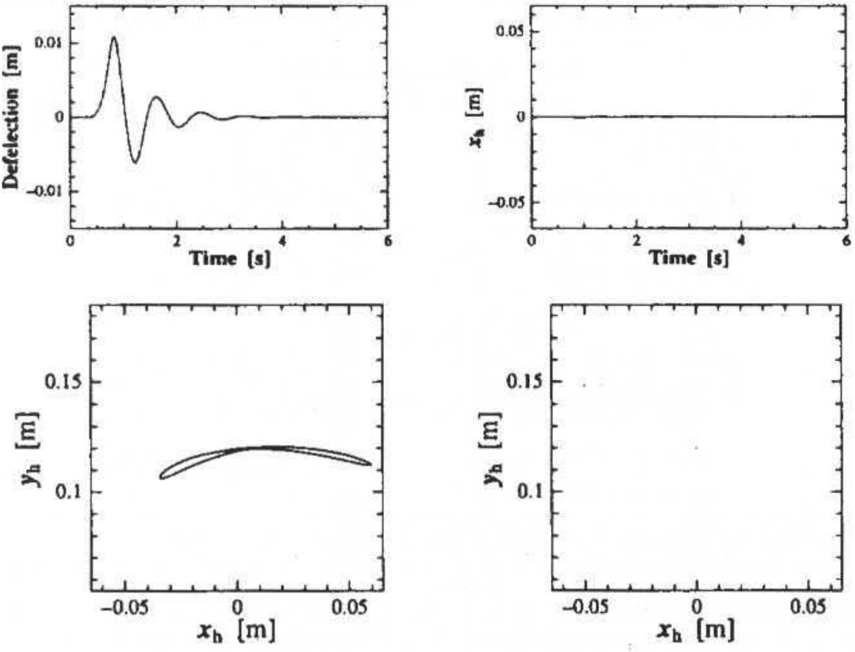

(a) (b)

Fig. 8 Dynamic redundancy utilization with the dual-arm FSMS: (a) Base deflection and lower arm (vibration suppressing) end-tip path; (b) upper arm (end-tip position controlled) end-tip x-coordinate time history and end-tip path

Conclusions

We proposed a control law for space-born robots, based on the reaction null space concept. The control is able to satisfy two subtask simultaneously: the conventional end-effector subtask and in addition, a control subtask for base motion control via inertial coupling/decoupling. We have shown that the method is efficient for various systems comprising kinematic redundancy and/or dynamic redundancy, but also for a nonredundant system with the notion of selective reaction null space.

Acknowledgment

Experimental data is due to Mr. Prasert Vichitkulsawat and Mr. Naoya Saruhashi. The support through the Ippan C Research Project 07805027 Grand-in-Aid for Scientific Research from the Ministry of Education, Science and Culture of Japan is also acknowledged.

References

M. Oda, 1996, "Coordinated control of spacecraft attitude and its manipulator," in Proc. 11th Int. Astrodynamics Symposium, Gifu, Japan, May, pp. 265-270.

Space Robotics: Dynamics and Control. Y. Xu and T. Kanade (eds). Kluwer Acad. Publ. 1992.

W. J. Book and S. H. Lee, 1989, "Vibration control of a large flexible manipulator by a small robotic arm," in Proc. American Control Conference, Pittsburgh, Pennsylvania, pp. 1377-1380.

M. A. Torres, S. Dubowsky and A. C. Pisoni, 1994, "Path-planning for elastically-mounted space manipulator: experimental evaluation of the coupling map," in Proc. IEEE Int. Conf. Robotics and Automation, San Diego, California, May, pp. 2227-2233.

K. Yoshida and D. N. Nenchev, 1995, "Space robot impact analysis and satellite-base impulse minimization using reaction null space," in Proc. 1995 IEEE Int. Conf. Robotics and Automation, Nagoya, Japan, May, pp. 1271-1277.

K. Yoshida, D. N. Nenchev and M. Uchiyama, 1996, "Moving base robotics and reaction management control," Robotics Research: The Seventh International Symposium, Ed. by G. Giralt and G. Hirzinger, Springer Verlag., pp. 101-109.

D. N. Nenchev, K. Yoshida and Y. Umetani, 1990, "Analysis, design and control of free-flying space robots using fixed-attitude-restricted Jacobian matrix," The Fifth Int. Symposium on Robotics Research, ed. by H. Miura and S. Arimoto, The MIT Press, pp. 251-258.

D. N. Nenchev, Y. Umetani and K. Yoshida, 1992, "Analysis of a redundant free flying spacecraft/manipulator system," IEEE Trans. on Robotics and Automation, Vol. 8, No. 1, pp. 1-6.

D. Rohn and C. Lawrence, 1990, "Reaction-compensation technology for microgravity laboratory robots," in Proc. i-SAIRAS' 90, Kobe, Japan, Nov., pp. 299-302.

D. N. Nenchev, K. Yoshida and M. Uchiyama, 1996, "Reaction null-space based control of flexible structure mounted manipulating systems," in Proc. 35th IEEE CDC, Kobe, Japan, Dec., pp. 4118-4123.

M. W. Spong, 1994, "Partial feedback linearization of underactuated mechanical systems," in Proc. 1994 IEEE/RSJ Int. Conf. Intelligent Robots and Systems (IROS'94), Sept., Munich, Germany, pp. 314-321.

T. Arai et al, 1992, "Proposal of dynamic redundancy in robot control," in Proc. IEEE/RSJ Int. Workshop on Intelligent Robots and Systems IROS', July, Raleigh, North Carolina, pp. 1921-1926.

D. N. Nenchev et al, 1995, "Reaction nullspace based space teleoperation," JSME Annual Conf. ROBOMEC', Kawasaki, June, pp. 1003-1006.

D. N. Nenchev, 1993, "Restricted Jacobian matrices of redundant manipulators in constrained motion tasks," Int. J. Rob. Res., Vol. 11, No. 6, pp. 584-597.

D. N. Nenchev et al., 1997, "Experiments on reaction null-space based decoupled control of a flexible structure mounted manipulator system," in Proc. IEEE Int. Conf. Robotics and Automation, Albuquerque, New Mexico, April, pp. 2528-2534.

K. Yoshida et al., 1997, "Positioning control of an elastic base robot," JSME Annual Conf. ROBOMEC' 97, Kanagawa, (in Japanese).

RBCM - J. of the Braz. Soc. Mechanical Sciences
Vol. XXI - No.2 - 1999 - pp. 185-199

ISSN 0100-7386
Printed in Brazil

Integrated Design of Flight/Propulsion Control Systems for Helicopters Using μ-Synthesis

Christian Montenegro Jardim
Takashi Yoneyama
Instituto Tecnológico de Aeronáutica
Divisão de Engenharia Eletrônica
Departamento de Sistemas e Controle
12.228-900 São José dos Campos, SP
takashi@ele.ita.cta.br

Abstract

This work concerns the application of μ-synthesis to the integrated design of a flight/propulsion control system for a typical high performance single-main-rotor helicopter. In order to improve the handling qualities, the controllers are designed to yield accurate control of vertical velocity, yaw rate, pitch and roll attitude. Multivariable robust control theory is required in view of the presence of un-modelled rotor dynamics and parameter uncertainty as well as exogenous disturbances such as wind gusts. Performance and stability tests are carried out both in frequency-domain and time-domain. The end result is a flight/propulsion control system that is stable, robust and ensures good closed loop tracking, disturbance rejection and decoupling properties.

Keywords: *Helicopter, Robust Control, Multivariable, μ-Synthesis.*

Introduction

Effective control of large-scale, multivariable, nonlinear, naturally unstable and highly cross-coupled systems such as helicopters presents a significant challenge to control engineers. Two of the general issues with importance in the control of helicopters are handling qualities and robustness. Handling qualities define its operating characteristics: how easy and effective it is to fly and perform particular tasks without demanding excessive effort or unreasonable skills from the pilot. Robustness specifications concerning helicopter stability and control are due to model uncertainty, which is usually represented by un-modelled rotor dynamics and variation of the stability derivatives along the flight envelope, approximations due to linearization, actuator nonlinear dynamics such as deflection and rate saturations, and off-design operation of the closed-loop system.

This work proposes the application of μ-synthesis to design a flight/propulsion control system for the UH-60, a typical Sikorsky high performance single-main-rotor helicopter. Propulsion is considered in an explicit form because the performance of the helicopter is highly dependent upon it. The integrated design can be carried out effectively by breaking the overall problem into a flight control problem and a propulsion control problem (Rock and Neighbors, 1994).

Additionally, structured variations in the aircraft's aerodynamics properties suggest the use of μ-synthesis as a possible design method, since it is a very powerful design tool to account for such uncertainties in the plant dynamics (Jackson, 1990).

H^∞ Optimal Control and the Structured Singular Value

The importance of H^∞ optimal control arises from the natural characterization of uncertainty provided by the H^∞-norm of a transfer matrix (Zames, 1981), which is the maximum over all frequencies of its largest singular value. A more detailed explanation about the H^∞ space, including the definition of the H^∞ norm, can be found, for instance, in (Francis, 1987; Zhou and Doyle, 1998).

The standard block diagram used in H^∞ control synthesis is shown in figure 1, where **w** represents the exogenous input vector (typically consists of command signals, disturbances, sensor and/or actuator noises); **u** is the control signal; **z** is the error signal vector (typically represents, for example, tracking errors and filtered actuator signals); **y** is the vector of measured outputs. The augmented plant **P**(s) usually contains the nominal plant model $\mathbf{G_0}$(s) and frequency-dependent weights that reflect the stability and performance design requirements to be met by the closed-loop system. The uncertainty block is represented by $\tilde{\Delta}$. This block-diagonal structure is assumed to be stable but unknown, although norm-bounded ($\|\tilde{\Delta}\|_\infty \le 1$).

Manuscript received: June 1997; revision received : February 1999. Technical Editor: Agenor de Toledo Fleury

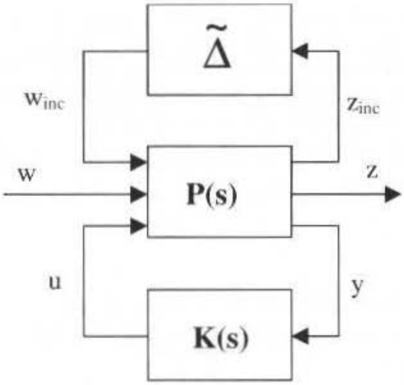

Fig. 1 Standard representation of a plant with uncertainties and under feedback control

Assuming initially that $\tilde{\Delta}$ is absent, the H^∞ control problem is to design a controller $\mathbf{K}(s)$ such that the closed-loop transfer function from $\mathbf{w}$ to $\mathbf{z}$ is minimized. If $\mathbf{z} = \mathbf{P}_{11}\mathbf{w} + \mathbf{P}_{12}\mathbf{u}$ and $\mathbf{y} = \mathbf{P}_{21}\mathbf{w} + \mathbf{P}_{22}\mathbf{u}$, then, provided that $\mathbf{u} = \mathbf{K}\mathbf{y}$, it is possible to write:

$$\mathbf{z} = \left[\mathbf{P}_{11} + \mathbf{P}_{12}\mathbf{K}\left(\mathbf{I} - \mathbf{P}_{22}\mathbf{K}\right)^{-1}\mathbf{P}_{21}\right]\mathbf{w} \tag{1}$$

Therefore, the H^∞ control problem can be stated as:

$$\underset{\mathbf{K}\ stabilizing}{minimize} \left\|\mathbf{P}_{11} + \mathbf{P}_{12}\mathbf{K}\left(\mathbf{I} - \mathbf{P}_{22}\mathbf{K}\right)^{-1}\mathbf{P}_{21}\right\|_\infty \tag{2}$$

The expression whose H^∞-norm is to be minimized in (2) is commonly known as "Linear Fractional Transformation" and will be denoted by LFT(**P**, **K**) in the remainder. By suitably defining **w** and **z** it is possible to cast a number of practical design problems into the form of expression (2) (Maciejowski, 1989; Balas et al., 1994; Skogestad and Postlethwaite, 1996), where the specifications are met by the nominal system if and only if the cost function is less than 1 (nominal performance criterion).

The solution to the H^∞ problem is well established in literature, including the frequency-domain approach (Francis, 1987; Xu, 1989; Kwakernaak, 1993) as well as the traditional state-space approach (Glover and Doyle, 1988). However, as far as robust stability and performance are concerned, the H^∞ control and singular value tests may be conservative. Therefore, it is of paramount importance to define the so-called "structured singular value" (μ) which may reduce considerably the conservativeness imposed by the H^∞ design.

Let **Q** be a transfer function matrix, and consider a block-diagonal structure Δ which depends on the uncertainty and performance objectives of the problem (Balas et al., 1994). Denoting by "B_δ" the set of block-diagonal Δ perturbations satisfying $\|\Delta\|_\infty \leq \delta$, the structured singular value of $\mathbf{Q}(j\omega)$ with respect to the block-diagonal structure Δ is defined as:

$$\mu_\Delta(\mathbf{Q}(j\omega)) \overset{\Delta}{=} \begin{cases} 0, \ if \ \ det\left[\mathbf{I} - \mathbf{Q}(j\omega)\Delta(j\omega)\right] \neq 0 \ \ \forall\omega \in \Re, \forall\Delta \in B_\infty \\ \dfrac{1}{\underset{\Delta \in B_\infty}{min}\left[\overline{\sigma}(\Delta(j\omega))\right]}, \ if \ \ \exists\Delta \in B_\infty, \exists\omega \in \Re \mid det\left[\mathbf{I} - \mathbf{Q}(j\omega)\Delta(j\omega)\right] = 0 \end{cases} \tag{3}$$

Since $\mu_\Delta(\mathbf{Q}(j\omega))$ is frequency-dependent, it is interesting to define $\|.\|_\mu$ as

$$\|\mathbf{Q}\|_\mu = \sup_\omega \mu \ \ (\mathbf{Q}(j\omega)) \tag{4}$$

In the general case $\|.\|_\mu$ does not constitute a norm because of the failure to satisfy the triangle inequality as shown in (Maciejowski, 1989)). It is used in the specialized literature (Maciejowski, 1989; Jackson, 1990; Balas et al., 1994) because some important properties of the structured singular value (Doyle, 1982) are useful in the investigation of the stability and performance of systems when model uncertainty is explicitly considered as in figure 1.

Two important results related to robust stability and performance of the closed-loop system are given in the sequel (Doyle, Wall and Stein, 1982), where **Q**(s) denotes the closed-loop transfer function from $[\mathbf{w}_{\mathbf{inc}}{}^T \quad \mathbf{w}^T]^T$ to $[\mathbf{z}_{\mathbf{inc}}{}^T \quad \mathbf{z}^T]^T$:

a) Robust Stability: The system shown in Fig. 1 achieves robust stability (the closed-loop system remain stable for all $\Xi \in B_l$) if and only if $\|\mathbf{Q}_{\mathbf{11}}\|_\mu < 1$, where the μ is computed with respect to the block-diagonal structure Ξ.

b) Robust Performance: The system shown in Fig. 1 achieves robust performance (the closed-loop system remain stable and satisfy the design requirements for all $\Xi \in B_l$) if and only if $\|\mathbf{Q}\|_\mu < 1$, where the μ is computed with respect to the block-diagonal structure $\Xi = diag\{\Xi, \Delta_0\}$. The "performance block" Δ_0 is fictitious and connects **w** and **z**.

The objective of μ-synthesis is to solve the following frequency optimization problem:

$$\underset{\mathbf{K}\ stabilizing}{minimize} \ \|\mathbf{Q}(\mathbf{P},\mathbf{K})\|_\mu \tag{5}$$

Robust performance is achieved if the cost function is less than 1, which also implies robust stability and nominal performance. The problem can also be stated in the form:

$$\underset{\substack{\mathbf{K}\ stabilizing \\ \mathbf{D_L},\mathbf{D_R} \in \mathbf{D}}}{minimize} \ \left\|\mathbf{D_L}(s)\mathbf{Q}(\mathbf{P},\mathbf{K})\mathbf{D_R}^{-1}(s)\right\|_\infty \tag{6}$$

where the diagonal matrices $\mathbf{D_L}$ and $\mathbf{D_R}$ are stable, minimum phase and have a similar structure to the block-diagonal matrix Ξ. Unfortunately, only approximate solution to the problem can be found and, therefore, μ-synthesis involves a sequence of minimizations, first over the controller variable **K** (holding the **D** variables fixed), and then over the variables **D** (holding the **K** variable fixed). This is often referred to as the "D-K iteration".

Integrated Flight/Propulsion Control Systems Design for Helicopters

This section presents a methodology for the design of flight/propulsion control systems for helicopters, using linearized models for rigid body fuselage, rotor and engine dynamics.

In order to develop the integrated design of the FCS (Flight Control System) or "autopilot" and the propulsion system, rigid body and rotor/engine dynamics are separated (Rock and Neighbors, 1994) according to Fig. 2.

The rigid body dynamics model generates outputs ($\mathbf{y_R}$, $\mathbf{w_R}$) in response to inputs (**d** , $\boldsymbol{\delta}_\mathbf{R}$, $\mathbf{w_E}$). The outputs of interest ($\mathbf{y_R}$) include vehicle attitude, position and their associated rates. The inputs include exogenous disturbances such as wind gusts (**d**), rotor or tail cyclic and collective ($\boldsymbol{\delta}_\mathbf{R}$) and rotor/engine states ($\mathbf{w_E}$). The rotor/engine dynamics model generates outputs ($\mathbf{w_E}$) in response to inputs ($\mathbf{w_R}$, $\boldsymbol{\delta}_\mathbf{E}$, w_f). The outputs might include internal engine quantities (e.g., pressure and spool speeds), rotor dynamics (e.g., inflow, flapping, lead-lag, blade torsional modes) as well as rotor speed (Ω). The rotor/engine dynamics inputs include rigid body states ($\mathbf{w_R}$), rotor or tail cyclic and collective ($\boldsymbol{\delta}_\mathbf{E}$) and fuel flow ($w_f$).

The outer control loop is closed by the autopilot and adjusts the controlled variables in response to command signals ($\mathbf{y_{cmd}}$) and measured outputs ($\mathbf{y_A}$). The performance requirements for this loop are derived from mission-level objectives of the helicopter and include flying and handling quality specifications.

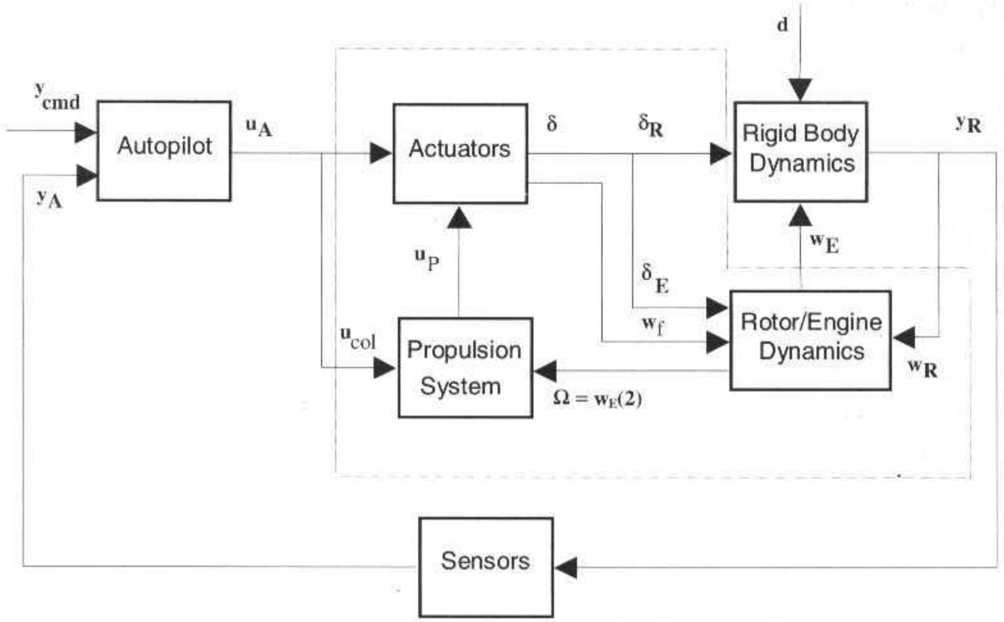

Fig. 2 **Separation between rigid body and rotor/engine dynamics for the integrated design of flight/propulsion control systems for helicopters, where the outer-loop concerns the design of the autopilot and the inner –loop refers to the propulsion sub-system**

The inner control loop is closed by the propulsion system and adjusts the fuel flow (w_f) in response to rotor speed variations (Ω) and vertical collective generated by the autopilot (u_{col}). Its primary purpose, as viewed from a mission-level perspective, is to regulate the rotor speed.

Clearly, the designs of these two control loops must be coordinated since the performance of one affects greatly the performance of the other.

The integrated design is then a sequence of iterative procedures that lead to the synthesis of flight and propulsion control laws. The connection between these two systems is represented by the vectors $\mathbf{w}_E$, $\mathbf{w}_R$ and $\boldsymbol{\delta}_E$. The vector $\mathbf{w}_E$ will be considered as an exogenous perturbation on the rigid body dynamics as well as the vectors $\mathbf{w}_R$ and $\boldsymbol{\delta}_E$ will be on the rotor/engine dynamics. In the H^∞ framework, these vector-valued time signals are properly modelled as:

$$\mathbf{w}_E = \mathbf{W}_E \eta_E, \left\| \eta_E \right\|_\infty \leq 1 \tag{7}$$

$$\mathbf{w}_R = \mathbf{W}_R \eta_R, \left\| \eta_R \right\|_\infty \leq 1 \tag{8}$$

$$\delta_E = \mathbf{W}_\delta \eta_\delta, \left\| \eta_\delta \right\|_\infty \leq 1 \tag{9}$$

where the diagonal matrices $\mathbf{W}_E$, $\mathbf{W}_R$ and $\mathbf{W}_\delta$ are weights used to shape the spectral content of the signals.

The iterations should be interrupted when simulations related to the propulsion system show that the actual components of the vector $\mathbf{w}_E$ have lower magnitude than those associated to the matrix weight $\mathbf{W}_E$ used in the autopilot design, or when the relative difference between them is less than a pre-specified tolerance. In this work, the magnitude of each vector or matrix component will be expressed by the H^∞-norm, which can be applied either in time-domain or frequency-domain (Doyle, Francis and Tannenbaum, 1992).

Application Example

The procedure described above is now applied to an example. A 13 DOF (degrees of freedom) mathematical model which characterizes the open loop UH-60 flight dynamics in hover whose stability derivatives were identified from flight test data using a frequency-response-error identification method (Fletcher, 1995) is considered. The model includes rigid body fuselage dynamics, regressing rotor flap and lead-lag dynamics, main rotor inflow, rotor RPM, and engine torque. The helicopter model has 18 states and 5 inputs, and is unstable and non-minimum phase at trimmed hover condition. Actuators are modelled as first-order lags with a time constant of 50 ms and are included in the original plant description for μ-synthesis design in order to avoid a sluggish aircraft response (Yue and Postlethwaite, 1990). Rate and amplitude saturations are considered by suitably defining weights on the control signals. Sensors are modelled as first-order lags with a time constant of 10 ms, but their dynamics will be left out of the nominal plant description.

The state-space description of the linearized equations of motion, taken from (Fletcher, 1995) is expressed in the standard form as:

$$\begin{aligned}\dot{\mathbf{x}} &= \mathbf{A}\mathbf{x} + \mathbf{B}\mathbf{u} \\ \mathbf{y} &= \mathbf{C}\mathbf{x}\end{aligned} \qquad (10)$$

The state variables, measured outputs and plant inputs are described in Tables 1 and 2. .

Table 1 State variables description

State	Description	State	Description
u	horizontal velocity (ft/s)	v	vertical inflow (ft/s)
v	lateral velocity (ft/s)	Ω	rotor speed (rd/s)
w	vertical velocity (ft/s)	Q	engine torque (lbf.ft)
p	roll rate (rd/s)	a_{1s}	longitudinal flapping angle (rd)
q	pitch rate (rd/s)	b_{1s}	lateral flapping angle (rd)
r	yaw rate (rd/s)	x_1	longitudinal lead-lag
ϕ	roll angle (rd)	x_2	longitudinal lead-lag
θ	pitch angle (rd)	y_1	lateral lead-lag
ψ	yaw angle (rd)	y_2	lateral lead-lag

Table 2 Plant input description and actuator rate/amplitude saturations

Input	Description	Actuator Rate Sat.	Actuator Ampl. Sat.
δ_{lat}	lateral cyclic (in)	24.0 (in/s)	6.0 (in)
δ_{lon}	longitudinal cyclic (in)	20.0 (in/s)	5.0 (in)
δ_{ped}	tail rotor collective (in)	20.0 (in/s)	5.0 (in)
δ_{col}	vertical collective (in)	20.0 (in/s)	5.0 (in)
w_f	fuel flow (lb/s)	2.0 (lb/s^2)	0.5 (lb/s)

The singular value plot of the linearized helicopter model is shown in figure 3, where each curve corresponds to one singular value of $G(j\omega)_{8\times5}$ as a function of ω. This figure shows that the plant is almost singular at low frequencies, since there's a considerable difference in magnitude between the largest and lowest singular values ($\overline{\sigma}/\underline{\sigma} \cong 10^4$). The design implication of this fact is that any attempt to provide compensation at low frequency by inverting the plant (LQG/LTR, loop-shaping) may lead to erroneous results (Yue and Postlethwaite, 1990).

Table 2 also provides the maximum actuator rate and amplitude associated to each of the five control inputs. The μ-synthesis design must take these values into account if acceptable performance and stability properties are required.

Performance Requirements

The specifications outlined in this section concern Level 1 Handling Qualities (Sun and Clarke, 1994) and are related to: helicopter response modes in each of the four input channels (vertical velocity, yaw rate, roll and pitch angles); disturbance attenuation; cross-coupling effects; actuators rate and amplitude saturation limits; robustness to un-modelled dynamics and parameter uncertainty; main rotor speed regulation; maximum engine torque excursion due to power limitations (Prouty, 1990).

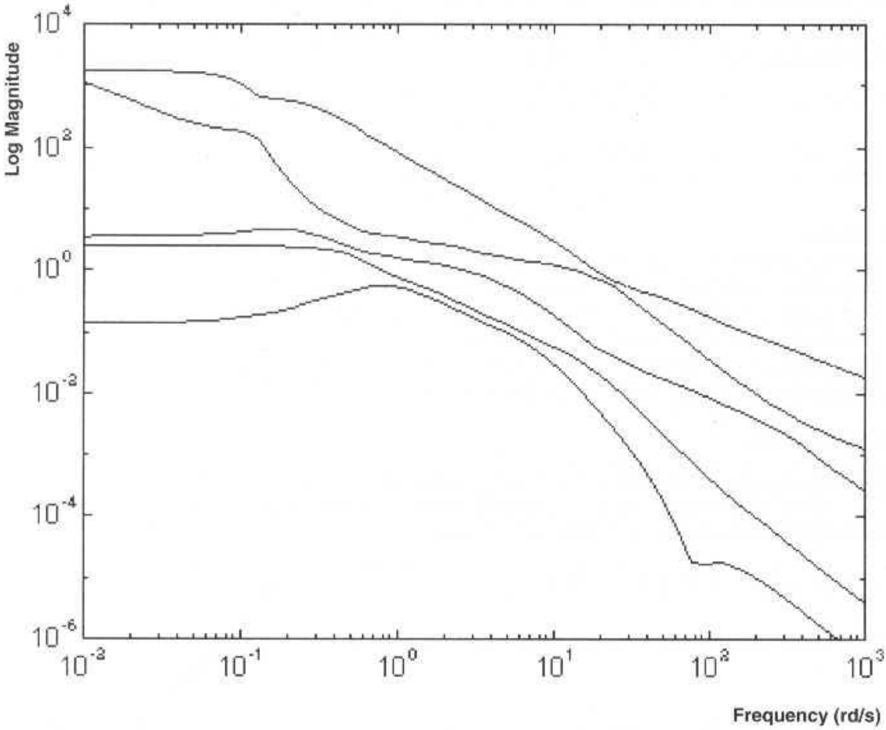

Fig. 3 Singular value plot of uncompensated helicopter at the hover

The helicopter response modes are formulated as a series of transfer functions relating pilot inputs and vehicle response. Through assessment of rotorcraft mission objectives, handling qualities specifications for three response types have been developed (Sun and Clarke, 1994):

1. ACAH (Attitude Command with Attitude Hold): "A control input results in a proportional attitude displacement, for hover and low speed operations in conditions of degraded visual cueing."
2. RC (Rate Command): "Angular velocities about the vehicle roll, pitch or yaw axes are proportional to control inputs, for fully attentive operations in conditions of good visual cueing."
3. TRCPH (Translational Rate Command with Position Hold): "A constant control input must produce a constant translational rate, and the rotorcraft must hold position if the control input is zero. The mode is required for precision hovering tasks and for achieving Level 1 Handling Qualities in NOE (nap-of-the-earth) maneuvers in fair-to-poor visual cueing environments."

For ACAH, the roll attitude and the pitch attitude are of great importance. Desired transfer functions are:

Roll:
$$\frac{\varphi}{\varphi_{cmd}} = \frac{\omega_\varphi^2}{s^2 + 2\xi_\varphi \omega_\varphi s + \omega_\varphi^2} \tag{11}$$

Pitch:
$$\frac{\theta}{\theta_{cmd}} = \frac{\omega_\theta^2}{s^2 + 2\xi_\theta \omega_\theta s + \omega_\theta^2} \tag{12}$$

where typical values for the natural frequency ω_i and the damping ξ_i that will satisfy Level 1 HQ requirements are $\omega_i = 2.071$ rd/s and $\xi_i = 0.707$.

For RC and TRCPH, the desired transfer functions for vertical velocity and yaw rate are:

Vertical Velocity:
$$\frac{w}{w_{cmd}} = \frac{2}{s+2} \tag{13}$$

Yaw Rate:
$$\frac{r}{r_{cmd}} = \frac{2}{s+2} \tag{14}$$

Additionally:

- The steady-state error must be less than 0.1% in each channel;
- Disturbance attenuation must be greater than 40 dB at the frequency range $0 < \omega < 0.43$ rd/s;
- Roll-to-pitch and pitch-to-roll couplings must be less than 25%;
- The steady-state error must be less than 1%;
- The maximum excursion speed of the rotor must be less than 1 rd/s;
- The maximum engine torque excursion must be less than 200 lbf.ft.

Uncertainty Models

All of the uncertainty in modelling the helicopter is captured into the normalized, unknown transfer function $\tilde{\Delta}_G$, used to parametrize the eventual differences between the nominal model $\mathbf{G_0}(s)$ and the actual behavior of the real helicopter, denoted by $\mathbf{G}(s)$.

$$\mathbf{G}(s) = \mathbf{G_0}(s)\left[\mathbf{I_5} + \tilde{\Delta}_\mathbf{G}\mathbf{W_m}\right],\ \tilde{\Delta}_G \text{ stable},\ \left\|\tilde{\Delta}_G\right\|_\infty \le 1 \tag{15}$$

The uncertainty weight $\mathbf{W_m}$ is of the form $\mathbf{W_m}(s) = w_m(s)\mathbf{I_5}$, for a particular scalar valued function $w_m(s)$.

$$\mathbf{W_m}(s) = 0.5\frac{s+1}{s+100}\mathbf{I_5} \tag{16}$$

Hence the set of plants represented by this uncertainty weight is:

$$\mathbf{G}(s) = \left\{\mathbf{G_0}(s)\left[\mathbf{I_5} + \tilde{\Delta}_\mathbf{G}\left(0.5\frac{s+1}{s+100}\right)\right] : \tilde{\Delta}_\mathbf{G} \in \mathbf{C}^{5x5}, \left\|\tilde{\Delta}_\mathbf{G}\right\|_\infty \le 1\right\} \tag{17}$$

This particular choice for $\mathbf{W_m}$ shows that there are potentially 0,5% of modelling error at low frequencies. This percentage tends to be increased up to 50% at higher frequencies. The magnitude of these modelling error percentages indicates that the unstructured uncertainty model is a high-pass filter, which is a typical feature of aerospace control systems (Sun and Clarke, 1994; Jardim, 1997).

The major source of structured uncertainty in the helicopter model is in the stability derivatives. These parameters were identified by a frequency-response-error method (CIFER) and therefore some level of uncertainty due to the inaccuracy of this numerical method still remains. Given the Cramer-Rao bound and insensitivity associated to the identification of each stability derivative, it is possible to verify that the more significant levels of parametric uncertainty are in derivatives Z_p, N_u and N_v (Fletcher, 1995). The nominal values, positions in the stability matrix **A** of the open-loop dynamics model and amount of uncertainty associated to these parameters are shown in Table 3.

Table 3 Uncertainties on elements a_{ij} of the stability matrix A

Derivative	Position	Nominal Value	Uncertainty
Z_p	3,4	-2.495	0.8856
N_u	6,1 and 11,1	-0.01260	4.131e-3
χN_u	10,1	-0.0174	5.705e-3
N_v	6,2 and 11,2	9.681e-3	4.095e-3
χN_v	10,2	0.0134	5.655e-3

Autopilot Design

The autopilot design concerns the synthesis of a controller for the rigid body dynamics as shown in the outer-loop of the diagram in figure 2. Therefore, the helicopter model should be partitioned. Only the first 9 states will be considered as the rigid body modes, whereas the remaining are considered as perturbations from the rotor/engine dynamics.

There are three basic sources of exogenous signals in the autopilot design: perturbations from the rotor/engine dynamics, command signals and wind gusts.

The perturbations from the rotor/engine dynamics are modelled according to expression (7). The command signals are provided by the pilot and/or the guidance law and are modelled similarly as:

$$y_{cmd} = \boldsymbol{W}_{cmd}\, \eta_{cmd}\,,\ \|\, \eta_{cmd} \,\|_{\infty} \leq 1 \tag{18}$$

where

$$\boldsymbol{W}_{cmd} = \text{diag}\ \{\ \text{W}_{\text{cmd,w}};\ \text{W}_{\text{cmd,r}};\ \text{W}_{\text{cmd},\phi};\ \text{W}_{\text{cmd},\theta}\} = \text{diag}\ \{\ 5.0;\ 0.2;\ 0.2;\ 0.2\ \}. \tag{19}$$

The wind gusts are naturally represented by stochastic signals and can be incorporated into the μ-synthesis design by introducing the vector $\mathbf{d} = [\,d_u \quad d_v \quad d_w\,]^T$ into the helicopter model force and moment equations. They have the effect of modifying the translational velocities by a quantity "d_i" at each integration path of the equations of motion. In the H^{∞} framework, such signals are modelled as the unit ball in $L^2[0,\ \infty)$ filtered by a problem dependent weighting function that shape their spectral content. In this example, the vector **d** is properly modelled as (Pegollo, 1996):

$$\boldsymbol{d} = \boldsymbol{W}_g\, \eta_g\,,\ \|\, \eta_g \,\|_2 \leq 1 \tag{20}$$

where

$$\boldsymbol{W}_g = diag\left\{\text{W}_{\text{g,u}}; \text{W}_{\text{g,v}}; \text{W}_{\text{g,w}}\right\} = diag\left\{\frac{0.0043}{s+0.43}; \frac{0.043}{s+0.43}; \frac{0.043}{s+0.43}\right\}. \tag{21}$$

There are several variables which are to be kept "small" in the face of those exogenous signals:

Control signals levels: The control signals amplitude and rate should remain below certain limits to avoid actuator saturations. This can be effectively done by introducing the penalty weight $\boldsymbol{W}_u$:

$$z_u = \boldsymbol{W}_u \boldsymbol{u}_A \tag{22}$$

where

$$\boldsymbol{W}_u = diag\left\{\frac{0.5s}{s+20}; \frac{0.5s}{s+20}; \frac{0.5s}{s+20}; \frac{0.5s}{s+20}\right\}. \tag{23}$$

The first-order highpass filters with a cutoff frequency of 20 rd/s were introduced to limit the magnitudes of poles of the controller, in order that any digital implementation of it would not be an issue.

- Tracking errors: The tracking errors are defined as the difference between the aircraft actual and ideal responses to each of the four command signals. They are weighted according to:

$$z_e = W_e e = W_e\,(y_{actual} - W_d y_{cmd}) \tag{24}$$

where

$$\mathbf{W_d} = diag\left\{\frac{2}{s+2}; \frac{2}{s+2}; \frac{4.29}{s^2+2.93s+4.29}; \frac{4.29}{s^2+2.93s+4.29}\right\}. \tag{25}$$

The weighting function $\boldsymbol{W}_e$ is selected to ensure good tracking accuracy in each of the controlled outputs w, r, ϕ and θ. This can be accomplished (Yue and Postlethwaite, 1990; Balas et al., 1994) by using high-gain lowpass filters to ensure good tracking, disturbance attenuation and decoupling properties. The design weight $\boldsymbol{W}_e$ can be chosen as:

$$\mathbf{W_e} = diag\left\{\frac{s+12}{s+0.012};\frac{s+12}{s+0.012};\frac{s+40}{s+0.04};\frac{s+40}{s+0.04}\right\} \tag{26}$$

Fictitious sensor noises were introduced into the problem to make matrix $\boldsymbol{D}_{21}$ full row rank (Glover and Doyle, 1988). In this example, the sensor noises are modelled similarly as the wind gusts, with a diagonal weight equal to $10^{-4}\mathbf{I}_7$. The controller has 11 inputs and 4 outputs, and the block diagonal structure $\widetilde{\Delta}$ can be expressed as:

$$\widetilde{\Delta} = diag\left\{\delta_1;\delta_2;\delta_3;\widetilde{\Delta}_{\mathbf{R}}\right\}\delta_i \in C, \widetilde{\Delta}_{\mathbf{R}} \in \mathbf{C}^{4x4}, \left\|\widetilde{\Delta}\right\|_\infty \le 1 \tag{27}$$

Propulsion System Design

The propulsion system design concerns the synthesis of a controller for the rotor/engine dynamics as shown in the inner-loop of the diagram in Fig. 2. The last 9 states related to rotor vertical inflow, regressing flap, lead-lag, RPM and engine torque are the dynamic modes, whereas the remaining are perturbations from the rigid body dynamics.

There are two basic sources of exogenous signals in the propulsion system design: perturbations from the rigid body dynamics ($\boldsymbol{w}_R$) and perturbations from the autopilot dynamics ($\boldsymbol{\delta}_E$). These perturbations can be mathematically described by expressions (8) and (9), where the weighting functions $\boldsymbol{W}_R$ and $\boldsymbol{W}_\delta$ should be iteratively changed during the design until a satisfactory solution is found. Further details about this iteration could be found in (Jardim, 1997).

In the propulsion system design, the so-called "performance variables" are:

- Control signal level: The amplitude and rate of the fuel flow should remain below the limits imposed by table 2 to avoid actuator saturations in face of the exogenous signals. Similarly to the autopilot design case, this can be effectively done by introducing the penalty weight W_u:

$$z_u = W_u\, w_f \tag{28}$$

where

$$W_u = \frac{10s}{s+20}\,. \tag{29}$$

- Output excursion level: In order to limit the output excursions from the corresponding nominal values according to the design specifications, it is necessary to introduce the weighting function W_p which can be defined as:

$$z_p = W_p\, y_E = W_p\, w_E \tag{30}$$

where

$$W_p(s) = diag\left\{\frac{0.02}{s+2};0.5\frac{s+1}{s+0.005};\frac{0.01}{s+2};\frac{20}{s+2};\frac{20}{s+2}\right\}. \tag{31}$$

A fictitious sensor noise was introduced into the rotor speed (Ω) output channel to make matrix $\boldsymbol{D}_{21}$ full row rank, where the noise weighting function magnitude is the same as in the autopilot design case (10^{-4}). The controller has 2 inputs and 1 output, and the block-diagonal structure $\widetilde{\Delta}$ can be expressed as:

$$\tilde{\Delta} = diag\left\{\delta_1;\delta_2;\delta_3;\delta_4;\tilde{\Delta}_{\mathbf{P}}\right\} \delta_i \in C, \hat{\Delta}_{\mathbf{P}} \in \mathbf{C}^{5x5}, \left\|\tilde{\Delta}\right\|_\infty \le 1 \tag{32}$$

DK Iteration and Control Systems Integrated Design

This section presents the results of the D-K iteration applied to the integrated design of flight/propulsion control systems for the UH-60 helicopter. The procedure previously described converged when:

$$\mathbf{W_E} = diag\left\{W_v;W_\Omega;W_Q;W_{a_{1s}};W_{b_{1s}}\right\} = diag\left\{\frac{10}{s+1};\frac{0.5}{s+1};\frac{20}{s+1};\frac{0.05}{s+1};\frac{0.05}{s+1}\right\} \tag{33}$$

$$\mathbf{W_R} = diag\left\{W_u;W_v;W_w;W_p;W_q;W_r\right\} = diag\left\{\frac{80}{s+2};\frac{70}{s+2};\frac{10}{s+2};0.2;0.2;0.2\right\} \tag{34}$$

$$\mathbf{W}_\delta = diag\left\{W_{lat};W_{lon};W_{ped};W_{col}\right\} = diag\left\{6.0;0.06;1.0;0.6\right\} \tag{35}$$

The D-K iteration summary is presented in Tables 4 and 5 for the autopilot and propulsion system designs, respectively. It can be seen that both closed-loop subsystems achieve robust performance, since the corresponding cost functions are less than 1.

Table 4 D-K iteration summary for autopilot design

Iteration	1	2	3
Controller order	39	53	53
Total D-scale order	0	14	14
γ_{max}	5.0	1.249	1.006
γ_{min}	0.6	0.6	0.6
tol	0.1	0.01	0.01
$\gamma_{optimal}$	1.3562	0.9543	0.9400
$\|\|Q(P_A, K_A)\|\|_\mu$	1.221	0.953	0.9400

Table 5 D-K iteration summary for propulsion system design

Iteration	1	2
Controller order	24	42
Total D-scale order	0	18
γ_{max}	5.0	1.340
γ_{min}	0.6	0.6
tol	0.1	0.01
$\gamma_{optimal}$	3.3156	1.3205
$\|\|\mathbf{Q}(\mathbf{P}_E, \mathbf{K}_E)\|\|_\mu$	1.279	**0.899**

Analysis of the Controllers

The design process leads to high order controllers, which is a typical feature of μ-synthesis design. The frequency responses of the autopilot and propulsion system, which have 53 and 42 states, respectively, are shown in Figs. 4 and 5. It can be seen that they have high gain at low frequency, for good tracking, and low gain at high frequency, for robustness.

Figure 6 presents the plot of $\mu_{\tilde{\Delta}}\left[Q_{11}(P,K)\right]$ versus frequency in the integrated case. The system achieves robust stability to unstructured and structured uncertainties, since the corresponding μ-norm is less than 1.

The wind gust disturbance attenuation can be seen in Fig. 7, which compares the open and closed-loop disturbance to output transfer functions. In this figure, $1/\overline{\sigma}\left[W_e(j\omega)\right]$ is also shown to illustrate how the value of $W_e(s)$ was chosen.

The closed-loop tracking relates the helicopter response to the pilot input commands. (Sun and Clarke, 1994) present the desired transfer functions that relate the aircraft vertical velocity, yaw rate, roll and pitch attitude responses to vertical collective, tail rotor collective, lateral and longitudinal cyclic inputs, respectively. The most important and significant results are demonstrated in Figs. 8-11, where the transfer functions in the four input channels of interest are presented and compared with the

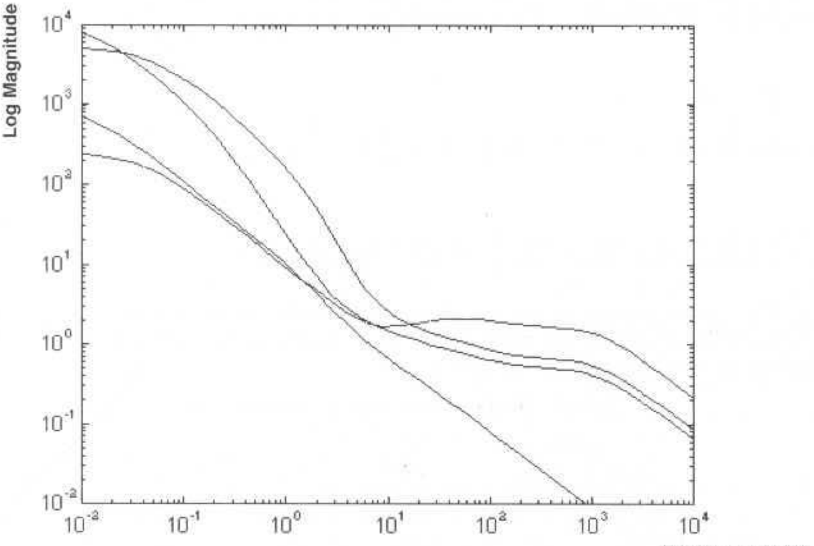

Fig. 4 Singular value plot of the autopilot

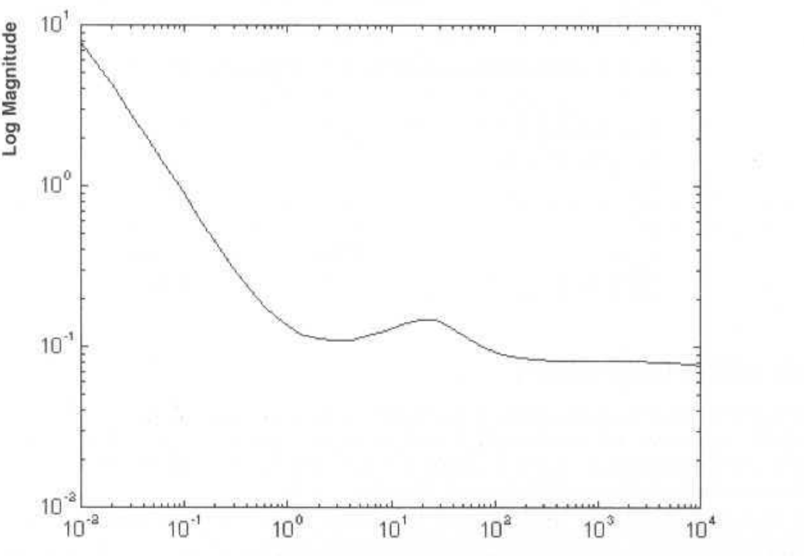

Fig. 5 Singular value plot of the propulsion system

desired handling qualities specifications in transfer function form. These figures show that the μ-synthesis design method produces a closed-loop system that achieves acceptable handling quality tracking properties, although it is possible to view some distortion in the yaw rate response (Fig. 9). Such a distortion is probably caused by the effect of the rotor lead-lag dynamics which responds at about 20 rd/s (Fletcher, 1995).

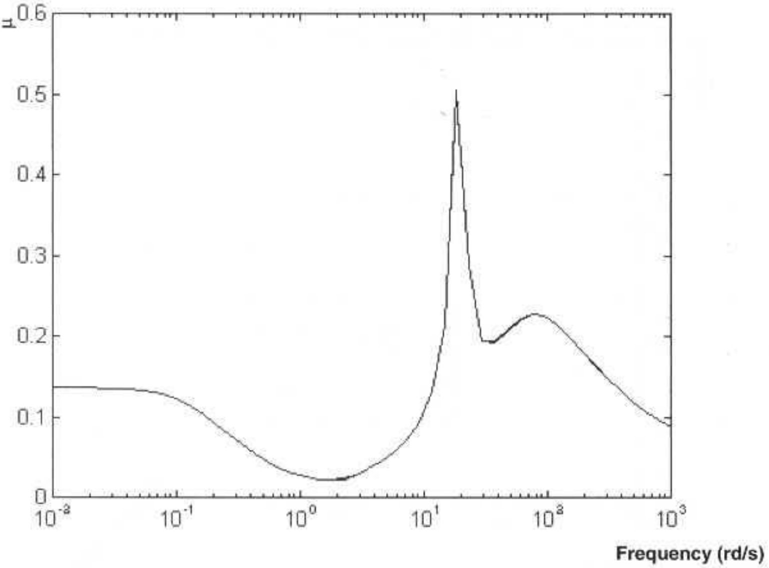

Fig. 6 Robust stability analysis of the integrated system using μ

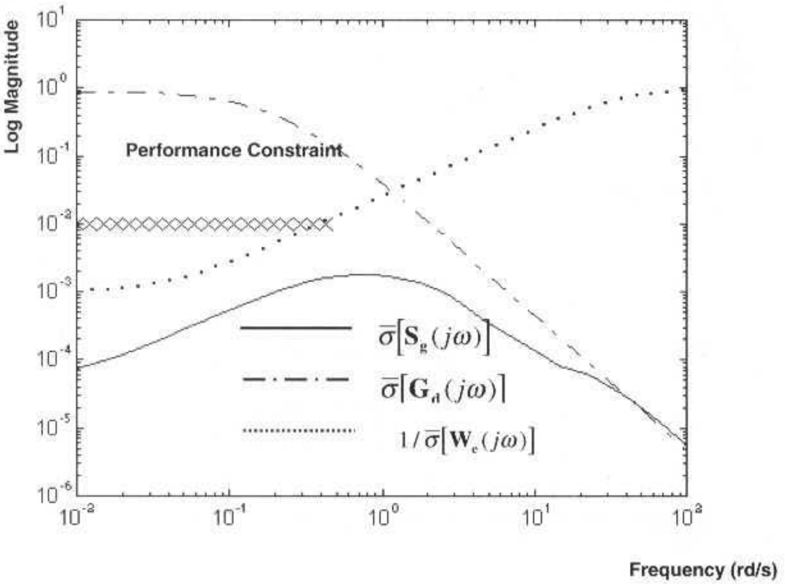

Fig. 7 Comparison of the open and closed-loop disturbance to output transfer functions for the continuous-time integrated system

In order to evaluate the proposed controller, a general simulation using the helicopter linearized model presented by (Fletcher, 1995) was developed and embedded within the ©MATLAB-based ©SIMULINK environment. In this manner, both linear and partial nonlinear flight simulations of the helicopter were carried out effectively and conveniently. The helicopter model, sensor dynamics and the controllers are loaded directly from a ©MATLAB file in matrix form. Actuator dynamics and relevant non-linearities are properly modelled. The nominal model, worst-case unstructured uncertainty

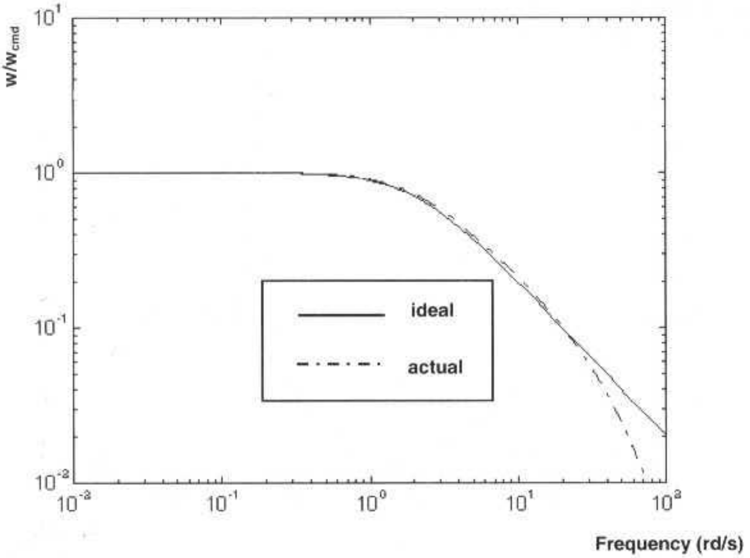

Fig. 8 Vertical velocity handling qualities matching for the integrated system

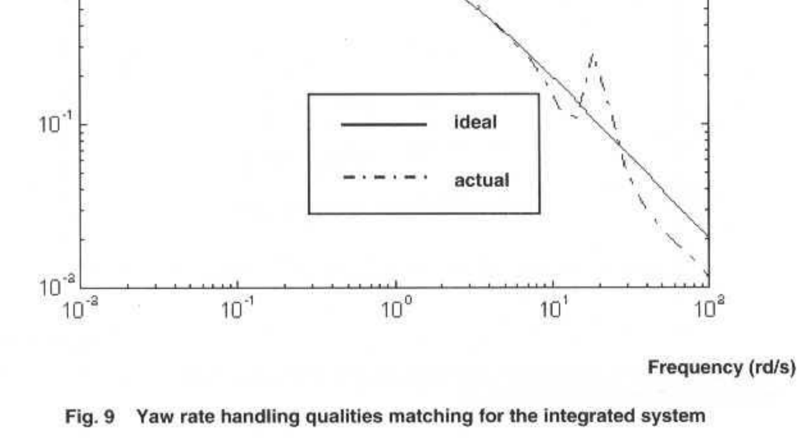

Fig. 9 Yaw rate handling qualities matching for the integrated system

and significant changes in the aircraft response profiles due to stability derivative variations (Z_p, N_u and N_v) were simulated. Wind gusts (η_g) were considered as band limited white noises with zero mean, unitary variance and sampled at every 0.5 s. As expected, an accurate decoupling control effect was obtained. The integrated control system also exhibited good robustness to un-modelled sensor dynamics (even thought they were not included in the original nominal plant description).

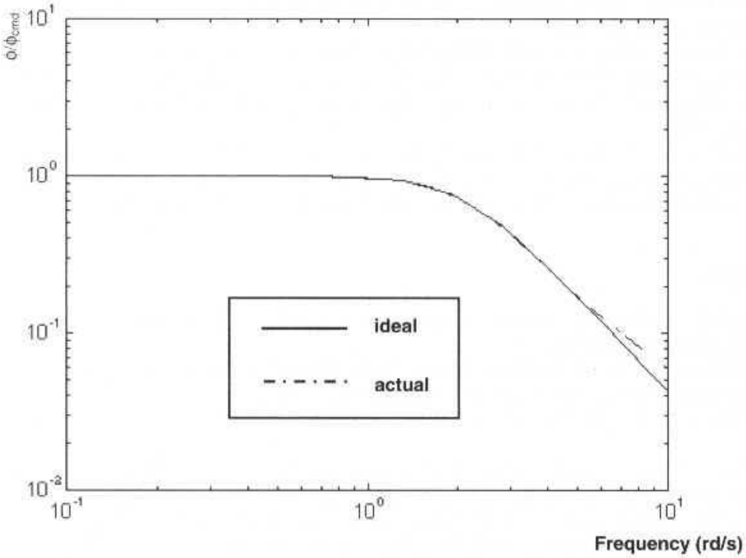

Fig. 10 Roll attitude handling qualities matching for the integrated system

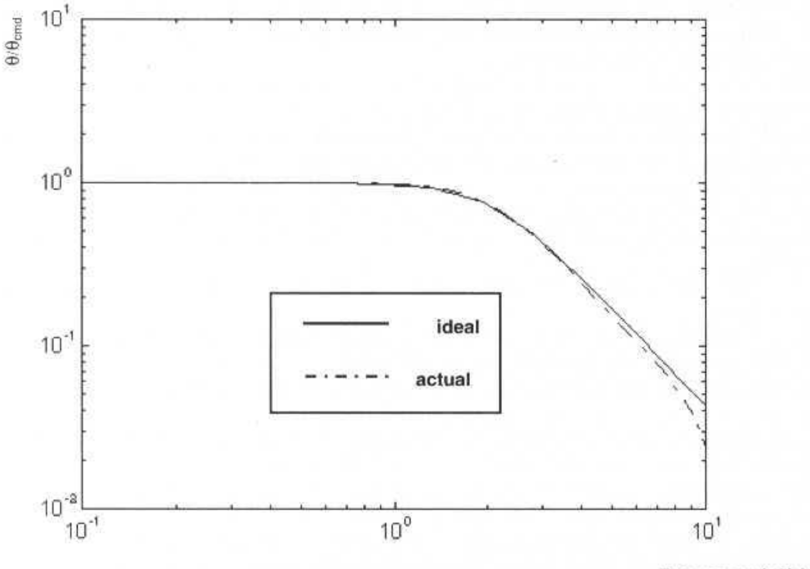

Fig. 11 Pitch attitude handling qualities matching for the integrated system

Conclusions

This work presents a straightforward and systematic methodology for the design of a robust flight/propulsion control system for a typical high performance single-main-rotor helicopter. The μ-synthesis approach is used, since it is a powerful design tool to account for structured variations in the plant dynamics. In this particular example, it incorporates a model-following approach to achieve the handling quality specifications and improve the aircraft robustness to un-modelled dynamics and parameter uncertainties. The end result is a closed-loop system that simultaneously satisfies criteria of robustness and design performance.

However, the μ-synthesis design method usually leads to high order controllers. Thus, controller model reduction is required in order to reduce the complexity of the flight/propulsion control systems. This could be effectively done, for example, by balancing and truncating the small Hankel singular values (Jardim, 1997).

Furthermore, as a suggestion for future works, after the requirements for a continuous-time control law are satisfied, a discrete-time version for implementation in an onboard computer should be designed such that the resulting sampled-data system retains the required robustness and performance.

References

Balas, G.J., Doyle, J.C., Glover, K., Packard, A. and Smith, R., 1994, "μ-Analysis and Synthesis Toolbox", MUSYN Inc. and The MathWorks, January.

Doyle, J.C., 1982, "Analysis of Feedback Systems with Structured Uncertainties", Proceedings, Institution of Electrical Engineers, Part D, No. 6, Vol. 129, pp. 242-250, November.

Doyle, J.C., Francis, B.A. and Tannenbaum, A.R., 1992, "Feedback Control Theory", Macmillan Publishing Company.

Doyle, J.C., Wall, J.E. and Stein, G., 1982, "Performance and Robustness Analysis for Structured Uncertainty", Proceedings, IEEE Conference on Decision and Control, pp. 629-636, Orlando, Florida.

Fletcher, J.W., 1995, "Identification of UH-60 Stability Derivatives Models in Hover from Flight Test Data", Journal of the American Helicopter Society, No. 1, Vol. 40, pp. 32-46, January.

Francis, B.A., 1987, "A Course in H^∞ Control Theory", Lecture Notes in Control and Information Sciences, Ed. Springer-Verlag, Vol. 88, Berlin.

Glover, K. and Doyle, J.C., 1988, "State-Space Formulae for All Stabilizing Controllers that Satisfy an H^∞ Norm Bound and Relations to Risk Sensitivity", System and Control Letters, Vol. 11, pp. 167-172.

Jackson, P., 1990, "Applying μ-Synthesis to Missile Autopilot Design", Proceedings, 29th Conference on Decision and Control, Honolulu, Hawaii, December.

Jardim, C.M., 1997, "Projeto Integrado dos Sistemas de Controle de Vôo e Propulsão de Helicópteros Utilizando a Metodologia μ/H^∞", (in portuguese), Master Thesis, ITA.

Kwakernaak, H., 1993, "Robust Control and H^∞ Optimization", Automatica, No. 2, Vol. 29, pp. 255-273.

Lin, C.-F., 1994, "Advanced Control Systems Design", Prentice-Hall Series in Advanced Navigation, Guidance, and Control, and Their Applications.

Maciejowski, J.M., 1989, "Multivariable Feedback Design", Addison-Wesley Publishers.

Pegollo, C.A., 1996, "Atenuação de Efeitos de Distúrbios Atmosféricos em Aeronaves", (in portuguese), Master Thesis, ITA.

Prouty, R.W., 1990, "Helicopter Performance, Stability, and Control", Robert E. Krieger Publishing Company, Malabar, Florida.

Rock, S.M. and Neighbors, W.K., 1994, "Integrated Flight/Propulsion Control for Helicopters", Journal of the American Helicopter Society, No. 3, Vol. 39, pp. 34-42, July.

Skogestad, S. and Postlethwaite, I, 1996, "Multivariable Feedback Control: Analysis and Design", John Wiley, New York.

Sun, X.D. and Clarke, T., 1994, "Application of Hybrid μ/H^∞ Control to Modern Helicopters", Proceedings, IEE International Conference on Control, Vol. 2, pp. 1532-1537, March.

Yue, A. and Postlethwaite, I., 1990, "Improvement of Helicopter Handling Qualities Using H^∞-Optimisation", Proceedings, Institution of Electrical Engineers, Pt. D, No. 3, Vol. 137, pp. 115-129, May.

Zames, G., 1981, "Feedback and Optimal Sensitivity: Model Reference Transformations, Multiplicative Seminorms, and Approximate Inverses", IEEE Transactions on Automatic Control, No. 2, Vol. AC-26, pp. 301-320.

Zhou, K. and Doyle, J.C., 1998, "Essentials of Robust Control", Prentice Hall, Upper Saddle River, New Jersey.

RBCM - J. of the Braz. Soc. Mechanical Sciences
Vol. XXI - No.2 - 1999 - pp. 200-210

ISSN 0100-7386
Printed in Brazil

The Influence of Gas Pressure on Single Solid Fuel Combustion

Carlos A. Gurgel Veras[1]
Universidade de São Paulo
Escola Politécnica
Departamento de Engenharia Mecânica
05508-900 São Paulo, SP Brazil

João Andrade de Carvalho Jr.
Instituto Nacional de Pesquisas Espaciais
Laboratório Associado de Combustão e Propulsão
12630-000 Cachoeira Paulista, SP Brazil

Jaakko Saatamoinen
Technical Research Centre of Finland
P. O. Box 1603
41101 Jyväskylä, Finland

Abstract

A model designed for the prediction of heat and mass transfer effects in the boundary layer of a reacting coal particle was extended to analyze the trends as the pressure is increased well above atmospheric conditions. The oxidation of volatile species in the boundary layer is based on a two step mechanism where the dependence of the flame speed on pressure is accounted for. The model was able to particle temperature in a broad range of gas composition and pressure as well as fuel type.

***Keywords**: Coal Combustion, Char Combustion, Pressurized Combustion, Combustion Modeling.*

Introduction

The field of pressurized coal combustion has gained great attention recently. The aim is mainly to improve thermal efficiency and reduce gas emissions. With pressurization, a 50% fuel energy recover can be attained using combined power cycles, against 38%, in average, without pressurization. Furthermore, a reduction in the size of the furnaces can also be accomplished.

Combustion of pulverized coal can be divided in four processes: particle heating, coal thermal degradation, homogeneous reactions in the boundary layer, and heterogeneous reactions at the walls of the porous network of the remaining char, as well as at the outer surface. All of these processes can somewhat occur distinctly in time or overlap to some extent. A numerical model, which simulates the burning of single coal particles, must rely on experimental parameters from all the processes cited above in order to close the mathematical formulation. Therefore, to simulate all the steps, experimental parameters for devolatilization, usually taken under inert reactor atmospheres, and char oxidation data from a wide range of reactor pressures and temperatures ought to be provided. For hydrocarbon reactions, data from atmospheric conditions give reasonable results as a first approximations to solve such a complex phenomenon. Nevertheless, modeling validation will be supported only by experiments taking place in a well controlled reactor atmosphere, in which the burning of the particles will be closer to a real situation.

Investigators have already studied the effect of increasing pressure on the product yields from pyrolysis of coal (Anthony, 1976; Griffin,1994). There seems to have a common observation, experimentally and theoretically, about the reduction in the total yields due to secondary reactions in the coal voids and pores (James, 1976). Mass transfer effects in the coal matrix were inferred as the reason why more char is formed. Since the escape of volatiles in reduced due to pressure effects, the more reactive compounds (tar) have an extra time inside the coal porous structure to undergo secondary deposition reactions.

The overall behavior of combustion of pulverized coal particles under pressure has been studied (Monson et al, 1995; Mühlen, 1995). It has been shown that, to a less or greater extent, pressure alters the ignition, temperature, and reactivity of coal particles. Up to 10 atm and 20 μm particle diameter the pressure effects on volatiles yields can be assumed of little importance. As the particle size and external pressure increase, the escape rate of volatiles becomes a competition between the internal transport and

---

[1] Currently at Laboratório Associado de Combustão e Propulsão, Instituto Nacional de Pesquisas Espaciais, 12630-000, Cachoeira Paulista, SP, Brazil.

Manuscript received: May 1997; revision received: October 1998. Technical Editor: Angela Ourívio Nieckele.

the secondary deposition reactions. For pulverized coal combustion, the devolatilization time is thought to be one order of magnitude smaller than char oxidation. As a consequence, surface reaction parameters for pressurized conditions must also be sought for proper modeling on char oxidation. Monson et al (1995) have performed many char oxidation experiments at atmospheric and elevated pressures allowing determination of global reaction rate coefficients which can be applied to coal combustion. The temperature range, in their experiments, comprises well those found in actual pulverized coal combustors.

The Combustion and Conversion Technology Research Group at the Technical Research Centre of Finland (VTT/Energy) has done studies of pulverized particle combustion and gasification in a pressurized entrained-flow reactor (PEF). The maximum operating temperature of the PEF is 1673 K and pressures as high as 2 MPa can be reached. The PEF is able to perform experiments under high precision controlled operating conditions. The results from a set of tests are used in this work, for model validation. Particle temperature and 90% burnout times are employed for comparison, since gas composition and temperature distribution in the boundary layer of a burning particle are still a challenge to be determined experimentally.

We present in this work a numerical model, novel in many aspects, which gives a good insight of the most important physical and chemical processes encountered in pulverized coal combustion. The model is fully transient and may treat particles of any size under a wide range of combustion conditions. Musarra et al (1986) presented a numerical model to describe heat and mass transfer in the vicinity of a single reacting cal particle in an atmospheric environment. The model is two dimensional, but one-dimensional simulations have shown meaningful results at low particle Reynolds numbers. The predictions were restricted to atmospheric pressure. Aho et al. (1995) have investigated the effects of pressure, oxygen partial pressure and temperature on the formation of N_2O, NO and NO_2 from pulverized coal. A reduction in NO emissions was identified as the reactor pressure was increased. Saastamoinen et al. (1996) presented a theoretical and experimental study on pressurized pulverized fuel combustion in different concentration of oxygen and carbon dioxide. The experiments were performed in the PEF reactor mentioned above. Their theoretical analysis covered the heat and mass transfer effects under pressure and, more importantly, the initial heating stage of a particle. Their results agreed well, in some cases, with experimental data from the PEF reactor.

Nomenclature

A_p = particle external area (m^2)
A_c = CO/CO_2 apparent frequency factor
B_i = pre-exponential factor for pyrolysis (s^{-1})
a_i = coefficient
c_g = specific heat of gas (J kg^{-1} K^{-1})
c_p = specific heat of particle (J kg^{-1} K^{-1})
D_{km}= binary diffusivity of specie k into the mixture (m^2 s^{-1})
E = activation energy (J $kmol^{-1}$)
E_c = CO/CO_2 activation energy (J $Kmol^{-1}$)
GR = total number of homogeneous reactions
h_k = heat of reaction (homogeneous) (J kg^{-1})
$h_{r,i}$ = heat of reaction (homogeneous) (J kg^{-1})
h_v = pyrolysis heat of reaction (J kg^{-1})
$k_{1,2}$ = rate of pyrolysis (s^{-1})
k_H = rate of homogeneous reaction (kmol m^{-3} s^{-1})
M_0 = particle initial mass (kg)
m'' = mass flow rate per unit area (kg m^{-2} s^{-1})
NS = number of species
P_i = partial pressure of species i
P = pressure (MPa)
R = particle initial diameter (m)
R_u = gas constant (Jkmol^{-1} K^{-1})
r = distance from particle center (m)
SR = total number of heterogeneous reactions
s'' = particle surface reactivity (kg m^{-2} s^{-1})
s = rate of combustion of char (carbon) (kg s^{-1})
t = time (s)
T = temperature (K)
u = velocity (m s^{-1})
V = volume or volatile
W = molecular weight (kg $kmol^{-1}$)
$\dot{w}'''$ = rate of reaction (kg m^{-3} s^{-1})
Y = mass fraction
α = volatile mass fraction
ε = particle emissivity
λ = thermal conductivity (W m^{-1} K^{-1})
μ = dynamic viscosity (kg m^{-1} s^{-1})
ρ = density (kg m^{-3})
ρ_v = undergraded part of coal (kg m^{-3})
σ = Stefan-Boltzmann constant (5.67×10^{-8} W m^{-2} K m^{-4})
ψ = fraction of CO/CO_2 production

Subscripts

1 = volatile 1
2 = volatile 2
c = surface heterogeneous reaction
g = gas
p = particle
s = surface
v = volatiles
w = wall

Mathematical Formulation

In order to make the problem numerically treatable, some assumptions have to be made. In the solid matrix, the particle temperature is time-dependent and a function of radial position. The particle is divided in shells where the local temperature history is used for pyrolysis reactions. This gives a local conversion for the particle interior. Devolatilization takes place with decreasing density and escape of volatiles is assumed to be instantaneous. Particle swelling is not considered. With no volatile matter, burning takes place with a shrinking radius. Nevertheless, as long as oxygen is reaching the particle surface, pyrolysis and char combustion may occur simultaneously. Radiation from the reactor walls is possible in the heat transfer to the particle. Oxidation of some species (tar) which are precursor of soot formation is observed during coal volatiles burning. As pointed by Cho et al. (1995), nonuniform mixing and particle dispersion on pulverized coal flames ensure that the products of primary devolatilization are transformed by secondary pyrolysis before they burn. Their experiments also showed an increase in burning velocities as the extent of secondary pyrolysis increases. Soot formation, however, is not accounted in the model. Therefore, soot radiation is neglected. No further simplifications of major importance were made.

The following system of equations is solved along with appropriate initial and boundary conditional. For the gas phase, conservation of mass, species, energy, and momentum and the state equation are given by

$$\frac{\partial \rho_g}{\partial t}+\frac{1}{r^2}\frac{\partial}{\partial r}(r^2\rho_g u)=0, \tag{1}$$

$$\frac{\partial}{\partial t}(\rho_g Y_k)+\frac{1}{r^2}\frac{\partial}{\partial r}(r^2\rho_g uT_k)=\frac{1}{r^2}\frac{\partial}{\partial r}\left(r^2\rho_g D_{km}\frac{\partial Y_k}{\partial r}\right)+\dot{w}_k''', \tag{2}$$

$$\frac{\partial}{\partial t}(c_g\rho_g T_g)+\frac{1}{r^2}\frac{\partial}{\partial r}(r^2 c_g\rho_g uT_g)=\frac{1}{r^2}\frac{\partial}{\partial r}\left(r^2\lambda_g\frac{\partial T_g}{\partial r}\right)-\sum_{k=1}^{k=GR}h_k\,\dot{w}_k''', \tag{3}$$

$$\frac{\partial}{\partial t}(\rho_g u)+\frac{1}{r^2}\frac{\partial}{\partial r}(r^2\rho_g uu)=\frac{1}{r^2}\frac{\partial u}{\partial r}\left(r^2\mu\frac{\partial u}{\partial r}\right)-\frac{\partial p}{\partial r}, \tag{4}$$

$$p=\rho_g R_u T_g\sum_{k=1}^{NS}\frac{Y_k}{W_k}. \tag{5}$$

CH_4,C_6H_6, O_2, CO, CO_2, H_2O and N_2 are the chemical species considered in this work. However, not all species rates are integrated since the mass fraction of N_2 is provided by balance. Equations related to the solid fuel are presented next.

For the solid phase, conversation of total mass and energy is given by

$$\frac{\partial \rho_p}{\partial t}=-\frac{1}{r^2}\frac{\partial}{\partial r}(r^2\dot{m}_v''), \tag{6}$$

$$\frac{\partial}{\partial t}(c_p\rho_p T_p)+\frac{1}{r^2}\frac{\partial}{\partial r}(r^2\rho_g uc_g T_p)=\frac{1}{r^2}\frac{\partial}{\partial r}\left(r^2\lambda_p\frac{\partial T_p}{\partial r}\right)+\frac{\partial \rho_p}{\partial t}h_v. \tag{7}$$

The initial conditions (at t = 0) are

$Y_k(0,r) = Y_{k,0},\ Y_g(0,r) = Y_{g,0},\ u(0,r) = 0,\ p(0,r) = p_0;\ \forall(r),$

The boundary conditional at particle surface and t>0 are

$T_p(0,R) = T_{p,0},\ \rho_k(0,R) = \rho_{p,0},$

$$(\dot{m}''_v + \dot{m}''_c)Y_k(t,R) = \left[\rho_g u Y_k + \rho_g D_{km}\frac{\partial Y}{\partial r}\right]_{r=R},\ T_g(t,R) = T_p(t,R),\ \rho_g u(t,R) = \dot{m}''_v + \dot{m}''_c,$$

where

$$\dot{m}''_c = \sum_{i=1}^{SR} \dot{s}_i \ \ and\ \dot{m}''_v = A_p \int_0^{V_p} \frac{d\rho_p}{dt} dV,$$

$$\left(\lambda_p \frac{\partial T_p}{\partial r}\right)_{r=R} = \left(\lambda_g \frac{\partial T_g}{\partial r}\right)_{r=R} + \varepsilon\sigma(T_w^4 - T_p^4) + \sum_{i=1}^{SR} \dot{s}_i h_{r,i},\ for\ \ r \in [0,R],$$

and at the undisturbed flow:

$Y_k(t,\infty) = Y_{k,\infty},\ T_g(t,\infty) = T_{g,\infty},\ p(t,\infty) = p_\infty,\ \forall(t \geq 0)$

To complete the boundary equations, symmetry condition is applied at particle center.

The heterogeneous reactions are considered to be fast enough to take place only at the particle surface. Oxygen thus cannot penetrate in the char porous structure. Hence, the particle is impermeable and the equation for the receding surface is given by

$$-\rho_p \frac{dr_p}{dt} = \sum_{i=1}^{SR} \dot{s}''_i \tag{8}$$

The transport coefficients for the gas phase are taken from kinetic theory of gases. Specifically in this work, properties calculated from the theory of Chapman and Enskog (Chapman and Cowling, 1939) are employed. Viscosity, thermal conductivity, binary diffusivity are all functions of mixture mass fraction, temperature or pressure. The specific heat is given as a polynomial function of temperature. The coefficients were taken from the NASA SP-273 computer code (Gordon and McBride, 1971):

$$c_g = \sum_{i=1}^{NS} R_u \left(\frac{Y_i}{W_i} \sum_{j=0}^{5} a_j T^j\right) \tag{9}$$

Specific heat and thermal conductivity for the coal are given by Merrick's formulation (1983), that is based on the Einstein form of quantum theory.

Devolatilization Model

The present formulation describes the combined phenomena that takes place in the boundary layer and their feed-back influence to the solid fuel particle. Devolatilization of coal particles in an oxidizing environment may proceed at different temperature levels. The presence of a volatile flame in the vicinity of a particle undergoing pyrolysis affects the particle heating rate and its time-dependent temperature. The devolatilization model associated to its kinetics seems to play an important role in such treatment. For modeling purposes, the devolatilization mechanism must also be related to composition of the volatiles released by coal pyrolysis. This is not a concern when the predictions are made on char combustion. As pointed by Anthony and Howard (1976), the sequence of evolution is such that, after drying, water produced by chemical reactions is released first, followed by carbon dioxide, carbon monoxide, higher hydrocarbons (included tar), ethane, methane, and finally hydrogen. This order is not precise and substantial overlap occurs. For a coal with 36.4% volatile matter content, 18.9% of the products appear as tar (in a mass basis) while the light gases reach 12.6% of the total volatiles released when particles are heated to 1050 ºC at 1500 ºC/s. The composition of light gases in a volumetric basis is 20.6% for CO, 6.1% for CO_2 13.1% for H_2 50.3% for CH_4 and 9.9% a mixed of other species. Suuberg and co-workers (1979) have studied extensively the product compositions and formation kinetics in rapid pyrolysis of pulverized coal. In their experiments, CO, CO_2 and H_2O dominated the lignite volatiles, while the main products from bituminous coals are tar and light hydrocarbons. Unger and Suuberg (1981) developed a model to explain the devolatilization behavior of softening coal. In the cases of softening coal, water and CO_2 are liberated first, preceding metaplast formation. This metaplast is the source of tar and gases, including hydrogen. However, the mechanism of formation of hydrogen is very distinct from the other gases. Hydrogen is liberated during metaplast repolymerization (char formation). They also observed that very little evolution of H_2 occurs while tar or hydrocarbon gases are being evolved. The evolution of hydrogen starts above 1100K and the yields (in a mass basis) never exceeded 1%, while tar yields were over 20%. More recent devolatilization models are based on the phenomenon of disintegration of the coal macromolecular structure into smaller volatiles fragments with subsequent reintegration of larger intermediates into char (Niksa, 1995). In this model, called FLASHCHAIN, predictions are made for gas and tar, in the same way of that proposed by Grant et al. (1989), named Chemical Percolation Devolatilization (CPD) Model. In both models, predictions are made for tar and gases. Gas composition is more difficult to predict, at least with great confidence. Currently, such models are being employed in comprehensive coal combustion codes. Another widely used model to predict volatiles release rates from bituminous and lignite coal where the coal's chemical diversity was brought to the devolatilization process, was introduced by Kobayashi et al. (1976). This model allows preferential char formation at lower temperatures. The model consists of two competing first order overall reactions, each degrading coal to residual chars (R_1 and R_2) and volatiles (V_1 and V_2) as shown in Fig. 1.

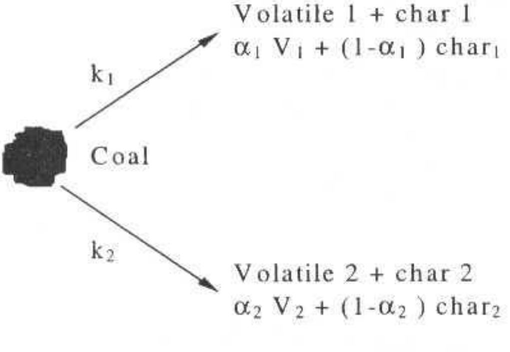

Fig.1 Schematic of thermal degradation of coal (Kobayashi et al., 1976)

The particle weight loss due to thermal decomposition is modeled with a pair of parallel first-order irreversible reactions. The rate equation is

$$\frac{\partial \rho_p}{\partial t} = -(k_1 + k_2)\rho_v. \tag{10}$$

The instantaneous mass production rate of volatiles is proportional to the undergraded part of the coal particle ρ_v. The parameters for the two competing reactions are given in Table 1.

Table 1 Kinetic for the Pyrolysis Model (Kobayashi et al., 1976)

$K_1 = B_1 \exp(-E_1 / R_u T_p)$	$K_2 = B_2 \exp(-E_2 / R_u T_p)$
$\alpha_1 = 0.4$	$\alpha_2 = 0.8$
$B_1 = 2x10^5$ (1/s)	$B_2 = 1.3x10^7$ (1/s)
$E_1 = 104.6x10^6$ (J/kmol)	$E_2 = 167.5x10^6$ (J/kmol)

The Reaction Mechanisms

The mechanisms proposed by Westbrook and Dryer (1981) are used for the homogeneous reactions in the boundary layer. The term boundary layer refers to the gas layer surrounding the particle, where concentrations, temperature and other properties are distinct from the stagnant gas. To use their mechanisms, the composition of the volatiles released must be known. The devolatilization of a coal particle produces innumerable compounds ranging from light hydrocarbons to large macromolecules (tar), water, CO, CO_2 and many other species. In the present work the lighter hydrocarbons are represented uniquely by CH_4, while the heavy ones (tar) by C_6H_6. The mass fractions of volatile components are taken from Anthony and Howard (1976). Volatile products (% by weight) contain light hydrocarbons, tar, water, CO, and CO_2. In the flame region, at high temperatures, there is an increase in the amount of free radical species and, more importantly, in the CO/CO_2 ratio, with lowers the adiabatic flame temperature. The detailed chemical kinetics takes such behavior into account at the expense of a large number of species being considered. Without increasing substantially the number of equations to be solved and still giving good results, Westbrook and Dryer (1981) have discussed the properties of the two-step reaction mechanisms based on the results from the detailed mechanisms. Parameters for the two-step reaction mechanisms in which the hydrocarbons oxidize first to CO followed by the conversion of CO to CO_2 are given by:

$$CH_4 + \frac{3}{2} O_2 \overset{k_R}{\Rightarrow} CO + 2H_2O, \tag{R1}$$

$$k_{R1} = 8.3 \times 10^5 \exp(-125.5 \times 10^6 / RT) [C_1 H_4]^{-0.3} [O_2]^{1.3},$$

$$C_6 H_6 + \frac{9}{2} O_2 \overset{k_R}{\Rightarrow} 6CO + 3H_2O, \tag{R2}$$

$$k_{R2} = 2.0 \times 10^{11} \exp(-125.5 \times 10^6 / RT) [C_6 H_6]^{-0.1} [O_2]^{1.85},$$

$$CO + \frac{1}{2} O_2 \overset{k_R}{\Rightarrow} CO_2, \tag{R3}$$

$$k_{R3} = 1.0 \times 10^{14.6} \exp(-167.4 \times 10^6 / RT) [CO]^1 [H_2O]^{0.5} [O_2]^{0.25}$$

$$CO_2 \overset{k_R}{\Rightarrow} CO + \frac{1}{2} O_2, \tag{R4}$$

$$k_{R4} = 1.0 \times 10^8 \exp(-167.4 \times 10^6 / RT [CO_2]^{1.0}.$$

The reserve reaction (R4) is necessary in order to keep the CO/CO_2 equilibrium ratio bounded for proper heats of reaction and dependence in the flame region.

Monson et al. (1995) presented a global model for char oxidation related to the external surface area for four different levels of pressure. This heterogeneous surface reaction for a single spherical particle in kg/m^2s of carbon is

$$\dot{s}'' = A\,exp(-E/RT\,)P_{O_2}^{0.5}. \tag{11}$$

The values of A and E for different pressures are given in Table 2.

Table 2 Global Char Reaction Rate Coefficients (Monson et al., 1995)

Pressure (atm)	A $(kg/m^2.s)\ (atm)^{-05}$	E (J/kmol)
1	17.8	60.21×10^6
5	0.382	14.24×10^6
10	0.227	15.90×10^6
15	0.098	20.51×10^6

The oxidation reaction at the surface of the particle may give CO or CO_2 at different amount as a function of surface particle temperature. Below 1400 K the CO_2 production is much greater than CO. As particle temperature increases, a shift leading to improvements in CO formation is expected, and above 2200 K CO is the only product. The heterogeneous reaction is given by

$$C + \frac{1+\psi}{2} O_2 \overset{k}{\Rightarrow} \psi CO_2 + (1-\psi\,)CO, \tag{R5}$$

where, the ratio of CO to CO_2 formed by the reaction R5, is

$$\frac{1-\psi}{\psi} = A_c\,exp(-E_c\,/RT_p\,), \tag{12}$$

The parameters A_c and E_c determined by Monson et al (1995) take the values 3.0×10^8 and 251.2×10^6 J/kmol, respectively. CO_2 gasification is also taken into account and the parameters from Bradley et al. (1984) were employed in this work. The heterogeneous reaction is

$$C + CO_2 \overset{k_r}{\Rightarrow} 2CO,$$

$$\dot{s}_2 = 9.0 \times 10^3 exp(-285.14 \times 10^6\ /RT_p\,)P_{CO_2}^{0.5}. \tag{R6}$$

Numerical Formulation and Solution Technique

The set of conservartion equations was discretized through using the method described by Patankar (1980), resulting in a system of algebraic equations, which were solved in sequence by a Thomas-algorithm. Nonlinearity and interlinkage are treated by iteration. To improve convergence, an adaptive grid generation routine was included. The steep gradients and high values of temperatures, oxygen and carbon monoxide concentrations served as a basis the equidistribution of a positive weight function technique employed for the grid point locations. The pressure term in the momentum equations brought an additional problem when calculating the field from the particle to its boundary. The SIMPLER procedure was employed in a staggered grid for the velocity field calculations. The computer program was written in FORTRAN 77 and calculations were carried out with double precision. The program runs in a HP-9000 series 700 workstation. When reactions are on the way, the number of iterations averages from 100 to 1000, for one time step. Total computational time averaged between 5 to 15 hours. Computations were carried out until 90% of the original mass of the particle was burned.

The initial grid is set for the domain of calculation, which consists of the coal particle and its boundary layer. The particle is divided in 20 control volumes (shells) and the boundary layer in at least 80 control volumes.

The stagnant film surrounding the particle is thought to be large enough so that particle interaction does not occur. In this, the numerical boundary extends to 40 times the particle radius. This system (particle and its surrounding stagnant film) is brought to one hot environments (reactor tube) which gives the boundary conditions for the undisturbed flow. Temperature and gas composition for this point is kept invariant throughout the simulation.

Results and Discussion

A set of simulations was carried out. Two different coals were chosen, one bituminous (coal B), with 31.9% volatile matter content, and a less reactive one (coal A), anthracite, with an average of 8.5% volatile. A third fuel was also investigated in order to check the parameters for global heterogeneous reactions: char particles, with initial density of 820 kg/m^3, burning at different gas temperature and pressures. Experimental results for the three fuel burning under pressurized conditions were available (coal data from Saastamoinen et al 1996, and char data from Monson et al, 1995)

Although the CO_2 partial pressure in the experiments was set to 1 atm, form the numerical simulations half of that value was used. Such a high concentration in carbon dioxide affects much the CO to CO_2 ratio in the flame region due to the reserve reaction R4. However, increasing the pressure of the reactor the effect is somewhat diminished.

In Figure 2 the unsteady particle surface temperature is shown along with the normalized overall mass of the burning particle, as functions of time, for a 160 μm initial diameter particle of the 39.5% volatile matter coal, in an environment at 1450 K and 2 atm.

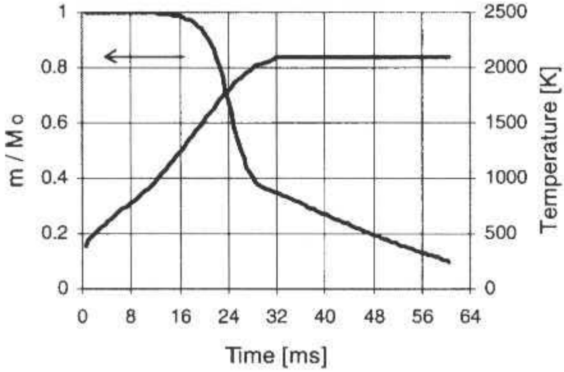

Fig. 2 **Surface temperature and normalized mass loss of a 80 μm bituminous coal particle at 1450 K and 2 atm reactor gas 0,27 atm O_2 partial pressure**

The curve of the normalized mass has two distinct regions. The first characterizes the devolatilization phase (decreasing density) which is followed by a second region (receding surface) where mass consumption rate is low. In spite of the fact that the coal has 31.9% volatile matter, determined by proximate analysis, a further 15% increase in volatile yield was obtained as a consequence of the heating rates and temperature reached by the particle.

This trend was observed experimentally by Kobayashi et al (1976). This enhancement in the yields is favorable on account of the particle mass consumption rate, since homogeneous reactions are much faster than the heterogeneous ones, which results in reduced reactor volume requirements for combustion. A peak in particle temperature is seen at about 32 ms, after escape of volatile has terminated. A this temperature level, CO is the sole gaseous product at particle surface. This CO is further oxidized close to particle surface but the heat generated is not enough to balance the combined conduction-radiation energy losses from the particle. However, a pseudo steady state may be assumed for the char oxidation phase as indicated by the mass curve of Fig. 2.

Figure 3 shows the time dependent history of gas mass fraction at the particle surface towards its burnout time.

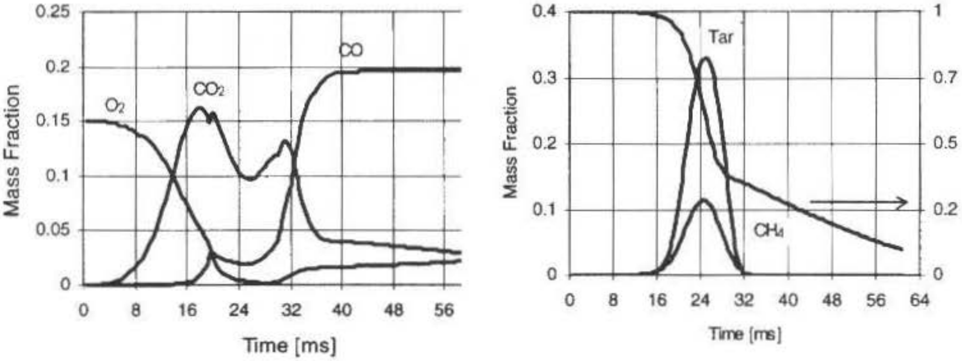

Fig. 3 Mass fraction of different species at surface as a function of time. Conditions are the same of Fig. 2

Coupled with Fig. 2, this figure gives a good insight of the highly unsteady combustion behavior of the coal particle before char oxidation prevails. Gas phase ignition takes place at nearly 19 ms, consuming all oxygen available in the immediacy of the particle. The formation of CO increases as well as that of water vapor and CO_2. A fraction of the heat generated by the reactions raises particle temperature, the leftover diffuses away. The mass flow rates of light and heavy hydrocarbons increase sharply, preventing oxygen to reach the particle surface. Heterogeneous reactions are not possible and the flame moves away from the particle surface where stoichimetry is more favorable for hydrocarbons and CO oxidation. By the end of the devolatilization, the flame is moving back to the particle surface and heterogeneous reactions resume, as depicted by fig. 4. At this point, the particle surface reaches its maximum temperature.

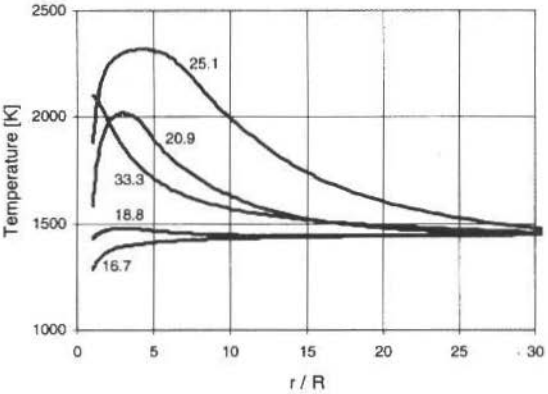

Fig. 4 Temperature distributions in the boundary layer at different times (ms)

Figure 4 shows the boundary layer temperature distribution for the case presented in Fig. 2. The oxidation of volatiles to CO, followed by the slower conversion of CO to CO_2, takes places in a broad region, which extends 8 particle radii. Such behavior indicates that a thin flame approach for the combustion of volatiles must be taken with care. For char oxidation, the conversion of CO to CO_2, is meaningful to 3 particle radii from the surface. This region produces almost 80% of energy on account of homogeneous reactions.

Figure 5 shows a comparison between experimental and simulation temperature data. The parameters concerning reactor gas and the fuel composition employed are listed in Table 3. The predicted temperatures are taken for pyrolysis corresponding to 90% burnout. The experimental temperature data also correspond to approximately 90% burnout, for which the flame is attached to the surface of the particle providing a more confident value of the particle temperature. Simulations were performed at low and elevated pressures. A reduction in the particle reaction rate is evident by comparison between cases 8 and 9, where total pressure is reduced from 8 to 5 atm, at constant oxygen partial pressure, and near the same gas bulk temperature. On the other hand, increasing oxygen partial pressure at constant total pressure greatly improves the char oxidation rate - cases 2 and 6. Such a behavior was observed for all simulations carried out, except when the total pressure was 15 atm. In this case, the experiment provided particle temperatures near 1900 K while the theoretical simulation produced 1650 K, as a maximum, at 70% burnout time.

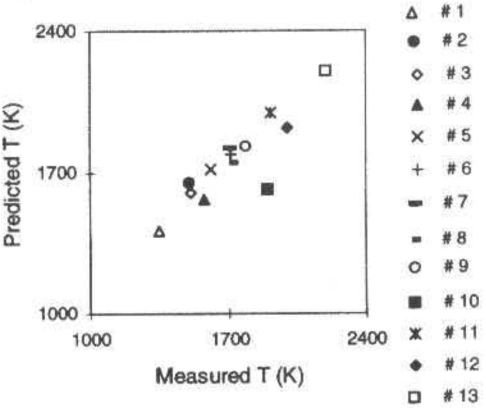

Fig. 5 Predicted particle temperature, comparison between modeling and experimental for two different coal and char

Particle's temperature higher than 1900 K for the 15 bar case was predicted when the global kinetic parameters, for the heterogeneous reactions, given by Hobbs et al. (1993) were employed. For coal A (anthracite) and coal B (bituminous) the trends were exactly the same. As pressure increases from 5 to 8 atm (cases 9 and 8, respectively) a reduction in particle temperature was obtained either experimentally or theoretically. The observed increase in the overall reaction rate, as oxygen partial pressure increases (the other conditions remaining constant) is a consequence of the faster heterogeneous reactions rates leaning the system more towards diffusion controlled. The model has a tendency of giving higher reaction rates than the measured ones. Nevertheless, this tendency is the same for a broad range of reactor's atmospheres and fuel sizes and types. As a whole, theoretical results are in good agreement with experimental ones, for most of the cases analyzed.

Table 3 Parameters for the Cases in Fig. 2. Units: atm and Kelvin. Coal Data Taken from Saastamoinen et al (1996) and Char Data from Monson et al (1995)

Case #	T_p (experimental)	P_{total}	PO_2	T_{gas}	Fuel
1	1350	15	0.75	987	char
2	1500	10	0.50	1170	char
3	1510	8	0.50	1150	coal A
4	1580	15	1.50	987	char
5	1610	5	0.50	1150	coal A
6	1700	10	1.00	1170	char
7	1705	8	0.50	1150	coal B
8	1720	8	0.50	1450	coal A
9	1790	5	0.50	1450	coal A
10	1900	15	3.25	987	char
11	1910	5	1.00	1130	char
12	2000	10	2.00	1170	char
13	2100	5	1.00	1330	char

Conclusion

The numerical model presented in this paper can simulate pressurized combustion of single solid fuel particles like coal and char. The model was able to predict the temperature of the particle in a broad range of burning conditions. The simulations indicated an increase in particle reaction rate when O_2 partial pressure was increased, keeping the other properties constant. For pressurized conditions, improvements in the burning are attained by virtue of the fast CO oxidation in the boundary layer. Further increase in O_2 concentration did not improve the reaction rates at the expected proportion. A tendency towards diffusion controlled process was identified. This suggests the existence of an ideal particle size for certain furnace condition. Simulations with the model here presented may give a first insight in the overall behavior of the pressurized burning system. Such a tool thus avoids the need of carrying out expensive experiments.

References

Aho, M. J., Paakkinen, K. M., Pirkonen, P. M., and Hupa, M., 1995 "The Effects of Pressure, Oxygen Partial Pressure and Temperature on the Formation of N_2O, NO, and NO_2 from Pulverized Coal", Combustion and Flame, vol. 102, pp. 387-400.

Anthony, D. B. and Howard, J B., 1976, "Coal Devolatilization and Hydrogasification", AIchE, vol. 22, n. 4, pp. 625-656.

Bradley, D., Dixon-Lewis, G., Habik, S. E., and Mushi, E. M. J., 1984 Twentieth Symposium (Int.) on Combustion, the Combustion Institute, Pittsburg, pp. 931-940.

Chapman, S. and Cowling, T. G.: 1939, "The Mathematical Theory of Nonuniform Gases", Cambridge, New York.

Cho, S., Marlow, D., and Niksa, S., 1995 "Burning Velocities of Multicomponent Organic Fuel Mixtures Derived from Various Coal", Combustion and Flame, vol. 101, pp. 399-410.

Gordon, S. and McBride, B. J., 1971, "Computer Program for Calculation of Complex Chemical Equilibrium Compositions", Rocket Performance, Incident and Reflected Shocks and Chapman-Jouguet Detonations, NASA SP-273.

Grant, D. M., Pugmire, R. J., Fletcher, T. H., and Kerstein, A. R., 1989, Energy and Fuels vol. 3, pp. 175-186.

Griffin, T. P., Howard, J. B., and Petters, W. A., 1994 "Pressure and Temperature Effects in Bituminous Coal Pyrolysis: Experimental Observations and a Transient Lumped-parameter Model", Fuel, vol. 73, n. 4, pp. 591-601.

Hobbs, M. L., Radulovic, P. T., and Smoot, L. D., 1993, "Combustion and Gasification of Coals in Fixed-Beds", Prog. Energ. Combust. Sci., vol. 19, pp. 505-586.

James, R. K. and Mills, A. F., 1976, Analysis of Coal Particle Pyrolysis, Letters in Heat and Mass Transfer, vol. 3, Pergamon Press.

Kobayashi, H., Howard, J. B., and Sarofim, A. F., 1976, "Coal Devolatilization at High Temperatures", Sixteenth Symposium (Int.) on Combustion, pp. 411.

Merrick, D., 1983, "Mathematical Models of the Thermal Decomposition of Coal", Fuel, vol. 62, pp.540-546.

Monson, R. C., Germane, G. J., Blackham, A. U., and Smoot, L. D., 1995, "Char Oxidation at Elevated Pressures", Combustion and Flame, vol. 100, pp. 669-683.

Mühlen, H. J. and Sowa, 1995, F., Fuel, vol. 74, No. 11, pp. 269.

Musarra, S. P., Fletcher, T. H., Niksa S., and Dwyer, H. A., 1986, "Heat and Mass Transfer in the Vicinity of a Devolatilization Particle", Comb. Sci. And Tech., vol. 45, pp. 289-307.

Niksa, S., 1995, "Predicting the Devolatilization Behavior of Any Coal from its Ultimate Analysis", Combustion and Flame, vol. 100, pp. 384-394.

Patankar, S. V., 1980, "Numerical Heat Transfer and Fluid Flow", McGraw-Hill Book Company, New York.

Saastamoinen, J., Aho, M. J., and Hämäläinen, J. P., 1996, "Pressurized Fuel Combustion in Different Concentration of Oxygen and Carbon Dioxide", American Chemical Society, vol. 10, pp. 121-133.

Suuberg, E. M., Peters, W. A. and Howard, J. B., 1979, "Product Compositions and Formation Kinetics in Rapid Pyrolysis of Pulverized Coal-Implications for Combustion", Proceedings 17th Symposium (Int.) on Combustion, Pittsburgh PA, pp. 117-130.

Unger, P. E. and Suuberg, E. M., 1981, "Modeling of the Devolatilization Behavior of a Softening Bituminous Coal", Proceedings 18th Symposium (Int.) on Combustion, Pittsburgh PA, pp. 1203-1211.

Westbrook, C. K. and Dryer, L. F., 1981 "Simplified Reaction Mechanisms for the Oxidation of Hydrocarbon Fuels in Flames", Comb. Sci. And Tech., Vol. 27, pp. 31-43.

RBCM - J. of the Braz. Soc. Mechanical Sciences
Vol. XXI - No.2 - 1999 - pp. 211-221

ISSN 0100-7386
Printed in Brazil

Transport Coefficients for Developing Laminar Flow in Isosceles Triangular Ducts

José Alberto dos Reis Parise
Pontifícia Universidade Católica do Rio de Janeiro
Departamento de Engenharia Mecânica
22453-900 Rio de Janeiro, RJ Brazil
parise@mec.puc-rio.br

Francisco Eduardo Mourão Saboya
Universidade Federal Fluminense
Departamento de Engenharia Mecânica
21410-240 Niterói, RJ Brazil

Abstract

Experiments were performed to determine overall heat transfer coefficients in the laminar entrance region of 30, 45, 60 and 90 degrees isosceles triangular ducts. The results were obtained by application of the analogy between heat and mass transfer in conjunction with the naphthalene sublimation technique. In accordance with the analogy, the experimental conditions simulated a heat transfer situation characterized by simultaneous developing of velocity and temperature fields in an isosceles triangular duct with isothermal lateral walls and adiabatic base. The measurements were performed for Reynolds numbers ranging from 100 to 1800 and a duct length to hydraulic diameter ratio from 2 to 40. In this manner, a long range of the dimensionless streamwise coordinate values was covered, including the neighborhood of entrance region. Curve-fitting equations were produced, providing the Sherwood number as a function of the Graetz number. Extension of the results for other apex angles, within the 20-100 degrees range, was also possible.

With the analogy between heat and mass transfer, similar correlations were provided for the corresponding Nusselt number. The triangular duct geometry finds application in the compact heat exchanger design such as solar collectors with triangular cavities for direct air heating.

***Keywords**: Heat and Mass Transfer Analogy, Duct Flow, Laminar Entrance Region.*

Introduction

The noncircular duct geometry is commonly employed in engineering applications, such as compact heat exchangers, solar collectors and others. In particular, triangular ducts are very suitable for the construction of compact conjuncts. A survey of the available published literature on the heat transfer characteristics of triangular ducts reveals a great lack of information about developing laminar flows.

Sparrow and Haji-Sheikh (1965) reported analytical results for laminar fully developed heat transfer in isosceles triangular ducts for a large range of apex angles. The thermal boundary condition was constant heat flux at the triangle walls. In addition, pressure drop coefficients were presented.

Schmidt and Newell (1967) gave results that can be applied to laminar flows. Several thermal boundary conditions were considered. All the situations were concerned with fully developed flows.

One of the most extensive sets of results in noncircular ducts is that of Shah and London (1978). Although only laminar flows were studied, the situation characterized by undeveloped velocity and temperature fields in triangular ducts was not presented.

Braga and Saboya (1986) presented experimental results for laminar heat transfer in the entrance region of an isosceles triangular duct with apex angle equal to 120 degrees, isothermal lateral walls and insulated base. The experimental conditions were characterized by simultaneous developing of velocity and temperature fields.

Recently, Braga and Saboya (1996) determined experimental information for turbulent heat transfer and pressure drop in an internally finned equilateral triangular duct. Results for unfinned duct were also reported.

The present research was undertaken to determine average heat transfer coefficients for developing laminar flow forced convection in isosceles triangular ducts. The velocity and temperature fields were both developing. The thermal boundary conditions were isothermal lateral walls and adiabatic base. The apex angle of the isosceles triangle assumed values of 30, 45, 60 and 90 degrees. Mass transfer experiments were performed using the naphthalene sublimation technique (Mendes,1991). During the experiments the flow Reynolds number was varied from 100 to 1800 and the duct length to hydraulic diameter ratio from 2 to 40. That allowed a long range of the dimensionless streamwise coordinate values to be covered, including the neighborhood of entrance region.

Manuscript received: July 1998; revision received: November 1998. Technical Editor: Angela Ourívio Nieckele.

For the thermal boundary conditions of the present experimental work, Schmidt and Newell (1967) gave the values of the overall heat transfer coefficients, as function of the apex angle, for fully developed velocity and temperature fields. As it will be seen later, these values will be useful to the objectives of the present research.

The experimental method employed in this work makes use of the analogy between heat and mass transfer in conjunction with the naphthalene sublimation technique. The overall heat transfer coefficients may be inferred from mass transfer experiments in which overall mass transfer coefficients are measured. Saboya and Sparrow (1974, 1976) showed that such technique is a very successful and powerful tool. It results from casting solid naphthalene plates in the form of the duct or flow channel. The naphthalene plates simulate isothermal walls while a metallic sheet simulates an adiabatic wall.

Due to the airflow through the duct, naphthalene sublimation occurs. The overall mass transfer rates are determined by weighing the naphthalene pieces before and after a data run and measuring the duration time of the data run. The air mass flow rate (discharge) is also monitored. The next step is to calculate the average Sherwood number and the Graetz number that characterizes the data run. The objective is to produce curve-fitting equations providing the Sherwood number as function of the Graetz number. The Sherwood number is analogous to the Nusselt number of the heat transfer problem. Extension of the results for other apex angles, within the 20-100 degrees range, could also be done.

Experimental Procedure and Test Apparatus

Figure 1 shows a schematic of the test section arrangement used for the experiments of the present work, where:

a Buffer
b Isosceles triangular duct with a metallic base and two naphthalene lateral walls
c Plenum chamber
d Pressure taps
e Calibrated rotameter to measure air mass flow rate
f Valve to control the air flow
g Cut-off valve to stop the air flow
h By-pass valve
i Blower

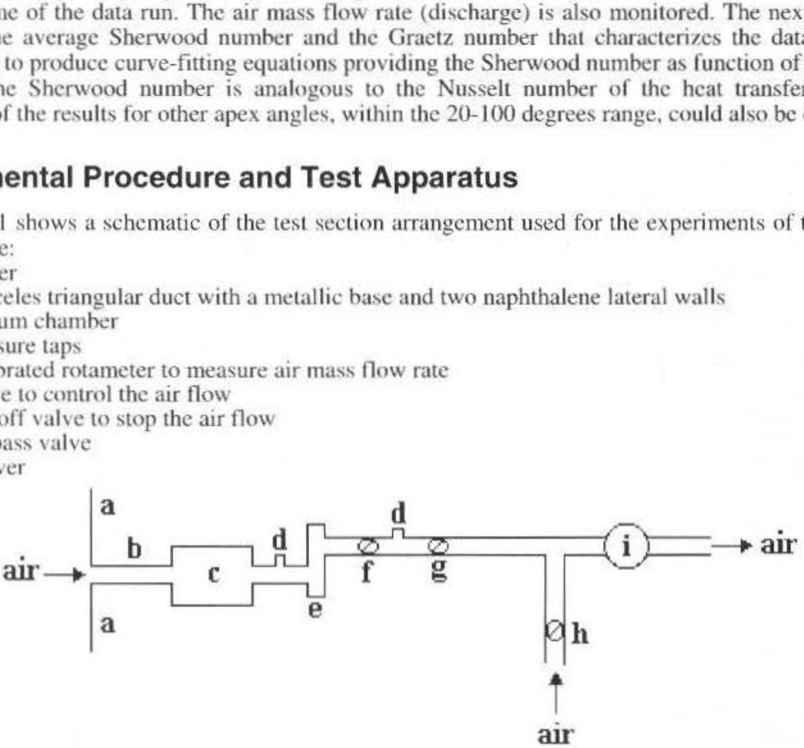

Fig. 1 View of the Test Section Used in the Experiments

As shown in Fig. 1, air from the laboratory room is suctioned through the triangular duct (analogous system) in an open-loop flow circuit. Upon traversing the naphthalene channel, the air passes successively through a plenum chamber, a calibrated rotameter, two valves, the blower, and is finally discharged to the atmosphere. The by-pass valve in Fig. 1 is used to avoid heating the blower at low air mass flow rates.

The flow circuit is operated in the suction mode with the analogous system located at the upstream end of the circuit. This arrangement prevents the flowing air from heating and lubricating oil contamination, before it reaches the naphthalene plates.

To employ the naphthalene sublimation technique, plates of this material were fabricated by using a casting procedure. The molds used in the casting process consisted of several aluminum pieces that were assembled together, forming a cavity. Molten naphthalene was poured into the mold cavity and allowed to solidify. The melting point of naphthalene is 353.45 K. After solidification, the molds were disassembled to free the naphthalene to be used in the experiments.

To guarantee purity, commercial naphthalene was submitted to a distillation process. Only pure naphthalene was used in the experiments, and the pieces never were reused. Contamination might modify the naphthalene properties, affecting the results.

To make certain that the air entering the flow circuit was free of naphthalene vapor, the exhaustion was done to the outside the laboratory room. In this situation, the naphthalene vapor concentration of the entering air was zero, and did not have to be measured.

During the operations of weighing, mounting and dismounting the triangular duct, extraneous mass losses occur due to natural convection. Preliminary runs were performed and correction factors were determined. In this way, it was possible to obtain the correct mass loss due to forced convection. The correction never was more than three percent of the total mass loss during the data run.

The naphthalene pieces were weighed before and after the data run with a high resolution Sartorius analytical balance. This balance has 200 g capacity and a smallest scale reading of 0.1 mg. By difference, the mass transferred from the wall to the airstream was determined. Typically, a naphthalene piece weighed 21.0 g and the sublimed mass was 23.5 mg. The length of the equal sides of the cross-section of the naphthalene isosceles triangular duct was typically 10.00 mm. The length of the naphthalene channel varied from 13.0 mm to 141.0 mm.

The duration time of a data run was measured with a timer capable of discriminating up to 0.1 seconds. Typically, the duration time of a data run was two hours.

As shown in Fig. 1, the air mass flow rate was measured by a calibrated rotameter. Typically, the experimental uncertainty of the air mass flow rate was two percent.

The air temperature at the laboratory room was sensed by a precision thermometer that could be read up to 0.1 °C. This temperature is also the temperature of the subliming naphthalene walls.

The atmospheric pressure was determined by a barometer of mercury column with a smallest scale division of 0.1 mm. The pressure at the rotameter inlet was also measured. A manometer of column of water with a smallest scale division of 0.25 mm was used.

Nomenclature

A = total mass or heat transfer area, m^2
A_t = cross section area of the triangular duct, m^2
C = constant defined by equation (19), dimensionless
C_1 = constant in equation (12),
C_2 = constant in equation (12),
D_h = hydraulic diameter, m
D_m = mass diffusivity of the air-naphthalene system, m / s
$\overline{h}_b$ = average heat transfer coefficient, W / (m^2.s)
k = thermal conductivity of the working fluid, W / (m.K)
L duct length, m
M_n = total naphthalene mass sublimed, kg
$\dot{m}_n$ = total naphthalene mass transfer rate, per unit area, kg / (m^2.s)
$\dot{m}_a$ = air mass flow rate (discharge), kg / s
n_1 = exponent in equation (12), dimensionless
n_2 = exponent in equation (12), dimensionless
$\overline{Nu}_b$ = average Nusselt number based on the logarithmic mean temperature difference, dimensionless
$\overline{Nu}_{b,d}$ = asymptotic value of $\overline{Nu}_b$ for fully developed flow, dimensionless
$\overline{Nu}_o$ = average Nusselt number based on wall to inlet temperature difference, dimensionless
$P_{n.w}$ = partial pressure of naphthalene vapor at the wall, N / m^2
Pr = Prandtl number, dimensionless
$\dot{Q}_W$ = heat transfer rate, W
Re = Reynolds number, dimensionless
R_n = ideal gas constant of naphthalene vapor, J / (kg.K)
S = length of the equal sides of the isosceles triangular duct cross-section, m
Sc = Schmidt number, dimensionless
$\overline{Sh}_b$ = average Sherwood number based on the logarithmic mean concentration difference, dimensionless
$\overline{Sh}_{b,d}$ = asymptotic value of $\overline{Sh}_b$ for fully developed flow, dimensionless
$\overline{Sh}_o$ = average Sherwood number based on wall to inlet concentration difference, dimensionless
T_o = inlet temperature, K
T_w = wall temperature, K
$\dot{V}$ = air volumetric flow rate, m^3 / s
X^+ = Graetz number, dimensionless

Greek Symbols

α = apex semiangle of the isosceles triangular duct, degree
ΔT_{log} = logarithmic mean temperature difference, K
$\Delta \rho_n$ = logarithmic mean concentration difference, kg / m^3
μ = air dynamic viscosity, kg / (m.s)
ν = air kinematic viscosity, m^2 / s
$\overline{\lambda}_b$ = average mass transfer coefficient, m / s
ρ = air density, kg / m^3
$\rho_{n.l}$ = naphthalene vapor concentration in the air, at the duct exit, kg / m^3
$\rho_{n.o}$ = naphthalene vapor concentration in the entering air, kg / m^3
$\rho_{n.w}$ = naphthalene vapor concentration at the wall, kg / m^3
τ = duration time of the data run, s

Data Reduction Procedure

The main objective of the data reduction procedure was to obtain the average Sherwood number as function of the Graetz number. Let M_n be the total naphthalene mass sublimed during a data run characterized by the flow Graetz number, A the total mass transfer area (two naphthalene plates) and τ the duration time of the data run.

Therefore, the total mass transfer rate per unit area, $\dot{m}_n$, is given by:

$$\dot{m}_n = \frac{M_n}{A\tau} \tag{1}$$

The average mass transfer coefficient, $\overline{\lambda}_b$, is defined as:

$$\overline{\lambda}_b = \frac{\dot{m}_n}{\Delta\rho_n} \tag{2}$$

where $\Delta\rho_n$ is the logarithmic mean concentration difference, given by:

$$\Delta\rho_n = \frac{(\rho_{n,w} - \rho_{n,o}) - (\rho_{n,w} - \rho_{n,l})}{ln[(\rho_{n,w} - \rho_{n,o})/(\rho_{n,w} - \rho_{n,l})]} \tag{3}$$

The logarithmic mean concentration difference is analogous to the logarithmic mean temperature difference (LMTD). In Eq. (3), $\rho_{n,w}$ is the naphthalene vapor concentration at the wall, $\rho_{n,o}$ the naphthalene vapor concentration in the entering air and $\rho_{n,l}$ the naphthalene vapor concentration in the air at the duct exit. In the present case $\rho_{n,o} = 0$.

The average Sherwood number, $\overline{Sh}_b$, is obtained from:

$$\overline{Sh}_b = \frac{\overline{\lambda}_b D_h}{D_m} \tag{4}$$

where D_h is the hydraulic diameter of the isosceles triangular duct and D_m the mass diffusivity of the air-naphthalene system. The hydraulic diameter is determined from the following equation:

$$D_h = \frac{S\, sin2\alpha}{1 + sin\alpha} \tag{5}$$

where S is the length of one of the equal sides of the isosceles triangular duct cross-section and 2α is its apex angle.

The mass diffusivity of naphthalene vapor into air is given by:

$$D_m = \frac{\nu}{Sc} \tag{6}$$

where Sc is the Schmidt number and ν the air kinematic viscosity. Sogin (1958) recommended a value of 2.5 for Sc, which was used in this work. The Schmidt number is analogous to the Prandtl number of the heat transfer problem.

To obtain the logarithmic mean concentration difference it is necessary to calculate the concentrations $\rho_{n,w}$ and $\rho_{n,l}$ ($\rho_{n,o}$ is zero). The naphthalene vapor concentration in the air, at the duct exit, is given by:

$$\rho_{n,l} = \frac{M_n}{\dot{V}\,\tau} \tag{7}$$

where $\dot{V}$ is the air volumetric flow rate, determined by the rotameter. The naphthalene vapor concentration at the wall is related to its partial pressure and temperature through the ideal gas law. This is so because the partial pressure of naphthalene in the air is very low. Hence:

$$\rho_{n,w} = \frac{P_{n,w}}{R_n\,T_w} \tag{8}$$

In Equation (8), $P_{n,w}$ is the partial pressure of naphthalene vapor at the wall, T_w the absolute temperature of the naphthalene surface and R_n the ideal gas constant of naphthalene vapor, equal to 64.87 J / (kg. K). It should be observed that T_w is equal to the ambient temperature. The partial pressure of naphthalene vapor at the wall is a function of the wall temperature alone. Sogin (1958) reported the following equation:

$$\log_{10} P_{n,w} = 13.564 - \frac{3729.4}{T_w} \tag{9}$$

In Eq. (9), $P_{n,w}$ is in N / m^2 and T_w in K.

At this point, one should notice that all the variables in Eq. (4) can be determined, and the average Sherwood number, $\overline{Sh_b}$, calculated as a function of the Graetz number, X^+, that characterizes the data run:

$$X^+ = \frac{L/D_h}{Re\,Sc} \tag{10}$$

In Equation (10), L is the duct length and Re the flow Reynolds number. The Reynolds number can be calculated from:

$$Re = \frac{\dot{m}_a\,D_h}{A_t\,\mu} \tag{11}$$

where m_a is the air mass flow rate (discharge), A_t the cross section area of the triangular duct and μ the air dynamic viscosity. It is known that $m_a = \rho v$, where ρ is the air density. For practical purposes, the mass flow rate through the duct can be considered constant and equal to the air mass flow rate, since the total mass of naphthalene vapor added to the airstream per unit time is, typically, not greater than 0.02 percent of the air mass flow rate. For the same reason, the properties of the binary mixture can be taken as those of pure air. Also, Sparrow and Niethammer (1979) showed that the air humidity can be neglected in naphthalene experiments.

Results and Discussion

To correlate $\overline{Sh_b}$ with X^+, (for Sc = 2.5) 77 data runs were performed. This number of data runs was divided, in an equitable manner, among the four apex angles used in the experiments, 30°, 45°, 60° and 90°. The minimum and maximum values of the flow Graetz number were 5.2×10^{-4} and 7.8×10^{-2}, respectively. To cover this Graetz number range, the Reynolds number varied from 100 to 1800, while (L / D_h) varied from 2.0 to 40.0. For further information about the values of the Reynolds numbers and (L / D_h) associated with each one of the 77 runs, one should consult Parise (1978).

To determine the equations of $\overline{Sh_b}$ as function of X^+, the following relationship was assumed:

$$\overline{Sh}_b = \overline{Sh}_{b,d} + \frac{1}{C_1(X^+)^{n1} + C_2(X^+)^{n2}} \tag{12}$$

Equation (12) is a general relationship proposed by Stephan (1959), for developing laminar internal flows. Its form is very suitable to the objectives of the present research and never was used for triangular ducts.

In Eq. (12), $\overline{Sh}_{b,d}$ is the asymptotic value of $\overline{Sh}_b$ obtained when the velocity and temperature profiles are fully developed. It is seen, from Eq. (12), that $\overline{Sh}_b = \overline{Sh}_{b,d}$ when $X^+ \to \infty$. $\overline{Sh}_{b,d}$ is a function of the apex angle 2α of the triangular duct and its values are given by Schmidt and Newell (1967).

By means of the experimental data (77 runs) and using the least squares method, the values of C_1, C_2, n_1 and n_2 in Eq. (12), were determined for each apex angle 2α. The curve-fitting equations are:

$$2\alpha = 30^o: \qquad \overline{Sh}_b = 2.10 + \frac{1}{1.64(X^+)^{0.5} + 5.90 \times 10^2 (X^+)^{1.9}} \tag{13}$$

$$2\alpha = 45^o: \qquad \overline{Sh}_b = 2.33 + \frac{1}{1.71(X^+)^{0.5} + 2.42 \times 10^2 (X^+)^{1.9}} \tag{14}$$

$$2\alpha = 60^o: \qquad \overline{Sh}_b = 2.35 + \frac{1}{1.56(X^+)^{0.5} + 2.82 \times 10^3 (X^+)^{2.8}} \tag{15}$$

$$2\alpha = 90^o: \qquad \overline{Sh}_b = 2.17 + \frac{1}{1.68(X^+)^{0.5} + 7.80 \times 10^6 (X^+)^{6.7}} \tag{16}$$

The mean deviations of Eqs. (13) – (16), in relation to the data points, are 9.88 %, 5.99 %, 6.56 % and 5.91 %, respectively.

Figures 2 to 5 present the experimental data points as well as the correlations determined for the four apex angles 2α. The relatively low scattering of the experimental points exhibited in the figures lends support to the present experimental method. It should be observed that the results displayed in these figures are valid for Sc = 2.5.

The average Sherwood number, $\overline{Sh}_b$, is, by definition, based on the logarithmic mean concentration difference given by Eq. (3). An alternative definition of the average Sherwood number, $\overline{Sh}_o$, that can be useful, is based on wall to inlet concentration difference, $(\rho_{n,w} - \rho_{n,o})$.

It is easy to show that $\overline{Sh}_o$ and $\overline{Sh}_b$ are related by the following equation:

$$\overline{Sh}_o = \frac{1 + \sin\alpha}{4X^+}\left[1 - \exp\left(-\frac{4X^+}{1+\sin\alpha}\overline{Sh}_b\right)\right] \tag{17}$$

Since $\overline{Sh}_b$ is known, $\overline{Sh}_o$ can be determined by Eq. (17).

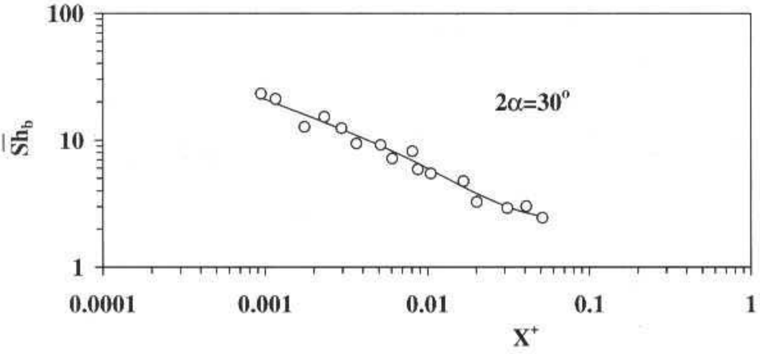

Fig. 2 Average Sherwood Number, $\overline{Sh}_b$, as Function of X^+, for $2\alpha = 30^o$ and Sc = 2.5

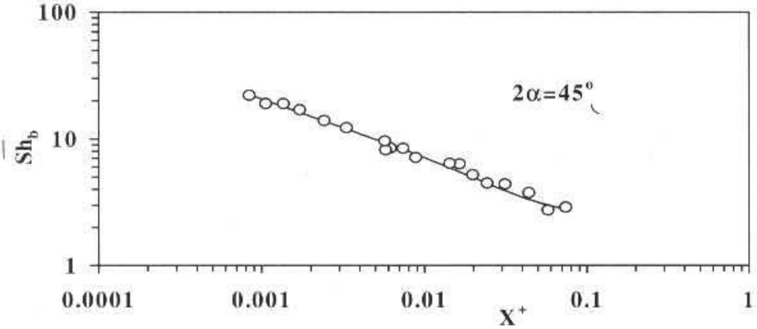

Fig. 3 Average Sherwood Number, $\overline{Sh}_b$, as Function of X^+, for $2\alpha = 45^o$ and Sc = 2.5

Although the experiments were performed for only four apex angles, the results make possible the estimation of $\overline{Sh}_b$ for other angles. The exponent n_1 in Eq. (12) is equal to 0.5 and does not depend on the angle 2α. Figure 6 gives the values of $\log_{10} C_2$ and of the exponent n_2 as function of 2α. Figure 7 presents the variation of $\overline{Sh}_{b,d}$ and C_1 with 2α. It is seen that a good approximation for C_1 is the mean value, equal to 1.65.

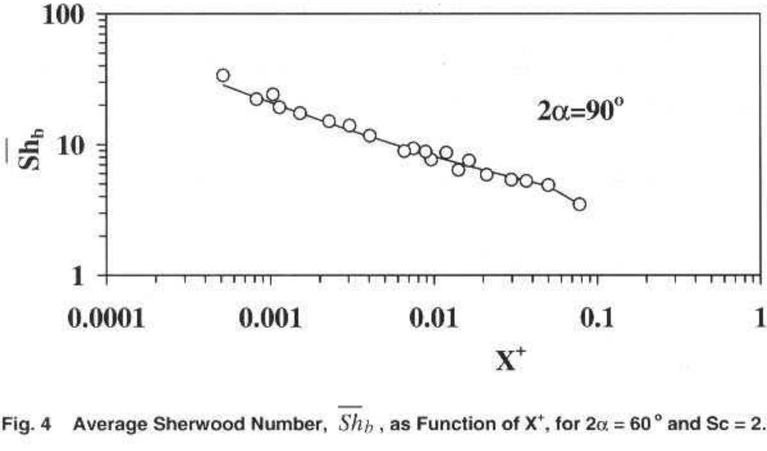

Fig. 4 Average Sherwood Number, $\overline{Sh}_b$, as Function of X^+, for $2\alpha = 60^o$ and Sc = 2.5

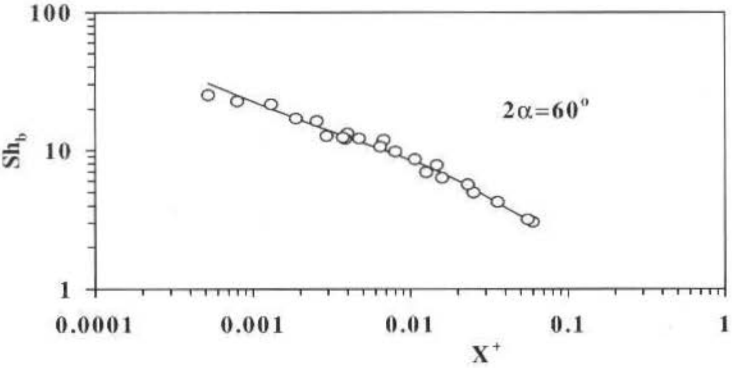

Fig. 5 Average Sherwood Number, $\overline{Sh}_b$, as Function of X^+, for $2\alpha = 90°$ and Sc = 2.5

In this manner, n_1, C_2, n_2, $\overline{Sh}_{b,d}$ and C_1 are known for all the apex angles between 30 ° and 90 °. Equation (12) permits the determination of the average number, $\overline{Sh}_b$, for all the situations under consideration.

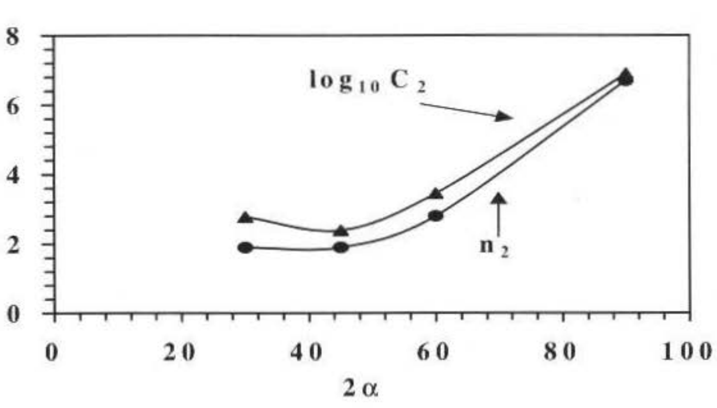

Fig. 6 Variation of $\log_{10} C_2$ and n_2 with 2α

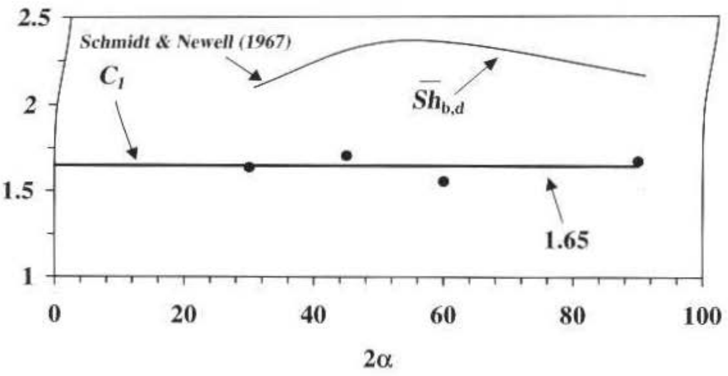

Fig. 7 Variation of $\overline{Sh}_{b,d}$ and C_1 with 2α

The value of X^+ for which the flow can be considered developed is commonly defined as that required for the average Sherwood number to decrease to within five percent of its fully developed value. Equations (13) – (16) can be used to give, for each apex angle, such X^+ values.

The Analogy Between Heat and Mass Transfer

The heat and mass transfer analogy permits the determination of the average Nusselt number, $\overline{Nu}_b$, for the analogous situation of heat transfer. At the entrance region of the triangular duct, X^+ is very small and, since $n_2 > 1$, $n_1 = 0.5$ and $\overline{Sh}_{b,d}$ becomes negligible, Eq. (12) is transformed into the following equation:

$$\overline{Sh}_b = \frac{1}{C_1 (X^+)^{0.5}} \tag{18}$$

$\overline{Sh}_{b,d}$, C_2, n_2 and n_1 are not functions of Sc. In the entrance region, Eq. (18) has the form of the well-known flat plate equation. Then, it is easy to show that C_1 is a function of Sc with the form:

$$C_1 = C (Sc)^{1/6} \tag{19}$$

Since C_1 and Sc are known, Eq. (19) yields the value of C.

Substitution of C_1, given by Eq. (19), into Eq. (12), yields:

$$\overline{Sh}_b = \overline{Sh}_{b,d} + \frac{1}{C (Sc)^{1/6} (X^+)^{n1} + C_2 (X^+)^{n2}} \tag{20}$$

To obtain the average Nusselt number, $\overline{Nu}_b$, it is necessary to replace, in Eq. (20) the Schmidt number, Sc, by the Prandtl number, Pr, and to observe that $\overline{Sh}_{b,d} = \overline{Nu}_{b,d}$. The following expression is obtained:

$$\overline{Nu}_b = \overline{Nu}_{b,d} + \frac{1}{C (Pr)^{1/6} (X^+)^{n1} + C_2 (X^+)^{n2}} \tag{21}$$

In Eq. (21), the values of $Nu_{b,d}$, n_1, C_2, n_2 and Pr are known. C is determined from Eq. (19).

Once $\overline{Nu}_b$ is calculated, the average heat transfer coefficient, $\overline{h}_b$, is determined from the Nusselt number definition:

$$\overline{Nu}_b = \frac{\overline{h}_b \, D_h}{k} \tag{22}$$

where k is the thermal conductivity of the working fluid. The heat transfer rate, $\dot{Q}_w$, analogous to the mass transfer rate, is obtained from:

$$\dot{Q}_w = \overline{h}_b \; A \, \Delta T_{log} \tag{23}$$

where ΔT_{log} is the logarithmic mean temperature difference.

The average Nusselt number, $\overline{Nu}_o$, based on wall to inlet temperature difference, $(T_w - T_o)$, is given by an equation similar to Eq. (17). For the analogous heat transfer problem, the Schmidt number used in the definition of X^+, given by Eq. (10), must be replaced by the Prandtl number.

As mentioned before, C_2 in Eq. (21) does not depend on Prandtl number, Pr. This was confirmed by Braga and Saboya (1986). They have reported experimental results for developing laminar flow in an isosceles triangular duct with the same boundary conditions of the present work and with an apex angle of 120 degrees. Water and air were used in heat transfer experiments and the results were very well correlated by an equation identical to Eq. (21), in which C_2 was taken as constant for both working fluids (water and air).

Uncertainty Analysis

An uncertainty analysis for the Graetz number was performed using the well-known Kline and McCklintock (1953) methodology. This methodology of describing uncertainties in experimental results is also presented by Moffat (1988).

Typically, the experimental uncertainty associated with the Graetz number was 2.5%, with maximum value of less than 3.5%. The uncertainties were evaluated by the responses of the Graetz number to changes in each of the variables used in the data reduction procedure (see Eqs. (10) and (11)). For the Graetz number, the most relevant parameter is the air mass flow rate, given by the rotameter.

The uncertainty associated with the determination of the overall Sherwood number was obtained by the same method and by means of Eq. (4) in conjunction with Eqs. (1) – (3). In this case, the most relevant parameter was the logarithmic mean concentration difference. Typically, the experimental uncertainty of the overall Sherwood number was 6%.

It has been demonstrated that the experimental technique used in the present investigation is a powerful tool for obtaining average transport coefficients. All the correlations presented in this work have a low degree of uncertainty.

Concluding Remarks

Within the knowledge of the authors, the results reported here are original. They are applicable in, for instance, solar collectors with triangular cavities for direct air heating. Gama et al. (1986) reported an analysis of such collectors. The cavities increase the solar absorption while air is heated in an isosceles triangular duct with the base insulated to avoid heat losses to the ambient.

Although the experiments, in the present research, were performed for isosceles triangular ducts having apex angles of 30, 45, 60 and 90 degrees, an extension of the results, for other angles, within the 20-100 degrees range, was possible.

To obtain $\overline{Sh_b}$ as function of X^+, for $Sc = 2.5$, 77 data runs were performed without reusing any of the naphthalene plates. This procedure lent confidence to the present experimental results. In future work, using the naphthalene sublimation technique, the situation were all the sides of the isosceles triangular duct are isothermal might be investigated.

Acknowledgements

The authors wish to acknowledge the Conselho Nacional de Desenvolvimento Científico e Tecnológico–CNPq for the financial support given during the course of this research.

References

Braga, S. L. and Saboya, F. E. M., 1986, "Heat Transfer and Pressure Drop in Triangular Ducts in Laminar and Turbulent Regimes", (in Portuguese), Proceedings of the First Brazilian Thermal Science Meeting, (ENCIT 86), Rio de Janeiro, RJ, Brazil, pp. 207-210.

Braga, S. L. and Saboya, F. E. M., 1996, "Turbulent Heat Transfer and Pressure Drop in na Internally Finned Equilateral Triangular Duct", Experimental Thermal and Fluid Science, Vol. 12, pp. 57-64.

Gama, R. M. S., Pessanha, J. A. O., Parise, J. A. R. and Saboya, F. E. M., 1986, "Analysis of a V- Groove Solar Collector with a Selective Glass Cover", Journal of Solar Energy, June, pp. 509-519.

Kline, S. J. and McClintock, F. A., 1953, "Describing Uncertainties in Single Sample Experiments", Mech. Eng. pp. 3-8.

Mendes, P. R. S., 1991, "The Naphthalene Sublimation Technique", Experimental Thermal and Fluid Science, Vol. 4, pp. 510-523.

Moffat, R. J., 1988, "Describing the Uncertainties in Experimental Results", Experimental Thermal and Fluid Science, Vol. 1, pp. 3-17.

Parise, J. A. R., 1978, "Transport Coefficients for Heat Exchangers of Triangular Ducts", (in Portuguese), M. S. Thesis, Mechanical Engineering Department, Pontifícia Universidade Católica do Rio de Janeiro, Rio de Janeiro, RJ, Brazil.

Saboya, F. E. M. and Sparrow, E. M., 1974, "Local and Average Transfer Coefficients for One- Row Plate Fin and Tube Heat Exchanger Configurations", Journal of Heat Transfer, Vol. 96, pp. 265-272.

Saboya, F. E. M. and Sparrow, E. M., 1976, "Transfer Characteristics of Two-Row Plate Fin and Tube Heat Exchanger Configurations", International Journal of Heat and Mass Transfer, Vol. 19, pp. 41-49.

Schmidt, F. W. and Newell, M. E., 1967, "Heat Transfer in Fully Developed Laminar Flow through Rectangular and Isosceles Triangular Ducts", International Journal of Heat and Mass Transfer, Vol. 10, pp. 1121-1123.

Shah, R. K. and London, A. L., 1978, "Laminar Flow Forced Convection in Ducts", Academic Press, New York.

Sogin, H. H., 1958, "Sublimation from Disks to Air Streams Flowing Normal to Their Surfaces", Transactions ASME, Vol. 80, pp. 61-71.

Sparrow, E. M. and Haji-Sheikh, A., 1965 "Laminar Heat Transfer and Pressure Drop in Isosceles Triangular, Right Triangular and Circular Sector Ducts", Journal of Heat Transfer, Vol. 87, pp. 426-428.

Sparrow, E. M. and Niethammer, J. E., 1979, "Natural Convection in a Ternary Gas Mixture - Application to the Naphthalene Sublimation Technique", Journal of Heat Transfer, Vol. 101, pp. 404-410.

Stephan K., 1959, "Wärmeübergang und Druckabfall bei nich Ausgebildeter Laminarströmug in Rohren und in Ebenen Spalten", Chemie Ingr. Tech., Vol. 31, pp. 773-778.

RBCM - J. of the Braz. Soc. Mechanical Sciences
Vol. XXI - No.2 - 1999 - pp. 222-232

ISSN 0100-7386
Printed in Brazil

Transferências Térmicas em Escoamentos Turbulentos Complexos: Leis de Parede e Sensibilidade a Condições na Entrada

Heat Transfer in Complex Turbulent Flow: Wall functions and Sensibility to Inlet Conditions

Marcos Vinicius Bortolus
Departamento de Engenharia Mecânica
Universidade Federal de Minas Gerais
31270-901 Belo Horizonte, MG Brazil
borta@vesper.demec.ufmg.br

André Giovannini
Institut de Mécanique des Fluides
Université Paul Sabatier
31062 Toulouse France

Abstract

First, different wall treatments based in wall functions are tested together with the Standard k - ε *turbulence model. These models are tested in the case of wall heat transfer prediction in complex turbulent flow. Then, the sensibility of these models to inlet conditions are analysed. Variations in the Nusselt distribution due to Reynolds number and initial boundary layer thickness are discussed. The incompressible flow over a backward facing step has been elected as a test case for which na extensive data base exists. Comparison between numerical results and experimental measurements is presented and discussed.*

Keywords: *Turbulence, Recirculating Flows, Heat Transfer, Wall Functions, Numerical Simulation.*

Resumo

Neste trabalho, inicialmente, propõe-se e compara-se correções ao modelo k - ε *Padrão devido aos efeitos de parede. Aborda-se modelos baseados em leis de parede aplicados à predição de transferências térmicas em escoamentos turbulentos complexos. Em seguida, testa-se a sensibilidade destes modelos a condições na entrada. São analisadas variações nas distribuições de Nusselt devido a mudanças no Número de Reynolds e à relação entre espessura da camada limite na entrada e altura do degrau. Utiliza-se como caso teste o escoamento incompreensível a jusante de um degrau descendente. Os resultados numéricos obtidos são comparados a resultados experimentais encontrados na literatura.*

Palavras-Chave: *Turbulência, Escoamento com Recirculação, Leis de Parede, Convecção Forçada, Simulação Numérica.*

Introdução

O estudo de escoamentos complexos, ou seja, com separação, recolamento e zona de recirculação é importante em diferentes aplicações da engenharia como, por exemplo, turbinas a gás, circuitos eletrônicos e trocadores de calor. Em relação ao aspecto térmico, o recolamento provoca fortes variações e aumentos consideráveis do coeficiente de transferência térmica local. Assim, a predição de transferências térmicas neste tipo de escoamento é importante no que diz respeito à eficiência térmica do sistema ou ao comportamento termomecânico dos materiais envolvidos, como por exemplo, na câmara de combustão de uma turbina a gás.

O escoamento incompreensível em torno de um degrau descendente (*backward-facing step flow* - Fig.1) é utilizado como caso teste neste trabalho. Esta geometria é bastante simples e, assim, muito utilizada na validação de métodos de cálculo. O ponto de separação é fixo permitindo que se concentre o estudo no processo de recolamento. No entanto, mesmo fixando este parâmetro, o escoamento resultante é complexo, especialmente na zona de recolamento onde a camada de cisalhamento se divide em duas: uma parte vai para a zona de recirculação e a outra para a zona de redesenvolvimento da camada limite. O ponto de recolamento flutua e o escoamento nesta zona é fortemente não-estacionário. Comparado com um escoamento turbulento dentro de um canal, a transferência térmica na zona de recirculação e perto do recolamento possui níveis mais elevados. Devido ao impacto da camada de

Manuscript received: October 1996; revised: October 1998. Technical Editor: Leonardo Goldstein Jr.

cisalhamento sobre a parede, ocorre um aumento no nível de energia cinética turbulenta e, conseqüentemente, da transferência de calor.

Os modelos de turbulência - incluindo o modelo k-ε - mais utilizados no cálculo deste tipo de escoamento não levam em consideração efeitos que são dominantes na região próxima à parede, a saber: i) difusão molecular; e ii) amortecimento de flutuações de velocidade na direção normal à parede. De maneira geral, os tratamentos utilizados próximo às paredes não alteram a dinâmica global do escoamento. No entanto, como o cálculo do fluxo de calor depende dos gradientes de temperatura junto à parede, estes tratamentos são fundamentais na predição de transferências térmicas. A fim de se considerar os efeitos de parede existem dois tipos de tratamento: i) modelos baseados em funções de parede; e ii) modelos a baixo número de Reynolds turbulento. Na década de 80, especialmente, diversos modelos baseados em leis de parede foram propostos, entre os quais, o modelo de Chieng e Launder (1980), o modelo de Amano (1984) e o modelo de Ciofalo e Collins (1989), a fim de substituir o modelo Padrão proposto por Launder e Spalding (1974) um dos mais utilizados em aplicações industriais. Assim, o objetivo inicial aqui é realizar uma comparação sistemática destes diferentes modelos baseados em leis de parede. Também, algumas simplificações são propostas.

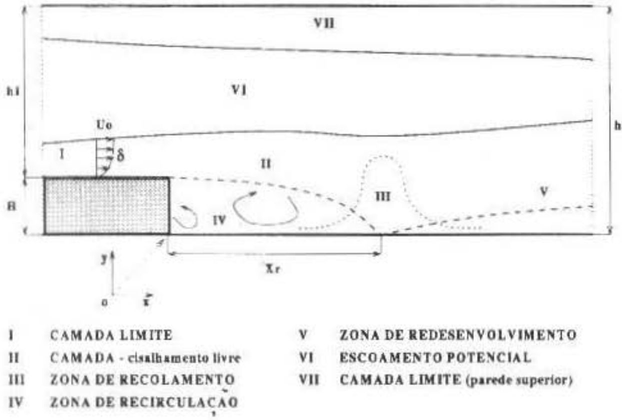

Fig. 1 Escoamento a jusante de um degrau descendente

Resultados experimentais têm mostrado que neste tipo de escoamento a estrutura turbulenta e, conseqüentemente, o coeficiente de transferência térmica local dependem significativamente das condições na entrada, ou seja, das condições a montante do ponto de separação (Adams e Johnston, 1988 e Vogel e Eaton, 1985). Alguns estudos numéricos, entre eles o de Chieng e Launder(1980) e o de Gooray et al.(1983) têm tecido comentários sobre a necessidade de se impor perfis de velocidade média e quantidades turbulentas mais realísticos na entrada. No entanto, a literatura é carente de estudos no que diz respeito à sensibilidade dos modelos de turbulência usuais a estas condições limites.

Nomenclatura

H = altura do degrau [m]
K = energia cinética turbulenta [m^2s^{-2}]
Nu = Nusselt, adimensional
P_k = Produção de k [m^2s^{-3}]
Pr = Prandtl, adimensional
Pr_t = Prandtl Turbulento, adimensional
q = fluxo de calor [wm^{-2}]
Re = Reynolds baseado em H, adimensional
S_ϕ = termo fonte para a variável ϕ
T = temperatura [K]
U = componente horizontal da velocidade média [ms^{-1}]
U_t = $\sqrt{\tau_w / \rho}\ ms^{[-1]}$
V = componente vertical da velocidade média [ms^{-1}]
Xr = comprimento da zona de recirculação [m]
X* = (x-Xr)/Xr, adimensional
y_v = espessura da subcamada laminar, adimensional

Símbolos gregos

Γ_ϕ = coeficiente de difusão de ϕ
δ = espessura da camada limite na entrada do canal [m]
ε = taxa de dissipação de k [m^2s^{-3}]
k = constante de von Karman
μ = viscosidade molecular [$kg.s^{-1}m^{-1}$]
μ_t = viscosidade turbulenta [$kgs^{-1}m^{-1}$]
μ_{ef} = $\mu + \mu_t$ [$kg.s^{-1}m^{-1}$]
ρ = densidade [kgm^{-3}]
τ = tensão de atrito [Nm^{-2}]
ϕ = variável escalar genérica
Ψ = $K^{1/2}/U$, intensidade de turbulência, adimensional

Subscritos

in = entrada do canal
Max = valor máximo
P = ponto genérico P adjacente à parede
ω = parede

Deste modo, o objetivo final deste trabalho é testar a sensibilidade do modelo k-ε padrão juntamente com modelos baseados em leis de parede, a condições na entrada no caso de predições de transferências térmicas parietais em escoamentos turbulentos complexos. São analisadas variações nas distribuições de Nusselt devido a mudanças no número de Reynolds e à relação entre espessura da camada limite na entrada e altura do degrau.

Modelo Matemático

O escoamento é governado pelas equações de Reynolds, obtidas a partir do cálculo das médias temporais das equações de Navier-Stokes. O modelo de turbulência utilizado é o Modelo k - ε Padrão tal como ele é apresentado no trabalho de Launder e Spalding (1974), inclusive sem se modificar as constantes que ali são propostas. Em relação à equação da Energia, utiliza-se o número de Prandtl turbulento $Pr_t = \mu_t c_P / \lambda_t$, onde μ_t é a viscosidade turbulenta e λ_T é a condutividade térmica turbulenta. Neste trabalho, considera-se que o número de Prandtl é constante e igual a 0,9. Todas as equações são colocadas na forma (Tabela 1):

$$\frac{\partial}{\partial t}(\rho\phi)+div(pu\phi)=div(\Gamma_\phi grad\phi)+S_\phi \qquad (1)$$

onde Γ_ϕ e S_ϕ são, respectivamente, os coeficientes de difusão e o termo fonte específicos da variável φ. As constantes do modelo de turbulência C_μ , C_1, C_2, σ_k, σ_ε, valem, respectivamente, 0,09, 1,44, 1,92, 1,00 e 1,30.

Tabela 1 Equações Resolvidas

Equação	φ	• φ	So
Continuidade	1	0	0
x-movimento	U	$\mu_{ef} = \mu_t + \mu$	$-\frac{\partial P}{\partial x}+\frac{\partial}{\partial x}(\mu_{ef} \frac{\partial U}{\partial x})+\frac{\partial}{\partial y}(\mu_{ef} \frac{\partial V}{\partial x})$
y-movimento	V	μ_{ef}	$-\frac{\partial P}{\partial y}+\frac{\partial}{\partial x}(\mu_{ef} \frac{\partial U}{\partial y})+\frac{\partial}{\partial y}(\mu_{ef} \frac{\partial V}{\partial y})$
Energia	T	$\frac{\mu}{Pr}+\frac{\mu_t}{Pr_t}$	0
Energia cinética	k	$\mu+\frac{\mu_t}{\sigma_k}$	$\rho P_k - \rho\varepsilon$
Dissipação	ε	$\mu+\frac{\mu_t}{\sigma_\varepsilon}$	$C_1 \frac{\rho\varepsilon P_k}{k} - C_2 \frac{\rho\varepsilon^2}{k}$

onde

$$\mu_t = \rho C_u \frac{k^2}{\varepsilon}$$

e

$$P_k = \frac{\mu_t}{\vartheta}[(\frac{\partial U}{\partial y}+\frac{\partial V}{\partial x})^2 + 2(\frac{\partial U}{\partial x})^2 + (\frac{\partial V}{\partial y})^2]$$

Condições de Contorno

Os resultados numéricos são comparados às experiências de Vogel e Eaton (1985) e Vogel, (1994) cujas condições de referência são (Fig. 1):

- Camada limite turbulenta na entrada
- Re=28.000 - comprimento de referência = H ; $\delta/H=1,1$; $h_2/h_1 = 1,25$.
- Fluxo de calor q_w constante na parede inferior após o degrau tal que: $(T_w - T_{in})_{min}$ é da ordem de 15K, onde Tw é a temperatura da parede e T_{in} é a temperatura na entrada.

Na entrada, impõe-se perfis de velocidade, de energia cinética e de dissipação obtidos a partir dos perfis experimentais de U e $\overline{u'^2}$ obtidos por Vogel (1994). Nas paredes, as condições são impostas utilizando-se as leis de parede apresentadas na seção seguinte. Finalmente, na saída, supõe-se que os gradientes das diversas variáveis na direção do escoamento sejam nulos. No que diz respeito à temperatura, impõe-se um perfil uniforme de temperatura na entrada e nas outras paredes a temperatura é considerada constante.

Leis de Parede

Nesta seção são descritos os diversos modelos de parede baseados em leis de parede utilizados neste trabalho.

O modelo Padrão - MODEL 1 - é apresentado em Launder e Spalding (1974). A discretização dos modelos é feita via método dos Volumes Finitos. Inicialmente, é necessário que os pontos das malhas adjacentes às paredes estejam na zona logarítmica – $(11 < y^+ < 400)$, onde, $y^+ = yU_\tau/\nu$, $U_\tau = \sqrt{\tau_w/\rho}$ é velocidade de atrito e τ_w é a tensão de atrito na parede.

A lei logarítmica, na sua forma original, não é apropriada aos escoamentos com recirculação pois a velocidade de atrito, usada para adimensionalizar a velocidade média e a distância normal à parede, é igual a zero no ponto de recolamento. Considerando-se que nesta zona a produção de energia cinética turbulenta é igual à sua dissipação, pode-se mostrar que (Cousteix, 1989)

$$\tau_w \approx \rho k p C_\mu^{1/2} \qquad (2)$$

e

$$\varepsilon = k^{3/2} / (Cl.y) \qquad (3)$$

onde P é o ponto da malha mais próximo da parede e $Cl = k_\mu^{3/4}$. Assim, pode-se colocar a lei logarítmica na forma

$$\frac{U k_P^{1/2} C_\mu^{1/4}}{\tau_w / \rho} = \frac{1}{k} log\,[\, Ey \frac{(C_\mu^{1/2} k_P)^{1/2}}{\nu} \,] \qquad (4)$$

A partir das equações (2), (3) e (4) e considerando-se que a energia cinética k e a tensão de atrito, τ turbulentas são constantes, determina-se a dissipação $\bar{\varepsilon}$ e a produção P_k médias de k na direção perpendicular à parede. No caso da equação da dissipação, impõe-se um valor ao ponto P: $\varepsilon_P = k^{3/2}/(Cl.y_P)$.

No caso da temperatura, de maneira semelhante, a lei logarítmica se transforma em

$$\frac{(T_P - T_w) c_P \rho C_\mu^{1/4} k_P^{1/2}}{q_w} = \frac{Pr_t}{k} log\,[\, \frac{Ey_P (C_\mu^{1/2} k_P)^{1/2}}{\nu} \,] + AJ$$

onde q_w et T_w são o fluxo de calor e a temperatura na parede, respectivamente, e AJ é a Função de Jayatilleke (Launder e Spalding, 1974).

O modelo de Chieng e Launder(1980) considera a região próxima à parede dividida em duas: i) subcamada laminar ($0 < y^+ \leq 11$); ii) zona logarítmica ($11 < y^+ < 400$). Assim, em relação ao modelo Padrão, no cálculo de $\bar{\varepsilon}$ e de P_k considera-se a influência da subcamada viscosa na dissipação de k (a produção de k é zero nesta zona). Além disto, utiliza-se a energia cinética no bordo da subcamada laminar k_v no lugar da energia cinética no ponto P, k_P, nas dimensionalizações. Neste trabalho, compara-se duas versões deste modelo. Uma - MODEL 2 - que considera k e τ constantes na zona logarítmica (Launder, 1986) e outra - MODEL 21 - que considera que estas quantidades variam linearmente nesta zona, como proposto originalmente no trabalho de Chieng e Launder(1980).

No modelo de Chieng e Launder a espessura adimensional da subcamada laminar é considerada constante ($y_v^+ = 11$). Mais recentemente, Ciofalo e Collins (1989), propuseram um modelo - MODEL 22 - no qual y_v^+ varia com a intensidade de turbulência no ponto P - $\psi_P = k_P^{1/2} / U_P$ de acordo com a relação:

$$\frac{y_v^+}{y_{vo}^+} = \left(\frac{\Psi_P}{\Psi_E} \right)^{-c}$$

onde Ψ_E e y_{vo}^+ são, respectivamente, a intensidade de turbulência e a espessura adimensional da subcamada laminar caso as condições no ponto P fossem as de uma camada limite turbulenta ordinária. Resultados experimentais sugerem que o valor da constante c está entre 1/3 e 2/3. Adota-se aqui o mesmo valor utilizado por Ciofalo e Collins(1989) em seus cálculos (c=0,4). Na zona de recolamento, Ψ_P é bem superior a Ψ_E e, assim, ocorre uma diminuição significativa de y_v^+.

O modelo de Amano(1984) - MODEL 3 - considera que, próximo à parede, existem três camadas: i) subcamada laminar ($0 < y^+ \leq 5$); ii) zona tampão *(buffer layer)* ($5 < y^+ \leq 30$); e iii) zona logarítmica ($30 < y^+ < 400$). Neste trabalho, duas simplificações são propostas em relação ao modelo proposto por Amano. No seu modelo k e τ variam linearmente na zona logarítmica. Aqui, considera-se como no caso do MODEL 2 que estas quantidades são constantes nesta zona. Amano propõe também correções nos termos de produção e destruição na equação da dissipação. Neste trabalho utiliza-se o mesmo tratamento dos modelos anteriores.

Método Numérico

As equações que governam o escoamento são discretizadas pela técnica de Volumes Finitos. O esquema Híbrido é utilizado para o tratamento dos termos difusivos e convectivos. As equações algébricas resultantes são resolvidas iterativamente utilizando-se uma versão do programa TEACH (Gosman e Ideriah, 1976), que incorpora o algoritmo SIMPLE. Este programa é bastante conhecido o que dispensa a apresentação de maiores detalhes.

Após a realização de testes de convergência - apresentados na referência (Bortolus e Giovannini, 1995) escolheu-se uma malha de 146x102 elementos. Neste caso a malha é tal que todos os pontos das malhas adjacentes à parede estão dentro da zona logarítmica.

As melhores características de convergência - robustez - foram apresentadas pelos modelos MODEL 1 e MODEL 2. Nos outros casos, para se obter a convergência, o processo iterativo é inicializado com os campos obtidos com o MODEL 2.

Apresentação e Discussão dos Resultados

Aqui, apresenta-se os resultados relativos ao aspecto térmico do problema. Os resultados da dinâmica do escoamento são discutidos em Bortolus e Giovannini, 1995. De maneira geral, os perfis de velocidade média e de energia cinética turbulenta concordam bem com as experiências. Longe da parede, os diferentes modelos de parede não afetam esses perfis. No entanto, a comparação das distribuições dos coeficientes de atrito determinadas com os diversos modelos de parede mostra que esses perfis variam muito com o modelo utilizado na região próxima à parede. Este mesmo comportamento é observado no caso da temperatura.

Nas figuras seguintes, devido às diferenças entre as posições de recolamento - Xr - numérica e experimental - da ordem de 15% - (Bortolus e Giovannini, 1995), utiliza-se nas comparações a coordenada adimensionalizada

$$X* = \frac{(x - Xr)}{Xr} \tag{7}$$

A posição de recolamento Xr é definida como sendo o ponto sobre a parede inferior do degrau onde o coeficiente de atrito é igual a zero.

Os perfis numéricos e experimentais de temperatura são comparados na Fig. 2. Observa-se uma boa concordância entre os dois. Nota-se que os gradientes de temperatura são significativos somente perto da parede. Estes perfis foram obtidos com o modelo Padrão. Longe da parede, não existem diferenças importantes entre os perfis calculados com os diferentes modelos de parede. As diferenças próximas à parede são analisadas a partir das distribuições de número de Nusselt baseado na altura do degrau (Nu) Figs. 3 e 4.

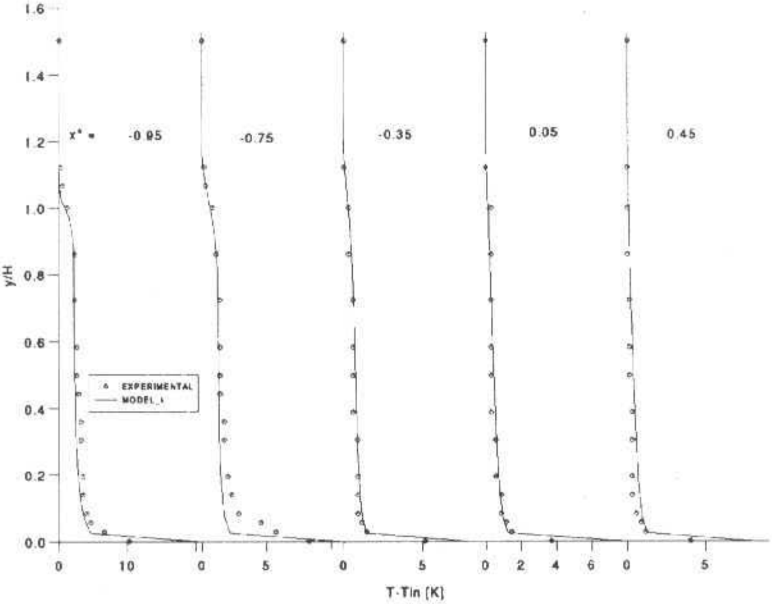

Fig. 2 Perfis de temperatura

Na Figura 3 pode-se acompanhar as evoluções do modelo Padrão - MODEL 1, inicialmente com o acréscimo da subcamada laminar - MODEL 2 - e, em seguida, com o acréscimo da zona tampão - MODEL 3. Em relação ao nível máximo de Nu, nota-se uma melhora sensível. No entanto, diferenças importantes continuam a existir na zona de recirculação e na zona de redesenvolvimento.

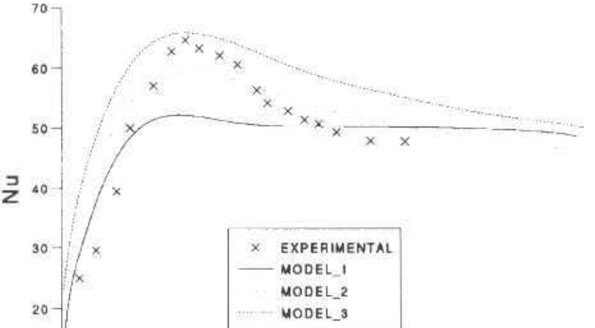

Fig. 3 Número de Nusselt: Leis da parede

Na Figura 4, nota-se que, praticamente, não há diferenças entre o MODEL 2 e o MODEL 21. Uma pequena diferença a favor do MODEL 2 é encontrada na zona de redesenvolvimento. Nesta figura mostra-se também os resultados obtidos com o MODEL 22. Observa-se um mínimo localizado perto do recolamento. Este mínimo aparece devido à limitação inferior na espessura adimensionalizada da subcamada laminar y_v imposta no modelo para que o perfil de velocidade não apresente descontinuidade no ponto interseção entre a subcamada laminar e a subcamada logarítmica. De acordo com a análise mostrada em detalhes no trabalho de Ciofalo e Collins, 1989) o valor de y_v não deve ser inferior a *1/k*. Isto faz com que no cálculo aconteça uma diminuição forçada da intensidade de turbulência diminuindo, assim, localmente a transferência de calor.

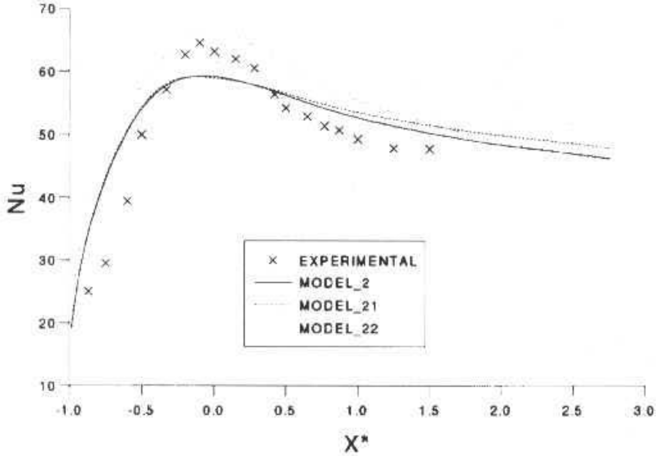

Fig. 4 Numero de Nusselt: Modelos de duas camadas

Para melhor compreender a evolução qualitativa das diferentes funções de parede, compara-se na Fig. 5 as distribuições de Nu normalizadas pelo valor máximo Nu_{max}. Comparando-se os resultados dos modelos MODEL 1 e MODEL 2, observa-se uma melhora sensível na zona de redesenvolvimento. Quando se compara os resultados dos modelos MODEL 2 e MODEL 3, diferenças pouco importantes são encontradas. Isto indica que a inclusão dos efeitos da subcamada laminar é mais significativa que a inclusão dos efeitos da zona tampão. Se bem que os resultados com o MODEL 22 não sejam satisfatórios na zona de recolamento, devido à presença de um mínimo local explicada anteriormente, nota-se que na zona de redesenvolvimento obtem-se com este modelo resultados melhores que com os modelos MODEL 2 e MODEL 3.

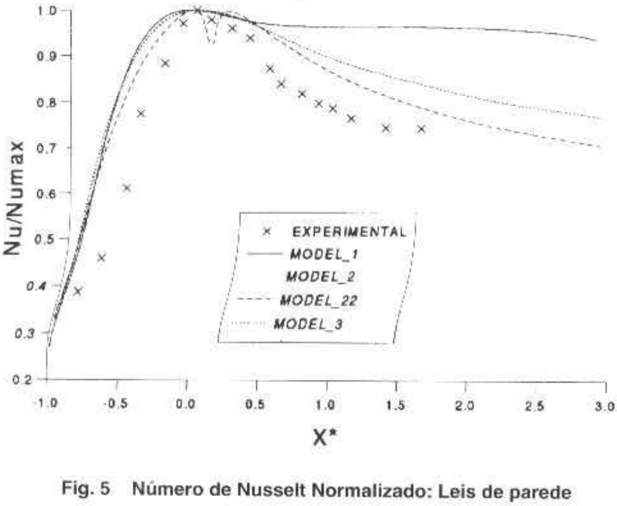

Fig. 5 Número de Nusselt Normalizado: Leis de parede

Analisa-se, em seguida, a sensibilidade aos parâmetros número de Reynolds, Re, e relação entre a espessura da camada limite na entrada e a altura do degrau, δ/H, do modelo k ε na predição do coeficiente de transferência térmica local - Número de Nusselt. Considerou-se apenas os modelos de parede MODEL 2 e MODEL 3 devido ao melhor desempenho apresentado por eles nas comparações mostradas anteriormente.

Na Figura 6, observa-se que os níveis de Nusselt aumentam com o aumento do número de Reynolds. Este comportamento é verificado também experimentalmente. As variações do número de Nusselt máximo, Nu_{max}, com Re calculadas com os modelos de parede MODEL 2 e MODEL 3 são comparadas às experiências na Fig. 7. Resultados experimentais indicam que $Nu_{max} \sim Re^n$. As experiências de Vogel e Eaton(1985) mostram que n é aproximadamente 0,6. Com os modelos MODEL 2 e MODEL 3, encontra-se 0,68 e 0,62, respectivamente. Percebe-se, assim, que os resultados quantitativamente dependem do modelo de parede que é associado ao modelo k - ε, mas as diferenças entre os dois modelos utilizados aqui não são excessivas, levando-se em consideração a complexidade do presente problema. Percentualmente, as diferenças máximas em relação à experiência são da ordem de 20% e 10% para os modelos MODEL 2 e MODEL 3, respectivamente. Em média, estas diferenças são da ordem de 13% e 5% para os modelos MODEL 2 e MODEL 3, respectivamente. Os resultados para o modelo MODEL 3 estão dentro da incerteza das experiências, no que diz respeito ao número de Nusselt, que é da ordem de 6\%.

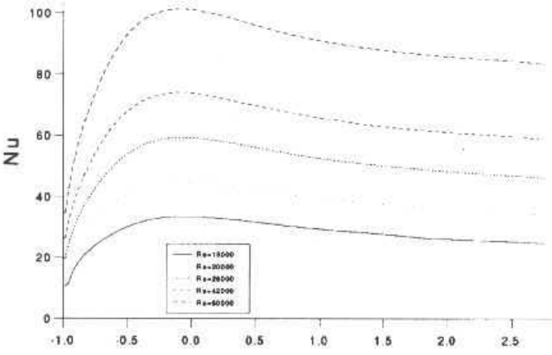

Fig. 6 Distribuição de Nusselt em função do número de Reynolds

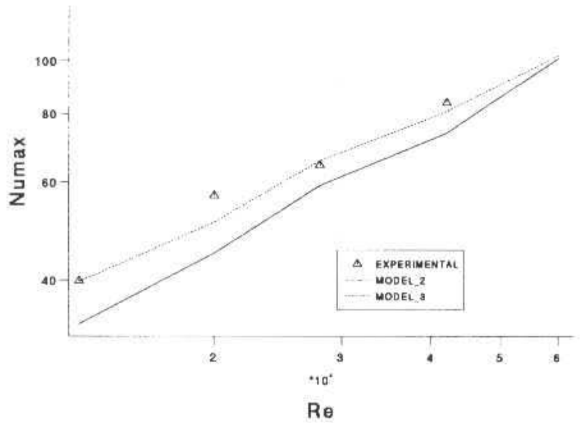

Fig. 7 Nusselt máximo em função do número de Reynolds

Para se analisar o efeito qualitativo do número de Reynolds na distribuição de Nusselt, compara-se na Fig. 8 as distribuições normalizadas pelo Nu_{max}. Nota-se que não existem diferenças significativas entre elas nas zonas de recirculação e recolamento, o que é verificado experimentalmente. No entanto, na zona de redesenvolvimento as diferenças nas distribuições determinadas experimentalmente parecem ser menores (Vogel e Eaton, 1985). Estas diferenças podem ter sido provocadas pelo tratamento da região de parede utilizado aqui baseado em {Leis de Parede. A jusante do ponto de recolamento, o escoamento é cada vez mais determinado pela região de parede e, assim, o seu comportamento se aproxima progressivamente do de uma camada limite turbulenta ordinária. Para se resolver este escoamento, o mais adequado parece ser um tratamento da região de parede baseado em modelos a Baixo Número de Reynolds, os quais apresentam, com malha adequada, comportamento assintótico em relação ao número de Nusselt satisfatório nesta região (Bortolus e Giovannini, 1995).

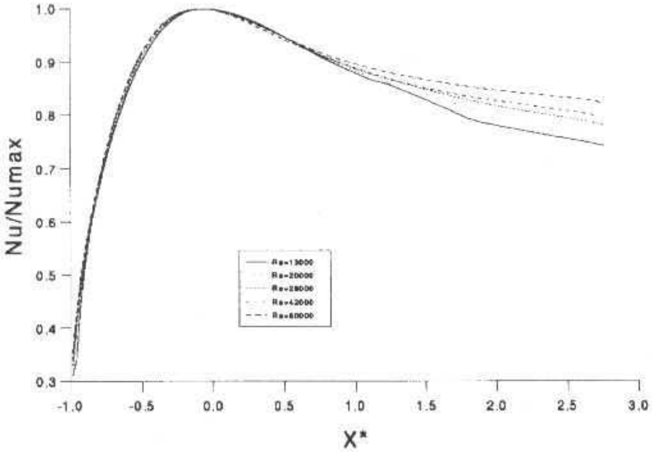

Fig. 8 Distribuição de Nulsselt normalizado em função do número de Reynolds

No que diz respeito à relação δ/H, o comportamento é oposto ao caso do número de Reynolds. Como observado também por Vogel e Eaton(1985), os níveis de Nusselt diminuem com o aumento de δ/H (Fig. 9). Os seus resultados sugerem que $Nu_{max} \sim (\delta/H)^{n_\delta}$, sendo que n_δ é aproximadamente -0.1. Com os modelos de parede MODEL 2 e MODEL 3 encontrou-se para n_δ os valores -0.08 e -0.09, respectivamente, que são próximos do experimental. No entanto, como mostrado na Fig. 10 os níveis de Nu_{max} determinados com o MODEL 3 são mais próximos das experiências. Neste caso, as diferenças entre os cálculos com os modelos MODEL 2 e MODEL 3 e as experiências estão, percentualmente, próximas às determinadas para o caso do número de Reynolds.

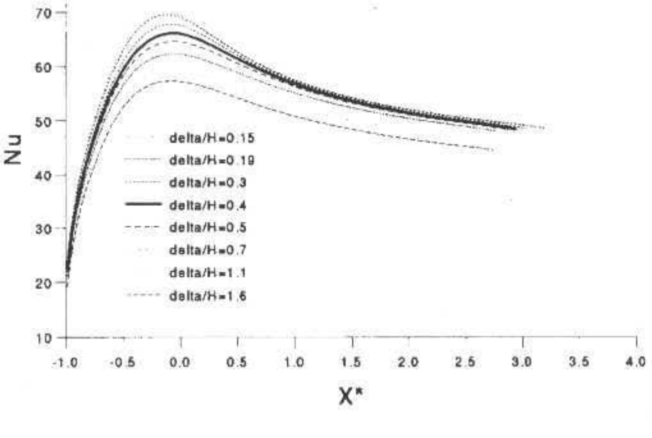

Fig. 9 Distribuição de Nusselt em função de δ/H (=delta/H)

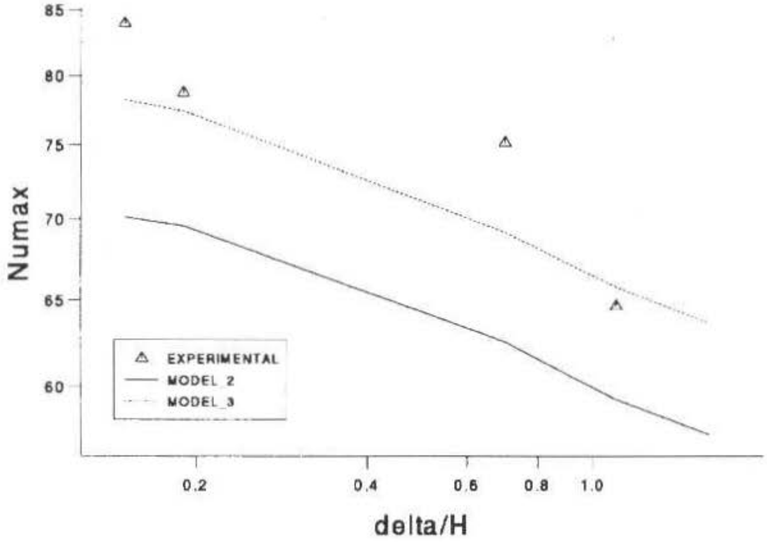

Fig. 10 Nusselt máximo em função δ/H (=delta/H)

Qualitativamente, as distribuições de Nusselt normalizadas pelo Nu_{max} apresentadas na Fig. 11 mostram que, ao contrário do caso do número de Reynolds, existem diferenças nas zonas de recolamento e, principalmente, na zona de redesenvolvimento com a variação de δ/H. No entanto, pode-se observar que as mudanças são mais importantes no intervalo de δ/H entre 0,3 e 0,5. Nas regiões $\delta/H > 0,5$ e $\delta/H < 0,3$, as distribuições são próximas. De fato, a partir dos estudos experimentais de Adams e Johnston (1988), conclui-se que $\delta/H = 0,4$ é o limite entre dois comportamentos do escoamento após o degrau: se $\delta/H < 0,4$, o degrau representa uma perturbação muito forte para a camada limite a montante; e se $\delta/H > 0,4$, a perturbação é menos importante.

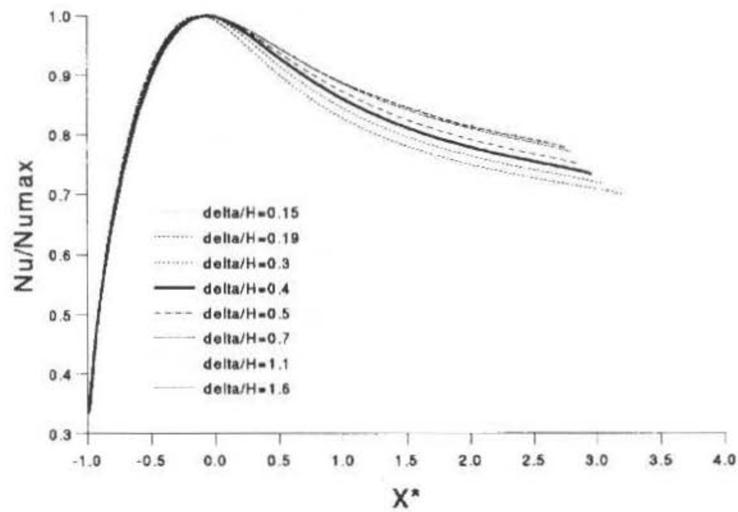

Fig. 11 Distribuição de Nusselt normalizado em função δ/H (=delta/H)

Conclusões

No caso das leis de parede, existem melhoras sensíveis com os modelos MODEL 2 e MODEL 3 em relação ao modelo Padrão, principalmente na zona de recolamento. A análise qualitativa mostra que existe um ganho mais significativo com a consideração da subcamada laminar que com a consideração da zona tampão. Além disto, esta análise mostra que a evolução das funções de parede passa pela consideração de situações de não-equilíbrio provocadas por níveis bem mais elevados de energia cinética turbulenta próximo à parede em relação à uma camada limite turbulenta ordinária.

Quantitativamente, os resultados com o MODEL 3 são mais próximos da experiência, embora as diferenças entre esta e o MODEL 2 não sejam excessivas. Tendo em vista as boas características de convergência do MODEL 2, pode-se dizer que entre os modelos de parede comparados este modelo representa o melhor compromisso robustez - capacidade de predição.

Além disto, não existe nenhum ganho sensível quando se considera que a energia cinética turbulenta e a tensão turbulenta variam linearmente na zona logarítmica - MODEL 21 - em relação ao caso em que estas quantidades são consideradas constantes - MODEL 2.

Tendo em vista os bons resultados obtidos com o MODEL 3, pode-se dizer que este modelo é uma opção ao modelo de três camadas originalmente proposto por Amano(1984), já que aquele, devido às simplificações propostas neste trabalho, seria mais fácil de ser implementado.

O presente estudo mostra que, no que diz respeito a predições de transferências térmicas parietais, se consegue captar satisfatoriamente com o modelo k - ε, corrigido com as leis de parede, variações nas condições na entrada - a montante do ponto de separação - no caso destes escoamentos turbulentos complexos.

Referências

Adams, E. W. and Johnston, J. P., 1988, "Flow Structure in the Near-Wall Zone of a Turbulent Separeted Flow", AIAA Journal, Vol 26, pp. 932-939.

Amano, R. S., 1984, "Development of Turbulence Near-Wall Model and Its Application to Separated and Reattached Flows", Numerical Heat Transfer, Vol 7, pp. 59-75.

Bortolus, M.V. e Giovannini, A., 1995, "Numerical Prediction of Wall Heat Transfer in Complex Turbulent Flow", Turbulence, Heat and Mass Transfer 1, edited by Hanjalic, K. and Pereira, J.C.F., Begell House, Inc., New York.

Chieng, C. C. e Launder, B. E., 1980, "On the Calculation of Turbulent Heat Transport Downstream from an Abrupt Pipe Expansion", Numerical Heat Transfer, Vol 3, pp. 189-207.

Ciofalo, H. and Collins, M. W., 1989, "k-ε Predictions of Heat Transfer in Turbulent Recirculating Flows Using an Improved Wall Treatment", Numerical Heat Transfer, Vol. 3, pp. 21-47.

Cousteix, J., 1989, "Turbulence et Couche Limite", Cepadues-Editions, Toulouse, França.

Gooray, A. M. et al., 1983, "A Two-Pass Procedure for the Calculation of Heat Transfer in Recirculationg Turbulent Flow", Numerical Heat Transfer, Vol 6, pp. 423-440.

Gosman, A. P. e Ideriah, F. J. K., 1976, "Manual TEACH-2E: A General Computer Program for Two-Dimensional, Turbulent, Recirculating Flows", Imperial College, Londres. Launder, B.E., 1986, "Low-Reynolds-Number Turbulence Near Walls", Report TFD/86/4, UMIST - Dept. Mechanical Engineering.

Launder, B. E. e Spalding, D. B., 1974, "The Numerical Computation of Turbulent Flows", Computer Method in Applied Mechanics, Vol 3, pp. 269-289.

Vogel, J. C., 1984, "Heat Transfer and Fluid Mechanics Measurements in the Turbulent Reattaching Flow Behind a Backward-Facing Step", Tese de Doutorado, Stanford University.

Vogel, J. C. e Eaton, J.K., 1985, "Combined Heat Transfer and Fluid Dynamic Measurements Downstream of a Backward-Facing Step", Journal of Heat Transfer, Vol 107, pp. 922-929.

RBCM - J. of the Braz. Soc. Mechanical Sciences
Vol. XXI - No.2 - 1999 - pp. 233-244

ISSN 0100-7386
Printed in Brazil

A Simple Model for Pressure Drop in Horizontal Core Annular Flow

Antonio C. Bannwart
Universidade Estadual de Campinas
Faculdade de Engenharia Mecânica
Departamento de Energia
13083-970 Campinas, SP Brazil
bannwart@fem.unicamp.br

Abstract

Based upon experimental data for heavy oil-water flow inside steel (26.7 mm ID) and cemented (23.9 mm ID) horizontal tubes, a very simple model for pressure drop in the core annular flow pattern was developed. The experiments were run at room temperature and the fluids used were a fuel oil (μ = 2.7 Pa.s, ρ = 989 kg/m^3) and tap water, both drawn from a separator tank. First, it is shown that for both tubes the so-callled "perfect core annular flow" approach (shortly PCAF) poorly correlates the data. This is due to the waviness of the interface and turbulence in the annulus flow. These effects are taken into account in the model proposed in this paper and justify the assumption of no-slip, which was earlier concluded by the author from wavespeed measurements for the same flow (Bannwart, 1998). As a result, a very simple correlation model for the pressure gradient is derived. The model was adjusted to fit the data and generalized to other tube sizes and fluids. Different correlations for oleophilic and oleophobic pipe walls are provided. Calculations using the correlation for oleophobic pipe behavior are in very good agreement with data from another source.

Keywords: *Multiphase Flow, Liquid-Liquid flow, Core Annular Flow, Pressure Drop, Modeling.*

Introduction

Since the pioneer works of Russel and Charles (1959) and Charles, Govier and Hodgson (1961) core annular flows have found important practical applications in the pipelining of heavy oils lubricated by water. This flow pattern is very stable when the two liquids are immiscible and do not emulsify. Under such circumstances the oil occupies the center of the tube surrounded by a thin water annulus adjacent to the wall. The correspondent pressure drop is comparable to the flow of water only, since the more viscous fluid does not touch the wall. Accurate predictions of pressure drop and holdup are essential for the design and optimization of such systems.

The simplest theoretical model for the analysis of core-annular flows is to consider a fully developed annular axisymmetric laminar two-phase flow with a smooth circular interface. This approach was followed by Russel and Charles (1959) and recently also employed by Bobok, Magyari and Udvardi (1996). It is sometimes called the "perfect core annular flow" (shortly PCAF) approach. Ooms *et al.* (1984) proposed to consider the waviness of the interface but their model, based on the Reynolds equation of the lubrication theory, assumes that the wave parameters are known *a priori*. Oliemans *et al.* (1986) further considered the turbulence in the annulus flow. Arney *et al.* (1993) proposed simply the use of correlations for friction factor and holdup. However, their Reynolds number definition comes directly from the PCAF approach whereas the water holdup is given by an empirical correlation.

Nomenclature

A = cross sectional area of the pipe, m^2
b = constant, dimensionless
C_w = water input fraction, dimensionless
D = tube diameter, m
G = pressure gradient, Pa/m
G_1 = pressure gradient for unity input ratio, Pa/m
G_w = pressure gradient for water flow at mixture flow rate, Pa/m
J = mixture superficial velocity, m/s
k = constant, kg/m^8
n = exponent, dimensionless
q = exponent, dimensionless
Q = mixture flow rate, m^3/s
Q_o = oil flow rate, m^3/s
Q_w = water flow rate, m^3/s
Q^* = modified mixture flow rate, m^3/s
r = number of runs
Re = Reynolds number, dimensionless
S = total relative variance, dimensionless
V = average velocity, m/s
α = volumetric fraction of the core, dimensionless
ϕ = two-phase multiplier, dimensionless
μ = viscosity, Pa.s
ρ = density, kg/m^3

Subscripts

calc = calculated using the model
exp = experimental value
o = oil
m = mixture
pcaf = perfect core annular flow
w = water

Manuscript received: September 1998; revision received: March 1999.Technical Editor: Angela Ourívio Niechele.

A very simple one-dimensional model for horizontal core annular flow is developed in this work, based on pressure drop data for oil-water flow inside steel (26.7 mm ID) and cemented (23.9 mm ID) horizontal tubes, within the range of conditions for which a stable core annular flow pattern is observed. Since carbon-steel pipes are usually oleophilic (i.e. they are likely to become fouled by the oil), cement-lined pipes have been proposed (Ribeiro, 1994; Arney *et al.*, 1996) because of their hydrophilic-oleophobic properties. The cement coat which covers the pipe wall is, in fact, easily wetted by water but becomes oil repellent, thus fouling by oil is minimized. It is shown that for both tubes the PCAF model poorly correlates the data. A new model is then proposed in order to take into account the waviness of the interface and turbulence in the water film.

Experimental Setup

The experimental apparatus is shown in Fig. 1. It is basically the same setup earlier used by Ribeiro (1994). The present author ran short-term experiments using oil and water at room temperatures in horizontal tubes at various flow rates of each fluid. From a 1 m^3 separator tank, oil was drawn by a progressive cavity pump (Moyno) with variable speed and the flow rate was measured through a direct mass flowmeter (Micro Motion). Water was drawn from the bottom of the tank by a centrifugal pump, filtered and measured through a rotameter. The oil-water input ratio was varied from 1 to 11. The injection nozzle was a simple device having a central tube inlet for oil and a surrounding shell for water. Pressure differences were measured with a simple U-tube manometer filled with water.

The manometer legs were connected to the tubes through boxes to minimize their contamination with oil. The distance between taps 1 and 2 (cement-lined tube, 23.9 mm ID) and between taps 3 and 4 (carbon-steel tube, 26.7 mm ID), see Fig. 1, was 400 cm. The oil used was the no. 6 fuel oil, whose properties measured at laboratory temperature where $\mu = 2.7$ Pa.s, $\rho = 989$ kg/m^3. Interfacial wavespeed was also measured through high-speed imaging and reported elsewhere (Bannwart, 1998). For each run, before doing measurements, one waited at least 15 minutes until steady state was observed. Prior to the next set of flow rates, the system was run with pure water until the pressure drop through the entry and exit steel tubes were low enough, so as to make sure that the tubes were clean from the fouling action by the oil.

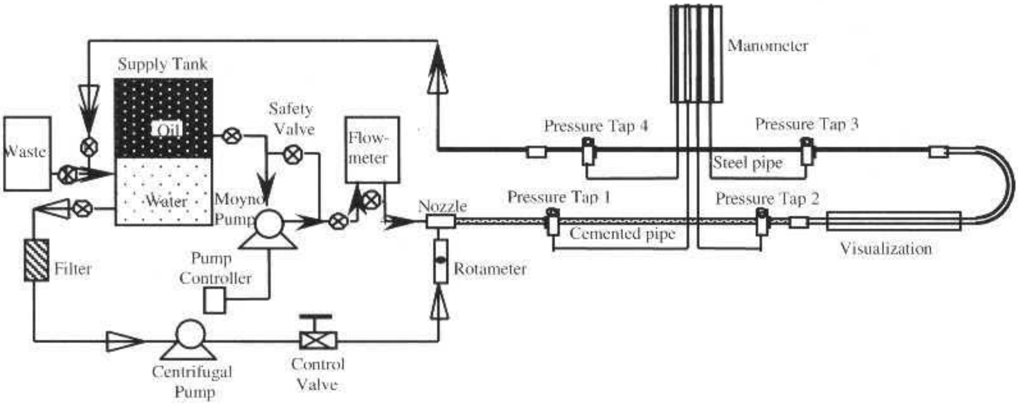

Fig. 1 Schematic of the experimental apparatus

Results and Analysis

Table 1 summarizes the experimental results for the flow rates of oil (Q_o) and water (Q_w), the pressure drops in the cemented and steel pipes, as well as the wavespeed (a).

Table 1 Experimental pressure drop and wavespeed data

Point no.	Temp. (^{o}C)	Q_o (l/s)	Q_w (l/s)	ΔP cemented (mm water)	ΔP steel (mm water)	a (m/s)
1	21.2	0.1597	0.1112	19.55	7.2	0.6700
2	21.5	0.1528	0.0905	17.1	6	0.5785
3	21.8	0.1501	0.0646	17.1	4.9	0.5077
4	21.9	0.1249	0.0388	10.4	3	0.4267
5	22.9	0.1283	0.0246	8.4	2.5	0.3387
6	22.4	0.2239	0.1086	36.3	19.3	0.8043
7	22.4	0.2026	0.0880	32.6	12.7	0.6907
9	22.8	0.1959	0.0646	30.2	7.8	0.6296
10	22.3	0.1984	0.0388	22.8	6.4	0.5895
11	21.5	0.1849	0.0272	15.4	5.5	0.5328
12	20.5	0.2592	0.1099	48.5	21.35	0.9094
13	20.6	0.2478	0.0905	44.7	18.33	0.8388
14	20.6	0.2527	0.0776	48.1	14.85	0.8084
15	20.5	0.2501	0.0479	46.5	11.6	0.7533
16	21.9	0.2495	0.0246	62.5	10.2	0.6899
17	21.4	0.1245	0.1151	14	5.5	0.6278
18	21.6	0.1269	0.0918	13.2	4.2	0.5312
19	21.7	0.1196	0.0685	11.2	3.3	0.4626
20	22.1	0.1179	0.0388	8.7	2.9	0.4158
21	20.5	0.1048	0.0142	5.5	2.4	0.3051
22	20.9	0.1872	0.1164	34.5	12.3	0.7643
23	21.5	0.1822	0.0931	25	8	0.6534
24	22.4	0.1761	0.0660	20.3	5.8	0.5822
25	24.9	0.1716	0.0401	15.2	4	0.4964
26	25.7	0.1777	0.0155	13.1	5.2	0.4869
27	26.9	0.2332	0.1125	31.8	12.2	0.8386
28	27.0	0.2386	0.0918	39.8	12.9	0.7741
29	27.0	0.2337	0.0646	42.4	10.4	0.7239
30	26.1	0.2323	0.0362	44.4	5.9	0.6328
31	25.6	0.2298	0.0246	45.3	7.7	0.6303

Figure 2 shows the superficial velocities of each fluid (defined as the volumetric flow rate divided by the pipe cross sectional area) corresponding to the experimental runs for both cemented and steel

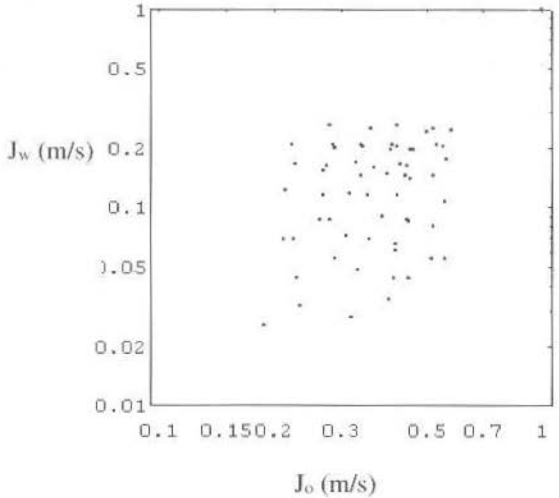

Fig. 2 Experimental range of superficial velocities

tubes. A more useful map showing the boundary layer Reynolds number for the water annulus flow Re_w *versus* the water-oil input ratio is shown in Fig. 3. As usual, Re_w is defined as

$$Re_w = \frac{\rho_w V_w (4\delta)}{\mu_w} \cong \frac{\rho_w J_w D}{\mu_w} \tag{1}$$

where ρ_w and μ_w are respectively the density and absolute viscosity of the water, V_w and J_w are respectively its average and superficial velocities, δ is the average thickness of the annulus flow and D is the tube diameter. From Fig. 3 it can be concluded that for most runs the water flow in the annulus was turbulent ($Re_w > 2000$).

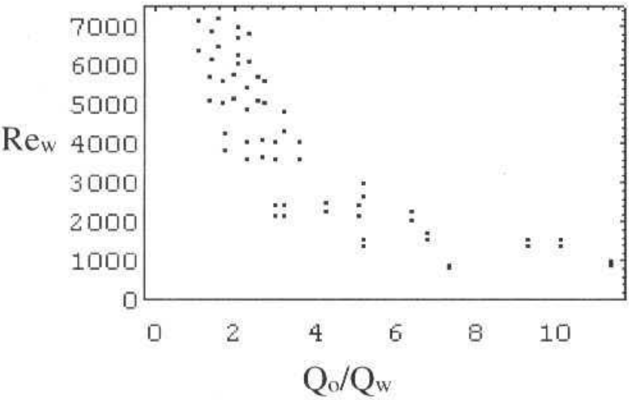

Fig. 3 Water Reynolds number versus oil-water input ratio

The experimental pressure drop in each tube is plotted in Figs. 4 and 5 using a set of coordinates compatible to those of PCAF model. According to this model the pressure gradient G can be expressed as

$$G = \frac{128\mu_w Q}{\pi D^4 \left[1 - \left(1 - \frac{\mu_w}{\mu_o} \right) \alpha^2 \right]}, \cong \frac{128\mu_w Q}{\pi D^4 \left(1 - \alpha^2 \right)} \tag{2}$$

where Q is the mixture flow rate

$$Q = Q_o + Q_w \tag{3}$$

and α is the volumetric fraction of the oil in the tube given by

$$\alpha = \frac{1}{1 + (Q_w/Q_o)[1 + \sqrt{1 + (\mu_w/\mu_o)(Q_o/Q_w)}]} \cong \frac{1}{1 + 2Q_w/Q_o} \tag{4}$$

The approximations in Eqs. (2) and (4) are valid for $\mu_w/\mu_o \ll Q_w/Q_o < 1$; this condition is true in the present experiments and is also verified in most applications. Equation (2) can be interpreted as the pressure drop of a laminar water flow at an equivalent flow rate Q_{pcaf} defined as

$$\begin{aligned} Q_{pcaf} &= Q/[1-(1-\mu_w/\mu_o)\alpha^2] \\ &\cong Q/(1-\alpha^2) \end{aligned} \tag{5}$$

The scattering of the data in Figs. 4 and 5 indicates that the PCAF approach is not effective to describe the experiments reported here. This fact can be attributed to two basic reasons: a) as observed in the experiments the interface is wavy and asymmetric; b) for most runs the water flow is turbulent (Fig. 3). Both facts contradict essential assumptions of PCAF theory.

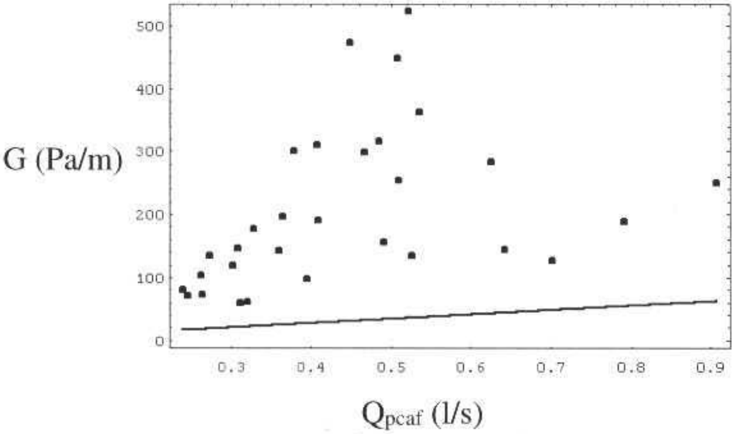

Fig. 4 **Experimental pressure drop G versus flow rate Q_{pcaf} defined by Eq. (5) – steel tube. The straight line stands for Eq. (2)**

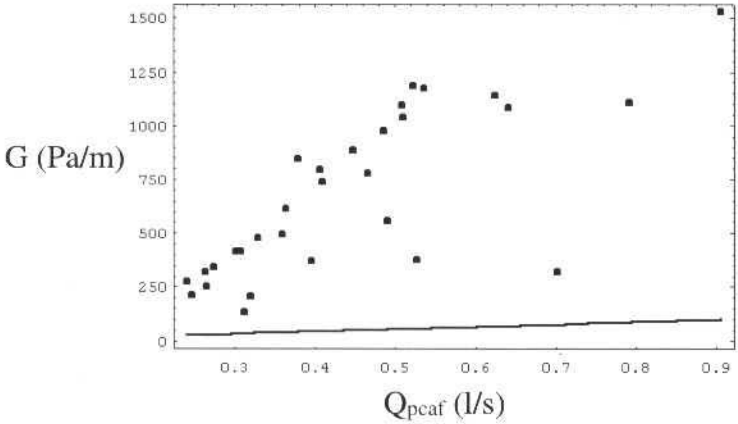

Fig. 5 **Experimental pressure drop G versus flow rate Q_{pcaf} defined by Eq. (5) – cemented tube. The straight line stands for Eq. (2)**

In order to incorporate these effects in the pressure drop model, Eq. (2) is re-written in a generalized form

$$G(Q,\alpha)=G_w(Q)f(\alpha), \tag{6}$$

where $f(\alpha)$ is an increasing function of α satisfying $f(0) = 1$ and $f(1) \to \infty$, and

$$G_w(Q)=\lim_{\alpha\to 0} G(Q,\alpha). \tag{7}$$

The pressure gradient $G_w(Q)$ can be interpreted as the pressure gradient for single-phase water flow in the same tube at the flow rate of the mixture (Q). Assuming that this flow is fully turbulent then

$$G_w(Q)=kQ^2 \tag{8}$$

where k depends on the water properties and tube size and roughness. The function $f(\alpha)$ depends on the interface shape and water flow regime. For a smooth circular concentric interface and laminar water flow $f(\alpha) = 1/(1-\alpha^2)$ in view of Eq.(2). For the wavy interfaces and turbulent annulus flow observed in the experiments it is suggested here the function

$$f(\alpha)=1/(1-\alpha)^{2n} \tag{9}$$

where n is a constant to be determined. Justification for this function will be provided in a later section. To complete the model an expression is needed for the core fraction α instead of Eq. (4). This quantity also depends on the interface shape and flow regime. However, it is not necessary to describe them in detail. In fact, measurements of interfacial wavespeed made by the author at the visualization section (see Fig. 1) for the same runs (Bannwart, 1998) indicated that a kinematic disturbance travels at the mixture superficial velocity, J $(=Q/A)$, as shown in Fig. 6.

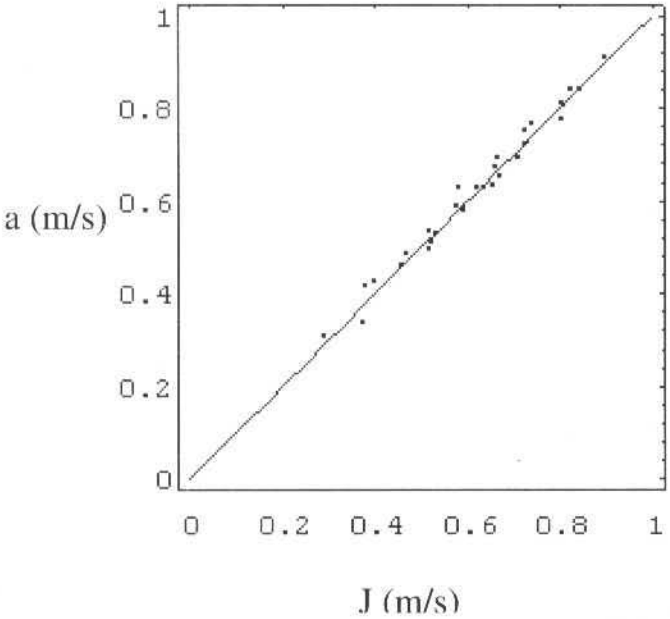

Fig. 6 Interfacial wavespeed a versus mixture superficial velocity J for a horizontal oil-water core-annular flow. The straight line represents a = J

This result can be understood as a homogenizing effect of the interfacial waves and film turbulence on the velocity field. In fact, a significant amount of water flows in the spot between two wave crests at essentially the same velocity of the wave; the turbulence in the water flow causes a flat velocity profile. Since there is no body force in the direction of the flow and the oil is very viscous, the average velocity of the core V_o also equals J. Letting J_o be the oil superficial velocity then

$$V_o = J_o / \alpha \tag{10}$$

and one concludes

$$\alpha = Q_o / Q = 1 - C_w \tag{11}$$

where C_w is the input water fraction

$$C_w = Q_w / Q \, . \tag{12}$$

The final form of the proposed pressure drop model is obtained by combining Eqs. (6) through (12):

$$G = k \left(Q^* \right)^2 \tag{13}$$

where

$$Q^* = Q / \left(1 - \alpha \right)^n = Q \, C_w^{-n} \tag{14}$$

and the exponent n is determined to fit the data. This was accomplished by minimization of the total relative variance

$$S(n,k) = \sum_{runs} \left(\frac{G - G_{exp}}{G_{exp}} \right)^2 . \tag{15}$$

The best values of n for steel and cemented tubes were obtained by simultaneously minimizing S with respect to n and k. The minimization procedure was performed using the software *Mathematica®*. The results for n can be expressed as

$$\begin{aligned} n &= 0.050 \qquad \textit{for steel-walled pipe,} \\ n &= 0.143 \qquad \textit{for cement-walled pipe.} \end{aligned} \tag{16}$$

The k values were respectively 2358 x 10^6 kg/m^8 for the steel tube (26.7 mm ID) and 5780 x 10^6 kg/m^8 for the cemented tube (23.9 mm ID); these values obviously cannot be extended to other pipe sizes and materials. The standard deviation $\sqrt{S/(r-1)}$, where r is number of runs, was less than 20% for both correlations. Note that the cemented wall is rough, thus k is much higher for a cement-lined pipe than in a steel tube of same diameter. However, the higher pressure drop of the cemented pipe may be compensated by its better anti-fouling behavior. Figures 7 and 8 show the data points in the new coordinates, as well as the adjusted correlations. A much better representation of the data is observed in comparison with Figs. 4 and 5.

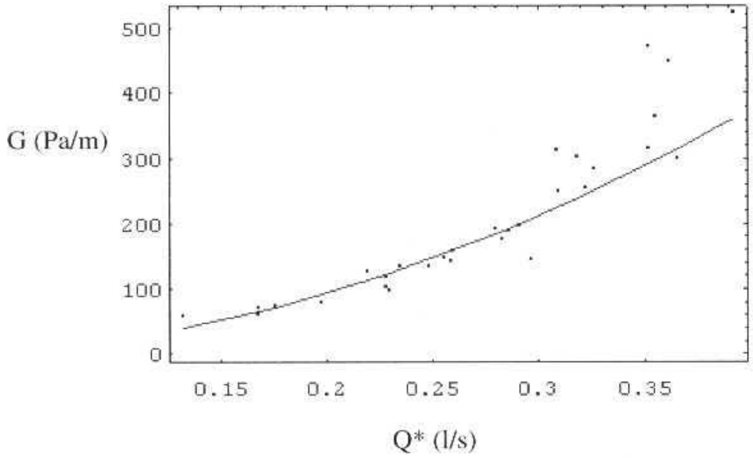

Fig. 7 **Experimental pressure drop G versus flow rate Q* defined by Eq. (14) – steel tube. The continuous line represents Eq. (13)**

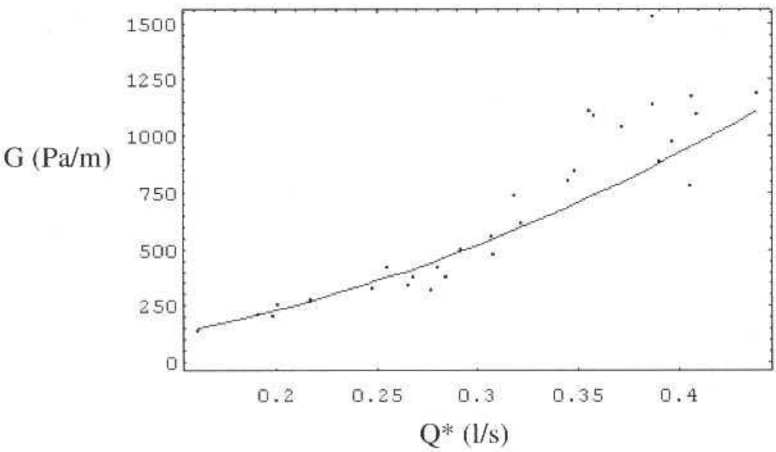

Fig. 8 **Experimental pressure drop G versus flow rate Q* defined by Eq. (14) – cemented tube. The continuous line represents Eq. (13)**

Proposed Correlations

The results obtained in the previous section can be extended to other pipes sizes and materials than used in the present experiments. From Eqs.(13), (14) and (16) the following correlations for pressure drop in horizontal oil-water core-annular flow are suggested:

$$G = G_w(Q)C_w^{-0.1} \quad \text{for oleophilic pipe walls ,} \tag{17}$$

$$G = G_w(Q)C_w^{-0.286} \quad \text{for oleophobic pipe walls} \tag{18}$$

where $G_w(Q)$ is the frictional pressure gradient for single-phase water flow in the same pipe at the flow rate of the mixture, and can be easily evaluated from traditional friction formulae. These equations are very easy to use because they involve no other information than flow rates, fluid properties, tube size and wall characteristics. The weak dependence on the water fraction C_w confirms the experimental findings of other authors, as for example Oliemans *et al.* (1987).

As an illustration of the use of the above correlations consider a horizontal core-annular flow of oil (μ_o = 3 Pa.s, ρ_o = 975 kg/m^3) and water inside a 5 cm ID smooth tube. This system was studied by Oliemans (1986). He used a transparent pipe and additivated water to get an oleophobic pipe wall behavior. This suggests using Eq. (18) with Blasius friction factor to determine G_w. The comparison with pressure drop data given in Table 1 (p. 64) of his work is shown in Fig. 9. The standard deviation between calculated and measured values is only 16 %, which is a very encouraging result since Eq. (18) was developed for a different oil and pipe size.

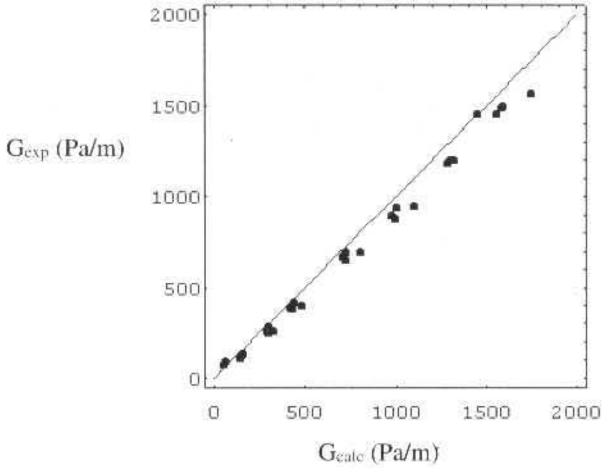

Fig. 9 Comparison between experimental pressure drop data (Oliemans, 1986) and calculated using Eq. (18). $G_{calc} = G_{exp}$ on the straight line

Optimal Input Ratio

The existence of an optimal water flow rate for a fixed oil flow rate, i.e. a water-oil input ratio for which the pressure gradient or pumping power is a minimum, has been reported by many authors, e.g. Russel and Charles (1959) and more recently by Arney *et al.* (1993). This happens because the addition of water helps the oil flow but at the same time increases the total flow rate. The proposed correlations also display this feature, as seen in Figs. 10 and 11.

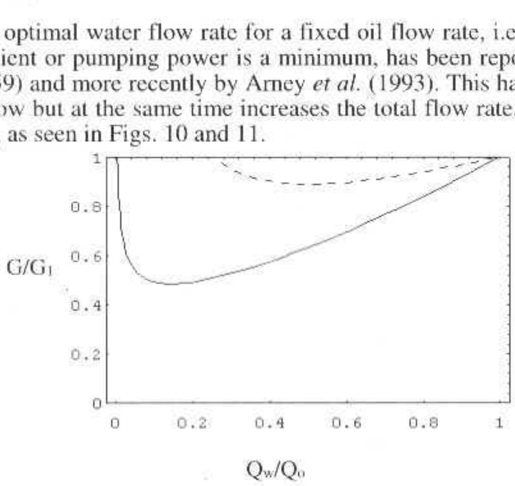

Fig. 10 Water-oil input ratio for minimum pressure drop using Eqs. (13-14) with n = 0.143 (continuous line). The dotted line represents predictions by PCAF model. G_1 is the pressure gradient for unity input ratio

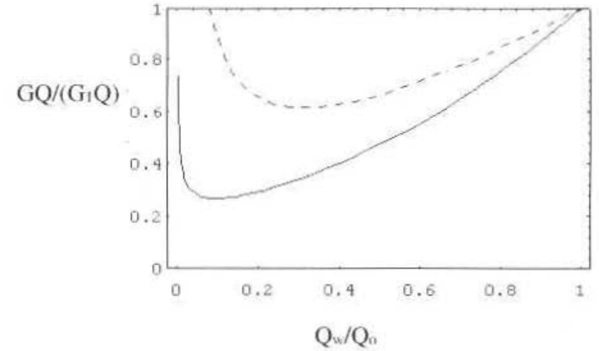

Fig. 11 **Water-oil input ratio for minimum power using Eqs. (13-14) with n = 0.143 (continuous line). The dotted line represents predictions by PCAF model. G_1Q is the power for unity input ratio**

It can be observed that the model proposed here predicts much lower optimal input ratios than PCAF theory. This is reasonable since the present model applies to wavy core and turbulent annulus flow ($Re_w > 2000$). From Eqs.(13) and (14), the water-oil input ratios for minimum pressure drop and minimum pumping power equals n and 2n/3 respectively. Using n = 0.143 for the optimal input ratio seems to be in good agreement with pressure drop plots shown in Figs. 5 through 7 in Arney *et al.* (1993).

Generalization of the Model

It is possible to generalize Eqs.(17) and (18) to other fluids not satisfying the present conditions $\rho_o \cong \rho_w$ and $\mu_w << \mu_o$. This can be done through the introduction of a two-phase multiplier, ϕ^2, defined as

$$\phi^2 = \frac{G}{G_w(Q)} . \tag{19}$$

Assuming power-law type friction factors to express both G_w and G, i.e.

$$G = b\left(\frac{\rho_m j D}{\mu_m}\right)^{-q} \frac{\rho_m j^2}{2D},$$
$$G_w = b\left(\frac{\rho_w j D}{\mu_w}\right)^{-q} \frac{\rho_w j^2}{2D}, \tag{20}$$

one obtains

$$\phi^2 = \left(\frac{\rho_m}{\rho_w}\right)^{1-q} \left(\frac{\mu_w}{\mu_m}\right)^{-q} \tag{21}$$

where ρ_m and μ_m are the mixture density and viscosity, respectively. From Eq. (2) it can be concluded that for the PCAF model

$$\left.\begin{array}{l} q = 1 \\ \dfrac{1}{\mu_m} = \dfrac{\alpha^2}{\mu_o} + \dfrac{1-\alpha^2}{\mu_w} \end{array}\right\} \text{ Perfect Core Annular Flow .} \tag{22}$$

The dependence of μ_m on α seems to be too strong for turbulent flow in the annulus, where the shear stress is essentially constant. This suggests that

$$\frac{1}{\mu_m}=\frac{\alpha}{\mu_o}+\frac{1-\alpha}{\mu_w}. \tag{23}$$

It must be noted that the mixture viscosity calculated using Eq. (23) can be much higher than using Eq. (22). Finally, expressing the mixture density as

$$\rho_m=\alpha\rho_o+(1-\alpha)\rho_w, \tag{24}$$

and using Eq. (11) to eliminate α, Eq. (21) becomes

$$\phi^2=\left[1-\left(1-\frac{\rho_o}{\rho_w}\right)(1-C_w)\right]^{1-q}\left[1-\left(1-\frac{\mu_w}{\mu_o}\right)(1-C_w)\right]^{-q}. \tag{25}$$

This result holds for turbulent annulus flow and recovers Eqs. (17) and (18) when $\rho_o \cong \rho_w$, $\mu_w << \mu_o$ and $q = 0.1$, 0.286 respectively. Note that this later q value, corresponding to the oleophobic pipe wall behavior, is very close to the Blasius law ($q = 0.25$). For laminar flow, however, Eq. (22) is required.

Concluding Remarks

Because oil-water core-annular flows are often wavy with a turbulent water flow in the annulus the perfect core-annular flow theory (PCAF) is inappropriate. In this case, the analysis of our laboratory data revealed a simple model that accurately describes the frictional pressure drop in a horizontal pipe. Two correlations are proposed, namely Eqs. (17) and (18), according to the oleophobicity of the pipe walls, i.e. the tendency for the wall to repel the oil. The correlations are very easy to use since they are expressed in terms of the water fraction and the pressure drop for single-phase water flow in the same pipe at the flow rate of the mixture. Comparisons using the correlation obtained for oleophobic pipe wall, namely Eq. (18), with data by Oliemans (1986) showed very good agreement (within 16 %) in spite of the difference in pipe size and oil he used. A generalization of the model to other fluids in terms of a two-phase multiplier is proposed.

Acknowledgments

This study was supported by the Department of Energy of the University of Campinas (UNICAMP) and by FAPESP, Brazil. My gratitude is also directed to Prof. Daniel D. Joseph for the support he provided during my visit to the Department of Aerospace Engineering and Mechanics of the University of Minnesota. I am also grateful to Dr. Oliemans for kindly sending me his thesis. Taehwan Ko collaborated during the experiments reported in the paper.

References

Arney, M. S., Bai, R., Guevara, E., Joseph, D. D. and Liu, K., 1993, "Friction Factor and Holdup Studies for Lubricated Pipelining-I: Experiments and Correlations", *Int. J. Multiphase Flow*, Vol. 19, pp. 1061-1076.

Arney, M. S., Ribeiro, G. S., Guevara, E., Bai, R. and Joseph, D.D., 1996, "Cement-Lined Pipes for Water Lubricated Transport of Heavy Oil", *Int. J. Multiphase Flow*, Vol. 22, pp. 207-221.

Bannwart, A.C., 1998, "Wavespeed and Volumetric Fraction in Core Annular Flow", *Int. J. Multiphase Flow*, Vol. 24, pp. 961-974.

Bobok, E., Magyari, D. and Udvardi, G., 1996, "Heavy Oil Transport Through Lubricated Pipeline", Proceedings of the 1996 SPE European Petroleum Conference, Milan, Italy, Vol. 1, paper SPE 36841, pp. 239-244.

Charles, M. E., Govier, G. W. and Hodgson, G. W., 1961, "The Horizontal Pipeline Flow of Equal Density Oil-Water Mixtures", *Can. J. Chem. Eng.*, Vol. 39, pp. 27-36.

Oliemans, R.V.A., 1986, "The Lubricating-Film Model for Core-Annular Flow", Ph.D. Thesis, Delft University, The Netherlands.

Oliemans, R. V. A., Ooms, G., Wu, H. L. and Duijvestijn, A., 1987, "Core-Annular Oil/Water Flow: The Turbulent-Lubricating-Film Model and Measurements in a 5 cm Pipe Loop", *Int.J.Multiphase Flow*, Vol. 13, pp. 23-31.

Ooms, G., Segal, A., van der Wees, A. J., Meerhoff, R. and Oliemans, R.V.A., 1984, "A Theoretical Model for Core-Annular Flow of a Very Viscous Oil Core and a Water Annulus Through a Horizontal Pipe", *Int. J. Multiphase Flow*, Vol. 10, pp. 41-60.

Ribeiro, G. S., 1994, "Topics in the Transport and Rheology of Heavy Crude Oils", Ph.D. Dissertation, University of Minnesota, Minneapolis.

Russel, T.W.F. and Charles, M.E., 1959, "The Effect of the Less Viscous Liquid in the Laminar Flow of Two Immiscible Liquids", *Can. J. Chem. Eng.*, Vol. 37, pp. 18-24.

RBCM - J. of the Braz. Soc. Mechanical Sciences
Vol. XXI - No.2 - 1999 - pp. 245-258

ISSN 0100-7386
Printed in Brazil

New Correlation for Convective Boiling of Pure Halocarbon Refrigerants Flowing in Horizontal Tubes

José M. Saiz Jabardo
Enio Pedone Bandarra Filho
Carlos Umberto da Silva Lima
Departamento de Engenharia Mecânica
Escola de Engenharia de São Carlos
Universidade de São Paulo
13560-970 São Carlos, SP Brazil
mjabardo@sc.usp.br

Abstract

An extensive literature survey of convective boiling has been performed in this study. Published correlations have been divided into three main groups: strictly convective, those based on the superposition rule, and strictly empirical. An empirical correlation has been developed from an experimental data bank obtained elsewhere through an optimized curve fitting procedure. Average deviations of results from the proposed correlation with respect to experimental data are significantly low compared to deviations from other correlations. Comparisons between local heat transfer coefficients from correlations and those obtained experimentally, though qualitatively sound, have shown distinct deviations. Improved physical models are needed to adequately correlate local heat transfer coefficients.

***Keywords**: Convective Boiling, Refrigerants, Horizontal Flow.*

Introduction

Convective boiling of refrigerants has been under intensive research during the last 40 years. Early studies sought the development of correlations for heat transfer and pressure drop based on empirical data. Some progress was made in correlating the limited amount of available data at that time. During the 60's a significant effort was put forward by the refrigeration community to better understand the physical mechanism. The significant increase in publications in the field at that time is an evidence of that effort. During the 70's and part of the 80's there was a lack of major achievements in convective boiling research. A surge of research started in the mid 80's, mostly related to the mandatory phase out of CFCs imposed to the industrialized nations by the Montreal Protocol for controlling Ozone Depleting Substances (ODS). Thus during the last decade the refrigeration industry has been faced with a scenario of phasing out CFCs, which has been composed with energy consumption regulations all over the world. These constrains have confronted industry with new challenges on the design of components, especially heat exchangers. The introduction into the market of a new generation of chlorine free refrigerants has triggered a renewed trend of research in convective boiling, in part due to the lack of generalization of previous results. Despite progress attained in the past, currently available correlations for the convective boiling heat transfer coefficient are still dependent, to a certain degree, upon the range of the operating conditions and the fluid (refrigerant).

Purposes of this paper are twofold. Initially, a summary of an extensive literature survey will be presented regarding heat transfer coefficient correlations for convective boiling. Correlations have been classified into three main categories: strictly convective, those based on a superposition rule, and strictly empirical. A second outcome of present study has been the development of a non-dimensional correlation for the heat transfer coefficient based on standard non-dimensional groups. The correlation has been developed through an optimized curve fitting procedure of experimental results covering some halocarbon refrigerants and a limited range of operating conditions.

Literature Survey

In a broad sense, convective boiling designates the liquid to vapor change of phase that takes place under forced flow of the fluid. In this study major attention has been focused on conditions prevailing in direct expansion evaporators, especially covering a region from the evaporator inlet to the section where dry out occurs. This is by large the most important region in the evaporator. Vapor qualities at the entrance of the evaporator are in general larger than 10%, varying from case to case. On the other

Manuscript received: October 1998; revision received: February 1999. Technical Editor: Angela Ourivio Nieckele.

hand, post dry out conditions encompass the misty two-phase flow and the superheated vapor regions. Misty flow heat transfer has not been adequately addressed in the literature. Regarding heat transfer, this has been generally considered as a single phase saturated vapor region. This study covers a region where the following two-phase flow regimes for horizontal tubes might occur: bubbly, stratified (mostly wavy), and annular. Heat transfer mechanisms in this region are associated to either nucleate boiling or evaporation at the liquid-vapor interface. The latter is referred by some authors as convective boiling, a designation more restrictive than the one used in this study. It must be noted that both mechanisms might occur simultaneously, as some of current models actually assume.

he literature survey reported in this paper is limited to those publications involving some sort of correlation for the heat transfer coefficient under convective boiling conditions for the range of vapor qualities varying from 10% to 100%. Publications listed here in were considered the most significant. Correlations were divided into three main categories:

(1) Strictly convective;
(2) Based on a superposition rule;
(3) Strictly empirical

The first group of correlations for heat transfer was based on the assumption of the only occurrence of saturated evaporation at the liquid/vapor interface. McAdams (1954), who proposed a simplified model based on an annular flow regime topology of the interface, adequately addressed this mechanism of heat transfer. The two-phase flow heat transfer coefficient, h_{tp}, is frequently presented in a non-dimensional form by referring it to the single-phase coefficient for the liquid phase of the mixture flowing in the same tube, h_f. Some authors have referred h_{tp} to the single-phase heat transfer coefficient for the mixture flowing totally as liquid in the tube, h_{fo}. It is rather simple to prove that this dimensionless heat transfer coefficient is a function of the Martinelli parameter, Saiz Jabardo (1988). This is in essence the main conclusion of the McAdams model, and the basic assumption of the strictly convective correlations. It must be noted that the version generally adopted for the Martinelli parameter is the one associated to the turbulent/turbulent regimes of the phases flowing separately in the tube, i. e. X_{tt}. Some of the first group correlations are listed in Table 1, along with the associated experimental conditions. In fact these correlations are empirical, since the numerical coefficients were obtained by curve fitting experimental results. As it should be expected, the excellent correlation reported by some of the authors could be explained by the fact that experiments were performed under the annular flow regime, typical for most of the physical conditions listed in Table 1.

Nomenclature

Bo = Boiling number (dimensionless); $Bo = \frac{\phi}{G\,D}$
Co = Convective number as defined by Shah (dimensionless); $Co = \left(\frac{1-x}{x}\right)^{0.8}\left(\frac{\rho_g}{\rho_f}\right)^{0.5}$
c_p = Specific heat (J/kg.°C)
D = Diameter (m)
D_b = Bubble departure diameter (m)
F = Two-phase multiplier for strictly convective heat transfer (dimensionless)
F_{fl} = Fluid parameter defined by Kandlikar (dimensionless)
Fr = Froude number (dimensionless)
G = Mass flux (kg/m^2.s)
g = Gravitacional acceleration (m/s^2)
h = Local heat transfer coefficient (W/m^2.°C)
i = Specific enthalpy (J/kg)
k = Thermal conductivity (W/m.°C)
L = Length in the correlation of Pierre (m)
M = Molecular weight (kg/kmol)
N = Dimensionless parameter as defined by Shah
p = Pressure (Pa)
Pr = Prandtl number (dimensionless); $Pr = \frac{\mu\, c_p}{k}$
R = Dimensionless factor as defined by Wattelet
Re = Reynolds number (dimensionless); $Re = \frac{GD}{\mu}$
S = Supression factor (dimensionless)
T = Temperature (°C)
x = Vapor quality (dimensionless)
X_{tt} = Martinelli parameter (dimensionless); $X_{tt} = \left(\frac{1-x}{x}\right)^{0.9}\left(\frac{\rho_g}{\rho_f}\right)^{0.5}\left(\frac{\mu_f}{\mu_g}\right)^{0.1}$

Greek symbols:

β = Contact angle
δ_c = Characteristic dimension (m)
φ = Heat flux (W/m^2)
μ = Viscosity (Pa.s)
ρ = Density (kg/m^3)
σ = Surface tension (N/m)

Subscripts:

BS = Bubble supression
C = Convective
CB = Convective boiling
cr = Relative to critical the state
exp = Experimental
f = Referring either to the liquid phase or to the liquid of the mixture flowing in the tube
fo = Mixture flowing like a liquid
fg = Relative to the difference between the values of the properties of the vapor and liquid
g = Gas phase
NB = Nucleate boiling
r = Reduced pressure
sat = Saturated conditions
tp = Two-phase flow

Table 1 A summary of strictly convective correlations

Author	Correlation	Fluids	Physical Conditions
Dengler &Addoms (1956)	$\frac{h_{tp}}{h_{fo}} = 3.5\,(X_{tt})^{-0.5}$	Water	Vertical D: 25.4mm G: 55 a 1100 kg/m^2.s x: 0 a 70%
Guerrieri & Talty (1956)	$\frac{h_{tp}}{h_f} = 3.4\,(X_{tt})^{-0.45}$	Hydrocarbons	Vertical D: 19 e 25.4mm p_{sat} = 100 kPa x: 1 to 12%
Chaddock & Noerager (1966)	$\frac{h_{tp}}{h_{fo}} = 3.0\,(X_{tt})^{-(2/3)}$ $\frac{h_{tp}}{h_f} = 3.0\,(X_{tt})^{-1}$	CFC-12	D: 12.7mm G: 100 to 433 kg/m^2.s ϕ: 2.2 to 11 kW/m^2 x: 0 to 70%
ACRC-1 [Wattelet] (1991)	$\frac{h_{tp}}{h_f} = 2.30\,(X_{tt})^{-(0.666)}$	CFC-12 HFC-134a	D: 12.7mm x: 20% T_{sat} = 4.4 °C
ACRC-2 [Panek] (1992)	$\frac{h_{tp}}{h_f} = 3.686\,(X_{tt})^{-(0.563)}$	CFC-12 HFC-134a	D: 10.2 and 12.7 mm G: 100 to 500 kg/m^2.s ϕ: 5 to 30 kW/m^2 x: 20% to 60%
Chaddock & Buzzard (1986)	$\frac{h_{tp}}{h_f} = (\frac{0.785}{X_{tt}})\,(1 + 3.83\,X_{tt}^{0.81})$	CFC/HCFC-502	D: 12.7 mm G: 45 to 500 kg/m^2.s ϕ: 1.9 to 23.6 kW/m^2 x: 1 to 23%

The second group corresponds to those correlations based on the superposition of heat transfer mechanisms, namely those due to nucleate boiling and evaporation at the liquid/vapor interface (strictly convective boiling). Some of the published correlations of this group are listed in Table 2. Similarly to the ones of the first group, correlations based on the superposition rule are mostly empirical, but applicable to a wider range of operating conditions. However, it must be recognized that the extent of applicability of these correlations is limited since the superposition rule is a rather simple model of the heat transfer mechanism under convective boiling conditions. Kutateladze (1961), who proposed a non-linear superposition of effects, was probably the first researcher to introduce the idea. Later on, Chen (1966) successfully proposed a linear superposition. His model assumes that the two-phase flow heat transfer coefficient results from the sum of strictly convective and nucleate boiling effects. In other words,

$$h_{tp} = (F)\,h_l + (S)\,h_{NB} \tag{1}$$

The first term of the right hand side can simply be evaluated by a strictly convective correlation, whereas the latter, h_{NB}, is associated to a typical nucleate boiling correlation. Chen (1966) suggested the Foster and Zuber (1955) model for h_{NB}. This coefficient must be corrected by the so-called suppression factor, S, which was introduced to allow for convective effects on bubble nucleation. In that respect it must be noted that higher Reynolds number flows tend to promote thinner boundary layers and higher temperature gradients at the wall. As a result, the effective temperature of the liquid around the bubble is diminished, reducing the chances for bubble nucleation. Thus, according to Chen's model, *S* must vary inversely with the two-phase flow Reynolds number. Other authors have used similar arguments as Chen. However, to account for surface and nucleate boiling effects, some have gone further by making *F* and *S* dependent on other dimensionless groups, such as the Froude and the Boiling numbers (see nomenclature for definition). Finally it must be noted at this point that, for higher vapor qualities, strictly convective boiling effects are dominant due to impaired conditions for bubble nucleation, as one can easily conclude from the physical behavior of annular flow. In other words, S must decrease with vapor quality. To a certain extent most of the correlations based on the superposition rule include this vapor quality effect. On the other hand, some tend to overweight nucleate boiling effects to adequately correlate experimental results.

Table 2 A summary of correlations based on the superposition rule

Author	Correlation	Fluids	Physical Conditions
Chen (1966)	$h_{tp} = h_f \; F_{CH} + h_{NBF} \; S_{CH}$ $h_f = \frac{kf}{D} \; 0.023 \, Re_f^{0.8} \, Pr_f^{0.4}$ $F_{CH} = 1$ for $\frac{1}{X_{tt}} \leq 0.1$ $F_{CH} = 2.35 \left(\frac{1}{Xtt} + 0.213 \right)^{0.736}$ for $\frac{1}{Xtt} > 0.1$ $h_{NBF} = 0.00122 \left[\frac{kf^{0.79} cPf^{0.45} r\phi^{0.49}}{s^{0.5} m\phi^{0.29} i\phi\gamma^{0.24} \; r\gamma^{0.24}} \right] \Delta T_{sat}^{0.24}$ $\Delta P_{sat}^{0.75}$ $S_{CH} = \frac{1}{(1 + 2.53 X 10^{-6} Re_f^{1.17})}$	Water Methanol Benzene Pentane Hexane Heptane	Vertical p_{sat}: 55 to 3500 kPa G: 500 to 3600 kg/m^2.s x:1 to 71%
Gungor & Winterton (1986)	$h_{tp} = h_f \; F_{GW} + h_{NBC} \; S_{GW}$ $F_{GW} = 1 + 24000 \, Bo^{1.16} + 1.37 \left(\frac{1}{X_{tt}} \right)^{0.86}$ $h_{NBC} = 55 \, p_r^{0.12} \, (-\log_{10} p_r)^{0.55} \, M^{-0.5} \, \phi^{0.67}$ $S_{GW} = \frac{1}{(1 + 1.15 X 10^{-6} F_{GW}^2 Re_f^{1.17})}$ For $Fr < 0.05$, multiply F_{GW} and S_{GW} by F_1 e S_1: $F_1 = Fr^{(0.1 - 2 Fr)}$ $\quad S_1 = \sqrt{Fr}$	Water CFC-11 CFC-12 CFC-113 CFC-114 HCFC-22 Ethylene-glycol	G: 60 to 8180 kg/m^2.s ϕ: 1 to 2600 kW/m^2 x: 0 to 99% D: 3 to 32mm
Liu & Winterton (1991)	$h_{tp}^2 = (F_{LW} \; h_{fo})^2 + (S_{LW} \; h_{NBC})^2$ $h_{fo} = \frac{k_f}{D} \; 0.023 \, Re_{fo}^{0.8} \, Pr_f^{0.4}$ $F_{LW} = \left[1 + x \; Pr_f \left(\frac{\rho_f}{\rho_g} - 1 \right) \right]^{0.35}$ $S_{LW} = \frac{1}{(1 + 0.055 FLW^{0.1} \; Re \, fo^{0.16})}$ For $Fr < 0.05$, multiply F_{LW} and S_{LW} by F_1 e S_1 from Gungor-Winterton.	Water CFC-11 CFC-12 CFC-113 CFC-114 HCFC-22 Ethylene-glycol	G: 12.4 to 8180 kg/m^2.s ϕ: 0.4 to 2600 kW/m^2 x: 0 to 94.8% D: 3 to 32mm
Jung & Radermacher (1991)	$h_{tp} = h_f \, F_{JR} + S_{JR} \, h_{NBS}$ $F_{JR} = 2.37 \left(0.29 + \frac{1}{X_{tt}} \right)^{0.85}$ $h_{NBS} = 207 \frac{k_f}{D_b} \left(\frac{\phi \, D_b}{k_f \, T_{sat}} \right)^{0.745} \left(\frac{\rho_g}{\rho_f} \right)^{0.581} (Pr_f)^{0.533}$ $D_b = 0.0146 \, \beta \left[\frac{2\sigma}{g \, (\rho_f - \rho_g)} \right]^{0.5}$ For $X_{tt} \leq 1 \Rightarrow S_{JR} = 4048 X_{tt}^{1.22} \, Bo^{1.13}$ For $1 < X_{tt} \leq 5 \Rightarrow S_{JR} = 2.0 - 0.1 X_{tt}^{-0.28} \, Bo^{-0.33}$	CFC-11 CFC-12 CFC-13 HCFC-22 HFC-32 CFC-114 HCFC-123 HCFC-124 HFC-134a HCFC-141b HCFC-142b HFC-143a HFC-152a	T_{sat}: -10 to 10°C G: 100 to 700 kg/m2.s ϕ: 5 to 40 kW/m^2 x: 10 to 90% D = 8mm
Wattelet (1994)	$(h_{tp})^{2.5} = (h_f \, F_W \, R)^{2.5} + (h_{NBC})^{2.5}$ $F_W = 1 + 1.925 \, X_{tt}^{-0.83}$ $R = 1.32 \, Fr^{0.2}$ for $Fr < 0.25$ $R = 1$ for $Fr \geq 0.25$	CFC-12 HFC-134a	G: 25 to 500 kg/m^2.s ϕ: 2 to 30 kW/m^2 x: 10 to 90% T_{sat}: -15 to 5°C D = 12.7 and 15.87mm

(Table 2 cont.)

Author	Correlation	Fluids	Physical Conditions
Murata & Hashizume (1993)	$h_{tp} = h_l F_{MH} + h_{NBN} S_{MH}$ $F_{MH} = 2.44 X_{tt}^{-0.863}$ $h_{NBN} = 31.4 [\frac{Pcr^{0.2} Fp}{M^{0.1} Tcr^{0.9}}] \phi^{0.8}$ $S_{MH} = \frac{[1 - exp(\frac{(-hfFMH)dX}{\kappa\phi})]}{[\frac{(\eta\phi\Phi MH)dX}{\kappa\phi}]}$ $F_P = \frac{pr^{0.23}}{[1 - 0.99 pr]^{0.9}}$ $\delta_C = 0.08 [\frac{s}{\gamma(r\phi - r\gamma)}]^{0.5}$	HCFC-123	G: 100 to 300 kg/m^2.s ϕ: 0 to 30 kW/m^2 x: 1 to 100% D = 12.7mm p_{sat}: 200kPa

Probably Pierre (1956) was the first researcher to empirically correlate experimental results obtained from an evaporator operating with refrigerants CFC-12 and HCFC-22, both for pure refrigerants and their mixtures with low oil content. Pierre approached the problem from a pragmatic point of view by introducing two dimensionless groups to correlate the Nusselt number. One was a two-phase flow Reynolds number, based on the mixture flowing as saturated liquid in the tube, whereas the other, designated as K, corresponds to a modified version of the Boiling number. The latter includes the length of the evaporator tube, which is a major nuisance in applications. Pierre's results were written in terms of average heat transfer coefficients, applicable to evaporator exit conditions corresponding to either vapor qualities up to 90% or 6°C superheated vapor. The correlations proposed by Pierre are listed in Table 3 along with the other two corresponding to the third group of correlations, the so-called strictly empirical.

Shah (1982) proposed a correlation developed from an extensive data bank of experimental results. The basic approach taken by Shah (1982) was to start with the introduction of non-dimensional groups, based on previous experience instead of a dimensional analysis, which would be rather complex for this problem. Shah (1982) introduced the following dimensionless groups in his correlation: the Boiling, the Froude, and the Convective numbers. The latter corresponds to a modified Martinelli parameter, without the viscosity ratio. Initially Shah introduced a chart for the dimensionless heat transfer coefficient, defined with reference to the coefficient corresponding to the liquid of the mixture flowing in the same tube, h_l. Later on he proposed the correlation listed in Table 3.

Table 3 A summary of strictly empirical correlations

Author	Correlation	Fluids	Physical Conditions
Pierre (1956)	Complete evaporation: • 6°C of superheat at exit and $10^8 < Re_{lo}^2 K < 0.7 \times 10^{12}$ $h_{tp} = \frac{k_l}{D} 0.0082 [Re_{lo}^2 K]^{0.4}$ Incomplete evaporation: • $x_{exit} < 0.9$ and $10^9 < Re_{lo}^2 K < 0.7 \times 10^{12}$ $h_{tp} = \frac{k_l}{D} 0.0009 [Re_{lo}^2 K]^{0.5}$ $K = (\frac{i_{lg} \Delta x}{L g})$	CFC-12 HCFC-22	D = 12 to18mm x: 15% in 6°C of superheating

(Table 3 cont.)

Author	Correlation		Fluids	Physical Conditions
Shah (1982)	$\Psi = \frac{h_{tp}}{h_l}$ $N = Co$ vertical and horizontal flows for $Fr > 0.04$ $N = 0.38\, Fr^{-0.3}\, Co$, horizontal flow for $Fr < 0.04$ • For $N > 1$: $\Psi_{NB} = 230\, Bo^{0.5}$ for $Bo > 0.3 \times 10^{-4}$ $\Psi_{NB} = 1 + 46\, Bo^{0.5}$ for $Bo \leq 0.3 \times 10^{-4}$ $\Psi_C = \frac{1.8}{N^{0.8}}$ Ψ higher value between Ψ_{NB} and Ψ_C. • For $0.1 \leq N < 1.0$: $\Psi_{BS} = F\, Bo^{0.5} \exp(2.74\, N^{-0.1})$ • For $N \leq 0.1$: $\Psi_{BS} = F\, Bo^{0.5} \exp(2.47\, N^{-0.15})$ $F = 14.7$ for $Bo \geq 11 \times 10^{-4}$ $F = 15.4$ for $Bo < 11 \times 10^{-4}$ Ψ higher value between Ψ_{BS} and Ψ_C.		Water CFC-11 CFC-12 HCFC-22 CFC-113 Hexane	G: 100 to 2000 kg/m^2.s ϕ: 1.2 to 2000 kW/m^2 x: 0 to 100% T_{sat}: -50 to 190°C
Kandlikar (1990)	$\frac{h_{tp}}{h_l} = [A\, Co^B\, (25\, Fr)^E] + (C\, Bo^D\, F_{fl})$		F_{fl} values Water: 1.0	
	Convective Boiling:	Nucleate Boiling:	CFC-11: 1.30	G: 15 to 8180 kg/m^2.s
	$A = 1.1360$	$A = 0.6683$	CFC-12: 1.50	ϕ: 1.2 to 2000 kW/m^2
	$B = -0.9$	$B = -0.2$	CFC-13B1: 1.31	x: 0.1 to 95%
	$C = 667.2$	$C = 1058.0$	HCFC-22: 2.20	
	$D = 0.7$	$D = 0.7$	CFC-113: 1.30	
	$E = 0.3$	$E = 0.3$	CFC-114: 1.24	
	For $Fr > 0.04 \Rightarrow E = 0$	For $Fr > 0.04 \Rightarrow E = 0$	HFC-152a: 1.10	
			HFC-134a: 1.63	

Kandlikar (1990) followed the same steps as Shah in developing a generalized correlation from a data bank of experimental results. He introduced the same non-dimensional groups as Shah but differently organized. A major set back of Kandlikar's correlation is the Fluid Coefficient, F_{fl} (see Table 3 for reference), dependent upon the particular fluid. Kandlikar (1990) suggested values of F_{fl} for several fluids in his original paper. The original list has been enhanced by several authors along the years. Eckels and Pate (1991), for example, based on their own experimental results, suggested the value of 1.63 for the Fluid Coefficient of refrigerant HFC-134a. Due to its excellent results, Kandlikar's correlation has found a widespread application in the refrigeration field.

Bandarra Filho (1997) has performed an in depth analysis of the correlations listed in Tables 1 to 3. Results can be summarized as follows:

(1) Correlations of the same group present significant discrepancies among each other and with those from the other groups.

(2) Comparison of correlations with experimental results from an available data bank[1] resulted in average deviations as listed in Table 4. The average deviation has been defined as

---

[1] Experimental results have been kindly provided by the Air Conditioning and Refrigeration Center of the University of Illinois at Urbana-Champaign, USA. A summary of experimental conditions and fluids can be found in Table 5.

$$\varepsilon(\%) = \frac{100}{N_{experimental}} \sum \frac{\left[h_{correlation} - h_{experimental}\right]}{h_{experimental}} \qquad (2)$$

(3) A close examination of Table 4 allows for the following conclusions:
   (a) In general, strictly convective correlations present the highest deviations, whereas the strictly empirical ones, the least.
   (b) Deviations diminish for mass fluxes higher than 100 kg/m^2.s, possibly due to the occurrence of annular flow. It must be noted that most of the correlations have been developed for high mass fluxes, which explains the observed trend.
   (c) Kandlikar's correlation along with the one proposed by Wattelet (1994), developed from the same data bank used in the present study, produced the least average deviations.
   (d) It is interesting to note that correlations of the second group, corresponding to those based on the superposition rule, present unexpectedly high average deviations. The only exception is Wattelet's correlation as it should be expected, given the comment on the previous paragraph.

(4) As a general rule, low mass flux data are poorly correlated. Probably this behavior is related to the occurrence of the stratified flow regime (particularly the wavy flow) with its horizontal liquid/vapor interface. Apparently, the introduction of the Froude number in some of the correlations, to take into account horizontal interface effects, have not produced the expected results. Further research is needed to elucidate physical behavior of the heat transfer mechanism under stratified flow.

(5) As a final conclusion, it must be noted that all correlations adopt the traditional approach of referring heat transfer coefficients to their single-phase counter parts.

Table 4 Average deviations of correlations from experimental results

Correlation	Average deviation (Complete set of experimental results)	Average deviation ($G > 100$ kg/m^2.s and $\phi \leq 20$ kW/m^2)
Group 1 (Strictly convective)		
Dengler & Addoms (1956)	54.0%	46.0%
Guerrieri & Talty (1956)	32.0%	24.0%
Chaddock & Noerager (1966)	86.0%	69.0%
ACRC-1 (1991)	36.0%	30.0%
ACRC-2 (1992)	20.0%	14.6%
Chaddock & Buzard (1986)	21.0%	14.9%
Group 2 (Superposition rule)		
Chen (1966)	24.0%	16.0%
Gungor & Winterton (1986)	20.0%	18.3%
Liu & Winterton (1991)	19.0%	13.3%
Jung & Radermacher (1989)	22.0%	16.2%
Wattelet (1994)	12.3%	9.60%
Murata & Hashizume (1993)	28.0%	21.0%
Group 3 (Strictly empirical)		
Shah (1982)	17.7%	13.7%
Kandlikar (1990)	14.2%	10.0%

Heat Transfer Correlation

In the last section the most representative heat transfer correlations for convective boiling were introduced. As noted before, the strictly convective ones, though rather simple, correlate with acceptable precision only the annular flow regime. On the other hand the superposition rule is not completely satisfactory, since it is rather complex to adequately weight the relative importance of convective and nucleate boiling effects for different conditions. Finally, it has been proved that strictly empirical correlations are accurate, but are either fluid dependent, such as the one by Kandlikar (1990), or present a complex form for practical applications. Given the present state of the art, the main objective of this study has been to develop a simple yet accurate correlation that would incorporate all significant effects of convective boiling of halocarbon refrigerants flowing inside horizontal tubes under typical conditions for refrigeration applications. The correlation should include all significant mechanisms affecting heat transfer through pertinent dimensionless groups. As in previous correlations, a certain degree of empiricism will be exercised in the determination of numerical coefficients and the establishment of the range of dimensionless parameters. The experimental data bank used as reference in this study was obtained for experimental conditions summarized in Table 5. It must be noted that data were obtained for only three refrigerants and limited ranges of operating conditions, mostly covering refrigeration applications.

Table 5 A summary of operating conditions for experimental results used in this study

Refrigerant	D [mm]	ϕ [kW/m^2]	G [kg/m^2.s]	x_{in} [%]	Tsat [°C]
CFC-12	7.04	1.9 to 5	25 to 100	20 to 60	-20 to 5
HFC-134a	7.04 and 10.92	1.9 to 40	50 to 500	5 to 95	-15 to 20
HCFC-22	7.75 and 10.92	1.9 to 40	50 to 500	1 to 94	-5 to 15

Three dimensionless parameters, already mentioned in this paper, were introduced "ad hoc" to incorporate the intervening physical mechanisms.

(1) The Martinelli parameter, Xtt, to take into account strictly convective effects due to evaporation at a liquid vapor interface, according to the McAdams (1954) model.

(2) The Boiling number, Bo, intended to take into account nucleate boiling effects, generally associated to the heat transfer coefficient dependence on the heat flux.

(3) The Froude number, Fr, to incorporate horizontal free surface effects, typical of the stratified flow regimes.

In this case, contrary to most of the previous correlations, nucleate and strictly convective effects have not been evaluated separately. Instead, the dimensionless heat transfer coefficient was set equal to a product of the dimensionless parameters, according to the following general form:

$$\frac{h_{tp}}{h_f} = 1 + C\ X_{tt}^{m}\ Bo^{n}\ Fr^{p} \tag{3}$$

It is interesting to note that the first term in the right hand side of Eq. (3) is intended to make the equation compatible with the asymptotic condition corresponding to a single phase flow of liquid. Since the exponent m is always negative, when the vapor quality goes to zero so does the second term ($X_{tt} \rightarrow \infty$), and, as a result, the dimensionless heat transfer coefficient goes to 1. The numerical coefficient and exponents were obtained as follows.

(1) Initially *Fr* was dropped from the general equation, and the following dimensionless parameter was correlated exclusively by the Martinelli parameter for experimental data:

$$\frac{\dfrac{h_{tp}}{h_f} - 1}{Bo^{n}} \tag{4}$$

(2) For each value of n, values of m and C would result from the correlation of experimental data. A trial procedure was set up to determine de value of n that would produce the minimum average deviation. Table 6 displays results from several trials. It can be noted that the optimum value of n is 0.3. The corresponding values of m and C for this value of n are: -0.65 and 40.

Table 6 Average deviation for several values of n

n	Average deviation [%]
0	19.2
0.1	16.0
0.3	13.5
0.5	16.9

(3) Despite the limited range of Froude numbers available from the experimental results, a clear trend has been devised according to which this group would exert no apparent influence over the heat transfer mechanism for $Fr \geq 0.1$. The value of the exponent p in Eq. (3) was set to zero for this range of Froude numbers. On the other hand, for $Fr < 0.1$, the optimum value of p was determined through a trial procedure in such a way to minimize the average deviation. The optimum value of p was found to be equal to 0.5.

(4) The resultant correlations for the two ranges of the Froude number can be summarized as follows:

$Fr < 0.1$

$$\frac{h_{tp}}{h_f} = 1 + 125\, X_{tt}^{-0.65}\, Bo^{0.3}\, Fr^{0.5} \tag{5}$$

$Fr \geq 0.1$

$$\frac{h_{tp}}{h_f} = 1 + 40\, X_{tt}^{-0.65}\, Bo^{0.3} \tag{6}$$

Equations (5) and (6) reflect the physical behavior of convective boiling. In fact, this can be qualitatively demonstrated by considering isolated effects of the intervening parameters as follows.

(1) Given the geometry, saturation temperature, and heat and mass fluxes, one should expect that the two-phase flow heat transfer coefficient would be exclusively dependent upon the vapor quality through X_{tt}. A clear picture of the problem could be drawn by considering the annular flow regime, for which h_{tp} would increase with vapor quality. Equations (5) and (6) are in accordance with this behavior, since, for constant Bo and Fr, the dimensionless heat transfer coefficient diminishes with X_{tt}, as expected. This conclusion is in accordance with that previously drawn for the strictly convective correlations.

(2) The Boiling number is intended to take into account nucleate boiling effects for which the heat transfer coefficient depends upon the heat flux, increasing with it. This dependency is clearly reflected in Eqs. (5) and (6). It is interesting to note that, according to the above equations, the relative importance of the Boiling number increases with X_{tt} or, in other words, for reduced vapor qualities. This is consistent with the physical behavior, since the probability of nucleate boiling occurrence increases for lower vapor qualities. On the other hand, the form of Eqs. (5) and (6) allows for the progressive reduction with vapor quality of the relative influence of the Boiling number.

(3) The Froude number is associated to horizontal liquid/vapor interfaces, as in the stratified two-phase flow regime. The occurrence of this regime is clearly determined by the mass flux. Low values of the mass flux, corresponding to low Froude numbers, are associated to the stratification of the phases. The annular flow regime could be attained by progressively increasing the mass flux. The influence of the Froude number on the two-phase flow heat transfer coefficient is strictly related to the stratified flow regime. The upper region of the lateral surface of the tube under this regime remains in contact with vapor. This region is characterized by reduced values of local heat transfer coefficients. As a result, the average two-phase flow heat transfer coefficient is rather low compared to the one under the annular flow regime. The lower the mass flux (corresponding to lower Froude numbers), the higher the surface exposed to vapor, which in turn, results in reduced heat transfer coefficient. Equation (5) clearly reflects that behavior. In Equation (6) the heat transfer coefficient is independent from the Froude number due to possible transition to the annular two-phase flow for values of this parameter of the order of 0.1. This value has been determined empirically in this study, and should be more intensively investigated in the future.

Discussion of Results

Equations (5) and (6) were developed from experimental results obtained for conditions summarized in Table 5. Two sets of data were considered in the analysis. The first involves the whole set of experimental results whereas for the second only data for values of the mass flux higher than 100 kg/s.m^2 were considered. A comparison between the heat transfer coefficient from Eqs. (5), (6) and the experimental one is shown in Fig. 1 (a), (b). Clearly Eqs. (5) and (6) correlate better the experimental results for G>100 kg/s.m^2. The other correlations considered in this paper show the same trend, as the average deviations from Table 4 demonstrate. A possible explanation could be related to the fact that, for experiments under lower values of the mass flux, the vapor quality variation along the test section is higher for a given heat flux. Variations of vapor quality higher than 30% were common for experiments at G≤100 kg/s.m^2, what makes the assumption of local heat transfer coefficient rather questionable. In addition, it must be noted that some experiments were carried out at relatively high vapor qualities at the entrance, and, as a result, due to the elevated vapor quality variation, a possible dry out might have acurred at some point along the test section. Under these circumstances, the average heat transfer coefficient evaluated in such a way might not be representative of the one corresponding to the average vapor quality at the test section considered in this study.

Average deviations of the heat transfer coefficient from the proposed correlation with respect to the experimental one were respectively equal to 12.0% and 8.2%, depending upon the G value (the lower deviation corresponds to $G>100$ kg/s.m^2). It can be argued that these figures are lower than those obtained for the other correlations, since Eqs. (5) and (6) were developed from the same set of experimental data.

In order to check for the significance of the proposed correlation, other experimental results from the open literature have been used for the sake of comparison. Figures 2 (a), (b) present comparisons with data from Chaddock and Noerager (1966), and Anderson et al (1966), respectively. Table 7 shows the average deviation of the heat transfer coefficient from some of the correlations considered in this paper with respect to data from Chaddock and Noerager (1966) and Anderson et al (1966) as well. It can be noted that deviations from the proposed correlation are consistently lower than those from the others. The closest correlations from the point of view of average deviation are those due to Wattelet (1994) and Kandlikar (1990), respectively.

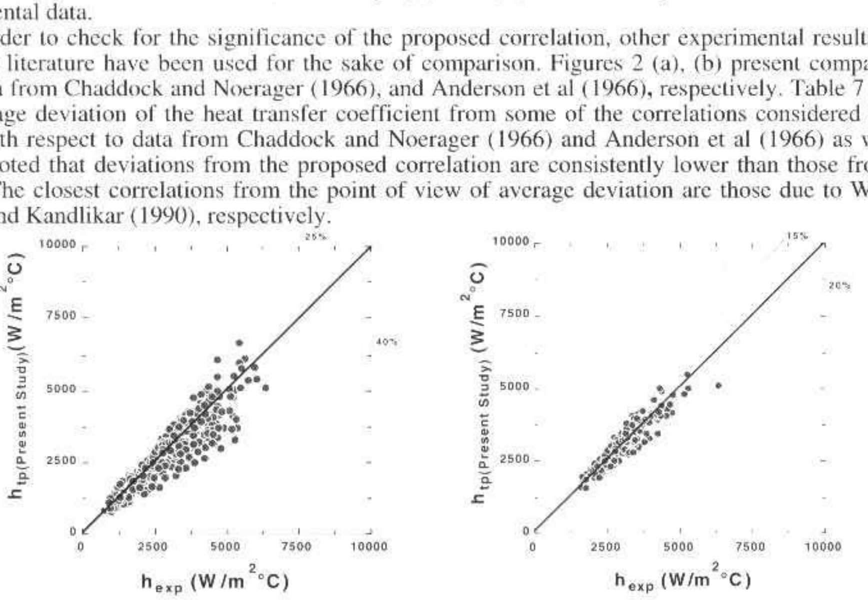

(a) (b)

Fig. 1 Comparison between the heat transfer coefficient from the proposed correlation, Eqs. (5) and (6), with the experimental one. (a) Complete set of experimental results; (b) results for G>100 kg/s.m^2

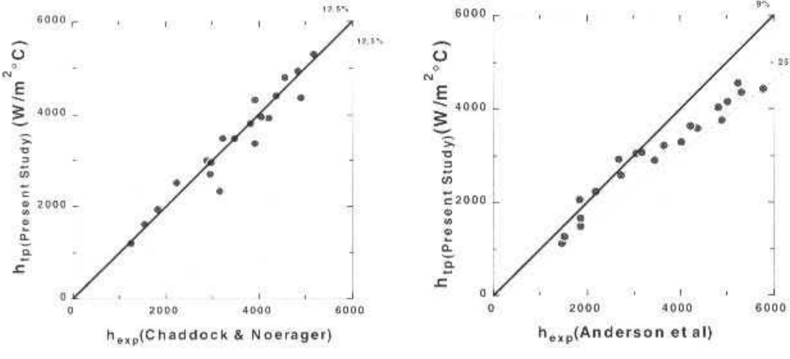

(a) (b)

Fig. 2 Comparison between heat transfer coefficient from proposed correlation and the experimental one for (a) data from Chaddock and Noerager (1966); and (b) Anderson et al (1966)

Table 7 Average deviation of the heat transfer coefficient from several correlations with respect to the experimental from Chaddock and Noerager(1966) and Anderson et al (1966)

Correlation	Average deviation [%]	
	Chaddock and Noerager (1966)	Anderson et al (1966)
ACRC-1 (1992) [Group 1]	20.0	25.0
Jung & Radermacher (1989) [Group 2]	12.5	18.0
Wattelet (1994) [Group 2]	12.5	15.0
Kandlikar (1990) [Group 3]	7.70	16.0
Present study (1997)	6.00	14.0

Finally, Figs. 3 and 4 present comparisons of some of the correlations with experimental data used in this study for typical operating conditions and two refrigerants: HFC-134a and HCFC-22. It can be noted that all the correlations predict qualitatively well experimental results in terms of the variation of the heat transfer coefficient with vapor quality, though Eqs. (5) and (6) are the best fitted. Among the other correlations, the one proposed by Wattelet (1994) is the closest, as expected, since it was developed from the very same data bank as the present study. All the empirical correlations, in different ways, present some difficulty in adequately representing experimental results over an extensive range of vapor qualities. This pattern is clearly seen in Figs. 3 and 4. A possible explanation to the observed deviations of correlations from experimental results is the lack of correspondence between the model and the physical mechanism along the test section. In fact, regarding experimental results from Fig. 3a,

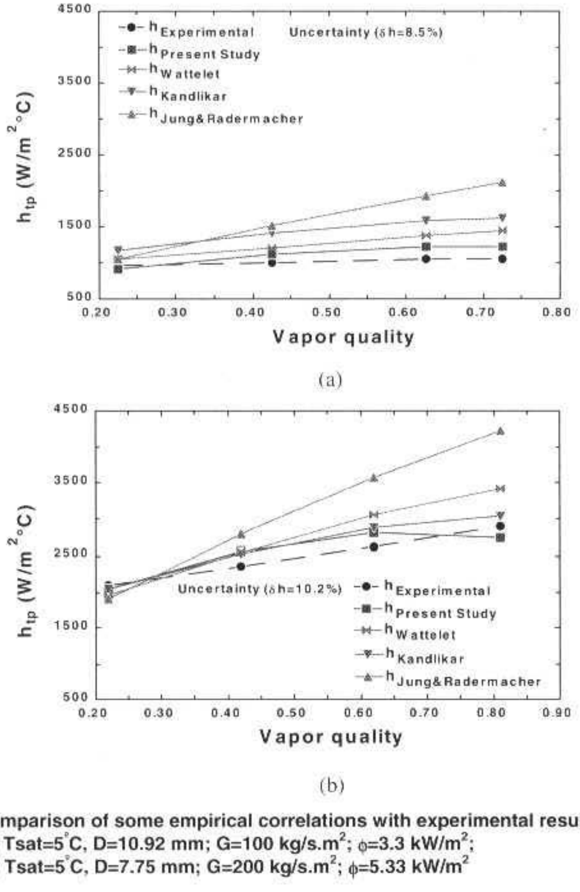

(a)

(b)

Fig. 3 Comparison of some empirical correlations with experimental results for HCFC-22
(a) Tsat=5°C, D=10.92 mm; G=100 kg/s.m^2; ϕ=3.3 kW/m^2;
(b) Tsat=5°C, D=7.75 mm; G=200 kg/s.m^2; ϕ=5.33 kW/m^2

a stratified wavy flow pattern is clearly established along the test section. Under this flow pattern, liquid remains in the bottom region of the tube, whereas the vapor flows over the liquid surface in the upper region. The surface temperature of the tube varies significantly over the circumference, indicating that the local heat transfer coefficient varies too due to alternate contact of the surface with liquid and vapor. However, the average heat transfer coefficient at the tube cross section remains constant along the test section, as it can clearly be noted in Fig. 3a. This behavior is typical of stratified flows in convective boiling. On the other hand, it can be noted in Figs. 3b and 4a, b that the heat transfer coefficient increases continuously along the test section. This is an indication that the annular flow regime has set in, for under this regime the internal surface of the tube is covered by a thin layer of liquid, which thickens on the bottom of the tube. As intensive evaporation occurs on the film surface, its thickness diminishes, causing a reduction of the its thermal resistance, and, as a result, a continuous increment of the heat transfer coefficient. In convective boiling, effects like the ones corresponding to the wavy and annular flow regimes have been associated to the Martinelli parameter and the Froude number, as suggested before. The former takes on strictly convective effects, such as interface evaporation, whereas the latter should correlate horizontal liquid-vapor interface effects. Regarding nucleate boiling,

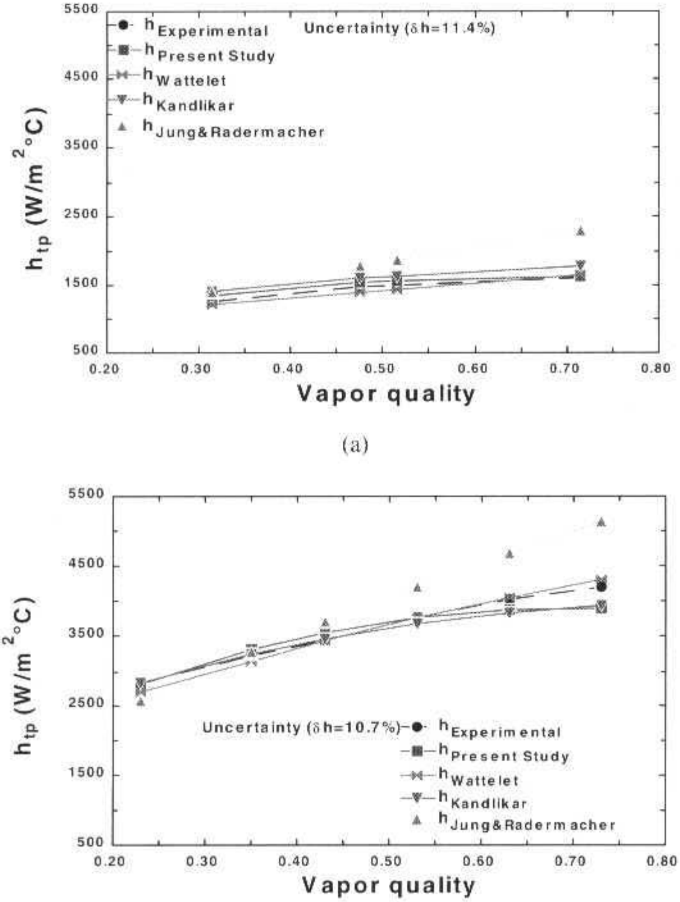

(a)

(b)

Fig. 4 Comparison of some empirical correlations with experimental results for HFC-134a
(a) Tsat=5°C, D=7.04 mm; G=100 kg/s.m^2; ϕ=3.15 kW/m^2;
(b) Tsat=5°C, D=10.92 mm; G=300 kg/s.m^2; ϕ=10 kW/m^2.

it is a common procedure to include the Boiling number to physically correlate the presence of bubbles on the heating surface. Summing up it can be said that most of the empirical correlations include dimensionless groups to supposedly take into account the occurrence of some physical mechanisms. However, an adequate procedure to switch on and off these groups under flow regime transition is still to be developed. As a result, given that over a wide range of vapor qualities there might be the possibility of occurrence of more than one flow regime, correlations should include a reliable flow regime transition model. Few studies have focused on flow regimes under convective boiling conditions. Papers by Kandlikar (1991) and Kattan et al. (1998) are significant exceptions, though not exhaustive.

Conclusions

The literature survey performed in this study has revealed that convective boiling heat transfer correlations from the open literature might present significant deviations from experimental results in addition to important discrepancies among themselves. A simple empirical correlation in terms of standard dimensionless groups has been proposed, developed through an optimized curve fitting procedure of experimental results obtained elsewhere. Despite the limited extent of the available data, the correlation produced results with significantly lower average deviations than the other correlations considered in this paper. Results from the correlation have been confirmed by comparison with other experimental data banks from the literature. However it must be stressed that none of the correlations predict adequately local variations of the heat transfer coefficient along the evaporator (variation with vapor quality). This result is predictable, since the empirical correlations, like the ones considered in this study, do not take into account neither physical mechanisms or flow regimes along the evaporator. Thus further research is needed in that respect in order to develop physically sound and accurate models for convective boiling.

Acknowledgements

The authors gratefully acknowledge the support by Fundação de Amparo à Pesquisa do Estado de São Paulo, FAPESP, for the support to this research through a doctoral assistantship to the second author and a research grant.

References

Anderson, S. W.; Geary, D. F. and Rich, D. F., 1966, "Evaporation pf R-22 in a Horizontal ¾ in OD Tube", ASHRAE Transactions, V. 72, part I, pp. 28-42

Bandarra Filho, E. P., 1997, "Study of Convective Boiling Heat Transfer of Halocarbon Refrigerants in Horizontal Tubes" (In Portuguese), MSc thesis - Escola de Engenharia de São Carlos, Universidade de São Paulo.

Chaddock, J. B. and Noerager, J.A., 1966, "Evaporation of R12 in Horizontal Tube with Constant Wall Heat Flux", ASHRAE Transactions, V. 72, part I, pp. 90-103.

Chaddock, J. B. and Buzzard, G., 1986, "Film Coefficients for in-tube evaporation of ammonia and R502 with and without small percentages of mineral oil", ASHRAE Transactions, V. 92, part I, pp. 22-40.

Chen, J. C., 1966, "Correlation for Boiling Heat Transfer to Saturated Fluids in Convective Flow", I&EC Process Design & Development, V. 5, No. 3, pp. 322-329.

Dengler, C. E. and Addoms, J.N., 1956, "Heat Transfer Mechanism for Vaporization of Water Tube", Chemical Engineering Progress Symposium, V. 52, No.18, pp. 95-103.

Dittus, F. W.and Boelter, L. M. K., 1930, "University of California Publications on Engineering", V. 2, No. 3, pp. 443-459.

Eckels, S. J. and Pate, M. B., 1991, "An Experimental Comparison of Evaporation and Condensation Heat Transfer Coefficient for HFC-134a and CFC-12", International Journal of Refrigeration, V. 14, No. 2., pp 70-77.

Guerrieri, S. A. and Talty, R. D., 1956,"A Study of Heat Transfer Organic Liquids in Single Tube, Natural Circulation, Vertical Tube Boilers", Chemical Engineering Progress Symposium Series, V. 52, No. 18, pp. 69-77.

Gungor, K. E. & Winterton, R. H. S., 1986, "A General Correlation for Flow Boiling in Tubes and Annuli", International. Journal of Heat and Mass Transfer, V. 29, No. 3, pp. 351-358.

Jung, D. S. and Radermacher, R., 1991, " Prediction of Heat Transfer Coefficient of Various Refrigerants During Evaporation", Paper No. 3492, ASHRAE Annual Meeting, Indianapolis, June 1991.

Kandlikar, S. G., 1990, "A General Correlation for Saturated Two-Phase Flow Boiling Heat Transfer Inside Horizontal and Vertical Tubes", Journal of Heat Transfer - Transactions of the ASME, V. 112, No. 1, pp. 219-228.

Kandlikar, S. G., 1991, "Development of a Flow Boiling Map for Subcooled and Saturated Flow Boiling of a Different Fluids Inside Circular Tubes", Journal of Heat Transfer - Transactions of the ASME, V. 113, No. 1, pp. 190-200.

Kattan, N.; Thome, J. R. and Favrat, D., 1998, "Flow Boiling in Horizontal Tubes: Part 1 – Development of a Diabatic Two-Phase Flow Pattern Map", Journal of Heat Transfer - Transactions of the ASME, V. 120, No. 1, pp. 140-147.

Kutateladze, S. S., 1961, "Boiling Heat Transfer", International Journal of Heat and Mass Transfer, V. 4, No. 9, pp. 31-45.

Liu, Z. e Winterton, H. S., 1991, "A General Correlation for Saturated and Subcooled Flow Boiling in Tubes and Annuli, Based on a Nucleate Pool Boiling Equation", International Journal of Heat and Mass Transfer, V. 34, No. 11, pp. 2759-2766.

McAdams, W. H., 1954, "Heat Trasmission", McGraw-Hill Book Co., Inc.

Murata, K. and Hashizume, K., 1993, "Forced Convective Boiling of Nonazeotropic Refrigerant Mixtures Inside Tubes", Journal of Heat Transfer, Transactions of the ASME, V. 115, No. 3, pp. 680-688.

Panek, J., 1992, "Evaporation Heat Transfer and Pressure Drop in Ozone-Safe Refrigerants and Refrigerantt-Oil Mixtures", M.S. Thesis, University of Illinois at Urbana-Champaign.

Pierre, B., 1956, "Coefficient of Heat Transfer for Boiling Freon-12 in Horizontal Tubes", Heating and Air Treatment Engineer, V. 19, pp. 302-310.

Saiz Jabardo, J. M., 1988, "Two phase Flow Heat Transfer", Class notes, Escola Politécnica da Universidade de São Paulo.

Shah, M. M., 1982, ".Chart Correlation for Saturated Boiling Heat Transfer: Equations and Further Study", ASHRAE Transactions, V. 88, part I, pp. 185-196.

Wattelet, J. P.;Chato, J. C.; Jabardo, J. M. S.; Panek, J. P. and Renie, J. P., 1991, "An Experimental Comparison of Evaporation Characteristics of HFC-134a and CFC-12", Paper 54, XVIIIth International Congress of Refrigeration Montreal, Canada, August/1991.

Wattelet, J. P., 1994, "Heat Transfer Flow Regimes of Refrigerants in a Horizontal-Tube Evaporator", Doctoral Thesis, University of Illinois at Urbana-Champaign, USA.

RBCM - J. of the Braz. Soc. Mechanical Sciences
Vol. XXI - No.2 - 1999- pp. 259-270

ISSN 0100-7386
Printed in Brazil

A Numerical Study of Thermal Storage on Encapsulated Phase Change Materials

Sergio Leal Braga
Carlos Eduardo Leme Nóbrega
Departamento De Engenharia Mecânica
Pontifícia Universidade Católica do Rio de Janeiro
22453-900 Rio de Janeiro, RJ Brazil
Slbraga@mec.puc-rio.br

Abstract

The role of thermal energy storage in the energetic scene has been continuously increasing over the last years, since electrical utilities started to adopt different rates for "peak" and "off-peak" power consumption periods. As a result, several works have been devoted to modeling and predicting the transient response of both sensible and latent heat storage devices, over a variety of geometric forms. Following the current trend, latent heat storage on encapsulated phase change material (PCM) was chosen as the object of the present work. Since the main feature is to take advantage of the high storage capacity offered by the latent heat, this work only deals with situations with small values of the Stefan number (Ste) which allow the solidification to be predicted by a quasi-stationary model. To obtain more general results, all the physical variables are arranged in non-dimensional groups, the influence of which on the response of the storage unit is evaluated in order to provide guidelines to the design and operation of those devices. Several assumptions are made with a view to maintain the model as simple as possible, without disregarding a careful reflection about its accuracy and impact on the reliability of the solution. The transient behavior of the storage unit is described by the evolution of the outlet temperature, as well as the thermal resistance ratio (TRR) through the discharge process. To ratify the model, some comparisons with previously published works are provided, showing not only qualitative but quantitative concurrency as well.

Keywords: *Thermal Storage, Phase Change.*

Introduction

Among the publications devoted to investigate the use of latent heat, the majority refers to "bulk" storage (rather than encapsulation), to which many analytical and numerical solutions can be easily found, such as in Szego and Schmidt (1978), Shamsundar and Srinivasam (1980) and Smith et al. (1980), to name a few. However, since encapsulation is becoming the most popular thermal storage architecture, one would ask what advantages it might have over "bulk" storage. That is, why many (smaller) capsules should be used rather than just one. The objective of the present work is to answer that question. Arnold, (1990 and 1991), used a semi-empirical model to describe latent heat storage on spherical capsules. Although extremely enlightening, his development was restricted to a dimensional formulation, which prevents its conclusions to be extended to a wider scope. Also, rather than spherical, we shall consider cylindrical capsules (tubes) transversally disposed to the flow, as shown in Fig. 1. Alexiades and Solomon (1993) proposed a quite simple analytical model to this configuration; however its application is restricted to situations where the thermal resistance imposed to heat diffusion through the phase change material is negligible. Unfortunately, this is not always the case. In fact, the growth of the thermal resistance due to the solidified - or melted - layer is a rather common and relevant feature of latent heat storage.

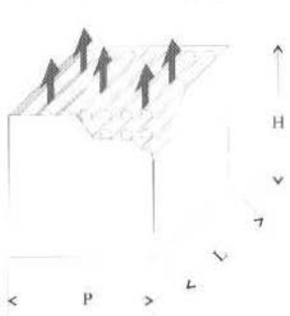

Fig. 1 Storage Tank

Manuscript received: July 1998; revision received: February 1999.Technical Editor: Angela Ourivio Nieckele.

Model Development

All the equations will be written for a solidification process, although the model is capable to simulate both heat (or cold) storage and recovery. The problem is posed as follows: at a time $t = 0$, the PCM is "hot", molten inside the tubes at a uniform melting temperature T_m ; at this very moment "cold" heat transfer fluid (HTF) is admitted through the bottom of the tank. To make the model practical, some assumptions are necessary:

1. The tank is represented by a control volume with one inlet and one outlet.
2. The tank, initially, is at uniform temperature, T_m.
3. All walls are perfectly insulated.
4. All vertical walls are impermeable.
5. The thermal capacitance and resistance of the tubes walls are negligible.
6. The sensible heat stored within the PCM is negligible when compared to the latent heat.
7. There is no natural convection inside the tubes, before or during the phase change.
8. The thermal resistance imposed by the PCM continuously increases with the solidification front progress.
9. The flow of the HTF throughout the tank can be modeled as a "plug-flow".
10. The heat transfer from the PCM to the recovery fluid is represented by concentrated sources, placed in the center lines of the tubes (Fig. 2).

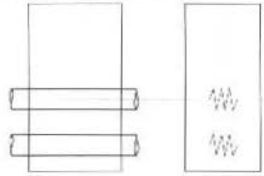

Fig. 2 Physical and numerical domains

All the assumptions are realistic within certain ranges. The first four assumptions are common to all model and experimental devices. The fifth is as good as smaller the thickness and higher the thermal conductivity of the tube walls, while the sixth is good for most of the PCMs. The seventh assumption is reasonable because the capsules diameter are usually small and PCM viscosity is usually high enough to prevent any buoyancy induced flow, whereas the eight assumption is good when the PCM is a pure substance. The ninth gets better with the decrease of the flow rate and/ or the increase of the tank height. Finally, one should notice that the direction of the phase change (radial to the tubes) not coincide with the direction of the flow. Assumption number ten enable us to split this two-dimensional domain into two one-dimensional domains.

Nomenclature

A_{AVE} = average flow area
A_{min} = minimum flow area
A_o = surface area of one capsule
C_0 = constant
C_1 = constant
C_2 = constant
C_p = heat transfer fluid specific heat
D_o = diameter of one capsule
G = heat generation
h = convective heat transfer coefficient
H = tank height
HTF = heat transfer fluid
K = heat transfer fluid thermal conductivity
K_{pcm} = phase change material thermal conductivity
K_R = thermal conductivity ratio
L = tank length
NR = number of rows
NT = number of tubes
NTPR = number of tubes per row
Nu = Nusselt number
P = tank length
PCM = phase change material
Pe = Peclet number
Pr = heat transfer fluid Prandtl number
Pr_{pcm} = phase change material Prandtl number
R_0 = capsule radius
R_H = radii ratio
R_t = global thermal resistance
Re = Reynolds number
RO = rate of occupation
Ste_{mo} = modified Stefan number
t = time
T = temperature through the flow field
T_n = heat transfer fluid inlet temperature
T_{pcm} = temperature through the phase change layer
T_m = temperature of change of phase
u = characteristic velocity of the flow
u_{max} = maximum velocity of the flow
$\dot{V}$ = volumetric flow rate
x. = flow direction
x = non-dimensional flow direction

Greek symbols:

ρ = density
μ = viscosity
γ = PCM latent heat
τ = non-dimensional time
θ = non-dimensional temperature

Subscripts

m = melting
pcm = phase change material
O = relative to capsule
sf = solidification front

It is worthwhile to notice, while observing Fig. 2, that the flow cross-section in the real tank is wider than in the model. This happens because when one assumes a plug-flow condition under a given flow rate, a representative area can only be found on a volume rate basis:

$$A_{AVE}=\frac{\left(HPL-\frac{\pi}{4}NTLD_0^2\right)}{H} \tag{1}$$

If $\dot{V}$ is the volumetric flow rate of the HTF through the tank, then the flow velocity "u" is assumed to be uniform, and given by:

$$u=\frac{\dot{V}}{A_{AVE}} \tag{2}$$

This enables us to write the one-dimensional transport equation

$$\rho Cp\left(\frac{\partial T}{\partial t}+u\frac{\partial T}{\partial x}\right)=K\frac{\partial^2 T}{\partial x^2}+\dot{G} \tag{3}$$

As stated before, $\dot{G}$ is a heat generation which is present only on locations which correspond to the tubes centerlines, (otherwise $\dot{G}=0$). This heat source is distributed over a small element of arbitrary length Δx

$$\dot{G}=NTPR\frac{(T_m-T)}{R_t}\frac{1}{A_{AVE}}\frac{1}{\Delta x} \tag{4}$$

On the onset of the change of phase the thermal resistance is given by:

$$R_t=\frac{1}{hA_0} \tag{5}$$

After its beginning, the thermal resistance to conduction through the growing layer of PCM has to be added to the previous term

$$R_t=\frac{1}{hA_0}+\frac{ln\left(R_0/R_{sf}\right)}{2\pi K_{pcm}L} \tag{6}$$

Then, if one places (6) in (4) and (4) in (3),

$$\rho Cp\left(\frac{\partial T}{\partial t}+u\frac{\partial T}{\partial x}\right)=K\frac{\partial^2 T}{\partial x^2}+\frac{NTPR}{A_{AVE}\ \Delta x}\frac{(T_m-T)}{\frac{ln\left(R_o/R_{sf}\right)}{2\pi k_{pcm}L}+\frac{1}{hA_0}} \tag{7}$$

Thermal resistance (Eq. 6) is composed by two terms. On the first one, which accounts for the convective resistance, the value of h is obtained by

$$h = Nu\ K/D_o \tag{8}$$

in which the Nusselt number Nu is given by Bejan (1995).

$$Nu = C_0 Re^{C1} Pr^{C2} \left(\frac{Pr}{Pr_w} \right)^{0.25} \tag{9}$$

where C_1 and C_2 are constants which depend on Re. C_0 varies from 0 to 1 for Re $<10^3$ and NR (number of rows) < 16. For any other conditions, $C_0 = 1$. The Reynolds number is based on the maximum velocity, u_{max}, which occurs at the minimum cross section, A_{min}

$$Re = \frac{\rho\, u_{max}\, D_0}{\mu} \tag{10}$$

$$u_{max} = u\ (A_{ave}/A_{min}) \tag{11}$$

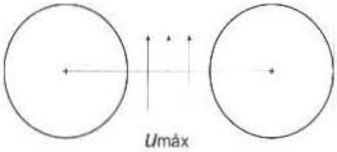

Fig. 3 **Maximum velocity flow area**

The ratio between the capsule radius and the solidification front radius R_{fs} will be obtained by using a quasi-stationary phase change model (Alexiades and Solomon, 1993), which, according to assumption (6), is suited to this case. If the phase change at the J row starts at t_j, temperature throughout the PCM is governed by

$$\frac{k_{pcm}}{R} \frac{d}{dR} \left(R \frac{dT_{pcm}}{dR} \right) = 0 \quad R_0 > R > R_{sf}\ , t > t_j \tag{12}$$

Subjected to the following boundary conditions:

$$T_{pcm}(R_{sf}, t) = T_m\ , \ t > t_j \tag{12a}$$

$$K_{pcm} \left. \frac{dT_{pcm}}{dR} \right|_{R_0} = h[T(t) - T_{pcm}(R_o, t)] \quad t > t_j \tag{12b}$$

to obtain

$$T_{pcm}(R,t) = T_m + (T(t) - T_m) \frac{ln\, R/R_{sf}}{ln \frac{R_o}{R_{sf}} + K_{pcm}/hR_o} \quad R_0 > R > R_{sf}\ , t > t_j \tag{13}$$

On the possession of the temperature profile through the PCM, it is possible to apply a differential energy balance on the solidification front

$$\rho_{pcmf}\gamma\frac{dR_{sf}}{dt} = K_{pcm}\frac{dT_{pcm}}{dR}\bigg|_{R_{fs}} \quad t > t_j \tag{14}$$

$$R_{sf}(0) = R_o \tag{14a}$$

to obtain

$$2R_{sf}^2 \ln\frac{R_{sf}}{R_o} = \left(1+\frac{2K_{pcm}}{hR_o}\right)\left(R_{sf}^2 - R_o^2\right)+\frac{4K_{pcm}}{\rho_{pcm}\,\gamma}\int_0^t (T - T_m)dt \tag{15}$$

The solution to this integral equation simultaneously with the partial differential equation which prescribes the temperature field through the tank, Eq.7, represent the physical process of heat recovery (or storage). However, to obtain more general results, it is advisable to rewrite Eqs. (7) and (15) in non-dimensional forms. Defining a characteristic advection time, t_c (Homan et al., 1996) and the following dimensionless variables,

$$t_c = H/u \tag{16}$$

$$\tau = t/t_c \tag{17}$$

$$x^* = x/H \tag{18}$$

$$R_R = R_{sf}/R_0 \tag{19}$$

$$\theta = (T-T_m)/(T_m-T_{in}) \tag{20}$$

$$Pe = Hu/\alpha_{pcm} \tag{21}$$

$$K_R = K/K_{pcm} \tag{22}$$

and replacing them in Eq.(7)

$$\frac{\partial\theta}{\partial\tau}+\frac{\partial\theta}{\partial x^*} = \frac{1}{Pe}\frac{\partial^2\theta}{\partial x^{*2}}+\pi\frac{HL}{A_{AVE}}\frac{(\theta_m-\theta)}{Pe}\frac{NTPR}{\Delta x^*}\frac{1}{\left(\frac{1}{Nu}-\frac{1}{2}K_R\ln R_R\right)} \tag{23}$$

Initial condition: $\theta(x^*,0) = 1$ (23a)

Boundary conditions $\theta(0,\tau) = 0\,,\ \tau > 0$ (23b)

$at\ x^* = 1\,,\ \frac{\partial\theta}{\partial x^*} = 0$ (23c)

Also, defining the modified Stefan number

$$Ste_{mo} = \frac{\rho C_p (T_m - T_{in})}{\rho_{pcm}\gamma} \tag{24}$$

and introducing the non-dimensional variables into Eq. (15) one would obtain

$$lnR_R = \left(\frac{1}{2}+\frac{1}{NuK_R}\right)\left(1-R_R^2\right)+8\left(\frac{D_0}{H}\right)^{-2}\frac{1}{K_R Pe}Ste_{mo}R_R^{-2}\int_0^{\tau}(\theta_m-\theta)d\tau \tag{25}$$

The solution is then obtained by solving simultaneously Eqs.(23) and (25). The domain relative to Eq.(23) is divided into a finite number of volumes, each one of lentgh Δx^* (Patankar,1980) by using the upwind scheme to represent advection and the fully implicit scheme for the transient term. The resulting tri-diagonal matrix is then solved, with guessed values of R_{fs} for each row, and the temperature field is used to evaluate R_{fs} on each row, using Eq. (25). This process continues until convergence has been achieved. Before evaluating the influence of the non-dimensional parameters over the energy recovery, some considerations are necessary:

- The storage tank is initially filled with both HTF and PCM at T_m. Since the inlet temperature T_{in} will necessarily be smaller than T_m, in addition to latent heat some sensible heat will be stored both on the PCM and the HTF. According to the quasi-stationary model of solidification, sensible heat storage on the PCM can be neglected (assumption 6). Sensible heat storage on the recovery fluid is naturally taken into account by the left side of Eq.(23). This explains why a modified Stefan number definition (Ste_{mo}) is used, rather than the traditional one.
- Since Zukauskas correlation, Eq.(9), is the only one available, the Nusselt number can only be obtained from Reynolds and Prandtl numbers. Hence, Prandtl and Pe number are used to feed the code, instead of Reynolds and Nusselt numbers. Then the code evaluates Reynolds and Nusselt numbers.
- Since it's difficult to attribute typical values for the geometric parameter HL/A_{med}, a slenderness ratio H/P is used instead. It can be shown that

  $$\frac{HL}{A_{med}} = \frac{1}{\left(\frac{H}{P}\right)^{-1} - NT\frac{\pi}{4}\left(\frac{D_0}{H}\right)^2} \tag{26}$$

  and the geometry of the storage tank is defined by H/P , D_0/H, NTPR, NR.
- An important auxiliary parameter is the rate of occupation, RO, which can be defined as the ratio between the tank and PCM volumes. It can be written in terms of the input parameters according to

  $$RO = \frac{V_{pcm}}{V_T} = \frac{\pi}{4}NT\left(\frac{D_0}{H}\right)^2\left(\frac{H}{P}\right) \tag{27}$$

Results

The non-dimensional (input parameters) which feed the code are H/P , D_0/H, NTPR, NR, Pe, Pr, K_R, Ste_{mo}. Non-dimensional such as Re, Nu, HL/A_{med} and RO are derived (output) parameters, values of which are calculated by the code. All input parameters values were chosen so as to match the values of dimensional running parameters of actual devices, largely described on literature. For instance, the analysis shall be restrained to low Reynolds number values, since the HTF flow is described as being laminar on all experimental and commercial devices (Arnold,(1991); Cryogel,(1990); Dorgan and Elleson,(1993)). As stated before, the objective is to evaluate the influence of the fragmentation of a given amount of PCM over the extraction of the energy previously stored. To conduct this investigation, the number of tubes NT will be varied simultaneously with D_0/H, in such a way that the rate of occupation RO (Eq. (27)) remains constant. Some parameters, which are shown on Table 1, are held constant through cases 1 to 9. All auxiliary parameters are somber, to distinguish them from the input parameters. Results are ratified in the appendix, by a comparison to an analytical solution.

Table 1 Constant Parameters

H/P	1
Ste_{mo}	0.2
K_R	1
Pr	4.5
RO	60%

Table 2 The influence of NT over the energy recovery

	Pe	NR	NTPR	NT	D_h/L	Re	Nu
Case 1	10^5	10	10	100	0.073	70	13.2
Case 2	10^5	50	50	2500	0.015	15	7.2
Case 3	10^5	100	100	10000	0.007	9	5.8
Case 4	2×10^5	10	10	100	0.073	134	19
Case 5	2×10^5	50	50	2500	0.015	27	9.5
Case 6	2×10^5	100	100	10000	0.007	15	7.5
Case 7	5×10^5	10	10	100	0.073	334	37
Case 8	5×10^5	50	50	2500	0.015	70	13.7
Case 9	5×10^5	100	100	10000	0.007	37	10.3

It can be seen from Table 2 that, in spite of the decrease on the Nusselt number values, the time required by the energy recovery decreases with an increase on the number of tubes. Although each capsule becomes less effective, there are many more capsules (heat sources), making the energy storage/recovery faster as a whole. Figures 4, 5 and 6 were drawn after Table 2 and show the influence of the increase on the number of tubes NT over the outlet temperature, for three values of the Peclet number. In all cases, it can be seen that the higher NT, the higher will be the (average) outlet temperature, which is also a consequence of the better heat transfer rates proportioned by fragmentation.

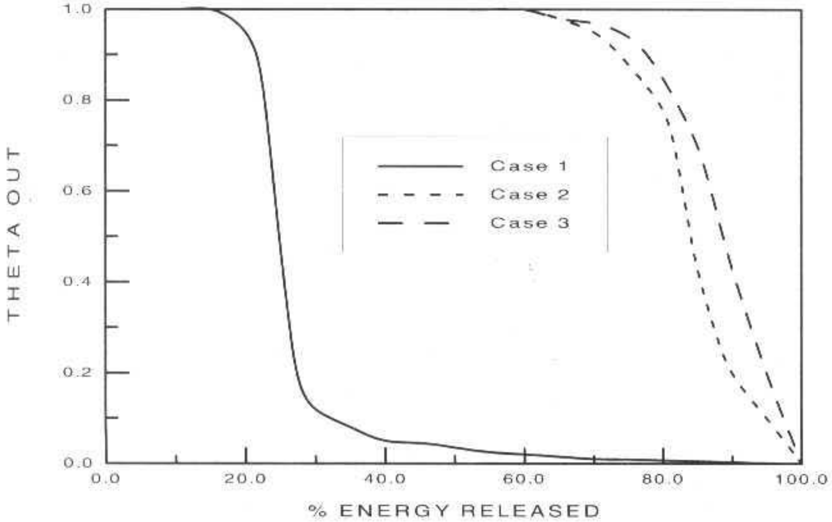

Fig. 4 Outlet temperatures for a low Peclet value

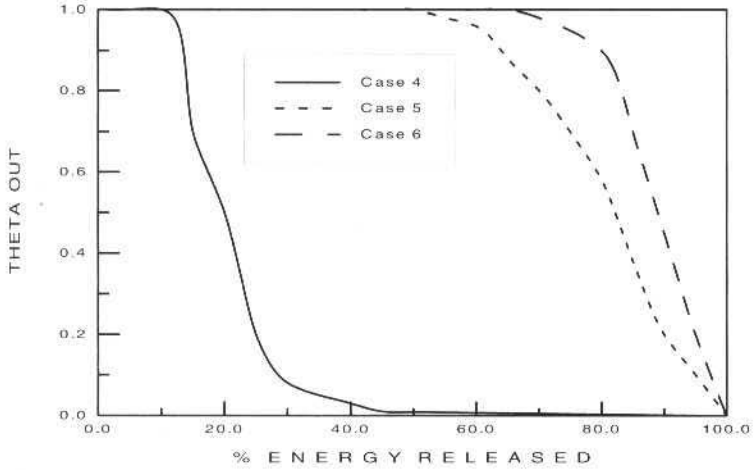

Fig. 5 Outlet temperatures for a moderate Peclet value

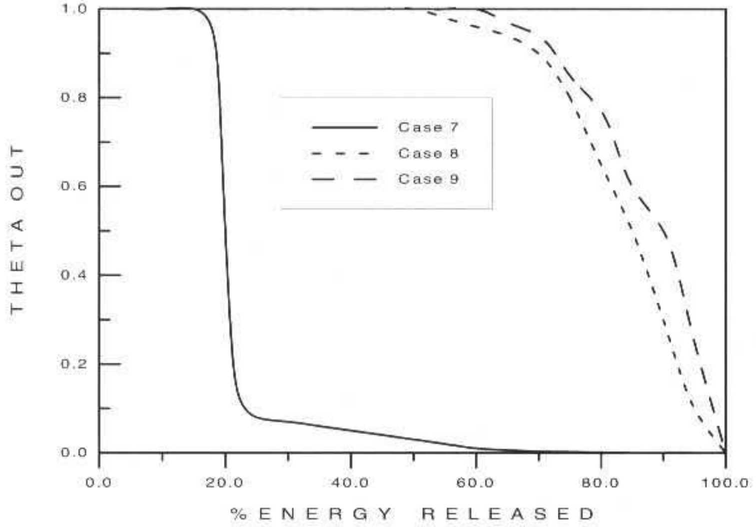

Fig. 6 Outlet temperatures for high Peclet value

It is also possible to observe that the increase of NT produces a "steady-state" discharge process, with a constant outlet temperature up to 70% of the storage capacity. To better understand this behavior, it is convenient to introduce the definition of thermal resistance ratio, TRR, as the ratio between the initial and the instantaneous thermal resistance,

$$TRR = \frac{\left(\dfrac{1}{hA_0} - \dfrac{lnR_R}{2\pi K_{pcm}}\right)}{\dfrac{1}{hA_0}} = 1 - \frac{Nu}{2K_R} LnR_R \tag{28}$$

which is a measure of the growth of the thermal resistance imposed by the phase change. Figures 7 to 9 show the influence of the number of tubes NT through TRR. It can be seen that the higher the NT, the less significant will be the resistance to conduction through the PCM, allowing the phase change to occur almost in steady-state.

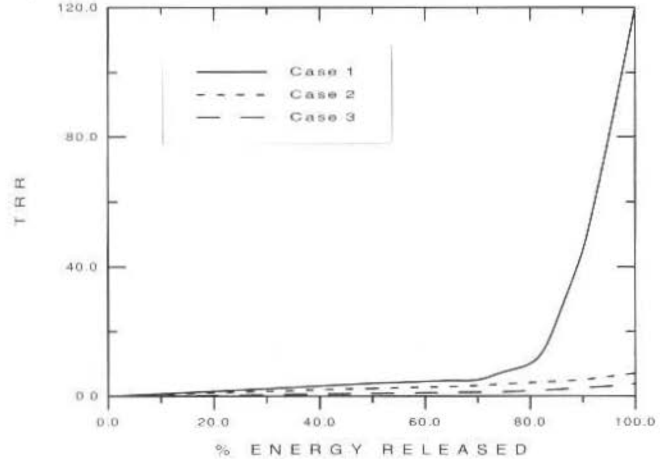

Fig. 7 Thermal resistance ratio evolution

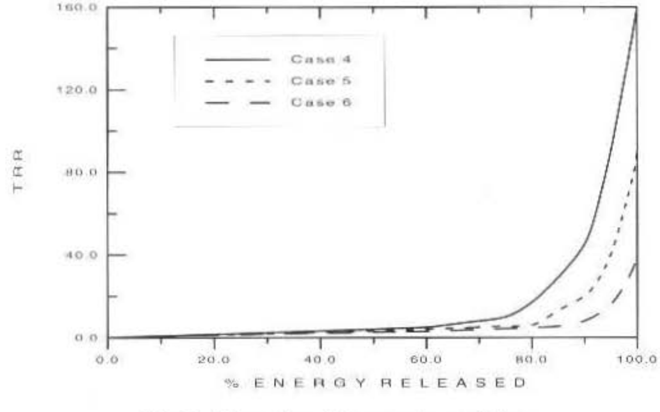

Fig. 8 Thermal resistance ratio evolution

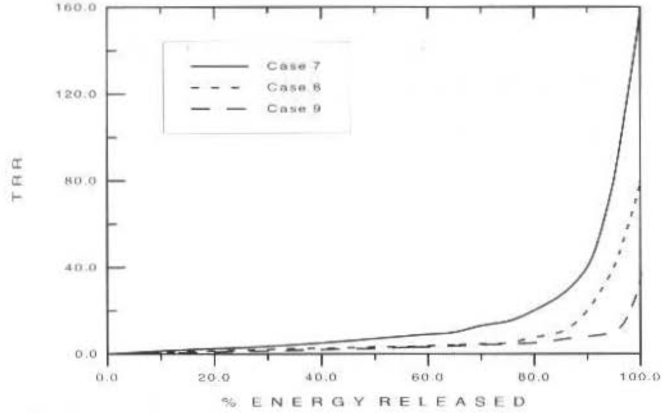

Fig. 9 Thermal resistance ratio evolution

Conclusion

The general conclusion is that, over the range studied, the increase of fragmentation of a certain amount of PCM (i.e., the increase in the number of tubes) results on better average heat transfer rates. As a consequence, the required time to discharge the storage unit decreases, while the average outlet temperature increases. Although unavoidable, the variation on the thermal resistance is also minimized by increasing the number of capsules. This will lead to nearly constant energy recovery rates, which is frequently refereed to as an advantage of sensible heat over latent heat storage. Excessive fragmentation, however, could lead to phenomena which the model is unable to predict, such as subcooling or PCM fracture, as described by Arnold (1990). The model shows good agreement with independently obtained results (Appendix).

References

Alexiades, V. and Solomon, A.D., 1993, "Mathematical Modeling of Melting and Freezing Processes" . Hemisphere Publishing Corporation.

Arnold, D., 1990, "Dynamic Simulation of Encapsulated Ice Stores", Part 1: The Model ASHRAE Transactions.

Arnold, D., 1991, "Dynamic Simulation of Encapsulated Ice Stores", Part 2: Model Development and Validation , ASHRAE Transactions.

Bejan, A., 1995, "Convection Heat Transfer", J. Wiley & Sons, 2ed.

Cryogel 103, 1990, "Technical Manual".

Dorgan, C.E. and Elleson, J.S., 1993, "Design Guide for Cool Thermal Storage", ASHRAE.

Homan, K.O, Sohn, C.W. and Soo, S.L., april 1996, "Thermal Performance of Stratified Chilled Water Storage Tanks", HVA&R Research.

Patankar, S.V., 1980, "Numerical Heat Transfer and Fluid Flow", Hemisphere Publishing Corporation.

Shamsundar, N. and Srinivasam, R., 1980, "Effectiveness- Ntu Charts for Heat Recovery From Latent Heat Storage Units", Journal of Solar Engineering, vol.102.

Smith, R.N., Ebersole, T.E. and Griffin, F.P., 1980, "Heat Exchanger Performance in Latent Heat Thermal Energy Storage", Journal of Solar Engineering, vol.102.

Szego, J. and Schmidt, F.W., 1978, "Transient Behavior of a Solid Sensible Heat Thermal Storage Exchanger" , Journal of Heat Transfer, vol.100.

Appendix

Model Validation

Since this work consists of a mathematical model and its numerical solution, it requires a comparison with independently obtained results. However experimental data for this configuration was not available in literature, so it was only possible to compare the results with those obtained by Alexiades and Solomon (1993), who proposed a quite simple model to describe the evolution of the discharge temperature through time. Instead of considering the whole tank, consider just a row of tubes (Fig. 10), containing PCM initially melted at T_m. At $t = 0$, the tank is instantaneously flood with heat transfer fluid at T_{in}. The cylinders begin to freeze and cool, while the heat transfer fluid gains heat as it flows through the array.

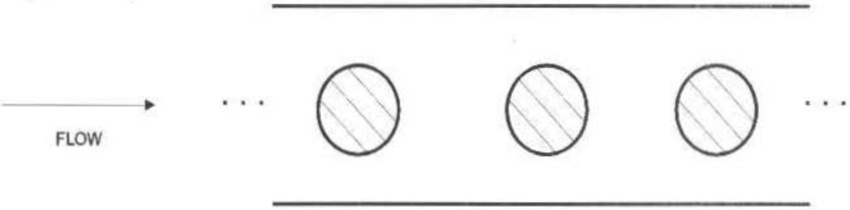

Fig. 10 Alexiades and Solomon's model

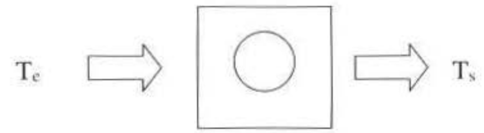

Fig. 11 Single cylinder

Consider now a control volume, which contains a single tube (Fig. 11). If T_{sf} is the temperature on the surface of the cylinder, an energy balance would result in

$$(T_s - T_e)\,\dot{m}\,Cp = 2\,\pi R_0\,L\,h\,(T_{sf} - T_e) \tag{29}$$

For small thermal solicitations, $T_{sf} \approx T_m$, therefore

$$T_S = T_e - \frac{2\pi R_0 h L}{\dot{m} C_P}(T_e - T_m) \tag{30}$$

Defining $\lambda = \frac{2\pi R_0 h L}{\dot{m} C_P}$,

$$T_s = T_e + \lambda\,(T_m - T_e) \tag{31}$$

This equation provides the temperature at a given location as a function of its backwind neighbor. One can deduce a formula for any position T_J as a function of the inlet temperature T_{in}:

$$T_1 = T_{in} + \lambda\,(T_m - T_{in}) \tag{32}$$

$$T_2 = T_1 + \lambda\,(T_m - T_1) \tag{33}$$

Eliminating T_1 and completing the square

$$T_2 = T_m - (T_m - T_{in})(\lambda - 1)^2 \tag{34}$$

By induction,

$$T_J = T_m - \Delta T\,(\lambda - 1)^J \tag{35}$$

in which

$$\Delta T = T_m - T_{J-1} \tag{36}$$

The temperature field is described by Eq.35 until t_1, when cylinder #1 completely freezes, ceasing any influence on the temperature field. Then, for $t_1 < t < t_2$ the field is shifted one position to the left, and cylinders #2,3,4…play the role of their respective backwind neighbors played the instant before. This "steady-state" field continues to shift upwind anytime a cylinder freezes completely. To obtain the time required by each row to achieve complete solidification, the quasi-stationary model (Eq. 25) is used:

$$2R_{FS}^2\,Ln\frac{R_{sf}}{R_o} = \left(1 + \frac{2K_{mmf}}{hR_o}\right)\left(R_{sf}^2 - R_o^2\right) - \frac{4K_{pcm}}{\rho_{pcm}\,\gamma}\int_0^t (T - T_m)\,dt \tag{37}$$

taking Lim $R_{fs} \to 0$, one would obtain an indeterminate form $0 \times \infty$. Rewriting R_{fs}^2 as $1/R_{fs}^{-2}$ one could apply L'Hopital theorem and obtain

$$Lim\ 2\ R_{fs}^{2}\ Ln\ (R_{fs}/R_{o}) = 0 \tag{38}$$

So the time required by #J is given by

$$t_J = \frac{R_0^2\, \rho_{pcm}\, \gamma}{2k_{pcm}(T_m - T_{J-1})}\left[\frac{1}{2} + \frac{k_{pcm}}{hR_0}\right] = \frac{t_1}{(1-\lambda)^{J-1}} \tag{39}$$

in which t_1 is the time required by the first row to achieve complete solidification. Now, it is possible to compare the results obtained using Solomon's and the present model in Fig. 12. It can be seen that there is a qualitative concurrency between the proposed and Solomon's model. However, since the present model takes on account the growth of the thermal resistance due to the phase change, it predicts a slower energy recovery. This happens even for a small value of the Biot number ($Bi = 0.15$), because according to Eq. (6), the thermal resistance to conduction grows to an infinite value as $R_{fs} \rightarrow 0$, no matter how small the value of k_{pcm} might be.

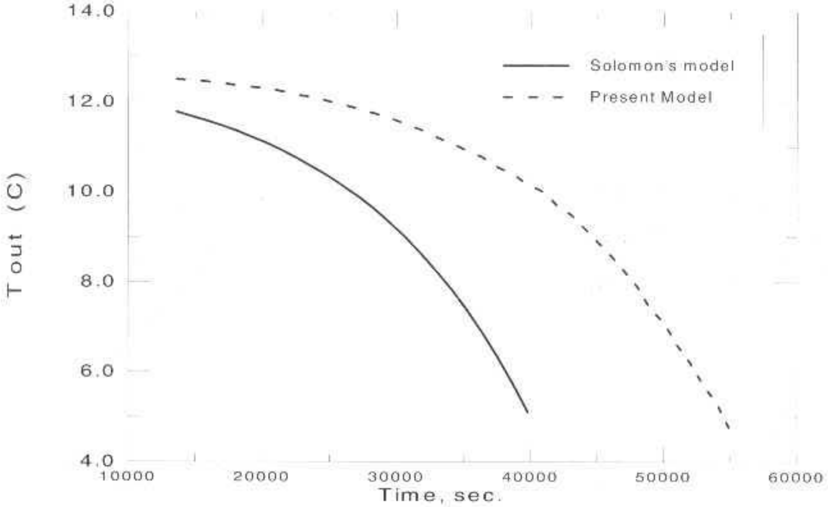

Fig. 12 A comparison between Solomon's and present model

RBCM - J. of the Braz. Soc. Mechanical Sciences
Vol. XXI - No.2 - 1999 - pp. 271-278

ISSN 0100-7386
Printed in Brazil

A Wind-Tunnel Investigation of Ground-Wind Steady Loads on a Strap-on Launch Vehicle

Paulo Moraes Jr.
Divisão de Sistemas Espaciais/Aerodinâmica
Instituto de Aeronáutica e Espaço
Centro Técnico Aerospacial
12228-904 São José dos Campos-SP Brazil
moraes@iae.cta.br

Abstract

The effect of wind loads on slender bodies has been observed and investigated for many years by many authors. The present paper deals with an experimental investigation of wind induced loads on strap-on launch vehicle configurations. The work is firstly restricted to the observation of steady global loads acting on a configuration based on an arrangement of four cylinder shaped boosters around a cylindrical central core of equal diameter. The paper discusses the results obtained for the transversal or drag force, the rolling moment, and the longitudinal position of center of pressure, as function of several parameters.

***Keywords**: Aerodynamics, Wind-Loads, Wind-Tunnel, Launch Vehicle.*

Introduction

Wind-induced loads concern designers of launch vehicles to attempt to keep minimum structural weight, flight safety during lift-off, collision-free lift-off, and structural integrity of the global launch assembly, i.e. launch vehicle, launch table, service tower, umbilicals, etc.

Steady and oscillatory wind-induced loads result from the flow around the vehicle, including flow separation generated by edges or protuberances on the vehicle's surface, creating a complex flow environment. Such complex flow fields have been investigated for several launch vehicles of different shapes and configurations, however no accurate procedure has been formulated for predicting the loads on a previously untested configuration. For this reason space vehicle designers are forced to evaluate experimentally the aerodynamic characteristics of new configurations.

On simple bodies of revolution like cylinders the steady drag loads can be well estimated using drag coefficients for two-dimensional cylinders or cone-cylinder combinations, Hoerner 1965. For more complex configurations, such as clustered cylinders, cylinders with protuberances, or those influenced by the presence of adjacent tower structures, steady loads may be estimated from wind-tunnel tests on rigid models.

General Considerations

The model of the herein presented investigation simulates a vehicle that is standing vertically on the launch pad prior to lift-off, Fig. 1 .

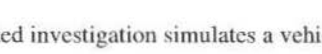

Fig. 1 Lift-off model

Manuscript received: February 1997; revision received: November 1998. Technical Editor: Agenor de Toledo Fleury

The launch configuration includes:

- launch vehicle (clustered)
- launch table with flame deflectors and
- service tower.

The wind direction is 90° from the axis of symmetry. The pitching moment acts in a plane which is parallel to the wind direction and passes through the axis of symmetry. The lateral forces and moments act in a plane which is perpendicular to the wind direction and passes through the axis of symmetry. The center of moments is the intersection of the floor with the axis of symmetry as shown in Fig. 1. The wind profile has a characteristic similar to an atmospheric wind without consideration of any topographic obstacles.

Experiments

The experimental investigation was carried out in the TA-2 wind-tunnel of the Aerodynamic Testing Laboratory of the *Centro Técnico Aeroespacial*, in São José dos Campos-SP, Brasil, (Fig. 2).

Wind-Tunnel

The main characteristic of the wind-tunnel are given bellow:

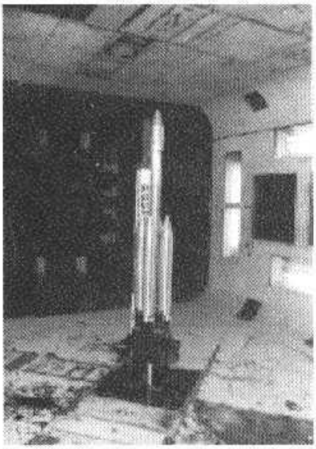

- Type: closed circuit
- Test section size: 3.0 m x 2.1 m
- Operation: continuous.

Fig. 2 TA-2 Wind tunnel

Instrumentation:

The main instrumentation used for the present investigation consists of a six-component Taller & Cooper external balance with six load cells BLH (three for forces and three for moments). Each sensor was connected with an assembly of signal conditioner, amplifier and filter Honeywell.

Measurements:

The following types of measurements were made during the course of the investigation:

Nomenclature

C_Z, C_d = transversal (drag) force coefficient [-]
C_l = rolling moment coefficient [-]
Dref = reference diameter [m]
L = total length of model exposed to wind [m]
Lref = reference length [m], Lref = L
PHI, φ = wind direction [degrees]
q = dynamic pressure [N/m^2]
Re = Reynolds number [-]
S = frontal area of model exposed to wind [m^2]
Sref = reference area [m^2], Sref = $(\pi/4)\ D^2_{ref}$
TU = service or umbilical tower
V, V_{wind} = wind velocity [m/s]
UTd = distance between vehicle surface and service tower [m]
Xcp/L = relative longitudinal position of center of pressure, (Xcp/L= 0.0 : vehicle nose) [-]

- Steady-state transversal and lateral forces,
- Rolling moment,
- Oil flow and smoke visualization, and
- Steady-state pressure measurements.

The data acquisition and reduction were conducted using a set of Hewlett Packard equipment's comprised of:

- Micro-computer HP-9825
- Digital voltmeter HP-3456A (300 readings/s)
- Channel scanner HP-3497A
- Matrix printer HP-2631G.

For each measuring point 30 data sets were taken and compiled. The final result was then determined as an arithmetic mean value for every point.

Models

The wind-tunnel models were manufactured from steel in a 1:15 scale, so that the mean geometry details have been reproduced with accuracy, Fig. 3.

The models comprise:

- Launch vehicle,
- Launch table with flame deflectors, and
- Service tower.

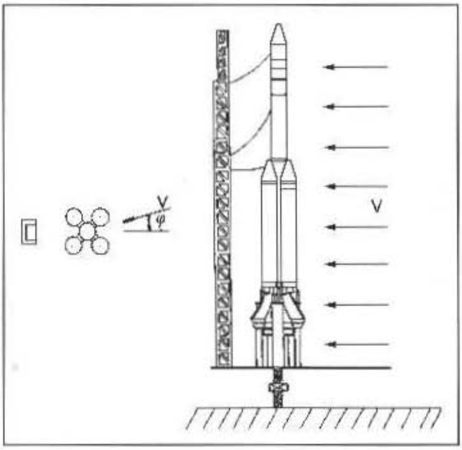

Fig. 3 Wind tunnel test model

Model dimensions:

- Length = 1.23 m,
- Diameter of central core = 0.067 m .

Test variables

Wind velocity, wind direction and Reynolds number were the principal test variables. The Reynolds number was slightly varied by changing the wind velocity. During the investigation the Mach number was keept below 0.3, so that major compressibility effects could be neglected.

The other variables included:

- Absence and presence of the service tower, and
- Distance between service tower and vehicle.

Tests

The tests were performed with the models described in (Moraes and Neto, 1988), considering basically the configurations, shown in Fig. 4.

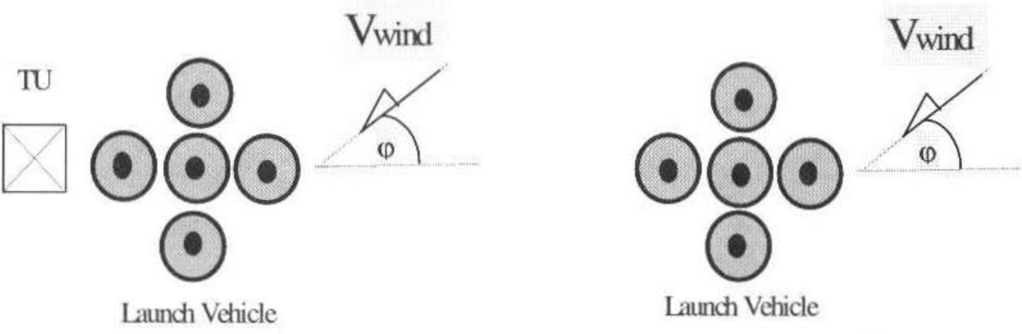

VC+ET :Launch vehicle standing on the launch pad in presence of the service tower

VC-ET :Launch vehicle standing on the launch pad in absence of the service tower

	Wind direction	Wind velocity	Reynolds number	UTd
Configuration	Phi (degrees)	V_{wind} (m/s)	(10^6)	s (m)
VC+ET				0.15; 0.30
	0; 45; 90; 135; 180	31.0; 36.0; 43.0	0.223 - 0.306	
VC-ET				-

Fig. 4 Launch vehicle testing configurations

Results and Discussion

The experimental investigation was conducted in conditions simulating the lift-off of a strap-on launch vehicle. The main goal of this investigation was the determination of the aerodynamic global characteristics for simulation of the dynamics of lifting-off. The lift-off configuration is comprised of the launch vehicle, in its flight configuration, standing on the launch table, with flame deflectors, and service tower.

With the purpose of investigating the dynamic behaviour of such a kind of configuration, attempt has been given to following characteristics:

- Transversal (drag) force coefficient C_Z, defined as C_z = transversal force / (q x S_{REF})
- Rolling moment coefficient C_l , defined as C_l = roll moment / (q x L_{REF} x S_{REF}) and
- Longitudinal position of centre of pressure Xcp/L (position where the resultant of the transversal force acts), defined as Xcp/L = pitch moment / transversal force .

Following are presented in graphs and tables the main aerodynamic characteristics for the lift-off phase, which are commented with respect to influence of the test variables. The results obtained were analyzed and later slightly corrected for real flight conditions, so that they could be used for design purposes.

Influence of wind velocity

Due to limitations of the wind-tunnel, the wind velocity was restricted to a minimum value of 31.0 m/s. In order to investigate the influence of this variable and the corresponding Reynolds number on the aerodynamic characteristics of the whole assembly, three different velocities were produced: V = 31.0, 36.0 e 43.0 m/s.

The following Figs. 5 to 7, show that the wind velocity does not influence considerably C_Z, C_l e Xcp/L. For that reason is reasonable to assume that these coefficients remain practically constant for smaller velocities. So, it is possible for further analysis to extrapolate all the coefficients for V = 10 m/s, which is the maximum admissible velocity for lifting-off of launch vehicles. The continuous curves connecting the experimental data drawn in the figures were obtained through polynomial functions.

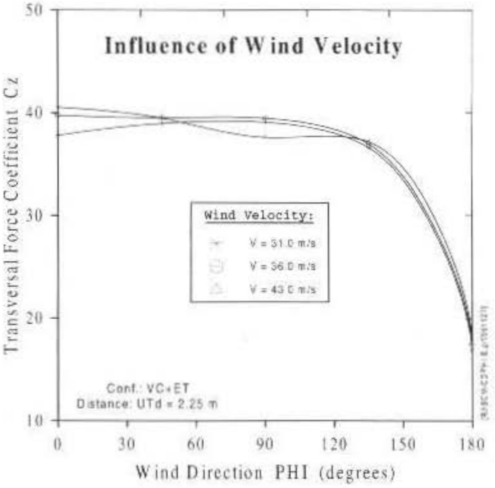

Fig. 5 Influence of wind velocity on transversal force

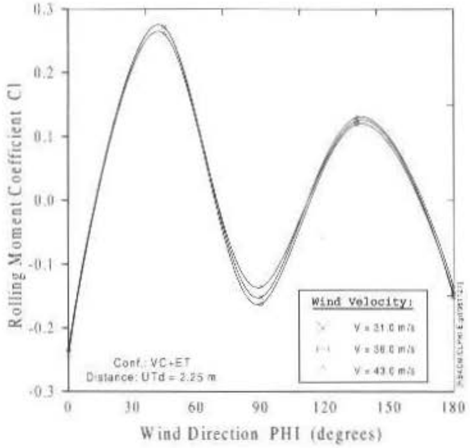

Fig. 6 Influence of wind velocity on roll moment

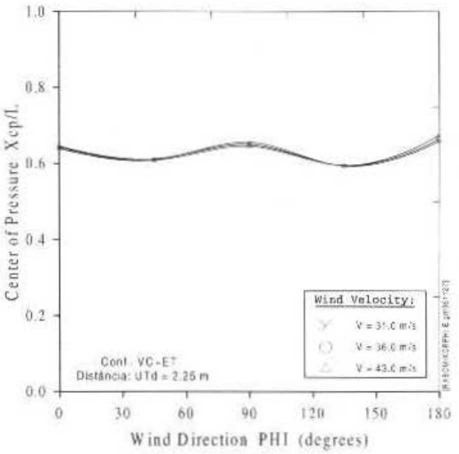

Fig. 7 Influence of wind velocity on center of pressure

Influence of wind direction

In order to investigate the influence exerted by the wind direction (azimuth) on the aerodynamic characteristics, the wind direction was varied between 0 and 180 degrees, firstly for the configuration without service tower. Figure 8 shows the results obtained.

It can be observed from Fig. 8 that the variations of the coefficients, due to variation of the wind direction, are within a band of accuracy of the measurement technique employed, or they are due to velocity variations or turbulence level of the flow in the test section of the wind-tunnel. It is also true, that the flow around the complex geometry under investigation makes possible the formation of vortices and their displacement, which are sometimes asymmetric (NASA, 1965). This conclusion may explain the variation of the measured data encountered for total symmetry of the configuration (see Cz for $\phi = 0$ °, 90° e 180°). Larger variations, in intervals of approximately 45°, are due to differences of the frontal shape of the configuration which is exposed to the wind.

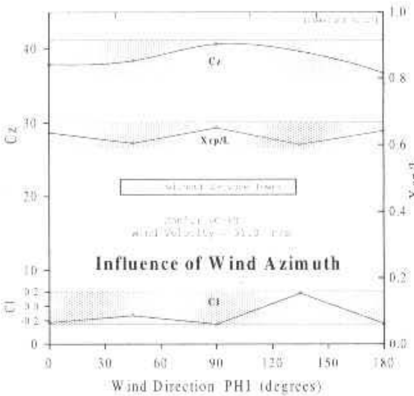

Fig. 8 Influence of wind direction without service tower

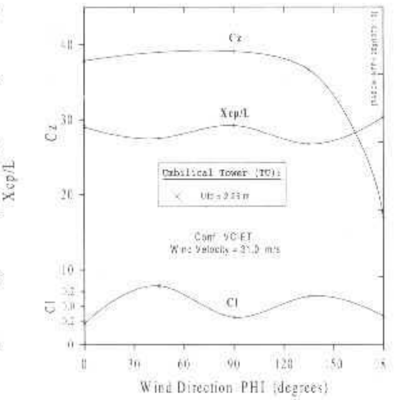

Fig. 9: Influence of wind direction with service tower

In Figure 9, the influence of the wind direction is now investigated, considering the presence of the service tower, Conf. VC+ET, for a given distance between the tower and the plane of the longitudinal axis of the central core, UTd = 0.15 m (real size = 2.25 m), and a wind velocity of 31.0 m/s. In this case, the influence on the coefficients of transversal force and rolling moment, is clearly stated, when the launch vehicle is positioned behind the service tower.

The roll moment coefficient also shows a variation when compared with the previous case for ϕ = 45°. However it presents the same value and direction for ϕ = 135°, and agrees again with the result obtained for the configuration without service tower.

Influence of the Service (Umbilical) Tower

The influence exerted by the presence of the service (umbilical) tower can be observed from Fig. 10. The umbilical tower is positioned by 180°, generating in this way a reduction on the coefficient of transversal force. This reduction is related to the fact that the whole assembly is in a region of strongly perturbated flow field (aerodynamic shadow of the tower). From the other side no influence can be observed on the roll moment coefficient and on the center of pressure.

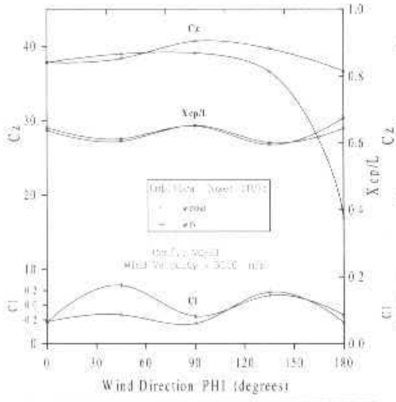

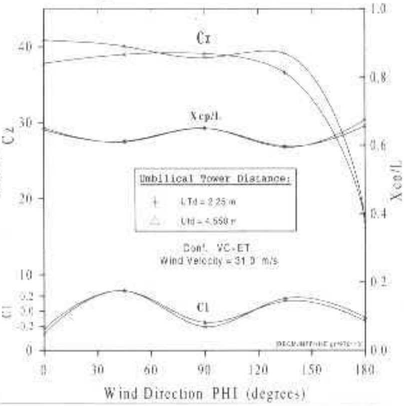

Fig. 10 Influence of service tower **Fig. 11 Influence of distance of service tower**

With respect to the distance between umbilical tower and vehicle (longitudinal axis plane), denoted by UTd, following tests were made: UTd = 0.15 m (2.25 m) and 0.30 m (4.50 m). Figure 10 shows that differences encountered for both situations are minimal. This allows to conclude that a variation of the distance, in the interval 0.15 m ≤ UTd ≤ 0.30 m, or 2.25 m ≤ UTd ≤ 4.50 m (real size), has only a very small influence on the coefficients of transversal forces, roll moment and center of pressure.

The final results for application in the simulation of the dynamics and attitude control of strap-on launch vehicles during lifting-off are presented in Table 1.

Table 1 Aerodynamic Coefficients of Strap-on Launch Vehicles During Lifting-off

VC + ET

Utd = 0.15 m	**V** (m/s)								
	31.0			36.0			43.0		
PHI	C_Z	C_l	Xcp/L	C_Z	C_l	Xcp/L	C_Z	C_l	Xcp/L
0	37.81	-0.2353	0.6460	39.75	-0.2457	0.6436	40.54	-0.2353	0.6395
45	38.99	0.2719	0.6122	39.53	0.2719	0.6091	39.50	0.2614	0.6097
90	39.11	-0.1516	0.6506	39.49	-0.1621	0.6460	37.63	-0.1359	0.6561
135	36.62	0.1307	0.5950	36.98	0.1203	0.5941	37.20	0.1255	0.5931
180	16.89	-0.1359	0.6753	17.41	-0.1464	0.6648	17.90	-0.1516	0.6594

Utd = 0.30 m	**V** (m/s)								
	31.0			36.0			43.0		
PHI	C_Z	C_l	Xcp/L	C_Z	C_l	Xcp/L	C_Z	C_l	Xcp/L
0	40.88	-0.3033	0.6520	39.91	-0.2457	0.6429	42.17	-0.2248	0.6449
45	40.07	0.2719	0.6107	39.98	0.1830	0.6067	39.85	0.1830	0.6096
90	38.55	-0.2091	0.6503	39.30	-0.2248	0.6463	39.78	-0.2196	0.6441
135	39.11	0.1673	0.5979	39.76	0.1621	0.5955	39.72	0.1778	0.5955
180	16.14	-0.0889	0.6573	16.45	-0.0889	0.6535	16.91	-0.1046	0.6456

VC - ET

	V (m/s)								
	31.0			36.0			43.0		
PHI	C_Z	C_l	Xcp/L	C_Z	C_l	Xcp/L	C_Z	C_l	Xcp/L
0	37.87	-0.2248	0.6378	40.39	-0.2457	0.6384	40.95	-0.2614	0.6371
45	38.36	-0.1307	0.6051	38.70	-0.1412	0.6030	38.94	-0.1307	0.6047
90	40.68	-0.2510	0.6522	39.83	-0.1987	0.6472	39.75	-0.2091	0.6395
135	39.68	0.1778	0.6010	40.12	0.1621	0.6000	40.30	0.1778	0.6005
180	36.67	-0.2405	0.6432	37.69	-0.2405	0.6425	38.69	-0.2353	0.6395

The data can be summarized for design purposes as follows:

PHI	**Cz**	**Cl**	**Xcp/L**
°	-	-	-
0	37.81	-0.2353	0.6460
45	38.99	+0.2719	0.6122
90	39.11	-0.1516	0.6506
135	36.62	+0.1307	0.5950
180	16.89	-0.1359	0.6753

assuming $V_{wind} = 10$ m/s and 2.25 m ≤ UTd ≤ 4.50 m

Due to the complexity of the investigated geometry and the interaction of the wind with the complex vehicle - tower - launch pad, and also considering the general local topography and that influence on the wind profile, variations of wind velocity and direction, it is strongly recommended to consider discrepancies of: CZ ±10%, Cl ±15%, Xcp/L ±1% . In order to consider dynamic effects due to wind gusts and vortex shedding, it is also recommended to compute an increase of approximately 50% on the steady load coefficients, particularly the drag coefficient.

Conclusions

Using results from an aerodynamic experimental investigation in a low speed wind tunnel, an analysis of the aerodynamic characteristics at lift-off of satellite launchers of strap-on configuration was performed. The complete configuration on the launch pad with and without the presence of a service tower was considered.

For the analysis, different wind intensities and directions were considered, and all steady aerodynamic characteristics were analyzed.

The results of the investigation have shown that the aerodynamic coefficients, transversal force and roll moment, are meanly influenced by the wind direction, while the influence of the wind velocity is of secondary order. The center of pressure could not be influenced by varying these variables.

The distance between umbilical tower and vehicle does not excert any influence on the aerodynamic coefficients, if this is varied in the interval 2.25 m $\leq$ UTd $\leq$ 4.50 m.

The results obtained in this investigation allow a better simulation of the dynamics and control system of such type of launch vehicles during their lifting-off.

Acknowledgement

The author would like to thank CNPq for the financial support given to this project.

References

Fung, Y. C., 1960, "Fluctuating lift and drag acting on a cylinder in a flow at supercritical Reynolds number", Journal of Aerospace Sciences, Vol. 27, 11, 801-813

Hanh, K.-U., 1989, "Effect of wind shear on flight safety", Progresss in Aerospace Sciences, Vol. 26, 225-259

Hoerner, S. F., 1965, "Fluid Dynamic Drag", (Published by author: 148 Busteed Dr., Midland Park, N. J., USA, 1965)

NASA SP-8008, 1965, "Prelaunch Ground Wind Loads", NASA Space Vehicle Design Criteria

Moraes, P. Jr., 1996, "VLS, Aerodinâmica de Decolagem", Anais do VI Encontro Nacional de Ciências Térmicas, Vol. I, pp. 55, Florianópolis-SC

Moraes, P., Jr.; Neto, Adriano A., 1988, "Ensaios Aerodinâmicos de Simulação da Decolagem do VLS", Relatório Interno, Subdivisão de Aerodinâmica, CTA/IAE/ASE, São José dos Campos-SP

Roshko, A., 1955, "The wake and drag of bluff bodies", Journal of the Aeronautical Sciences, Feb 1955, 124-132

Roshko, A., 1960, "Experiments on the flow past a circular cylinder at very high Reynolds number", Journal of Fluid Mechanics, 10, 345-356

RBCM - J. of the Braz. Soc. Mechanical Sciences
Vol. XXI - No.2 - 1998 - pp. 279-293

ISSN 0100-7386
Printed in Brazil

On the Use of CFD Methods in the Design of Transonic Wind Tunnel Nozzles

Nide Geraldo do Couto Ramos Fico Jr.
João Luiz Filgueiras de Azevedo
Marcos Aurélio Ortega
CTA/IAE/ASE-N
12228-904 São José dos Campos, SP Brazil
azevedo@iae.cta.br

Abstract

A numerical investigation of the flowfield in three proposed geometries for the nozzle and contraction of a transonic wind tunnel facility is performed. The primary objective was to understand details of the flow in the tunnel in order to try to maximize test section flow quality. The calculations presented here include preliminary 2-D simulations and full 3-D computations. The codes used for the present calculations were previously validated by the authors and co-workers, and these validation studies are available in the literature. The primary flow solvers implement an Euler formulation, and use the Beam and Warming implicit approximate factorization algorithm for the solution of the discretized equations. A boundary layer code was typically run at a post-processing stage in order to estimate boundary layer growth and its impact on flow quality. Results obtained for a sonic nozzle and for two Laval nozzles are presented, and they were instrumental in the selection process which led to the transonic facility which is currently being built.

***Keywords**: Transonic Nozzle Flow, Transonic Wind Tunnel, CFD Methods, Tunnel Design.*

Introduction

Transonic wind tunnels usually operate from low subsonic Mach numbers ($M \cong 0.25$) to the supersonic regime ($M \cong 1.6$). The tunnel nozzle is a key element in achieving the desired test-section Mach number, M_{TS}. Mach numbers up to unity are obtained using a sonic nozzle. There are two possible solutions for M_{TS} above this value: (*i*) the installation of a flexible Laval nozzle or (*ii*) a sonic nozzle used in conjunction with test-section mass extraction. In the case of test-section evacuation, the amount of mass extraction varies with M_{TS}, being around 2.5% of the tunnel total mass flow. The extracted mass enters the plenum chamber, which surrounds the test section, and it re-enters the tunnel closed circuit at an appropriate location downstream of the test section. While the first option is mechanically complex and much more expensive, it yields better test-section flow quality than the second one. Moreover, the second option is also limited to $M_{TS} \leq 1.3$, since above this test section Mach number value the mass extraction needed is prohibitive as it would demand very large auxiliary compressors and it would also have an adverse impact upon the tunnel flow quality. The authors refer to flow quality here in the sense that M_{TS} should be constant along the complete test section length. Anything that disrupts such behavior is having a negative impact on the tunnel flow quality.

Centro Técnico Aeroespacial (CTA) is designing a large transonic wind tunnel facility with a 2.0 x 2.4 *m* test section (TTS Project). To minimize the technical risks involved in such an enterprise, the project's first phase consists of the construction and operation of a pilot facility (TTP). Among the many important points to be checked in the TTP emerges the nozzle design. The design of the nozzle is of utmost importance as it is directly related to the flow quality at the test section. On the other hand, Computational Fluid Dynamics (CFD) methods are enjoying increasing application assisting in the selection of tunnel airline component geometry (Davis et al., 1986). These techniques have been used to design diffusers and flexible nozzles as well as investigate other aspects of the tunnel flow. Therefore, the major objective of the present work is to study, using CFD techniques, three possible nozzles for the TTP. One of them is a sonic nozzle, and the other two are Laval nozzles with a nominal Mach number of 1.3. It was decided that, in the TTP context, the optimum choice for the nozzle element would be to have fixed interchangeable nozzle blocks, instead of the flexible nozzle planned for the full size facility.

The calculations presented here include preliminary 2-D simulations and full 3-D computations. The codes used for the present calculations were previously validated by the authors and co-workers, and these validation studies are available in the literature (see, for instance, Azevedo, 1988, 1990, 1992, Azevedo, Zdravistch and Silva, 1991, Ortega and Azevedo, 1991, Azevedo et al., 1992, and Azevedo, Fico and Ortega, 1995). Both for the 2-D and the 3-D case, an Euler formulation is implemented in the codes, and the Beam and Warming implicit approximate factorization algorithm (Beam and Warming, 1976, 1978, and Pulliam and Steger, 1980) is used to discretize and solve the governing equations. The

Manuscript received: January 1997; revision received: January 1998. Technical Editor: Leonardo Goldstein Jr.

implicit Euler method is used for the time march and central differences are used to discretize the space derivatives. Artificial dissipation terms are explicitly added in order to control nonlinear instabilities. Considerable effort was invested in the accurate implementation of entrance and exit boundary conditions through the use of one-dimensional characteristic relations (Fico, 1991, Azevedo et al., 1992, and Azevedo, Fico and Ortega, 1995). The most stringent requirement for a tunnel nozzle, besides giving the desired test section Mach number, is the quality of the flow it provides for the test section. Therefore, the consideration of boundary layer growth is also an important issue in this case. Here, for the 3-D simulations, this is taken into account by a viscous-inviscid coupling. A boundary layer formulation, solved in the direct mode, is implemented and coupled to the 3-D Euler solver previously described. The boundary layer code was typically run at a post-processing stage in order to estimate boundary layer growth and its impact on flow quality.

The present work will briefly describe the formulation of the codes used and it will concentrate on the discussion of the results for the nozzle geometries considered. The authors are particularly interested in evaluating whether the nozzles can indeed produce the desired test section Mach number and on the quality of the flow provided by the contraction to the test section. On the latter subject, the existence, or not, of any shocks produced by the nozzle wall, and the amount of boundary layer growth and flow skewness at the test section entrance are of primary interest.

Theoretical Formulation

The compressible Euler equations can be written in strong conservation-law form for general, three-dimensional, body-conforming, curvilinear coordinates (Pulliam and Steger, 1980) as

$$\frac{\partial \overline{Q}}{\partial \tau} + \frac{\partial \overline{E}}{\partial \xi} + \frac{\partial \overline{F}}{\partial \eta} + \frac{\partial \overline{G}}{\partial \zeta} = 0, \tag{1}$$

where the vector of conserved quantities, $\overline{Q}$, is defined as

$$\overline{Q} = J^{-1} \begin{Bmatrix} \rho \\ \rho u \\ \rho v \\ \rho w \\ e \end{Bmatrix}. \tag{2}$$

The flux vectors $\overline{E}$, $\overline{F}$ and $\overline{G}$ can be written as

$$\overline{E} = J^{-1} \begin{Bmatrix} \rho U \\ \rho u U + p\xi_x \\ \rho v U + p\xi_y \\ \rho w U + p\xi_z \\ (e+p)U - p\xi_t \end{Bmatrix}, \tag{3}$$

$$\overline{F} = J^{-1} \begin{Bmatrix} \rho V \\ \rho u V + p\eta_x \\ \rho v V + p\eta_y \\ \rho w V + p\eta_z \\ (e+p)V - p\eta_t \end{Bmatrix}, \tag{4}$$

$$\overline{G} = J^{-1} \begin{Bmatrix} \rho W \\ \rho u W + p\zeta_x \\ \rho v W + p\zeta_y \\ \rho w W + p\zeta_z \\ (e+p)W - p\zeta_t \end{Bmatrix}. \tag{5}$$

In the above equations, the usual nomenclature is being used. Therefore, ρ is the density, u, v and w are the Cartesian components of velocity, and e is the total energy per unit of volume. The equations have been nondimensionalized following the work of Azevedo (1990). Hence, density is made dimensionless with respect to the stagnation density at the nozzle entrance conditions, ρ_t, and velocity components are referred to the critical speed of sound at the nozzle entrance conditions, a_*. Pressure and total energy per unit of volume are referred to $\rho_t a_*^2$ and the specific internal energy is nondimensionalized with respect to a_*^2.

The pressure, p, can be obtained by the equation of state for perfect gases

$$p = (\gamma - 1)\rho e_i = (\gamma - 1)\left[e - \frac{1}{2}\rho\,(u^2 + v^2 + w^2)\right], \tag{6}$$

where e_i is the specific internal energy of the fluid, and γ is the ratio of specific heats. The contravariant velocity components are defined as

$$\begin{aligned} U &= \xi_t + \xi_x u + \xi_y v + \xi_z w, \\ V &= \eta_t + \eta_x u + \eta_y v + \eta_z w, \\ W &= \zeta_t + \zeta_x u + \zeta_y v + \zeta_z w. \end{aligned} \tag{7}$$

Throughout this work, the Cartesian coordinate system is defined such that x is the direction along the axis of the tunnel, positive from upstream to downstream, and the y- and z-directions form a right-handed system with z positive upwards. The curvilinear coordinate system is defined such that ξ is the longitudinal direction, η is the nominally wall-normal direction which spans the tunnel from the centerline to the wall, and ζ is the circumferential direction. This coordinate system is obtained from the transformation of variables

$$\begin{aligned} \tau &= t, \\ \xi &= \xi\,(x, y, z, t), \\ \eta &= \eta\,(x, y, z, t), \\ \zeta &= \zeta\,(x, y, z, t). \end{aligned} \tag{8}$$

The Jacobian of the transformation, J, can be expressed as

$$\begin{aligned} J = (\, & x_\xi y_\eta z_\zeta + x_\eta y_\zeta z_\xi + x_\zeta y_\xi z_\eta \\ & - x_\xi y_\zeta z_\eta - x_\eta y_\xi z_\zeta - x_\zeta y_\eta z_\xi \,)^{-1}. \end{aligned} \tag{9}$$

Expressions for the various metric relations can be found, among other references, in Pulliam and Steger (1980, 1985).

The 2-D formulation is a straightforward simplification of the previously given equations in which one of the coordinate directions is considered infinite. We have considered the geometry of the tunnel vertical plane that passes through the tunnel centerline for the present 2-D simulations. More details of the 2-D formulation can be seen, for instance, in Azevedo (1990), Ortega and Azevedo (1991), and Azevedo, Fico and Ortega (1995). The effective flow displacement due to viscous effects close to solid walls was predicted by a boundary layer code developed by Rotta (1971). This is a direct-type, integral method, with the following main capabilities: (*i*) prediction of laminar and/or turbulent boundary layers; (*ii*) two laminar-turbulent transition criteria; (*iii*) appropriate treatment of shock wave interaction with the boundary layer.

Numerical Implementation

The previously given governing equations were implemented through the use of finite difference methods. The implicit Euler method was used for the time-march, and the spatial derivatives were approximated by three-point, second order central differences. The Beam and Warming implicit approximate factorization scheme (Beam and Warming, 1976, 1978) was used for the solution of the resulting finite difference equations in order to obtain a cost efficient algorithm. The resulting scheme is second order accurate in space, as mentioned, but it is only first order accurate in time due to the use of the implicit Euler method.

The factored finite difference equations can be written in the delta form as (Azevedo, 1988)

$$L_\eta L_\zeta L_\xi \Delta_t \overline{Q}^n = R_\xi + R_\eta + R_\zeta \, . \tag{10}$$

The various operators are defined as

$$\begin{aligned}
L_\xi &= (I + \Delta t \delta_\xi \hat{A}^n - \epsilon_I \, \Delta t J^{-1} \nabla_\xi \Delta_\xi J), \\
L_\eta &= (I + \Delta t \delta_\eta \hat{B}^n - \epsilon_I \, \Delta t J^{-1} \nabla_\eta \Delta_\eta J), \\
L_\zeta &= (I + \Delta t \delta_\zeta \hat{C}^n - \epsilon_I \, \Delta t J^{-1} \nabla_\zeta \Delta_\zeta J), \\
R_\xi &= - \Delta t \delta_\xi \overline{E}^n - \epsilon_E \, \Delta t J^{-1} (\nabla_\xi \Delta_\xi)^2 J \overline{Q}^n , \\
R_\eta &= - \Delta t \delta_\eta \overline{F}^n - \epsilon_E \, \Delta t J^{-1} (\nabla_\eta \Delta_\eta)^2 J \overline{Q}^n , \\
R_\zeta &= - \Delta t \delta_\zeta \overline{G}^n - \epsilon_E \, \Delta t J^{-1} (\nabla_\zeta \Delta_\zeta)^2 J \overline{Q}^n .
\end{aligned} \tag{11}$$

In the above, δ_ξ, δ_η and δ_ζ are central difference operators; ∇_ξ, ∇_η and ∇_ζ are backward difference operators; and Δ_ξ, Δ_η and Δ_ζ are forward difference operators in the ξ−, η- and ζ−directions, respectively. As an example,

$$\begin{aligned}
\delta_\xi \overline{Q}^n_{i,j,k} &= \frac{1}{2} \left[\overline{Q}^n_{i+1,j,k} - \overline{Q}^n_{i-1,j,k} \right], \\
\nabla_\xi \overline{Q}^n_{i,j,k} &= \overline{Q}^n_{i,j,k} - \overline{Q}^n_{i-1,j,k} \, , \\
\Delta_\xi \overline{Q}^n_{i,j,k} &= \overline{Q}^n_{i+1,j,k} - \overline{Q}^n_{i,j,k} \, .
\end{aligned} \tag{12}$$

The Δ_t is a forward difference operator in time given by

$$\Delta_t \overline{Q}^n = \overline{Q}^{n+1} - \overline{Q}^n . \tag{13}$$

Artificial dissipation terms have been introduced in the operators described by Eq. (11) in order to maintain the stability of the numerical solution process. Fourth order numerical dissipation terms were added to the right-hand side operators, and second order terms were used in the left-hand side operators. From a consistency and practical stability limit standpoint, one would like to also use fourth order artificial dissipation in the implicit operators. However, computational efficiency constraints prevent such use. The flux Jacobian matrices $\hat{A}^n$, $\hat{B}^n$ and $\hat{C}^n$ are described in detail elsewhere in the literature (see, for instance, Pulliam and Steger, 1985).

Boundary Conditions

The three-dimensional simulations here presented take advantage of the double geometric symmetry existing in the nozzles considered in order to reduce the computational effort. Hence, only one-quarter of the complete nozzles are represented, and flow symmetry boundary conditions are enforced at both the vertical and horizontal symmetry planes. This is clearly assuming that flow conditions at the entrance of the computational domain are symmetric or, in other words, that the flow velocity at the entrance of the contraction is aligned with the tunnel axis. Such an assumption does represent a simplification in the sense that some misalignment can certainly occur, especially for closed circuit tunnels. In the present case, we have decided to neglect this effect mainly due to computational power limitations and because the original planning considered to operate the TTP as an open facility in the first stages of its calibration tests. Moreover, one must also recognize that a well-designed settling chamber will minimize these misalignment problems. The symmetry boundary conditions are computationally enforced by allowing for an extra plane of grid points on the other side of the symmetry plane and forcing the appropriate symmetry, or anti-symmetry, of the conserved variables. Hence, boundary conditions in the ζ-direction are always symmetry, or reflection, conditions in the present case.

Due to the present code data structure, it is very difficult to strongly impose the flow tangency condition at the wall, at least at the boundary condition enforcement stage. Hence, the wall boundary condition is implemented by extrapolating all conserved variables from the computational surface adjacent to the wall, when explicitly enforcing the boundary conditions, and by imposing a zero convective flux in the wall normal direction in the residue computation. The reader should observe that, with such an scheme, the residue calculation sees the exact wall boundary condition at every time step, whereas the value of the conserved variables at the wall is progressively improved, as convergence is advanced, in order to reflect the correct flow tangency condition. Nozzle axis boundary condition is also implemented by extrapolation and by imposing a no-flux condition across the axis. A further complication arises in this case because the axis is a singularity of the transformation, in the sense that a line in physical space corresponds to a full plane in computational space. Hence, properties at a given point along the axis are obtained by extrapolating from the adjacent point (in the η-direction) and, then, averaging all values in the ζ-direction. The residue calculation is also modified in the centerline case in order to enforce the no-flux condition across the centerline.

Nozzle entrance and exit conditions are enforced using the concept of one-dimensional characteristic relations for the Euler equations. The concept is described in the 2-D case by Mac Cormack (1984). Complete details for its implementation in two dimensions for both the planar and the axisymmetric case are described by Azevedo, Fico and Ortega (1995). The present three-dimensional computations have used these ideas in order to define how many quantities should be specified at each boundary and how many should be extrapolated from interior information. However, in order to simplify the implementation, the actual extrapolation process (of whatever quantities should be extrapolated) does not use the characteristic relations but simple zero-th order extrapolation. As the authors have also used in previous work (Azevedo et al., 1992), the stagnation pressure, the stagnation temperature and the flow entrance angle are specified at a subsonic entrance. The exit static pressure is fixed at a subsonic exit and, as determined by a characteristic relation analysis, no property can be specified at a supersonic exit. Aside from the fact that zero-th order extrapolation is being used for the actual extrapolation process, the treatment of entrance and exit conditions here is an exact extension to3-D of the ideas discussed in Azevedo (1990), Azevedo et al. (1992), and Azevedo, Fico and Ortega (1995), and the interested reader is referred to these references for further details.

All boundary conditions in the two-dimensional simulations were treated precisely as presented in the previously cited references, and they will not be further discussed here.

Results and Discussion

Initial evaluation of the proposed nozzles was performed using a two-dimensional formulation. It is clear that the flowfield in the nozzles considered in the present work is truly 3-D. However, these initial 2-D calculations already pointed out some of the difficulties associated with obtaining high test section flow quality. A typical grid used for the 2-D simulations is presented in Fig. 1. This particular configuration corresponds to one of the proposed Laval nozzles, and the grid shown has 94 x 59 grid points. The 2-D grids were generated by algebraic methods and exponential grid stretching functions were used in order to cluster grid points towards the nozzle wall, in the η-direction. Although not shown in Fig. 1, some of the grids used also considered some grid clustering towards the throat in the ξ-direction. The wall contours for all three nozzles treated in the present 2-D simulations are shown in Fig. 2.

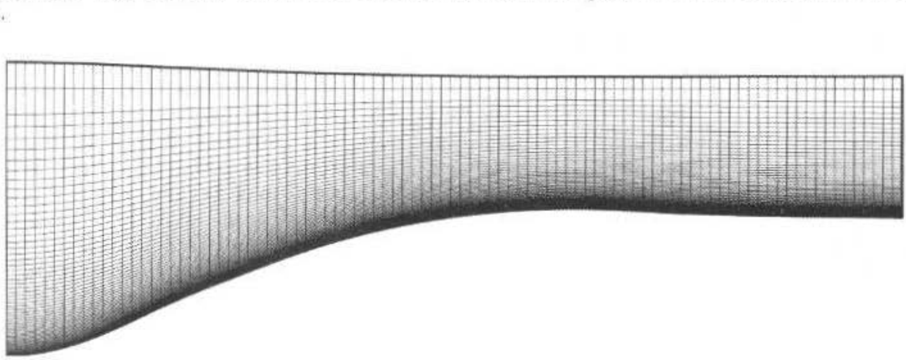

Fig. 1 View of a typical 2-D computational grid

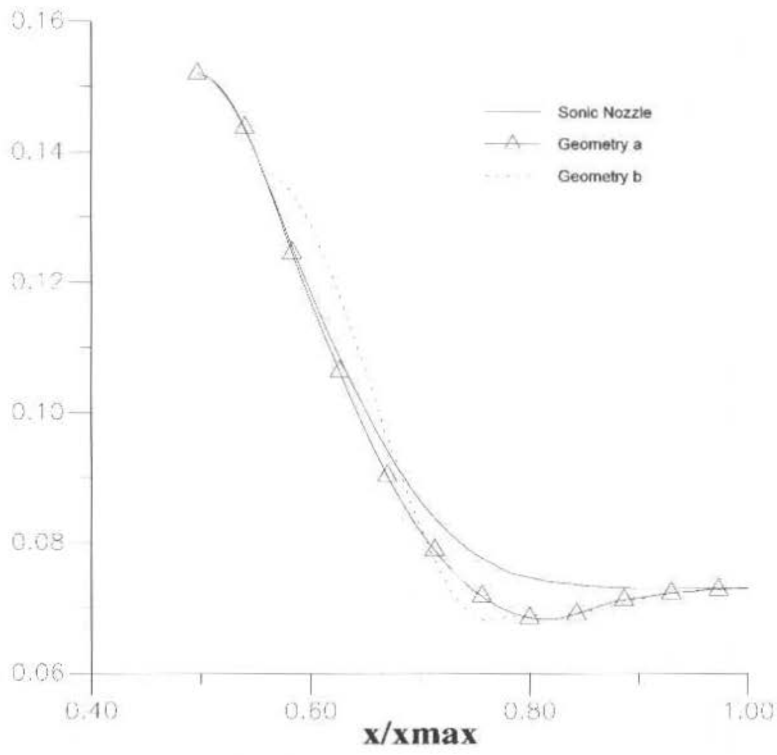

Fig. 2 2-D wall geometry for the sonic and the two Laval nozzles (the latter are indicated as geometries *a* and *b*)

The authors point out that the specific definition of the three geometries considered in the present simulations is beyond the scope of the present work. These geometries, both for the sonic and the two Laval nozzles, were determined by the TTS Project team and, then, given to the present authors for analysis. The authors are not fully aware of the procedures used by the TTS team to arrive at these configurations and, moreover, such information is part of project sensitive data which is not available in public domain.

An example of the type of results which can be obtained with the 2-D calculations can be seen in Fig. 3. This figure presents wall pressure distributions along the longitudinal direction for the two Laval nozzles, with a nominal test section Mach number of 1.3, and for the sonic nozzle, with a nominal test section Mach number of 0.6. It is clear from this figure that the much gentler expansion associated with geometry *a* yields compression waves that are weaker than those generated by geometry *b*. Compression waves at the nozzle should be avoided because they introduce undesirable disturbances at the test section. The wall pressure distributions for the sonic nozzle at the nominal test section Mach number of 0.6, also shown in Fig. 3, reproduce very well the expected behavior for this entirely subsonic case. In such a situation, the flow expands in the convergent section of the nozzle, but it does become sonic at the throat. As a result, there is no further expansion at the divergent section. In this particular case, since the geometry is tailored to yield a sonic flow at the entrance of the tunnel test section (which is the exit of the present computational domain), the so-called "divergent section" is almost straight. Therefore, the pressure should be constant in this region, as Fig. 3 is corretly indicating.

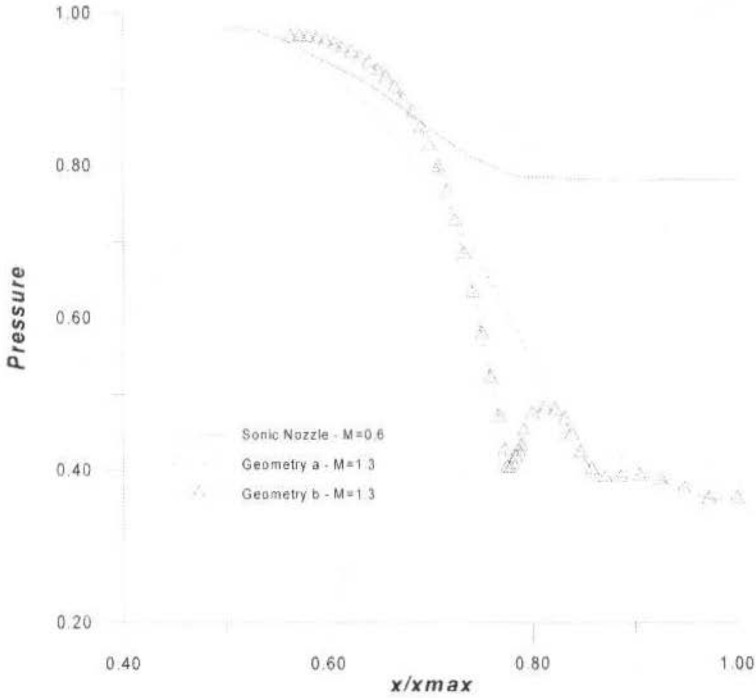

Fig. 3 Wall pressure distribution in the streamwise direction for the sonic nozzle and the two Laval nozzles (2-D simulation)

Further understanding of these results can be obtained from Fig. 4 which shows the wall Mach number distributions for the two Laval nozzles. Again, the strong shock present in geometry *b* is evident in this figure. According to the results shown in Figs. 3 and 4, geometry *a* is clearly a better nozzle candidate than geometry *b* for the $M_{TS} = 1.3$ case. Figure 4 also presents some effect of the grid refinement studies which were performed for these two nozzle configurations. The results are indicating that, especially for geometry *b*, the resolution obtained with the coarser mesh is poor and a finer computational grid is required. The effect is not so dramatic for geometry *a*, but one can still see some differences between coarse and fine grid results. For both geometries, however, the use of the finer grids is recommended, based on the results shown in Fig. 4. Incidentally, the corresponding finer grids were the ones used for the calculation of the pressure results indicated in Fig. 3.

The 3-D calculations were performed using 100 x 20 x 29 mesh points. Fig. 5 shows an overall view of a typical computational grid used in this work. The 3-D grids were also generated by algebraic methods, after the wall surface definition was provided by a CAD system. Particular attention was dedicated to obtain a detailed definition of the transition from the circular entrance section to the quadrilateral geometry of the throat and downstream regions. It should be noted that the present work takes advantage of the nozzle double symmetry in order to reduce computational costs.

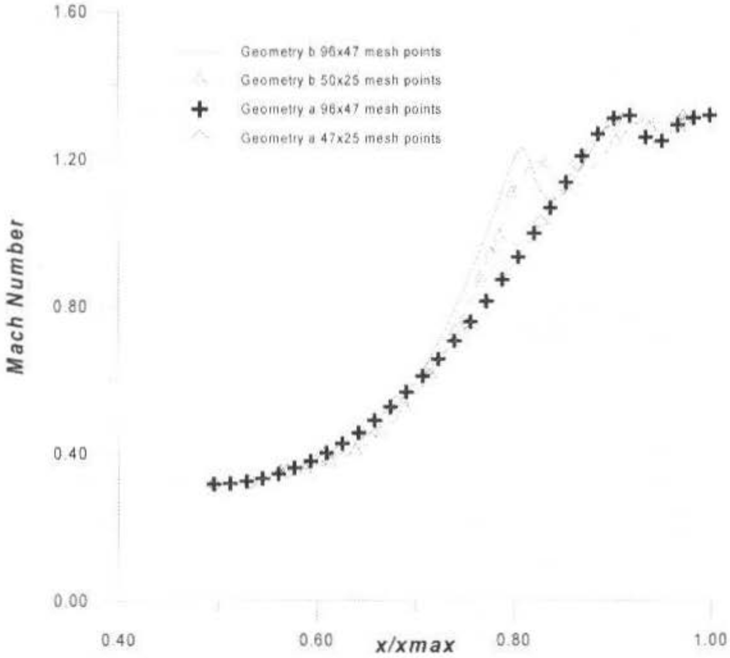

Fig. 4 **Wall Mach number distribution in the streamwise direction for the two Laval nozzles (2-D simulation)**

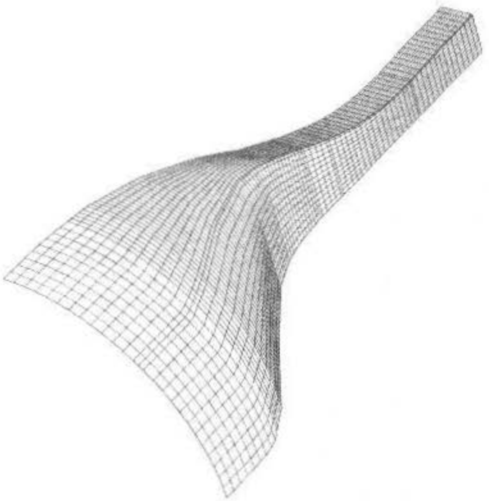

Fig. 5 **View of a typical 3-D computational grid**

The Mach number contours at planes perpendicular to the streamwise direction are shown in Figs. 6 and 7, for geometries *a* and *b*, respectively. These four planes correspond to $i=1$ (entrance plane), two interior planes $i=25$ and 75 and $i=100$ (exit plane). The misleading impression of a very non-uniform behavior rapidly disappears as one takes a closer look at the values shown by the graphic scales. These are indicating that the differences in the Mach number within each section are of the order of 10^{-3} or 10^{-4} for the more upstream sections (planes *i*=1 and *i*=25) on both cases. The different contour colors appear simply because the post-processing package used automatically assigns different colors when it detects any differences in the property values regardless of the legend used for the plot. Therefore, in fact, both Laval nozzles have a very smooth Mach number distribution at planes along their longitudional axis. Geometry *a* has the additional advantage of producing at its exit plane a very uniform flow at the nozzle nominal Mach number of 1.3.

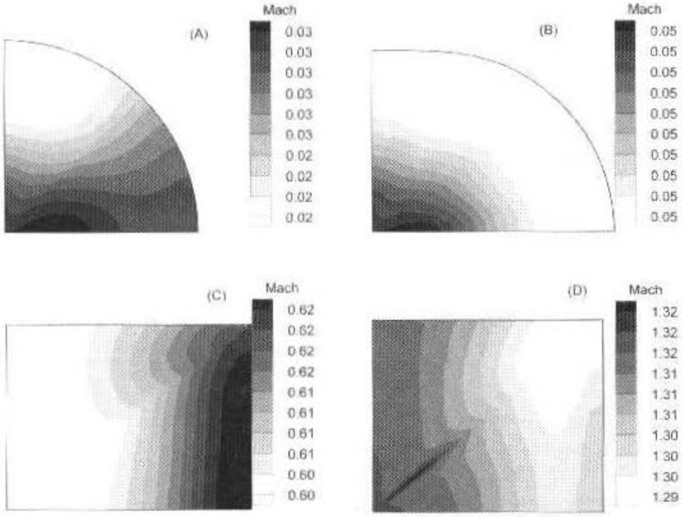

Fig. 6 **Mach number countours at planes perpendicular to the nozzle axis for geometry *a*, nominal M_{TS}=1.3.** (A) **Plane *i*=1,** (B) **Plane *i*=25,** (C) **Plane *i*=75, and** (D) **Plane *i*=100**

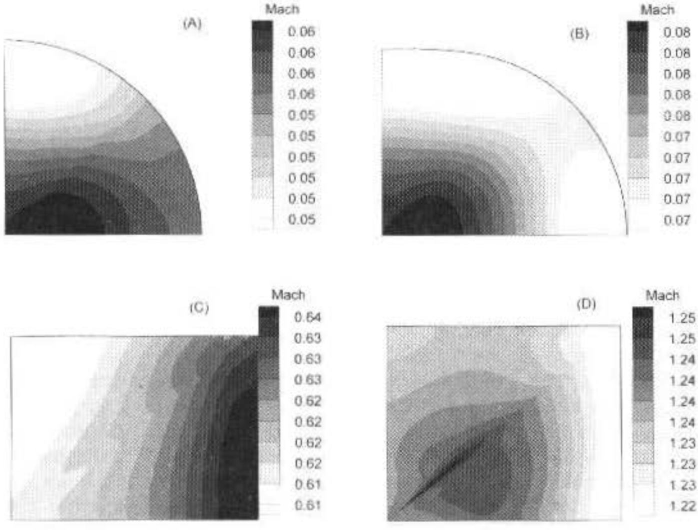

Fig. 7 **Mach number countours at planes perpendicular to the nozzle axis for geometry *b*, nominal M_{TS}=1.3.** (A) **Plane *i*=1,** (B) **Plane *i*=25,** (C) **Plane *i*=75, and** (D) **Plane *i*=100**

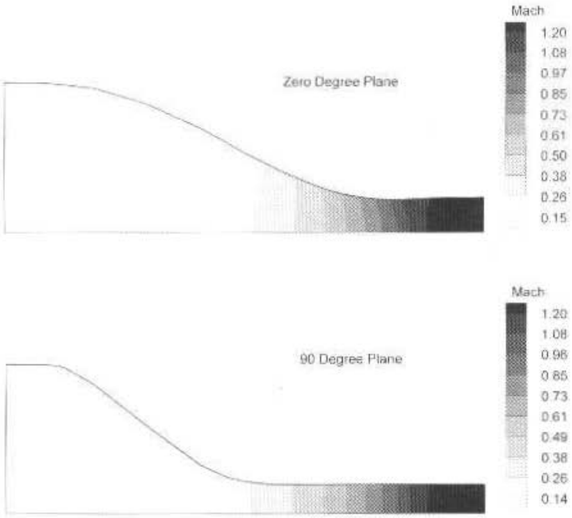

Fig. 8 Mach number contours at the symmetry planes for geometry *a*, nominal M_{TS}=1.3

Other relevant results for the same cases are plotted in Figs. 8 and 9. They show Mach number contours at the nozzle symmetry planes for geometry *a* and geometry *b*, respectively. The upper portion of both figures represent the plane $\theta = 0$ deg (horizontal plane), while at the lower part the Mach number contours for the plane $\theta = 90$ deg (vertical plane) appear. Contrary to the 2-D results (see Figs. 3 and 4) in which shock waves appeared in both geometries, the 3-D solution indicates a gentle expansion. The Mach lines in both cases are now fairly straight and extend themselves in the radial direction. It appears that the presence of the side walls, not accounted for in the 2-D case, helps guiding the flow more smoothly throught the nozzle. Moreover, the 90 deg-plane pressure distributions along both nozzles are shown in Figs. 10 and 11. For both Figs. 10 and 11, results for the nozzle wall and nozzle centerline are presented. The authors emphasize that, unlike the 2-D results, the 3-D solutions are indicating a monotonic behavior in the sense that no shock waves are present in these cases. This is in sharp contrast with the 2-D solutions shown in Figs. 3 and 4, as already pointed out. The behavior observed in the 3-D case is highly desirable as shock waves would have a tendency to "bump around" introducing flow disturbances at the test section.

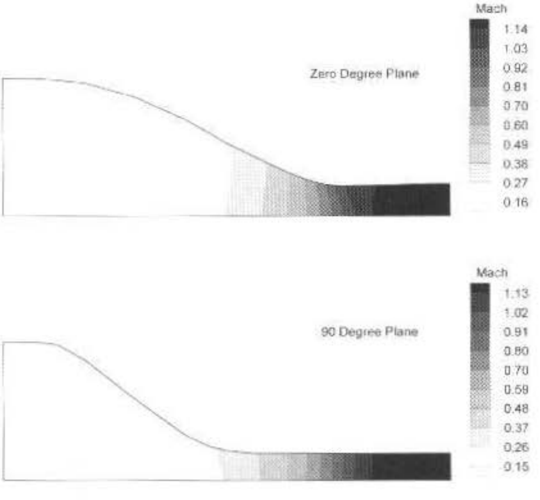

Fig. 9 Mach number contours at the symmetry planes for geometry *b*, nominal M_{TS}=1.3

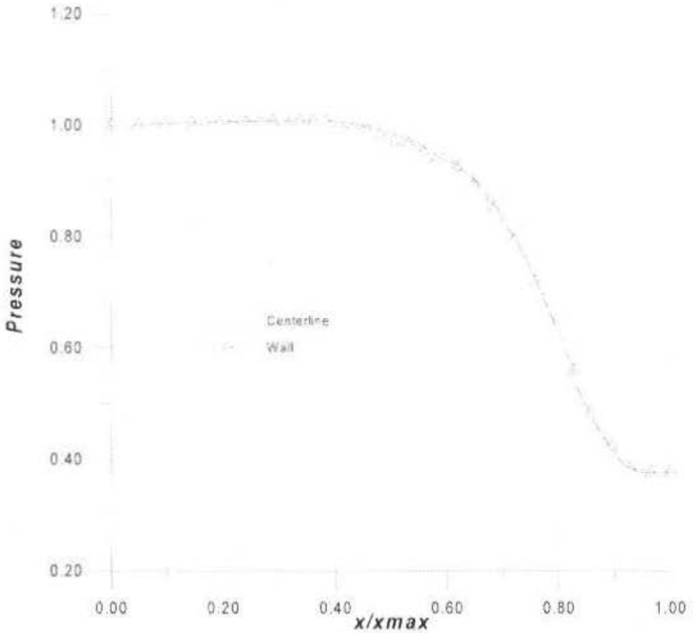

Fig. 10 Dimensionless pressure distribution in the streamwise direction for geometry *a*, nominal M_{TS}=1.3, 90 deg symmetry plane (3-D simulation). Pressure values are made dimensionless by the stagnation pressure at the entrance station

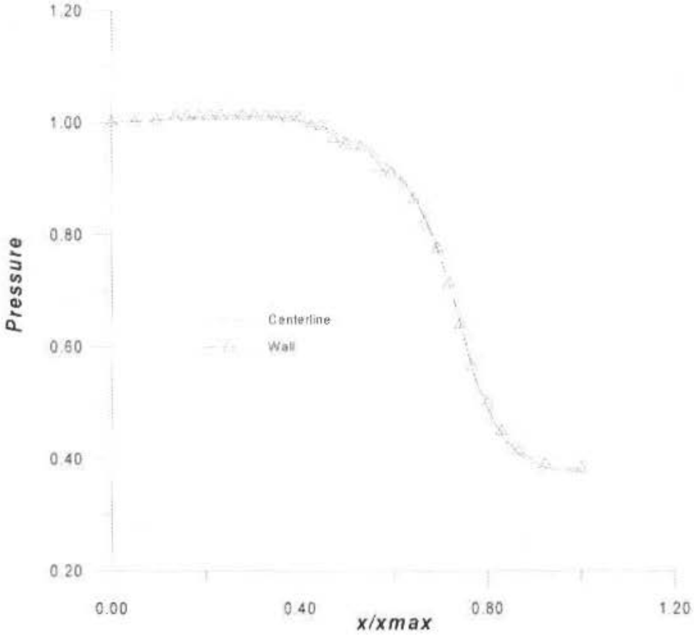

Fig. 11 Dimensionless pressure distribution in the streamwise direction for geometry *b*, nominal M_{TS}=1.3, 90 deg symmetry plane (3-D simulation). Pressure values are made dimensionless by the stagnation pressure at the entrance station

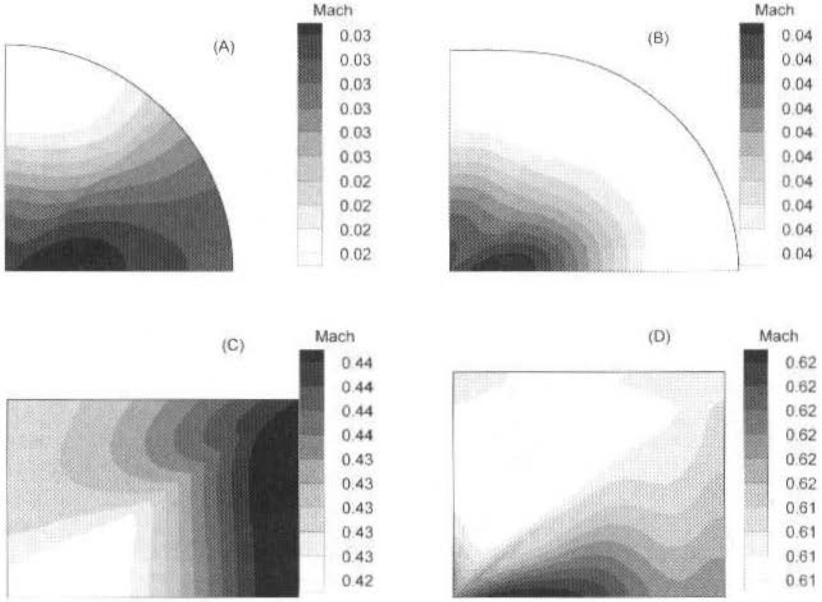

Fig. 12 **Mach number countours at planes perpendicular to the nozzle axis for the sonic nozzle, nominal M_{TS}=0.6.** (A) **Plane *i*=1,** (B) **Plane *i*=25,** (C) **Plane *i*=75, and** (D) **Plane *i*=100**

The sonic nozzle is responsible for feeding the test section with flow with Mach numbers up to 1.2. As usual in wind tunnel operation, low supersonic speeds are obtained with sonic nozzles plus test section mass extraction (Goethert, 1961). As an example of the flow quality that might be expected from the sonic nozzle simulated here, results for nominal test section Mach numbers of 0.6 and 1.0 are presented. Mach number contours in planes normal to the nozzle axis are shown in Fig. 12 for the M_{TS}=0.6 case. Mach number contours at both horizontal and vertical symmetry planes are shown in Fig. 13 for the same case. Corresponding results for the M_{TS}=1.0 case are shown in Figs. 14 and 15, respectively.

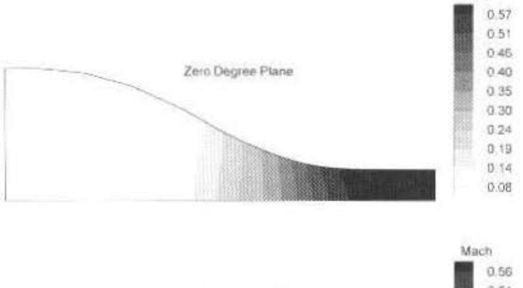

Fig. 13 Mach number contours at the nozzle symmetry planes, nominal M_{TS}=0.6

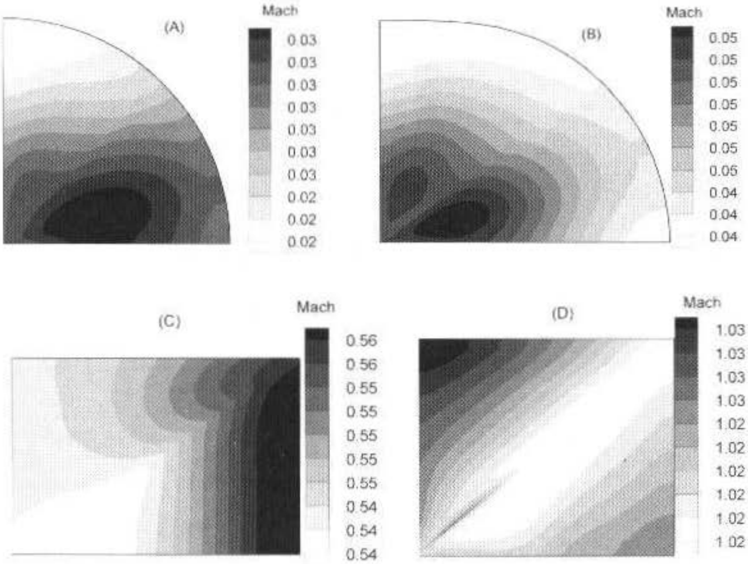

Fig. 14 **Mach number countours at planes perpendicular to the nozzle axis for the sonic nozzle, nominal M_{TS}=1.0.** (A) **Plane** *i*=**1,** (B) **Plane** *i*=**25,** (C) **Plane** *i*=**75, and** (D) **Plane** *i*=**100**

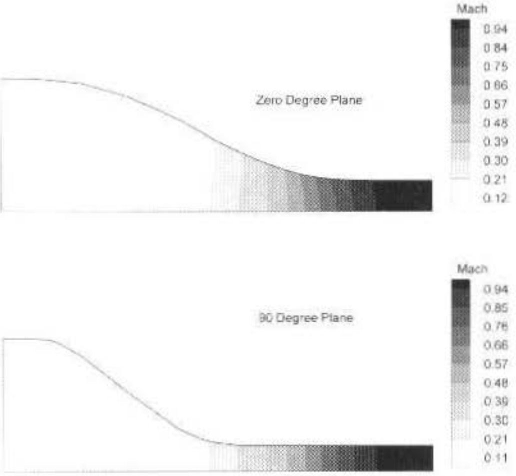

Fig. 15 **Mach number contours at the nozzle symmetry planes, nominal M_{TS}=1.0**

The pressure distributions for the Laval nozzles obtained through the solution of the 3-D Euler equations were used as input for a boundary-layer solver (Rotta, 1971). The results appearing in Table 1 are for the symmetry planes ($\theta = 0$ and 90 deg) and for the $\theta = 45$ deg plane. Geometry *a* shows a smaller value of the boundary-layer thickness, δ, at the the nozzle exit than geometry *b*. Further, its azimutal variation of δ is smaller. These two aspects are important when one remembers that the test-section walls must be diverged by a small angle to compensate for boundary-layer growth. The results indicate that geometry *a* demands less and more uniform wall divergence and, therefore, proves once more to be superior than geometry *b* as a nozzle candidate.

Table 1 Boundary-layer thickness at the exit plane for both Laval nozzle

θ plane	δ (mm)	
	Geometry *a*	Geometry *b*
0	4.66	5.84
45	4.65	5.67
90	4.52	5.43

Conclusions Remarks

In summary, the present work has used CFD techniques to perform 2-D and 3-D simulations of transonic wind tunnel nozzles. The flow was modeled with the aid of the Euler equations. In order to study the main viscous effects, in particular boundary-layer thickness at the test section entrance, the 3-D results were, then, used as input to a boundary-layer solver (Rotta, 1971). The full 3-D calculations seem to corroborate the earlier 2-D results in the sense that they point to geometry *a* as being a better nozzle candidate. The sonic nozzle studied proved to be able to give high-quality test section flow. These simulations are being used in an actual design environment in order to aid in the selection of appropriate nozzle geometries to equip the TTP facility which is currently being constructed.

Acknowledgements

The authors gratefully acknowledge that the present work has received partial support from Conselho Nacional de Desenvolvimento Científico e Tecnológico, CNPq, under the Integrated Project Research Grants No. 530109/93-0 and 522413/96-0.

References

Azevedo, J.L.F., 1988, "Aerodynamic Flow Simulation Using a Finite Difference Method," Proceedings of the 2nd National Meeting of the Thermal Sciences -- ENCIT 88, Águas de Lindóia, SP, pp. 3-6.

Azevedo, J.L.F., 1990, "Euler Solutions of Transonic Nozzle Flows," Proceedings of the 3rd Brazilian Thermal Sciences Meeting -- ENCIT 90, Vol. I, Itapema, SC, pp. 243-248.

Azevedo, J.L.F., 1992, "A Finite Difference Method Applied to Internal Axisymmetric Flows," Bulletin of the Brazilian Society of Applied and Computational Mathematics, Vol. 3, No. 1, Series II, pp. 1-20.

Azevedo, J.L.F., Fico, N.G.C.R., Jr., and Ortega, M.A., 1995, "Two-Dimensional and Axisymmetric Nozzle Flow Computations Using the Euler Equations," RBCM -- J. of the Braz. Soc. Mechanical Sciences, Vol. XVII, No. 2, pp. 147-170.

Azevedo, J.L.F., Fico, N.G.C.R., Jr., Ortega, M.A., and Luna, G.C., 1992, "Nozzle Flow Calculations Using the Euler Equations," ICAS Paper 92-4.1.2, Proceedings of the 18th Congress of the International Council of Aeronautical Sciences, Vol. 1, Beijing, China, pp. 97-107.

Azevedo, J.L.F., Zdravistch, F., and Silva, A.F.C., 1991, "Implementation and Validation of Euler Solvers for Launch Vehicle Flows," Proceedings of the 4th International Symposium on Computational Fluid Dynamics, Vol. I, Davis, CA, pp. 42-47.

Beam, R.M., and Warming, R.F., 1976, "An Implicit Finite-Difference Algorithm for Hyperbolic Systems in Conservation-Law Form," Journal of Computational Physics, Vol. 22, pp. 87-110.

Beam, R.M., and Warming, R.F., 1978, "An Implicit Factored Scheme for the Compressible Navier-Stokes Equations," AIAA Journal, Vol. 16, No. 4, pp. 393-402.

Davis, M.W., Gunn, J.A., Herron, R.D., and Kraft E.M., 1986, "Optimum Transonic Wind Tunnel", AIAA 14th Aerodynamic Testing Conference, West Palm Beach, Flórida.

Fico, N.G.C.R., Jr., 1991, "Simulation of the Flow in the Reentry Flap Region of a Transonic Wind Tunnel," Doctoral Dissertation, Instituto Tecnológico de Aeronáutica, São José dos Campos, SP.

Goethert, B.H., 1961, "Transonic Wind Tunnel Testing," Pergamon Press, New York.

MacCormack, R.W., 1984, "An Introduction and Review of the Basics of Computational Fluid Dynamics," AIAA Professional Study Series on Computational Fluid Dynamics, Snowmass, Colorado.

Ortega, M.A., and Azevedo, J.L.F., 1991, "Checking the Influence of Longitudinal Wall Curvature in the Implementation of Boundary Conditions at the Wall of a Convergent-Divergent Nozzle," Proceedings of the 11th Brazilian Congress of Mechanical Engineering -- COBEM 91, "Blue" Volume, São Paulo, SP, pp. 193-196.

Pulliam, T.H., and Steger, J.L., 1980, "Implicit Finite-Difference Simulations of Three--Dmensional Compressible Flow," AIAA Journal, Vol. 18, No. 2, pp. 159-167.

Pulliam, T.H., and Steger, J.L., 1985, "Recent Improvements in Efficiency, Accuracy and Convergence for Implicit Approximate Factorization Algorithms," AIAA Paper 85-0360, AIAA 23rd Aerospace Sciences Meeting, Reno, Nevada.

Rotta, J.C., 1971, "Fortran IV -- Rechenprogram für Grenzschichten bei Kompressiblen Ebenen und Achsensymmetrischen Strömungen," DLR-FB 71-51, DFVLR-AVA, Institut für Strömungsmechanik, Göttingen, Germany.

RBCM - J. of the Braz. Soc. Mechanical Sciences
Vol. XXI - No.2 - 1999 - pp. 294-312

ISSN 0100-7386
Printed in Brazil

Alguns Comentários sobre a Automação do Método εN para Dimensionamento à Fadiga sob Carregamentos Complexos

Some Comments on the Automation of the εN Method for Fatigue Design under Complex Loading

Jaime Tupiassú Pinho de Castro
Marco Antonio Meggiolaro[1]
Pontifícia Universidede Católica do Rio de Janeiro
Departamento de Engenharia Mecânica PUC-Rio
22453-900 Rio de Janeiro, RJ, Brasil
jtcastro@mec.puc-rio.br
meggi@mit.edu

Abstract

The εN fatigue design method is non-linear and depends on the loading order and on the initial state of the piece. Therefore, the traditional procedure based on rain-flow counting of the loading followed by Neuber, Ramberg-Osgood, Coffin-Manson and Miner rules does ***not*** *guarantee the prediction of physically admissible hysteresis loops at the notches in the complex loading case. Solutions for this problem are proposed, and their implementation in a powerful language named* ***ViDa****, developed to automatize the fatigue design process, is discussed.*
KeyWords: *εN Method, Fatigue Design Automation, Complex Loading.*

Resumo

O método εN de projeto à fadiga é não-linear e sensível à ordem do carregamento e ao estado inicial da peça. Logo, o procedimento tradicional que aplica as regras de Neuber, Ramberg-Osgood, Coffin-Manson e Miner à contagem rain-flow *de um carregamento complexo* **não** *garante a previsão de laços de histerese fisicamente admissíveis nos entalhes. São propostas soluções para este problema, e é discutida sua implementação numa poderosa linguagem chamada* ***ViDa****, desenvolvida para automatizar o dimensionamento à fadiga sob carregamentos complexos.*
Palavras-Chave: *Método εN, Automação do Projeto à Fadiga, Carregamentos Complexos.*

Introdução

Fadiga é o tipo de falha estrutural causada primariamente pela aplicação repetida de carregamentos variáveis. Estas falhas são localizadas, progressivas e cumulativas, e caracterizam-se pela geração e/ou propagação de uma *trinca*, a qual diminui paulatinamente a resistência da peça, podendo leva-la à fratura. Por isto, o projeto à fadiga é um problema *local* que depende dos detalhes da geometria, do material e do carregamento do *ponto* mais solicitado da peça.

O principal parâmetro gerador de trincas por fadiga é a gama das tensões $\Delta\sigma$ (ou das deformações $\Delta\varepsilon$) atuantes no ponto crítico. Por isto, as trincas geralmente partem das raízes de entalhes concentradores de tensão. Quando as solicitações cíclicas *locais* são baixas em relação à resistência ao escoamento S_Y, o processo é muito influenciado pelos detalhes (i) do acabamento superficial, (ii) do gradiente das tensões atuantes (incluindo as tensões residuais) e (iii) das propriedades mecânicas. Nestes casos, a resistência à iniciação de uma trinca por fadiga tende a aumentar com a resistência à ruptura S_u, com a melhoria do acabamento superficial, com o aumento do gradiente de tensões e com a presença de tensões residuais compressivas. Entretanto, a medida que as cargas alternadas aumentam, o escoamento cíclico localizado torna estes detalhes superficiais cada vez menos importantes, e a ductilidade passa a ser o principal parâmetro controlador da resistência à geração da trinca.

Já a propagação das trincas por fadiga é um fenômeno controlado primariamente pela gama de variação do fator de intensidade de tensões, ΔK_I, e independe das características superficiais da peça (o problema da propagação das trincas sob carregamentos complexos é discutido em Meggiolaro e Castro (96, 97), enquanto que em Castro e Kenedi (95) encontra-se um estudo do correlacionamento entre a

---

[1] Atualmente no Mech.Eng.Dept., M.I.T.

Manuscript received: January 1997; Technical Editor: Agenor de Toledo Fleury.

iniciação e a propagação das trincas).

Para modelar adequadamente o problema de fadiga são requeridas informações em seis áreas, que funcionam como uma corrente cuja precisão é controlada pelo seu elo menos acurado:

- (i) Dimensões Geométricas (incluindo principalmente as dos entalhes e das trincas, caso presentes)
- (ii) Cargas de Serviço (devem ser medidas e não estimadas, pois influenciam diretamente as previsões)
- (iii) Propriedades dos Materiais (também devem ser preferencialmente medidas, pela mesma razão)
- (iv) Análise das Tensões Elastoplásticas (nos pontos críticos, para prever a iniciação das trincas)
- (v) Análise das Trincas (para prever a sua propagação, segundo os conceitos da Mecânica da Fratura)
- (vi) Análise do Acúmulo de Dano (e.g., o modelo de Wöhler-Goodman-Miner no método SN)

Para se otimizar o dimensionamento à fadiga, todos estes elos devem ser conhecidos dentro da mesma precisão e confiabilidade. Não se pode pela sofisticação dos três últimos (que dependem de erudição acadêmica) suprir as informações experimentais indispensáveis aos três primeiros elos. Por outro lado, é impossível prever adequadamente a vida à fadiga usando modelos de cálculos que não descrevam a física do problema de forma apropriada. Dentro desta ótica, os objetivos deste trabalho são:

1. apontar as limitações da metodologia εN tradicional de projeto à iniciação de uma trinca por fadiga, no caso de carregamentos complexos,
2. detalhar as correções que devem ser implementadas no método εN para que se possa obter previsões fisicamente corretas naquele caso, e
3. descrever sua implementação numa poderosa linguagem chamada **ViDa**, desenvolvida para automatizar todos os métodos tradicionalmente usados no dimensionamento mecânico à fadiga (Meggiolaro e Castro 95, 96 e 98).

Note-se que neste trabalho a filosofia do método εN não é questionada. Este é um enfoque consagrado pelo uso e corroborado por forte suporte experimental. Apenas mostra-se aqui como suas equações devem ser corrigidas para se garantir a previsão de laços de histerese fisicamente admissíveis no caso de carregamentos complexos.

Resumo do Método εN Clássico

O dimensionamento mecânico à iniciação de uma trinca por fadiga pelo método εN tradicional correlaciona o número de ciclos que inicia a trinca, N, com a gama das deformações atuantes no ponto crítico da peça, $\Delta\varepsilon$ (que é um parâmetro diretamente mensurável, e é numericamente mais robusto que $\Delta\sigma$ no caso plástico). Esta modelagem requer quatro tipos de informação:

- uma relação $\Delta\sigma$-$\Delta\varepsilon$, para descrever os laços de histerese elastoplástica na raiz do entalhe,
- uma regra de concentração de deformações, para correlacionar as tensões nominais $\Delta\sigma_n$ aplicadas sobre a peça com as deformações $\Delta\varepsilon$ por elas induzidas na raiz do entalhe,
- uma relação entre a amplitude de deformações $\Delta\varepsilon$ e a vida à fadiga N, e
- uma regra de acúmulo de dano.

O método εN só se aplica ao dimensionamento à fadiga de peças não-trincadas mas, por quantificar explicitamente as deformações plásticas cíclicas macroscópicas, pode ser usado para prever qualquer vida de iniciação. (O método εN tem que ser usado quando o problema for fadiga oligocíclica ou de pouca ciclagem, isto é, quando a gama das deformações plásticas $\Delta\varepsilon_p$ atuantes na raiz do entalhe for da mesma ordem ou maior que as elásticas $\Delta\varepsilon_e$, e pode ser usado também para o dimensionamento às vidas longas). Na prática, o εN é um método moderno e poderoso, mas que apresenta certas idiossincrasias que devem ser respeitadas sob pena de graves insucessos.

A metodologia εN clássica (Farahmand 97, Dowling 93, Bannantine et al. 90, Hertzberg 89, Rice 88, Fuchs e Stephens 80, Mitchell 79, Duggan e Byrne 77, Sandor 72 e Manson 65, e.g.) trabalha com tensões e deformações reais, usa relações $\Delta\sigma$-$\Delta\varepsilon$ tipo Ramberg-Osgood e considera o amolecimento ou endurecimento cíclico do material, mas não o seu transiente a partir do comportamento monotônico. Este método assume uma relação única entre as amplitudes das deformações e das tensões impostas sobre a peça, logo uma equação única para todos os laço de histerese, expressa por:

$$\varepsilon_a = \frac{\Delta\varepsilon}{2} = \frac{\Delta\varepsilon_e}{2} + \frac{\Delta\varepsilon_p}{2} = \frac{\Delta\sigma}{2E} + \left(\frac{\Delta\sigma}{2K'}\right)^{1/n'} \tag{1}$$

onde E é o módulo de Young, K' o coeficiente e n' o expoente de encruamento da curva $\sigma\varepsilon$ cíclica estabilizada. Estas propriedades devem ser medidas experimentalmente.

Valores *típicos* para o expoente de encruamento cíclico estão entre $0.1 < n' < 0.2$, enquanto que o expoente de encruamento monotônico n varia mais, tipicamente entre $0 < n < 0.5$. K' é o valor da tensão (real) que corresponde à deformação plástica (real) de 100% na curva cíclica ou no seu prolongamento.

A relação de Ramberg-Osgood ajusta-se bem à resposta cíclica de muitos materiais, mas é apenas uma de muitas relações empíricas que podem ser usadas com este mesmo propósito. Sua maior limitação é não reconhecer um comportamento puramente elástico nem sequer para as deformações muito pequenas, e sua maior vantagem é a simplicidade matemática.

Na metodologia εN tradicional geralmente usa-se a regra de Neuber para modelar o problema da concentração de deformações nos entalhes. Quando aplicada a carregamentos cíclicos, esta regra pode ser escrita como:

$$K_t^2 = \frac{\Delta\sigma \cdot \Delta\varepsilon}{\Delta\sigma_n \cdot \Delta\varepsilon_n} \tag{2}$$

onde $\Delta\sigma$ e $\Delta\varepsilon$ são as gamas de tensão e deformação provocadas na raiz do entalhe pelas gamas de tensão e deformação nominais $\Delta\sigma_n$ e $\Delta\varepsilon_n$ (o termo nominal refere-se ao carregamento em relação ao qual é definido o valor de K_t, o fator de concentração de tensões linear elástico). No caso onde as tensões nominais sejam elásticas, obtém-se:

$$K_t^2 = \frac{\Delta\sigma \cdot \Delta\varepsilon \cdot E}{\Delta\sigma_n^2} \tag{3}$$

Neste ponto é interessante notar uma contradição na metodologia εN tradicional, a qual reconhece um comportamento linear elástico para as tensões nominais enquanto usa Ramberg-Osgood para modelar as tensões nos entalhes. É possível eliminar esta incongruência, mas o custo computacional não se justifica (a menos que as tensões nominais sejam da ordem ou maiores que a resistência ao escoamento do material).

Quanto à relação entre a amplitude das deformações atuantes na raiz do entalhe, $\Delta\varepsilon/2$, e a vida à fadiga dada em número de reversões, $2N$, ela é tradicionalmente expressa pela regra de Coffin-Manson:

$$\frac{\Delta\varepsilon}{2} = \frac{\sigma'_f}{E}(2N)^b + \varepsilon'_f(2N)^c \tag{4}$$

onde σ'_f, ε'_f, b, c são constantes do material, que devem ser obtidas experimentalmente.

Estimativas das Constantes εN

Na ausência de resultados experimentais específicos, vale a pena lembrar que os expoentes b e c têm valores *típicos* entre $-0.2 < b < -0.05$ e $-0.7 < c < -0.5$ (ver, por exemplo, SAE 96, que tem uma boa tabela de dados experimentais). Para estes casos, Manson propôs empiricamente em 65 o chamado método das Inclinações Universais:

$$\Delta\varepsilon = 3.5\frac{S_u}{E}N^{-0.12} + \left[ln\left(\frac{1}{1-RA}\right)\right]^{0.6} N^{-0.6} \tag{5}$$

onde $ln[1/(1\text{-}RA)] = 2ln(d_0/d_f) = \varepsilon_f$, sendo RA a redução de área, d_0 e d_f os diâmetros inicial e final, e ε_f a deformação real na ruptura do espécime de tração, respectivamente (assumindo constância de volume das deformações plásticas mesmo após a estricção). Note-se que este método estima $b = -0.12$ e $c = -0.6$ para todos os materiais.

Na mesma época, Morrow (65) estimou os valores de b e de c a partir do expoente de encruamento cíclico n' como:

$$b = -n'/(1 + 5n') \quad e \quad c = -1/(1 + 5n') \tag{6}$$

o que implicaria numa relação entre os três expoentes: b/c = n'. Deve-se notar que neste caso, usando-se os valores de b e c propostos em (5), o valor de n' também seria invariável e igual a 0.20.

As constantes σ'_f e ε'_f podem ser estimadas a partir de um teste de tração usando-se as aproximações de (5) mas, como esta equação trabalha com $\Delta\varepsilon$ e N e não com $\Delta\varepsilon/2$ e $2N$, deve-se notar que a estimativa de Manson prevê que:

$$\sigma'_f = 3{,}5 \cdot S_u/2^{1+b} = 1{,}90 \cdot S_u \quad e \quad \varepsilon'_f = 0.76 \cdot \varepsilon_f^{0.6} \tag{7}$$

Há diversas outras estimativas similares propostas na literatura como, por exemplo:

$$\sigma'_f \approx \sigma_f \approx S_u \cdot (1 + e_f) \approx S_u \cdot (d_0/d_f)^2 \tag{8}$$

$$\sigma'_f \approx (S_u + 345) Mpa \tag{9}$$

$$\varepsilon'_f \approx \varepsilon_f \approx 2ln(d_0/d_f) \tag{10}$$

O correlacionamento de resultados experimentais com estimativas como as apresentadas acima foi avaliado recentemente por Ong (93) e por Brennan (94).

Uma relação útil para se definir o limiar da fadiga oligocíclica é dada pela chamada vida de transição, N_t, na qual as deformações elásticas e plásticas da equação de Coffin-Manson são iguais. Para vidas menores que N_t há predominância das deformações plásticas sobre as elásticas, e aquelas certamente não podem ser desprezadas nos cálculos:

$$N_T = \frac{1}{2}\left(\frac{\sigma'_f}{E\varepsilon'_f}\right)^{\frac{1}{c-b}} \tag{11}$$

Segundo Landgraf (70), N_t decresce exponencialmente com a dureza Brinell (HB) dos aços, variando da ordem de 15000 ciclos para HB no entorno de 2GPa até tão baixo quanto 1 ciclo para HB ≈ 7GPa. Ajustando seus resultados experimentais, a vida de transição N_T dos aços pode ser estimada por:

$$N_T \approx 6.8 \cdot 10^5 \exp(-1.9 \cdot HB) \qquad (HB\ em\ GPa) \tag{12}$$

Por fim, assumindo que deva haver coerência entre as partes elásticas e plásticas dos ajustes dos laços de histerese por Ramberg-Osgood e da curva εN por Coffin-Manson, igualando as Eqs. (1) e (4) obtém-se:

$$\frac{\Delta\sigma}{2} = \sigma'_f (2N)^b = K' \varepsilon_f'^{n'} (2N)^{cn'} \Rightarrow K' = \frac{\sigma'_f}{\varepsilon_f'^{n'}}; \quad b = c \cdot n' \tag{13}$$

Logo, só quatro entre as seis constantes $\{K', n', \sigma'_f, \varepsilon'_f, b, c\}$ seriam independentes. Deve-se tomar cuidado, entretanto, para não assumir que este algebrismo possa ser usado para substituir experimentos. Tanto Coffin-Manson quanto Ramberg-Osgood são relações empíricas que podem descrever adequadamente testes de fadiga de vários materiais, mas não são leis físicas. O que realmente importa são os resultados efetivamente medidos, e todas as seis constantes devem, sempre que possível, ser obtidas pelo ajuste de resultados experimentais confiáveis.

Dimensionamento εN Clássico no Caso de Carregamentos Complexos

De fato, há vasto suporte experimental para justificar o uso das simplificações do método εN tradicional no caso do dimensionamento mecânico à fadiga sob carregamentos simples, mas em geral a literatura não reconhece explicitamente a fundamental importância do estado inicial da peça e da ordem do carregamento no resultado das previsões feitas com o seu uso no caso de carregamentos complexos.

A forma tradicional de se projetar pelo método εN nestes casos tem sido:

- Calcular o dano d_i provocado pela aplicação das $n_i/2$ reversões ou $1/2$ ciclos do i-ésimo carregamento nominal $\Delta\sigma_{ni}$, contadas pelo método Rain-Flow como se os diversos ciclos do carregamento fossem independentes: $d_i = n_i/2N_i$, sendo N_i o número de ciclos que a peça duraria se somente o carregamento nominal $\Delta\sigma_{ni}$ estivesse atuando, e
- Usar a regra de Miner para acumular o dano total causado pelos diversos eventos do carregamento.

Como o método tradicional não leva em consideração a história do carregamento, ele pode ser facilmente resumido à aplicação sucessiva de dois conjuntos de equações quando os carregamentos nominais são elásticos:

(i) Dado o i-ésimo evento do carregamento $\Delta\sigma_{ni}$, calcula-se a tensão $\Delta\sigma_i$ na raiz do entalhe usando Neuber:

$$\Delta\sigma_i^2 + 2E\cdot\Delta\sigma_i\cdot\left(\frac{\Delta\sigma_i}{2K'}\right)^{\frac{1}{n'}} = \left(K_t\Delta\sigma_{ni}\right)^2 \tag{14}$$

(ii) A seguir calcula-se o $\Delta\varepsilon_i$ causado por $\Delta\sigma_i$, e os correspondentes N_i e d_i:

$$\Delta\varepsilon_i = \frac{\Delta\sigma_i}{E} + 2\cdot\left(\frac{\Delta\sigma_i}{2K'}\right)^{\frac{1}{n'}} = \frac{2\sigma'_f}{E}\left(2N_i\right)^b + 2\varepsilon'_f\left(2N_i\right)^c \Rightarrow d_i = \frac{n_i}{2N_i} \tag{15}$$

Estas equações não são inversíveis, logo o uso do método εN é computacionalmente trabalhoso, o que explica (mas não justifica) a pouca divulgação dos problemas que o seu uso não criterioso pode acarretar. Por isto, é indispensável reconhecer e enfatizar que a aplicação destas equações a uma contagem *rain-flow* do carregamento não permite a previsão de laços de histerese fisicamente admissíveis.

De fato, para se poder usar confiavelmente o método εN, antes de mais nada deve-se garantir que o modelo de cálculo reproduza os laços de histerese que atuam na raiz do entalhe, para só então calcular o dano por eles provocado. Como a prática ensinou dolorosamente aos autores que a única maneira de se evitar erros com o uso do εN é desenhando os laços de histerese previstos, a seguir são didaticamente discutidos vários problemas que ilustram os cuidados necessários à correta aplicação desta metodologia.

Problema do 1º Evento Elastoplástico

Segundo a idéia básica do método εN, a trinca de fadiga será gerada pelo dano cumulativo causado pelas sucessivas gamas de deformação $\Delta\varepsilon_i$ atuantes no ponto mais solicitado da peça, em geral na raiz de um entalhe. É claro que para modelar este problema é indispensável calcular corretamente estes $\Delta\varepsilon_i$. Mas qualquer solicitação que cause plasticidade, ainda que pontualmente localizada, é *memorizada* pela peça, devido à irreversibilidade deste processo. Logo, a trajetória do material no plano $\sigma\cdot\varepsilon$ depende da história do carregamento.

Além disto, mesmo que a peça seja virgem, que o estado de tensões e deformações residuais no entalhe seja zero, e que se possa desprezar os transientes de amolecimento ou de endurecimento cíclico, ainda assim é necessário distinguir entre o comportamento do primeiro evento do carregamento σ_{n1} e os subseqüentes: a peça virgem parte da origem do plano σ-ε, logo o primeiro 1/2 ciclo do carregamento segue a equação da curva σ-ε cíclica,

$$\varepsilon = \frac{\sigma}{E} + \left(\frac{\sigma}{K'} \right)^{\frac{1}{n'}} \qquad (16)$$

e não as equações do laço de histerese, como mostrado na Fig. 1. Portanto, para se calcular o dano d_1 do primeiro 1/2 ciclo do carregamento é necessário usar:

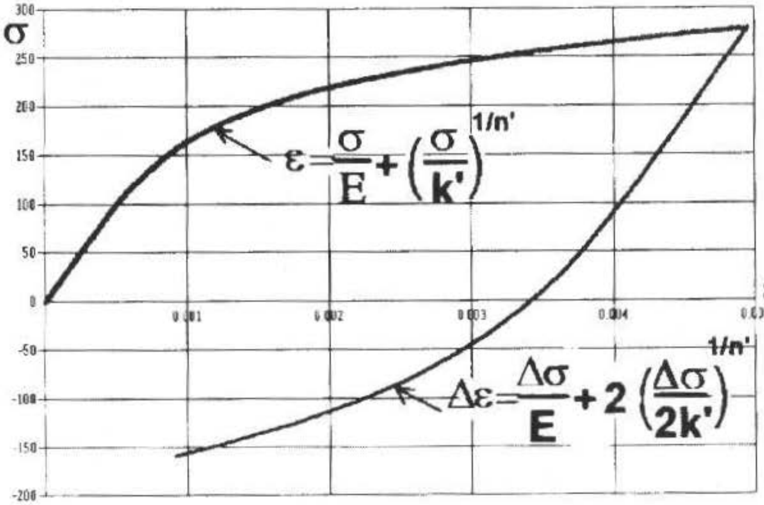

Fig 1 O primeiro evento elastoplástico segue a curva σ ε e não a do laço Δσ Δε

$$\sigma_1^2 + E \cdot \sigma_1 \cdot \left(\frac{\sigma_1}{K'} \right)^{\frac{1}{n'}} = (K_t \sigma_{n1})^2 \qquad (17)$$

$$\varepsilon_1 = \frac{\sigma_1}{E} + \left(\frac{\sigma_1}{K'} \right)^{\frac{1}{n'}} = \frac{2\sigma'_f}{E} (2N_1)^b + 2\varepsilon'_f (2N_1)^c \Rightarrow d_1 = \frac{1}{2N_1} \qquad (18)$$

Note-se que como $\sigma_0 = \varepsilon_0 = 0$, $\Delta\sigma_1 = \sigma_1 - \sigma_0 = \sigma_1$, mas não se usou a notação Δ nas equações acima, para enfatizar que o primeiro evento é diferente dos subseqüentes, os quais têm que ser modelados pela equação do laço de histerese (devidamente corrigida, como discutido abaixo).

Note-se também que do ponto de vista físico esta separação do evento inicial deveria ser mais apropriadamente enunciada como "deve-se separar o primeiro evento do carregamento capaz de gerar plasticidade (na raiz do entalhe crítico), o qual segue a curva σ-ε, dos eventos subseqüentes, que seguem curvas do laço $\Delta\sigma$-$\Delta\varepsilon$". Isto porque respostas completamente elásticas são reversíveis, logo isentas de memória. Entretanto, como já mencionado acima, a modelagem de Ramberg-Osgood prevê plasticidade para qualquer carregamento, e sempre gera no entalhe efeitos de memória que devem ser considerados.

Para exemplificar os problemas que podem ser gerados se o 1º ciclo não for separado dos subseqüentes, nada melhor do que desenhar alguns laços simples mas representativos. Na Figura 2a - b plota-se a previsão dos laços de histerese elastoplástica corrigidos, para a seqüência de carregamento

$\{0 \rightarrow 400 \rightarrow 0 \rightarrow 400\}MPa$, imposta sobre um corpo de prova *(CP)* εN não-entalhado. Nos cálculos usam-se as constantes de um aço 1020 (SAE 96):

$$E = 203GPa,\ K' = 772MPa,\ n' = 0.18,\ \sigma'_f = 896MPa,\ \varepsilon'_f = 0.41,\ b = -0.12,\ c = -0.51.$$

A deformação máxima resultante no CP neste caso é de 2.8%, e o dano causado por este evento, calculado segundo Coffin-Manson, é $d = 9.9 \cdot 10^{-4}$. Já na Fig. 2b, plotam-se os laços previstos para este mesmo evento sem separar o 1º ciclo dos demais. A máxima deformação prevista neste caso é de 0.31%, e o dano é de apenas $d = 8 \cdot 10^{-6}$, uma diferença não-conservativa de 12300%! É também importante notar que a Fig. 2a reproduz a forma e a aparência dos laços experimentalmente medidos, enquanto que a Fig. 2b é incompatível com a física do problema.

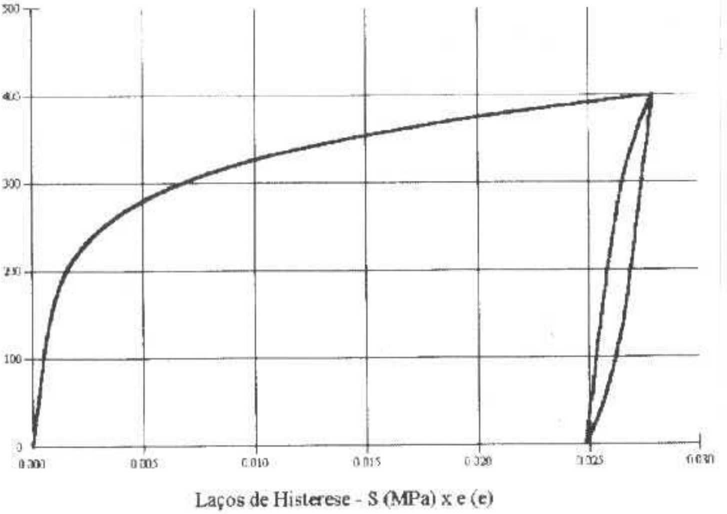

Fig. 2a Laços causados pelo carregamento {0 →400 → 0 → 400} MPa em CP padrão de aço 1020

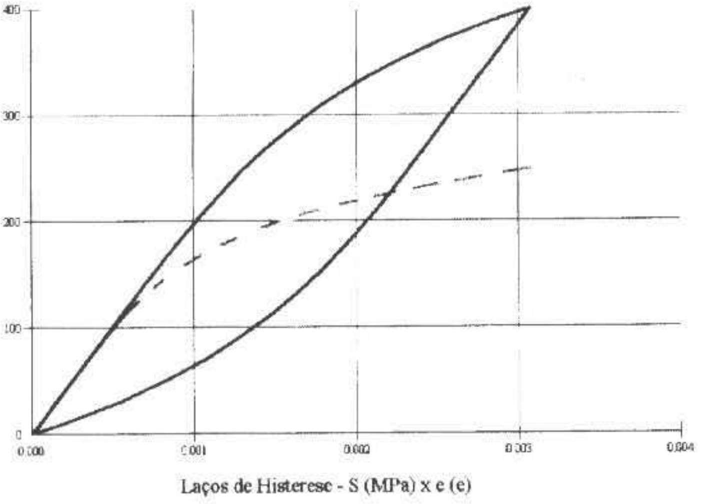

Fig. 2b Laços que seriam previstos para este mesmo evento sem separar o 1° ciclo dos demais

Este exemplo justifica muito bem a máxima "desenhe seus laços de histerese", mas não deve ser tomado como representativo dos erros numéricos que podem ser esperados em todos os casos práticos, caso não se separe o primeiro evento dos demais. Não é possível quantificar a priori a magnitude dos erros que podem ser cometidos, mas pode-se garantir que laços fisicamente inadmissíveis geram previsões não confiáveis.

Problema da Limitação Física dos Laços de Histerese

Separar o primeiro evento elastoplástico dos demais não é suficiente para garantir que a previsão de todos os laços de histerese esteja correta. E, novamente, o desenho dos laços calculados na raiz do entalhe é quase indispensável para que se possa compreender a complexidade mínima necessária à modelagem deste problema. Para ilustra-lo, aplica-se o carregamento da Fig. 3a (um evento principal que é interrompido por dois pequenos descarregamentos, na seqüência *{0 → 300 → 100 → 400 → -100 → 100 → -300}MPa)* sobre um CP idêntico ao do exemplo acima.

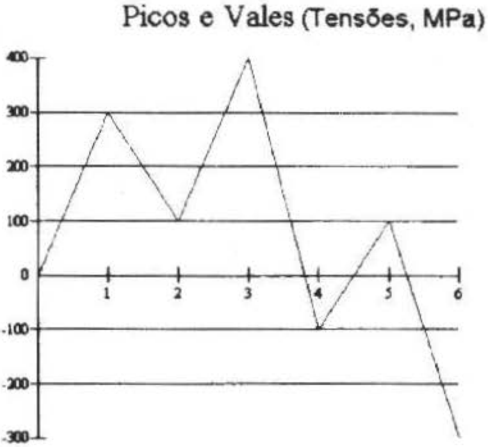

Fig. 3a Carregamento para ilustrar as limitações físicas dos laços de histerese elastoplástica

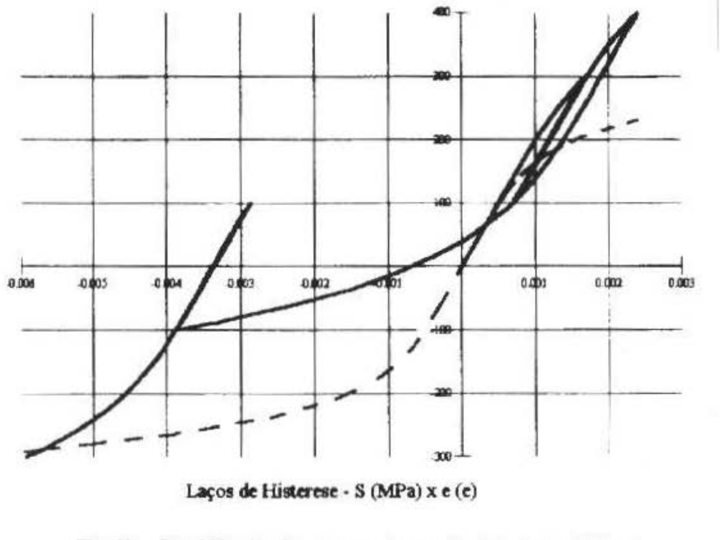

Fig. 3b Previsão dos laços usando a metodologia tradicional

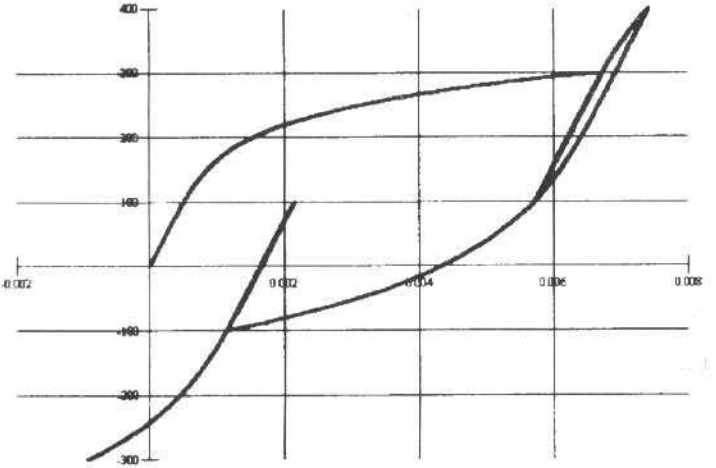

Laços de Histerese - S (MPa) x e (e)

Fig. 3c Previsão dos laços só separando o primeiro evento dos demais

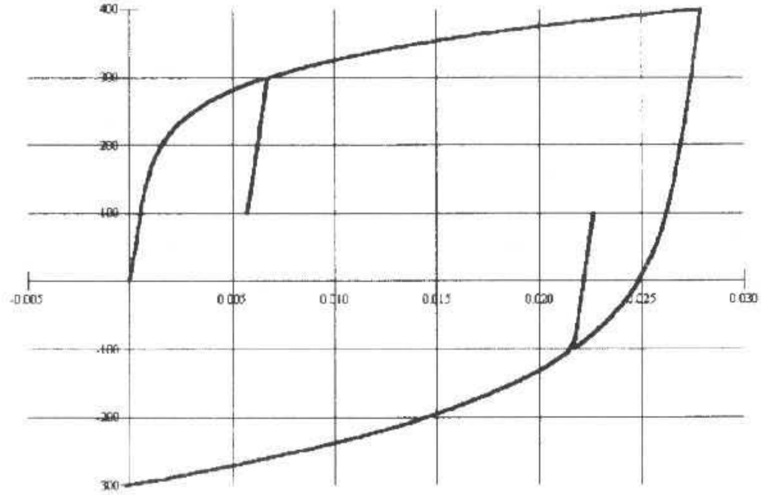

Laços de Histerese - S (MPa) x e (e)

Fig. 3d Laços corrigidos para evitar cruzamento das curvas $\sigma\,\varepsilon$ do "olhão"

Note-se que tanto a Fig. 3b, onde se usa o método εN tradicional, quanto a 3c, onde se aplica a curva σ-ε ao primeiro evento do carregamento e as equações do laço aos demais, mostram previsões absurdas. Como pode ser visto na Fig. 3d, para que os laços previstos sejam fisicamente admissíveis, eles também devem ser corrigidos para:

- Serem limitados pela curva σ-ε cíclica ou pelos maiores laços de histerese previamente gerados, e para
- Forçarem a simetria dos laços já iniciados.

Para isto, ao se calcular a seqüência dos laços induzidos por um dado carregamento complexo, deve-se verificar se a previsão cruza ou a curva σ-ε cíclica ou o maior dos laços previamente induzidos (aqui chamado de "olhão"). No caso de cruzamento, deve-se abandonar a equação do laço a partir de sua interseção com a curva σ-ε (ou com o olhão), e passar a seguir a curva σ-ε (ou a do olhão) até o fim do carregamento. Esta correção é complicada, mas é tão indispensável quanto a do 1º evento, sob pena de se fazer previsões:

(i) Fisicamente inadmissíveis, e
(ii) Provavelmente não-conservativas (o dano segundo Coffin-Manson da Fig. 3b é $2.9\cdot10^{-5}$ e o da 3c $6.1\cdot10^{-5}$, enquanto os laços corrigidos da Fig. 3d geram um dano de $1.3\cdot10^{-3}$, um valor duas ordens de grandeza maior).

Deve-se notar que simetria dos laços tem prioridade sobre a curva σ·ε, isto é, a curva σ·ε cíclica deve ser cruzada para forçar a simetria de um olhão já iniciado, como ilustrado na Fig. 4a (Meggiolaro e Castro 96). Este carregamento é dado em deformação: *{0 → 5000 → 3500 → 8000 → 5000 → 6500 → -1500 → 2000 → 500 → 8000}*μm/m. O CP é idêntico ao dos exemplos acima. Na Fig. 4b vê-se que o olhão do laço de histerese vai de -1500 a 8000μm/m, e que para forçar sua simetria e fechamento é necessário cruzar a curva σε duas vezes. Deve-se também observar nesta Fig. os três descarregamentos parciais de Δε = 1500μm/m, devidamente contidos por seus limites: o primeiro pela curva σ.ε, o segundo pela curva inferior e o terceiro pela curva superior do olhão. Para comparação, a Fig. 4c mostra quão absurdos ficariam os laços previstos se nenhuma das correções já discutidas fosse aplicada.

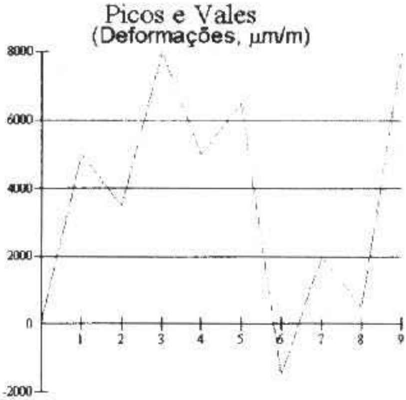

Fig. 4a Carregamento que ilustra o cruzamento da curva σ ε para forçar a simetria dos laços

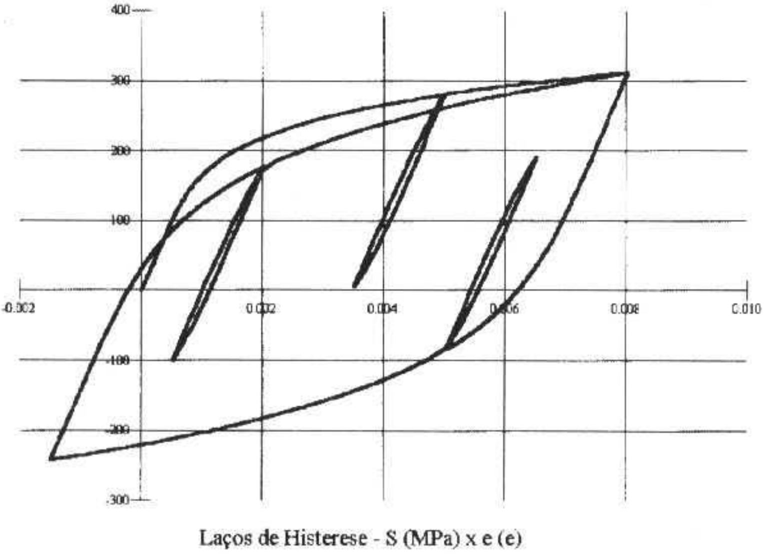

Fig. 4b Laços causados pelo carregamento da Fig. 4a, devidamente corrigidos

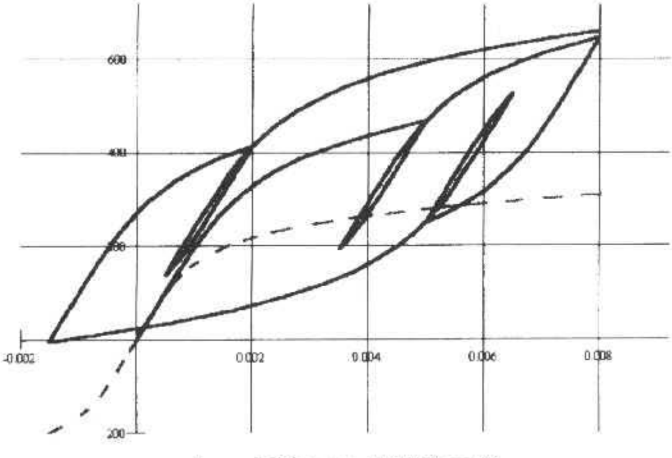

Laços de Histerese - S (MPa) x e (e)

Fig. 4c Laços que seriam previstos pela metodologia εN tradicional

Um outro ponto muito interessante também pode ser ilustrado por este exemplo: como foi imposta uma história de deformações sobre a peça, os danos causado pelos laços das Figs. 4b e 4c são idênticos! Em ambos os casos calcula-se um dano de $1.24\cdot10^{-4}$, porque o modelo de Coffin-Manson só depende dos $\Delta\varepsilon_i$, sem considerar os efeitos da carga média ou a forma dos laços. Logo, deve-se enfatizar que não se pode usar resultados experimentais de vida à fadiga obtidos em controle de deformação para justificar o comportamento de problemas controlados por tensão.

Para fugir destes problemas, as vezes é recomendada a reordenação dos carregamentos: colocando-se o maior deles em primeiro lugar todos os outros eventos estariam contidos dentro do olhão inicial, eliminando a necessidade das correções discutidas acima. Entretanto, este também não é um procedimento adequado, conforme mostrado a seguir.

Problema do Efeito da Ordem do Carregamento

A importância da ordem dos carregamentos é ilustrada através de mais um exemplo simples e convincente: Seja uma história de carregamentos e alívios crescentes como a mostrada na Fig. 5a, novamente aplicada sobre um CP não entalhado de aço 1020, idêntico aos dos exemplos acima. Os carregamentos e alívios foram escolhidos para gerarem laços espaçados aproximadamente da mesma distância, seguindo a seqüência:

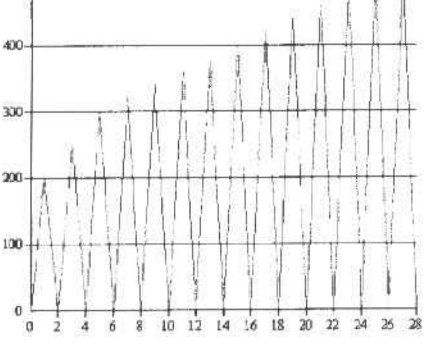

Fig. 5a Carregamento crescente para ilustrar os efeitos de ordem no método εN

$$\{0 \rightarrow 200 \rightarrow 0 \rightarrow 250 \rightarrow 0 \rightarrow 300 \rightarrow 0 \rightarrow 320 \rightarrow 0 \rightarrow 340 \rightarrow 0 \rightarrow 360 \rightarrow 0 \rightarrow 480 \rightarrow 0 \rightarrow 500 \rightarrow 0 \rightarrow 500 \rightarrow 0\} MPa$$

Os laços correspondentes, devidamente corrigidos, são mostrados na Fig. 5b: a maior tensão (real) aplicada é de 500MPa e a máxima deformação obtida chega a 9%. Já na Fig. 5c desenham-se os laços gerados pelo método εN tradicional, para mostrar como a forma dos laços previstos pelos procedimentos tradicionais é incompatível com a física do carregamento, ao contrário dos resultados que incluem as correções necessárias nos cálculos dos laços.

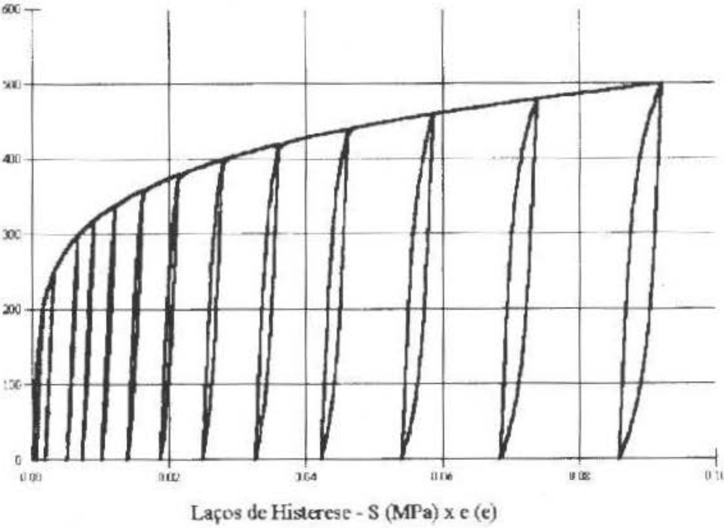

Fig. 5b Laços induzidos pelo carregamento da Fig. 5a, devidamente corrigidos

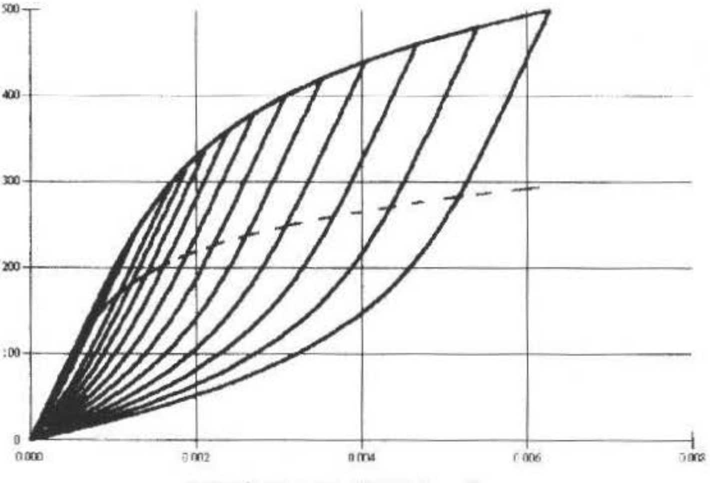

Fig. 5c Laços que seriam previstos pelo método εN tradicional

Aplicando-se Coffin-Manson aos laços da Fig. 5b para calcular o dano ciclo a ciclo, chega-se a d = $2.1 \cdot 10^{-3}$. (Para efeito de comparação, na Fig. 5c o dano calculado por Coffin-Manson é de $2.0 \cdot 10^{-4}$, cerca de dez vezes menor que o obtido a partir dos laços corrigidos). Mas provavelmente este é o tipo de carregamento que deve ser melhor analisado pelos modelos que consideram o efeito da carga média na relação εN, como:

$$\frac{\Delta\varepsilon}{2} = \frac{\sigma'_f - \sigma_m}{E}(2N)^b + \varepsilon'_f(2N)^c \qquad \text{(Morrow)} \qquad (19)$$

$$\frac{\Delta\varepsilon}{2} = \frac{\sigma'_f - \sigma_m}{E}(2N)^b + \varepsilon'_f\left(1 - \frac{\sigma_m}{\sigma'_f}\right)(2N)^c \qquad \text{(Morrow modificado)} \qquad (20)$$

$$\frac{\Delta\varepsilon}{2} = \frac{\sigma'^2_f}{E \cdot \sigma_{max}}(2N)^{2b} + \frac{\sigma'_f \cdot \varepsilon'_f}{\sigma_{max}}(2N)^{b+c} \qquad \text{(Smith-Topper-Watson)} \qquad (21)$$

onde σ_m e σ_{max} são a componente média e o valor máximo da tensão atuante.

Nas mesmas condições de cálculo do dano ciclo a ciclo nos laços corrigidos, o modelo de Morrow prevê um dano de $2.4 \cdot 10^{-3}$, o de Morrow modificado $4.2 \cdot 10^{-3}$ e o de STW $3.9 \cdot 10^{-3}$, todos valores coerentes entre si. Isto porque o modelo de Morrow só considera o efeito das cargas médias na componente elástica dos laços, enquanto que os modelos de Morrow modificado e de STW também quantificam dano causado pela carga média na componente plástica dos laços.

Para ilustrar os efeitos da ordem do carregamento, mostra-se na Fig. 6a o carregamento anterior aplicado na ordem invertida, e na Fig. 6b os laços obtidos, devidamente corrigidos. Deve-se notar como a forma dos laços gerados é totalmente diferente, isto é, como a inversão da ordem dos carregamentos altera completamente os laços de histerese induzidos no corpo de prova. Conforme afirmado acima, sem desenhar os laços de histerese previstos fica realmente difícil visualizar o problema da fadiga elastoplástica, quiçá equacioná-lo corretamente.

Problema do Momento Certo para se Efetuar a Contagem *Rain-Flow*

As histórias de carregamento das Figs. 5 e 6 também servem para ilustrar problemas que podem ocorrer na contagem de dano: quando se calcula ciclo a ciclo o dano causado pelos laços da Fig. 6b, obtém-se um valor uma ordem de grandeza maior que o obtido dos laços da Fig. 5b! (por Coffin-Manson $1.2 \cdot 10^{-2}$, por Morrow $1.3 \cdot 10^{-2}$, etc.). Isto apesar de nestes dois casos tanto o "olhão" como os laços internos terem amplitudes similares.

É claro que este problema é causado pelo procedimento de cálculo de dano ciclo a ciclo, o qual não reconhece todos os eventos do carregamento. Para se resolver este problema deve-se efetuar uma contagem tipo *rain-flow*. De fato, só após recalcular o dano causado pelos laços da Fig. 5b aplicando-se a contagem *rain-flow* às deformações induzidas, chega-se a valores de dano similares àqueles calculados na Fig. 6b. Isto porque nesta o 1º evento do carregamento também é o máximo, enquanto que na Fig. 5b justamente este maior valor não é contabilizado pela contagem ciclo a ciclo.

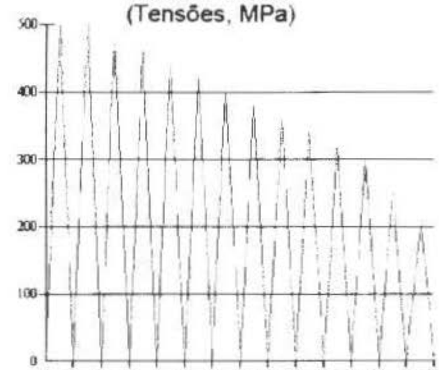

Fig. 6a Carregamento da Fig. 5a aplicados na ordem decrescente

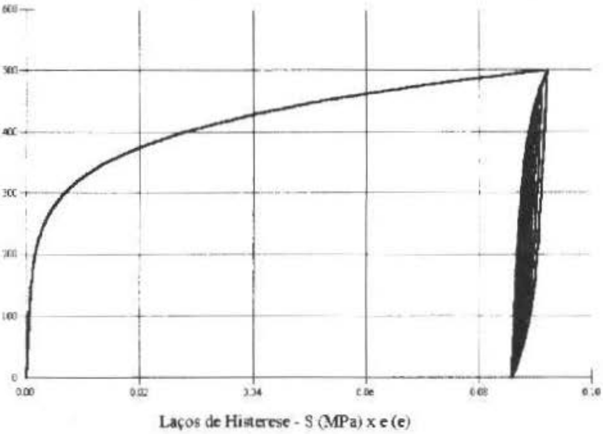

Fig. 6b Laços correspondentes ao carregamento da Fig. 6ª, devidamente corrigidos

Note-se que a contagem *rain-flow* foi aplicada nas deformações calculadas. Mas a prática usual, como se sabe, é contar o carregamento, com uma eventual filtragem de amplitude, como mostrado na Fig. 7. (A filtragem das pequenas cargas é um recurso muito útil para diminuir o esforço computacional nos cálculos de dano à fadiga sob carregamentos complexos, mas deve ser usada com cuidado para não eliminar carregamentos capazes de causar dano à peça Castro et al., 94). Quando se trabalha com um método linear elástico como o SN esta prática é correta e recomendável, pois a ordem dos carregamentos é irrelevante.

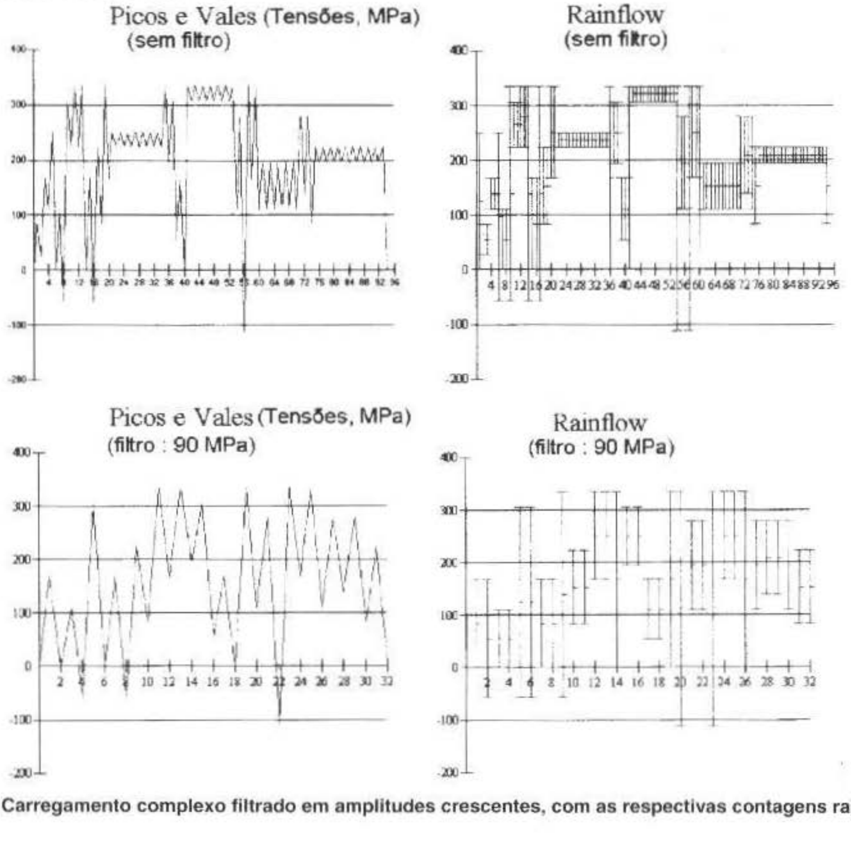

Picos e Vales (Tensões, MPa) (sem filtro)

Rainflow (sem filtro)

Picos e Vales (Tensões, MPa) (filtro : 90 MPa)

Rainflow (filtro : 90 MPa)

Fig. 7 Carregamento complexo filtrado em amplitudes crescentes, com as respectivas contagens rain-flow

Mas no caso elastoplástico, contar o carregamento (neste caso as tensões impostas) e não o seu efeito (as deformações resultantes) é um procedimento totalmente *inadequado*, como ilustrado nas Figs. 8: na 8a o carregamento complexo não-filtrado da Fig. 7 é tratado seqüencialmente, incluindo todas as correções recomendadas acima; na 8b plota-se o resultado obtido mantendo todas as correções dos laços mas fazendo a contagem *rain-flow* das tensões; e na Fig. 8c apresenta-se o resultado da metodologia *εN* tradicional. Os danos calculados nos três casos são:

Caso	Coffin-Manson	Morrow	Morrow mod.	S-T-W
Laços corrigidos, *rain-flow* nas deformações (fig.8a)	$1.4 \cdot 10^{-4}$	$1.7 \cdot 10^{-4}$	$2.4 \cdot 10^{-4}$	$2.2 \cdot 10^{-4}$
Laços corrigidos, *rain-flow* nas tensões (fig.8b)	$1.1 \cdot 10^{-4}$	$1.3 \cdot 10^{-4}$	$1.8 \cdot 10^{-4}$	$1.9 \cdot 10^{-4}$
Método εN tradicional (fig.8c)	$2.5 \cdot 10^{-5}$	$3.3 \cdot 10^{-5}$	$4.1 \cdot 10^{-5}$	$8.4 \cdot 10^{-5}$

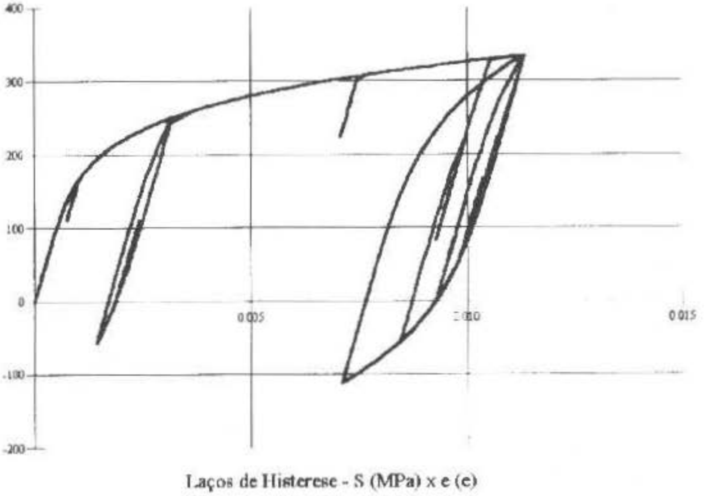

Fig. 8a **Laços induzidos pelo carregamento da Fig. 7 (sem qualquer filtragem), com as devidas correções**

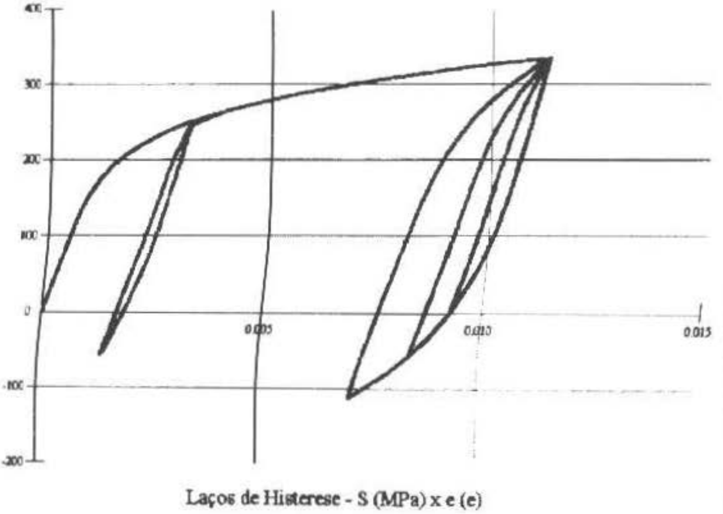

Fig. 8b **Laços corrigidos como na Fig. 8a, mas com rain-flow feito nas tensões solicitantes**

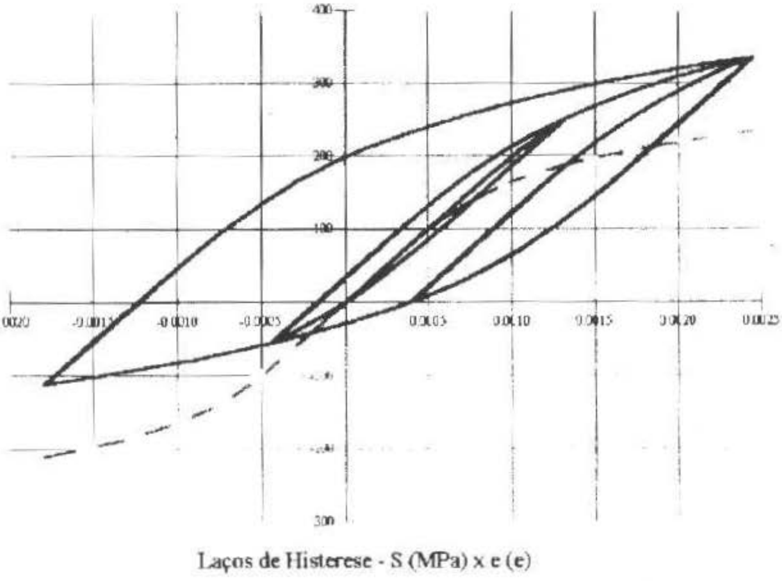

Fig. 8c Laços previstos pelo método εN tradicional para a contagem rain-flow do mesmo carregamento

Note-se que este carregamento se aproxima bem mais dos casos reais que os exemplos didáticos discutidos anteriormente, e que pode ser usado para ilustrar o tipo de erro que se pode obter na prática do dimensionamento mecânico. Por isto vale a pena enfatizar que a não linearidade do método εN tem sempre que ser considerada antes de sua aplicação. E como o método *rain-flow* tradicional gera uma tabela na qual a ordem dos carregamentos é alterada, o procedimento de cálculo de dano correto no caso de carregamentos complexos é:

- Calcular primeiro os laços de histerese induzidos pelo carregamento $\Delta\sigma_{ni}$ na raiz do entalhe, na seqüência em que eles efetivamente ocorrem (incluindo todas as correções necessárias!), e
- Fazer a contagem *rain-flow* nas deformações $\Delta\varepsilon_i$ resultantes.

Deve-se enfatizar que a contagem das deformações $\Delta\varepsilon_i$ resultantes é indispensável para o cálculo correto do dano! Isto porque a história das deformações resultantes de um carregamento complexo também é complexa, e só a contagem *rain-flow* pode quantificar o dano causado por todos os eventos.

Problema da Aplicação Correta da Regra de Neuber

No problema do dimensionamento mecânico real é indispensável considerar todas as correções discutidas acima na modelagem do comportamento elastoplástico cíclico dos pontos críticos das peças. Portanto, é indispensável estudar-se o comportamento da raiz de concentradores de deformação, que é onde as trincas de fadiga quase sempre se iniciam. Seguindo as idéias tradicionais, para isto deve-se aplicar a regra de Neuber em conjunto com as correções necessárias para garantir a qualidade dos laços previstos. Mas nestes casos não se pode usar a Eq. (14), que só se aplica quando o material permanece numa mesma curva σ-ε.

Neste ponto vale a pena lembrar que o problema na realidade resolvido por Neuber em 61 foi a concentração de tensões e deformações na torção monotônica de corpos prismáticos feitos de qualquer material não-linear elástico. Portanto, o uso da regra de Neuber no método εN tradicional é uma aproximação que, segundo Fuchs e Stephens (80), só é corroborada experimentalmente nos casos de tensão plana dominante na raiz do entalhe (por isto aqueles autores recomendam o uso da regra Linear de concentração de deformações ($K_t = K_\varepsilon = \Delta\varepsilon/\Delta\varepsilon_n$) para os casos de deformação plana). Para usar esta mesma aproximação nos casos das mudanças de curvas $\sigma\varepsilon$ necessárias para garantir a admissibilidade física dos laços de histerese, basta manter a constância dos produtos $\Delta\sigma\Delta\varepsilon = (K_t\Delta\sigma_n)^2/E$. Esta tarefa é conceitualmente simples, como ilustrado na Fig. 9, apesar de exigir uma implementação numérica não-trivial.

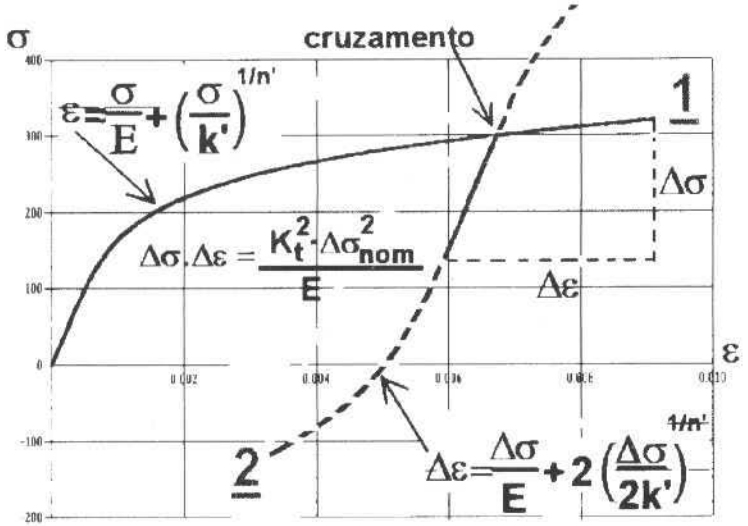

Fig. 9 Aplicação da regra de Neuber nas trocas de curvas σ ε necessárias às correções dos laços

A idéia é aplicar o carregamento $\Delta\sigma_n$ em pequenos incrementos $\Delta\sigma_{nj}$, e ir construindo o caminho $\Delta\sigma_j$, $\Delta\varepsilon_j$ correspondente no plano σ-ε, seguindo primeiro a curva 1 da Fig. 9 até o seu cruzamento com uma das curvas limitadoras do olhão, que no caso é a curva 2. O ponto de parada na curva 2 é localizado comparando-se a cada incremento do carregamento o valor do produto $\Delta\sigma_j.\Delta\varepsilon_j$ com $(K_t\Delta\sigma_n)^2/E$, que é um valor conhecido.

Note-se que este procedimento pode facilmente ser generalizado para carregamentos nominais elastoplásticos. Entretanto este caso, que é mais de interesse acadêmico do que prático, não será discutido aqui tendo em vista que o esforço computacional necessário dificultaria seu uso em uma ferramenta capaz de rodar em micros.

Problema da Solução Numérica dos Sistema de Coffin-Manson e de Neuber

A solução numérica das Eqs. (14) e (15) merece ser comentada. Para resolve-las foi desenvolvido um método baseado no fato daquelas equações constituírem essencialmente a combinação de duas retas, quando traçadas em escala bi-logarítmica. Uma vez que o método de Newton-Raphson é muito eficaz para resolver equações que possuam derivada aproximadamente constante, esse método foi adaptado a uma escala logarítmica, escrevendo-se as equações de Neuber e de Coffin-Manson na forma geral:

$$\delta = \beta exp(Bx) + \gamma exp(Cx) \qquad (22)$$

onde x é a incógnita a ser calculada numericamente. No caso da Eq. (14), tem-se:

$$\delta = (K_t\Delta\sigma_n)^2,\ \beta = 1,\ B = 2,\ \gamma = 2E/(2K')^{1/n'},\ C = 1 + 1/n',\ x = ln(\Delta\sigma_i) \qquad (23)$$

e no caso da Eq. (15)

$$\delta = \Delta\varepsilon/2,\ \beta = \sigma_f'/E,\ B = b,\ \gamma = \varepsilon_f',\ C = c,\ x = ln(2N) \qquad (24)$$

O procedimento para a solução da Eq. (16) pode ser resumido por:

- Encontra-se o valor de x_0 para a primeira iteração através de

$$x_0 = min\left(\frac{ln(\delta/\beta)}{B}, \frac{ln(\delta/\gamma)}{C}\right) \tag{25}$$

onde a função min retorna o menor dentre dois valores. No caso da regra de Coffin-Manson, a Eq. (19) avalia se o gradiente de deformações está na região predominantemente elástica ou plástica, tomando como valor inicial aquele que mais se aproximar da solução.

- Calcula-se o valor de x_{i+1} da nova iteração em função do valor de x_i $(i \geq 0)$:

$$x_{i+1} = x_i - \left(\beta e^{Bx_i} + \gamma e^{Cx_i}\right) \cdot ln\left[\frac{1}{\delta}\frac{\beta e^{Bx_i} + \gamma e^{Cx_i}}{\beta B e^{Bx_i} + \gamma C e^{Cx_i}}\right] \tag{26}$$

- Sendo (ξ-1) o erro relativo máximo admissível, prosseguem-se as iterações até que a expressão

$$ln\left[\frac{\left(\beta e^{B(x_i+ln(\xi))} + \gamma e^{C(x_i+ln(\xi))}\right)}{\delta}\right] \tag{27}$$

seja negativa. Para exemplificar o uso deste método, calcula-se a vida residual de um espécime cujo material (um aço) possui as propriedades dadas: $E = 203GPa$, $\sigma_f' = 896MPa$, $\varepsilon_f' = 0{,}41$, $b = -0{,}12$ e $c = -0{,}51$. A partir da Eq. (14), para um gradiente de deformações $\Delta\varepsilon = 2000\mu\varepsilon$ e $\xi = 1{,}001$ (erro máximo de 0,1%), calcula-se então :

$$x_0 = 6{,}60;\ x_1 = 11{,}12;\ x_2 = 11{,}87;\ x_3 = 11{,}91 \rightarrow 2N = e^{11{,}91} = 149000\ reversões$$

e o processo converge em 3 iterações.Se o método tradicional de Newton-Raphson fosse utilizado, considerando-se um valor inicial de 1 para 2N, seriam necessárias 15 iterações para calcular-se a solução na precisão de 0,1%. Além disso, mesmo se fosse utilizada a condição inicial definida no primeiro passo do algoritmo apresentado acima, o método de Newton-Raphson ainda necessitaria de 10 iterações para a convergência.

A Linguagem ViDa 98

Como o método εN é bem menos simples do que aparenta, para poder aplica-lo aos casos reais de carregamento complexo é indispensável usar suporte computacional adequado. Para isto, foi recentemente desenvolvida a linguagem **ViDa** (Meggiolaro e Castro 96), atualmente na sua versão **98**, da qual se faz uma breve descrição a seguir.

Esta linguagem foi concebida para automatizar todos os métodos tradicionalmente usados no projeto mecânico à fadiga sob carregamentos complexos: o SN, o IIW (para estruturas soldadas) e o εN para prever a iniciação da trinca, e o da/dN para estudar a propagação das trincas planas e 3D usando conceitos da Mecânica da Fratura. Nela também se incluiu inúmeras facilidades úteis ao projetista, como vários bancos de dados inteligentes, dois contadores *rain-flow* e um filtro *race-track*, gerador de laços de histerese elastoplástica (incluindo todas as correções necessárias no método εN, seguindo os procedimentos discutidos acima), ajuste automático de dados experimentais, interpretador de equações, e várias outras ferramentas similares, todas com uma interface gráfica amigável que roda num ambiente Windows.

Com o **ViDa 98** pode-se também desenhar a curva εN e sobre ela a curva SN tradicional, e forçar a componente elástica da deformação a atingir a curva SN no limite. O programa calcula o dano εN por todos os métodos discutidos (Coffin-Manson, IU, Morrow, STW, etc.), de forma seqüencial, e pode aplicar o rain-flow nas deformações resultantes. Há também as opções de trocar a regra de Neuber pela regra Linear de concentração de deformações, e de desenhar os laços de histerese devidamente corrigidos ou os previstos pelos métodos tradicionais (para quando não se conhecer a história prévia da peça e ainda assim se quiser fazer uma estimativa εN, ou para quando se quiser desconsiderar os efeitos do ordenamento apesar de todos os problemas de incompatibilidade física das previsões). Na realidade, todos os laços apresentados neste trabalho, bem como todos os danos calculados nos exemplos, foram gerados usando-se o **ViDa** num micro AMD586 de 133MHz, com 16MB de memória RAM.

Conclusões

Foram discutidas várias limitações do tradicional método εN de projeto à fadiga, e apresentadas soluções para eliminá-las. Também foi apresentada uma nova linguagem chamada **ViDa 98**, que automatiza o dimensionamento à fadiga sob carregamentos complexos e na qual estas soluções foram implementadas.

Os problemas causados pelo ordem do carregamento e pela limitação dos laços de histerese elastoplática nos levam a questionar o uso dos procedimentos tradicionais *εN* em peças usadas cuja história elastoplástica seja ignorada: o desconhecimento do estado inicial de tensões e deformações residuais na raiz do entalhe crítico pode invalidar as previsões feitas a partir da solução repetida das equações do laço de histerese. Para se aplicar adequadamente o método *εN* em peças que não sejam virgens, deve-se primeiro localizar a origem dos laços de histerese no plano σ-ε. Isto provavelmente requer a medição do estado inicial de tensões e deformações residuais no ponto crítico da peça (e, como é a história $\sigma\varepsilon$ na raiz do entalhe que importa, não adianta medir as tensões residuais fora deste ponto!). Esta é a única forma de prever os laços subseqüentes usando as correções necessárias para garantir sua admissibilidade física.

Referências

Bannantine, J. A.; Comer, J. J. e Handrock, J. L., 1990, "Fundamentals of Metal Fatigue Analysis", Prentice Hall.

Brennan, F. P., 1994, "The Use of Approximate Strain-Life Fatigue Crack Initiation Predictions", Fatigue, v.16, pp.351-356.

Castro, J. T. P.; Freire, J. L. F. e Vieira,R.D., 1994, "Fatigue Life Prediction of Repaired Welded Structures", J. Constructional Steel Research, Vol.28, pp.187-195.

Castro, J. T. P. e Kenedi, P. P., 1995, "Previsão das Taxas de Propagação de Trincas de Fadiga Partindo dos Conceitos de Coffin-Manson", Rev.Bras.Ciênc.Mecânicas XVII(3), pp.292-303.

Dowling, N. E., 1993, "Mechanical Behavior of Materials", Prentice-Hall.

Duggan, T. V. e Byrne, J., 1977, "Fatigue as a Design Criterion", Macmillan.

Farahmand,B., 1997, "Fatigue and Fracture Mechanics of High Risk Parts", Chapman e Hall.

Fuchs, H. O. e Stephens, R. I., 1980, "Metal Fatigue in Engineering", Wiley.

Hertzberg, R. W., 1989, "Deformation and Fracture Mechanics of Engineering Materials", Wiley.

Landgraf, R. W., 1970, "The Resistance of Metals to Cyclic Deformation", ASTM STP 467.

Manson, S. S., 1965, "Fatigue: A Complex Subject - Some Simple Approximations", Exp.Mech. v.5 n.4, pp.193-22.

Meggiolaro, M. A. e Castro, J. T. P., 1995, "**VIDA** - Programa para Previsão de Vida à Fadiga sob Carregamentos Complexos", Anais do III Simpósio de Análise Experimental de Tensões, pp.7-10, ABCM.

Meggiolaro, M. A. e Castro, J. T. P., 1996, "Desenvolvimentos na Automação do Projeto à Fadiga sob Carregamentos Complexos", II Sem.Mec.Fratura, pp.99-118, ABM.

Meggiolaro, M. A. e Castro,J. T. P., 1996, "Uma Nota Sobre o Projeto à Fadiga sob Carregamentos Complexos Segundo o Método εN", Anais do IX SIBRAT (COTEQ 96), pp.157-160, IBP e ABCM.

Meggiolaro, M. A. e Castro, J. T. P., 1996, "Alguns Comentários Sobre a Propagação de Trincas por Fadiga sob Carregamentos Complexos", Anais do IX SIBRAT (COTEQ 96), pp.145-148, IBP e ABCM.

Meggiolaro, M. A e Castro, J. T .P., 1997, "Modelagem dos Efeitos de Seqüência na Propagação de Trincas por Fadiga", Anais do 2° Cong. Int. de Tecnologia Metalúrgica e de Materiais (III Sem. Mec. Fratura), em CD, ABM.

Meggiolaro, M. A. e Castro,J.T.P., 1998 "**ViDa 98** - Danômetro Visual para Automatizar o Projeto à Fadiga sob Carregamentos Complexos", a ser publicado na Rev.Bras.Ciênc.Mecânicas, Vol. XX, No. 4, pp 666-685

Mitchell, M. R., 1979, "Fundamentals of Modern Fatigue Analysis for Design", in "Fatigue and Microstructure", ASM.

Morrow, J., 1965, "Cyclic Plastic Strain Energy and Fatigue of Metals", ASTM STP 378.

Neuber, H., 1961, "Theory of Stress Concentration for Shear- Strained Prismatical Bodies with Arbitrary Non-Linear Stress-Strain Law", J.Appl.Mech. 28, pp.544-551.

Ong, J. H., 1993, "An Evaluation of Existing Methods for the Prediction of Axial Fatigue Life from Tensile Data", Int.J.Fatigue, v.15, n.1, pp.13-19.

Rice, R. C., ed., 1988, "Fatigue Design Handbook", SAE.

SAE Handbook, 1996.

Sandor,B.I., 1972, "Fundamentals of Cyclic Stress and Strain", U.Wisconsin.

RBCM - J. of the Braz. Soc. Mechanical Sciences
Vol. XXI - No.2 - 1999 - pp. 313-321

ISSN 0100-7386
Printed in Brazil

Utilização de Técnicas de Ajuste de Modelos em Dinâmica para Identificação de Propriedades Elásticas de Estruturas Sanduíches em Materiais Compostos

The use of Model Updating Techniques in Dynamics for Identification of Stiffness Properties of Sandwich Composite Structures

Jesiel Cunha
Jean Piranda
Departamento de Engenharia Civil
Universidade Federal de Uberlândia
38400-902 Uberlândia, MG Brazil
jecunha@ufu.br

Abstract

The present paper consists of the identification of the stiffness properties of sandwich composite structures by using vibration measurement's data. The coefficients are identified by a model updating technique. The used formulation is based on the minimization of the eigensolution residuals (sensitivity method). This technique allows the simultaneous identification of several properties from a single test. Stiffness properties of extension, bending, twisting and transverse shear effects are identified, what is not evident from classical identification tests of sandwich structures. Results obtained by numerical simulations show the efficiency of the proposed methodology.

Keywords : *Composite Materials, Sandwich Structures, Elastic Constants, Identification, Model Updating, Vibration.*

Resumo

Este trabalho trata da identificação de constantes elásticas de estruturas sanduíches em materiais compostos à partir de ensaios de vibração. As propriedades são identificadas pela técnica de ajuste de modelos. O método utilizado é baseado na minimização de resíduos formados pelas auto-soluções (método de sensibilidade). A técnica permite a identificação simultânea de diversas propriedades à partir de apenas um ensaio dinâmico. Obtém-se desta maneira propriedades de flexão, torção, membrana e cisalhamento tranversal, o que não é evidente nos métodos clássicos de identificação em estruturas do tipo sanduíche. Os resultados obtidos por simulação numérica demonstram a eficiência da metodologia proposta.

Palavras-Chave : *Materiais Compostos, Estruturas Sanduíches, Constantes Elásticas, Identificação, Ajuste de Modelos, Vibração.*

Introdução

Com o aparecimento de novos materiais, elaborados à partir de novas filosofias de concepção e fabricação, o campo de aplicação dos materiais compostos evoluiu consideravelmente estes últimos anos. Novas gerações de estruturas ditas multi-funcionais, como os materiais híbridos ou mais recentemente os compostos adaptativos ou inteligentes, começam a aparecer (Chou, 1992).

As novas tecnologias requerem desta forma novas técnicas de análise do comportamento mecânico, adaptadas a estes novos materiais. Este trabalho trata da identificação de propriedades de rigidez de estruturas do tipo sanduíche à partir de ensaios dinâmicos. A peculiaridade da configuração estrutural e dos materiais constituintes de um sanduíche torna difícil a caracterização experimental dos mesmos à partir dos ensaios clássicos (tração, flexão, etc.). O interesse dos ensaios dinâmicos está no fato de que o comportamento vibratório de uma estrutura é caracterizado por várias energias de natureza diferente, o que vai de encontro ao caráter de identificação multiaxial, inerente aos compostos em geral. Pode-se identificar de maneira simultânea várias propriedades à partir de apenas um ensaio. Além disso, o método é do tipo não-destrutivo. Os coeficientes são identificados pela técnica de ajuste de modelos. A metodologia utilizada (do tipo modal) é baseada na minimização de um resíduo construído a partir das auto-soluções do modelo e da estrutura. Esta técnica é comumente chamada de método de sensibilidade.

Manuscript received: July 1997; revision received: January 1999. Technical Editor: Agenor de Toledo Fleury

Formulação do Método de Sensibilidade

O método de sensibilidade consiste na minimização de um resíduo baseado nas auto-soluções, consideradas como grandezas de saída (Fig. 1) (Piranda, 1994). Suas vantagens em relação à outros métodos de ajuste de modelos em elastodinâmica são, de maneira geral as seguintes : não há expansão ou condensação; é aplicável no caso onde o número de sensores é reduzido, portanto bem adaptado ao tratamento de grandes sistemas; é robusto em relação aos ruídos nas medidas; a manipulação e interpretação física das variáveis do problema considerado é facilitada. Seus principais inconvenientes são : má convergência ou possibilidade de mínimos locais, o que impõe um modelo inicial relativamente próximo da estrutura real; necessidade de emparelhamento dos modos; utilização das massas generalizadas; problemas numéricos no caso de autovalores múltiplos ou quase-múltiplos. A maioria destes inconvenientes pode no entanto ser resolvida através de procedimentos adaptados (Cunha, 1997).

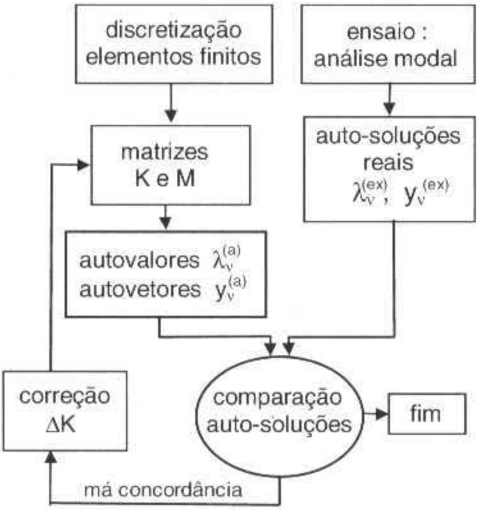

Fig. 1 Organograma geral do método de sensibilidade

Em ajuste de modelos, procura-se determinar as correções ΔK entre as matrizes de rigidez do modelo analítico (a) e da estrutura real (ex) :

$$K^{(ex)} = K^{(a)} + \Delta K \tag{1}$$

Para isto, supõe-se que o modelo de elementos finitos é composto de subdomínios, chamados macro-elementos, que possuem elementos dependentes dos mesmos parâmetros :

$$K = \sum_{e=1}^{r} K_e^{(E)} \in R^{N,N} \tag{2}$$

onde r é o número de elementos de um macro-elemento e $K_e^{(E)}$ é a matriz de rigidez associada ao elemento e. As correções são efetuadas nos p macro-elementos de rigidez, da seguinte maneira :

$$K^a = \sum_{i=1}^{p} k_i K_i \tag{3}$$

onde k_i é o coeficiente corretor que se procura identificar e K^o é a matriz de rigidez completa. O resíduo é construído à partir das distâncias entre as auto-soluções identificadas na estrutura e calculadas pelo modelo de elementos finitos, avaliadas nos graus de liberdade correspondentes aos c sensores:

$$\Delta y_{\nu} = y_{\nu}^{(ex)} - y_{\nu}^{(a)} \in R^{c.1} \qquad \Delta\lambda_{\nu} = \lambda_{\nu}^{(ex)} - \lambda_{\nu}^{(a)} \in R \qquad \nu = 1, \ldots, m \tag{4}$$

O método de sensibilidade consiste em expressar as distâncias em função das variações dos parâmetros de concepção dos macro-elementos. Para isto, desenvolve-se as auto-soluções medidas em série de Taylor de primeira ordem, nas vizinhanças das auto-soluções emparelhadas do modelo :

$$y_{\nu}^{(ex)} = y_{\nu}^{(a)} + \sum_{i=1}^{p} \frac{\partial y_{\nu}^{(a)}}{\partial k_i} dk_i \qquad \lambda_{\nu}^{(ex)} = \lambda_{\nu}^{(a)} + \sum_{i=1}^{p} \frac{\partial \lambda_{\nu}^{(a)}}{\partial k_i} dk_i \tag{5}$$

Sob forma matricial tem-se :

$$\begin{bmatrix} \Delta y_1 \\ \vdots \\ \Delta y_m \\ \hline \Delta\lambda_1 \\ \vdots \\ \Delta\lambda_m \end{bmatrix} = \begin{bmatrix} \frac{\partial y_1}{\partial k_1} & \cdots & \frac{\partial y_1}{\partial k_p} \\ \vdots & \ddots & \vdots \\ \frac{\partial y_m}{\partial k_1} & \cdots & \frac{\partial y_m}{\partial k_p} \\ \hline \frac{\partial \lambda_1}{\partial k_1} & \cdots & \frac{\partial \lambda_1}{\partial k_p} \\ \vdots & \ddots & \vdots \\ \frac{\partial \lambda_m}{\partial k_1} & \cdots & \frac{\partial \lambda_m}{\partial k_p} \end{bmatrix} \begin{bmatrix} dk_1 \\ \vdots \\ dk_p \end{bmatrix} \quad \Rightarrow \quad \begin{array}{c} \begin{bmatrix} \Delta y \\ \hline \Delta\lambda \end{bmatrix} = \begin{bmatrix} S_y^{(k)} \\ \hline S_\lambda^{(k)} \end{bmatrix} \begin{bmatrix} \Delta p^{(k)} \end{bmatrix} \\ \underset{[m(c+1),\,1]}{\Delta Z} = \underset{[m(c+1),\,p]}{S} \; \underset{[p,\,1]}{\Delta p} \end{array} \tag{6}$$

onde m é o número de autovetores identificados; c é o número de graus de liberdade instrumentados; p é o número de macro-elementos de rigidez; N é o número de graus de liberdade do modelo de elementos finitos; n é o número de autovetores calculados do modelo de elementos finitos. Em relação à matriz de sensibilidade S, as expressões das derivadas primeiras das auto-soluções em relação aos parâmetros de rigidez são obtidas derivando-se a equação de equilíbrio do modelo, considerando-se igualmente as relações de ortonormalidade (Piranda, 1994). Faz-se uma aproximação por combinação linear dos autovetores de uma base modal incompleta $Y^{(a)}$. As expressões resultantes são :

$$\frac{\partial y_{\nu}^{(a)}}{\partial k_i} = Y^{(a)} t_{\sigma\nu}^{i} = \sum_{\sigma=1} y_{\sigma}^{(a)} t_{\sigma\nu}^{i} \tag{7}$$

$$\frac{\partial \lambda_{\nu}^{(a)}}{\partial k_i} = {}^{T}y_{\nu}^{(a)} K_i^{(a)} y_{\nu}^{(a)} \tag{8}$$

com :

$$t_{\sigma\nu}^{i} = -\frac{{}^{T}y_{\sigma}^{(a)} K_i^{(a)} y_{\nu}^{(a)}}{\lambda_{\sigma}^{(a)} - \lambda_{\nu}^{(a)}}, \sigma \neq \nu$$

$$t_{\nu\nu}^{i} = 0$$

Consideração dos Erros das Massas Generalizadas

A definição do resíduo dos autovetores implica na normalização correta dos autovetores identificados, condição difícil de satisfazer experimentalmente em identificação modal. Os erros de identificação das massas generalizadas podem assim gerar correções errôneas do modelo. Para resolver este problema, introduz-se as massas generalizadas como incógnitas suplementares. Designando por $\tilde{y}_v^{(ex)}$ o autovetor identificado sem erro de norma e por $y_v^{(ex)}$ o autovetor realmente obtido, supõe-se que $\tilde{y}_v^{(ex)} = \tilde{y}_v^{(ex)}(1-\alpha_v)$, onde α_v é um coeficiente real desconhecido. O sistema completo a resolver torna-se então :

$$\left[\begin{array}{c} \Delta y_1 \\ \vdots \\ \Delta y_m \\ \hline \Delta\lambda_1 \\ \vdots \\ \Delta\lambda_m \end{array}\right] = \left[\begin{array}{c|ccc} & y_1^{(ex)} & & 0 \\ S_y^{(k)} & & \ddots & \\ & 0 & & y_m^{(ex)} \\ \hline S_\lambda^{(k)} & & 0 & \end{array}\right] \left[\begin{array}{c} \alpha_1 \\ \vdots \\ \alpha_m \\ \hline \Delta p^{(k)} \end{array}\right] \tag{9}$$

Aspectos Dinâmicos e Matemáticos do Problema

Diversos aspectos interdependentes são de fundamental importância para a aplicação prática da técnica de ajuste de modelos em dinâmica, visto que o problema comporta fatores de natureza física e matemática. Estes estudos foram abordados no trabalho de Cunha (1997). Pode-se citar alguns pontos : estudo do problema de otimização na solução da equação de sensibilidade (6); reanálise das auto-soluções; posicionamento ótimo dos sensores; simulação com introdução de ruídos nas medidas; desenvolvimento do método com aproximação de segunda ordem nas equações de Taylor; estudo aprofundado do problema de estimação inicial dos parâmetros a serem identificados, com utilização da técnica dos algoritmos genéticos.

Método de Otimização

O método de otimização utilizado para o cálculo da solução Δp na expressão de sensibilidade (6) é do tipo gradiente sob restrições de desigualdade. O princípio deste método, chamado Método das Direções Realizáveis Modificado (DOT, 1990), consiste em determinar a solução que minimiza a função custo $J(p)$, com a vantagem de precisar a direção e o ganho do passo de busca no espaço paramétrico. A função custo é formada à partir das distâncias entre as auto-soluções e as distâncias dos parâmetros de correção :

$$J(p) = {}^T\Delta y(p) W_y \Delta y(p) + {}^T\Delta\lambda(p) W_\lambda \Delta\lambda(p) + {}^T\Delta p(p) W_p \Delta p(p) \tag{10}$$

com as restrições de desigualdade :

$$\Delta p_i^{\inf} \le \Delta p_i \le \Delta p_i^{\sup} \, e \, p_i^{\inf} \le p_i \le p_i^{\sup}$$

onde:

$\Delta y = y^{(ex)} - y^{(a)} \in R^{mc,1}$ é o vetor das distâncias dos autovetores;
$\Delta\lambda = \lambda^{(ex)} - \lambda^{(a)} \in \mathrm{R}^{m,1}$ é o vetor das distâncias dos autovalores;
$\Delta p = p - p^{(0)} \in \mathrm{R}^{p+q,1}$ é o vetor das correções paramétricas;
$W_y \in \mathrm{R}^{mc,mc}$, $W_\lambda \in \mathrm{R}^{m,m}$ e $W_p \in \mathrm{R}^{p,p}$ são as matrizes de ponderação, escolhidas segundo a especificidade do problema.

Adaptação do Método de Sensibilidade aos Materiais Compostos

Dentro do contexto das Teorias de Placas e Cascas Estratificadas, considerando-se a variedade e a complexidade dos parâmetros que influenciam o comportamento mecânico dos compostos, existem diversas abordagens para a escolha do campo de deslocamentos, das tensões e das condições de contorno associadas (Bert, 1984; Cunha, 1997). Utilizou-se neste trabalho a chamada Teoria de Cisalhamento de Primeira Ordem, que considera o efeito do cisalhamento transversal, e que possibilita a obtenção de bons resultados para a maioria dos compostos estratificados, incluindo-se os sanduíches. A equação constitutiva é escrita da seguinte maneira :

$$\begin{bmatrix} N \\ M \\ Q \end{bmatrix} = \begin{bmatrix} A & B & 0 \\ B & D & 0 \\ 0 & 0 & H \end{bmatrix} \begin{bmatrix} \varepsilon_m \\ k \\ \gamma_c \end{bmatrix} \tag{11}$$

onde:

$[A] \in R^{3,3}$: matriz de rigidez em membrana;

$[B] \in R^{3,3}$: matriz de acoplamento em membrana-flexão/torção;

$[D] \in R^{3,3}$: matriz de rigidez em flexão/torção;

$[H] \in R^{2,2}$: matriz de rigidez em cisalhamento transversal.

$$\begin{aligned} A_{ij} &= \sum_{k=1}^{n} (\overline{Q}_{ij})_k (h_k - h_{k-1}) & B_{ij} &= \frac{1}{2}\sum_{k=1}^{n} (\overline{Q}_{ij})_k (h_k^2 - h_{k-1}^2) \\ D_{ij} &= \frac{1}{3}\sum_{k=1}^{n} (\overline{Q}_{ij})_k (h_k^3 - h_{k-1}^3) & H_{ij} &= k_{ij}\sum_{k=1}^{n} (\overline{Q}_{ij})_k (h_k - h_{k-1}) \end{aligned} \tag{12}$$

sendo $\overline{Q}_{ij}$ as constantes de rigidez de uma camada em uma direção qualquer; h_k a cota da face da camada k; n o número de camadas e k_{ij} os fatores de correção do cisalhamento transversal. Estes fatores visam corrigir as deformações de cisalhamento transversal ao longo da espessura da placa. Especificamente em relação aos sanduíches este aspecto é ainda mais importante devido à grande diferença entre as características mecânicas e geométricas das camadas, o que pode dificultar também a condição de continuidade dos deslocamentos e das tensões cisalhantes nas interfaces das camadas (Cunha, 1997).

A identificação de propriedades de rigidez de materiais compostos por métodos do tipo ajuste de modelos em dinâmica é relativamente recente. Dada a sua complexidade, o tema está bastante aberto. De fato, o caráter de anisotropia, a diversidade dos materiais e a variedade das formas estruturais faz com que o comportamento mecânico dos materiais compostos seja particular. Pode-se citar por exemplo o efeito de acoplamento dos esforços e o fenômeno de delaminação, típicos dos estratificados em geral (inclusive sanduíches). Desta forma, não existe na literatura formulações gerais que permitam resolver todos os casos de identificação. Encontra-se frequentemente estudos aplicados à casos particulares. A grande maioria destes estudos utiliza o método de sensibilidade, com estimação do tipo Bayes (Frederiksen, 1994; Pedersen, 1988; Deobald and Gibson, 1986). Uma maneira interessante de abordar o problema é de utilizar as constantes de rigidez da lei de comportamento da estrutura (Eq. 11) que expressa as resultantes e os momentos em função das deformações de membrana, de cisalhamento e das curvaturas (Sol, 1986; Link and Zhiqing, 1993). A utilização das matrizes **A**, **B**, **D** e **H** apresenta algumas vantagens em relação a outras formas de parametrização do problema :

- Facilidade para a compreensão do comportamento mecânico da estrutura : estas "propriedades globais" explicitam os efeitos de membrana, flexão, torção, cisalhamento, acoplamento, etc;
- Possibilidade de fazer a interface do método de sensibilidade com os programas de cálculo de elementos finitos, pois as constantes de rigidez são lineares em relação às matrizes elementares de rigidez;
- Finalmente, pode-se lembrar que os programas comerciais de elementos finitos permitem a utilização direta das constantes **A**, **B**, **D** e **H** como dados de entrada, o que evita a identificação das propriedades das camadas. Este aspecto pode ser interessante para o caso das estruturas sanduíches, pois a identificação das propriedades das camadas, em particular para as colméias, não é evidente.

No método de sensibilidade as correções são efetuadas nos macro-elementos, que são as componentes das matrizes **A**, **B**, **D** e **H**. Cada macro-elemento possui assim um papel bem definido no comportamento mecânico da estrutura. Para ilustrar a idéia, toma-se como exemplo o caso de uma placa estratificada simétrica. As correções nos p macro-elementos são feitas da seguinte forma :

$$K^a = \sum_{i=1}^{p} k_i K_i = k_1 D_{11} K_1 + k_2 D_{12} K_2 + k_3 D_{22} K_3 + k_4 D_{16} K_4 + k_5 D_{26} K_5 +$$

$$+ k_6 D_{66} K_6 + k_7 A_{11} K_7 + k_8 A_{12} K_8 + k_9 A_{22} K_9 + k_{10} A_{16} K_{10} + \qquad (13)$$

$$+ k_{11} A_{26} K_{11} + k_{12} A_{66} K_{12} + k_{13} H_{44} K_{13} + k_{14} H_{55} K_{14}$$

onde : $D_{11}K_1$, $D_{12}K_2$, . . ., $H_{55}K_{14}$ representam as matrizes de rigidez dos macro-elementos; k_i é o coeficiente de correção do macro-elemento i; K^a é a matriz de rigidez completa. As constantes de rigidez são : D_{11} - rigidez de flexão x; D_{12} - rigidez de acoplamento flexão x / flexão y; D_{22} - rigidez de flexão y; D_{16} - rigidez de acoplamento flexão x / torção; D_{26} - rigidez de acoplamento flexão y / torção; D_{66} - rigidez de torção; A_{11} - rigidez de membrana x; A_{12} - rigidez de acoplamento membrana x / membrana y; A_{22} - rigidez de membrana y; A_{16} - rigidez de acoplamento membrana x / cisalhamento xy; A_{26} - rigidez de acoplamento membrana y / cisalhamento xy; A_{66} - rigidez de cisalhamento xy; H_{44} - rigidez de cisalhamento transversal yz; H_{55} - rigidez de cisalhamento transversal xz.

Esquematicamente, a discretização elementos finitos dos macro-elementos, que permite a obtenção da matriz de rigidez completa, é mostrada na Fig. (2).

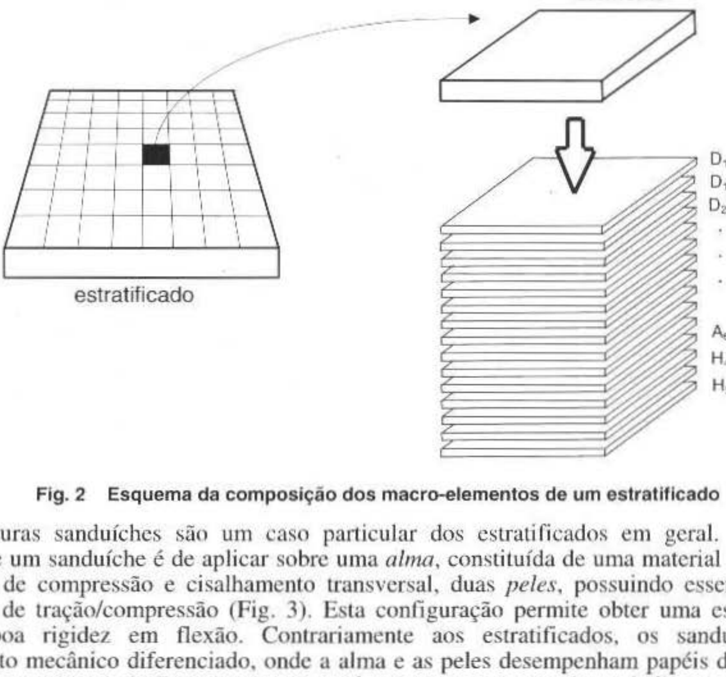

Fig. 2 Esquema da composição dos macro-elementos de um estratificado

As estruturas sanduíches são um caso particular dos estratificados em geral. O princípio de construção de um sanduíche é de aplicar sobre uma *alma*, constituída de uma material leve e com boas propriedades de compressão e cisalhamento transversal, duas *peles*, possuindo essencialmente boas propriedades de tração/compressão (Fig. 3). Esta configuração permite obter uma estrutura bastante leve, com boa rigidez em flexão. Contrariamente aos estratificados, os sanduíches têm um comportamento mecânico diferenciado, onde a alma e as peles desempenham papéis distintos. A alma trabalha basicamente em cisalhamento transversal, enquanto que as peles trabalham como membranas (Pagano, 1970; Dang, 1976; Donatus, 1989). Existem aspectos relativos ao comportamento mecânico das estruturas sanduíches que dificultam a modelização. Para tal, utilizam-se teorias aproximadas que simplificam o problema. Por exemplo, a determinação das propriedades físicas e mecânicas da alma não é evidente, dada a complexidade da geometria da mesma. Adota-se para este caso propriedades médias equivalentes. Quanto ao aspecto de identificação das propriedades elásticas dos sanduíches, desde que a modelização tenha sido feita corretamente, não existem problemas particulares com relação à identificação dos estratificados em geral. Isto será verificado na simulação numérica a seguir.

Simulação Numérica

A placa sanduíche analisada faz parte de uma estrutura real, chamada TSP (*Truss Supported Platform*), elaborada à partir de um acordo científico entre a Agência Espacial Européia e algumas universidades (Cunha, 1997). As características da estrutura e as condições de ensaio são (Fig. 3) : constituição das peles : estratificado em CFRP (*Carbon Fiber Reinforced Plastic*); constituição da alma: colméia em alumínio (*NIDA*); condição de contorno : livre-livre; número de sensores (acelerômetros) (🡅) = 17 (z); número de modos medidos "experimentalmente" = 10.

Propriedades das peles :

$E_1 = 1.35 \times 10^{11}$ N/m^2
$E_2 = 1 \times 10^{10}$ N/m^2
$G_{12}=G_{13} = 5 \times 10^9$ N/m^2
$G_{23} = 4.5 \times 10^9$ N/m^2
$\nu_{12} = 0.27$
$\rho = 1580$ Kg/m^3

Propriedades da alma :

$G_{13} = 1.52 \times 10^8$ N/m^2
$G_{23} = 7.88 \times 10^7$ N/m^2
$\rho = 36.8$ Kg/m^3

Estes valores levam às seguintes constantes elásticas a serem identificadas : $D_{11} = 1719$ N.m, $D_{12} = 526$ N.m, $D_{22} = 1719$ N.m, $D_{66} = 594$ N.m, $H_{44} = 7.6 \times 10^6$ N/m, $H_{55} = 8.0 \times 10^6$ N/m.

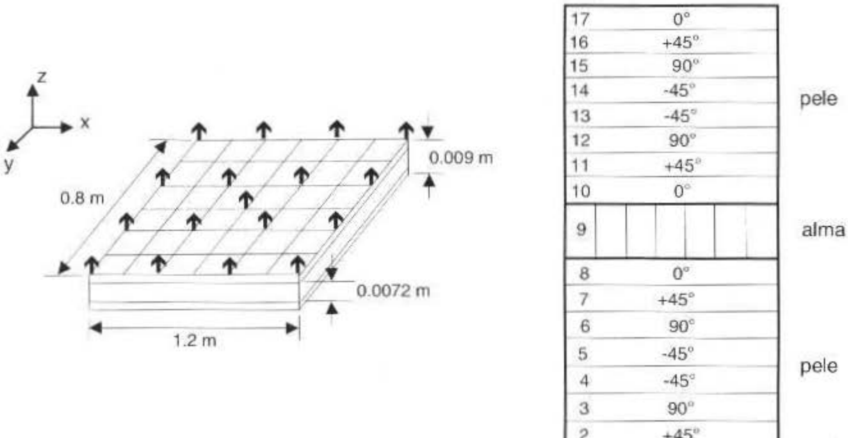

Fig. 3 Estrutura sanduíche e condições de ensaio

A distribuição dos sensores na estrutura foi obtida a partir de uma técnica de posicionamento ótimo, baseada na minimização do condicionamento da matriz modal (Cunha, 1997). As constantes de rigidez do modelo inicial foram perturbadas em ± 25%. O problema consiste em tentar recalcular os valores das perturbações introduzidas através da técnica de ajuste de modelos. Trata-se portanto de uma simulação numérica de identificação.

Os resultados obtidos foram bastante satisfatórios. A Figura 4 mostra a evolução dos parâmetros no processo de ajuste ao longo das iterações. Os gráficos mostram uma excelente convergência destes parâmetros, com uma redução significativa das distâncias entre as auto-soluções. Verifica-se uma boa sensibilidade para todas as constantes. A Tabela 1 confirma os bons resultados das correções, onde os valores das constantes de rigidez iniciais foram reencontrados (o número entre parênteses representa a diferença em relação ao modelo inicial).

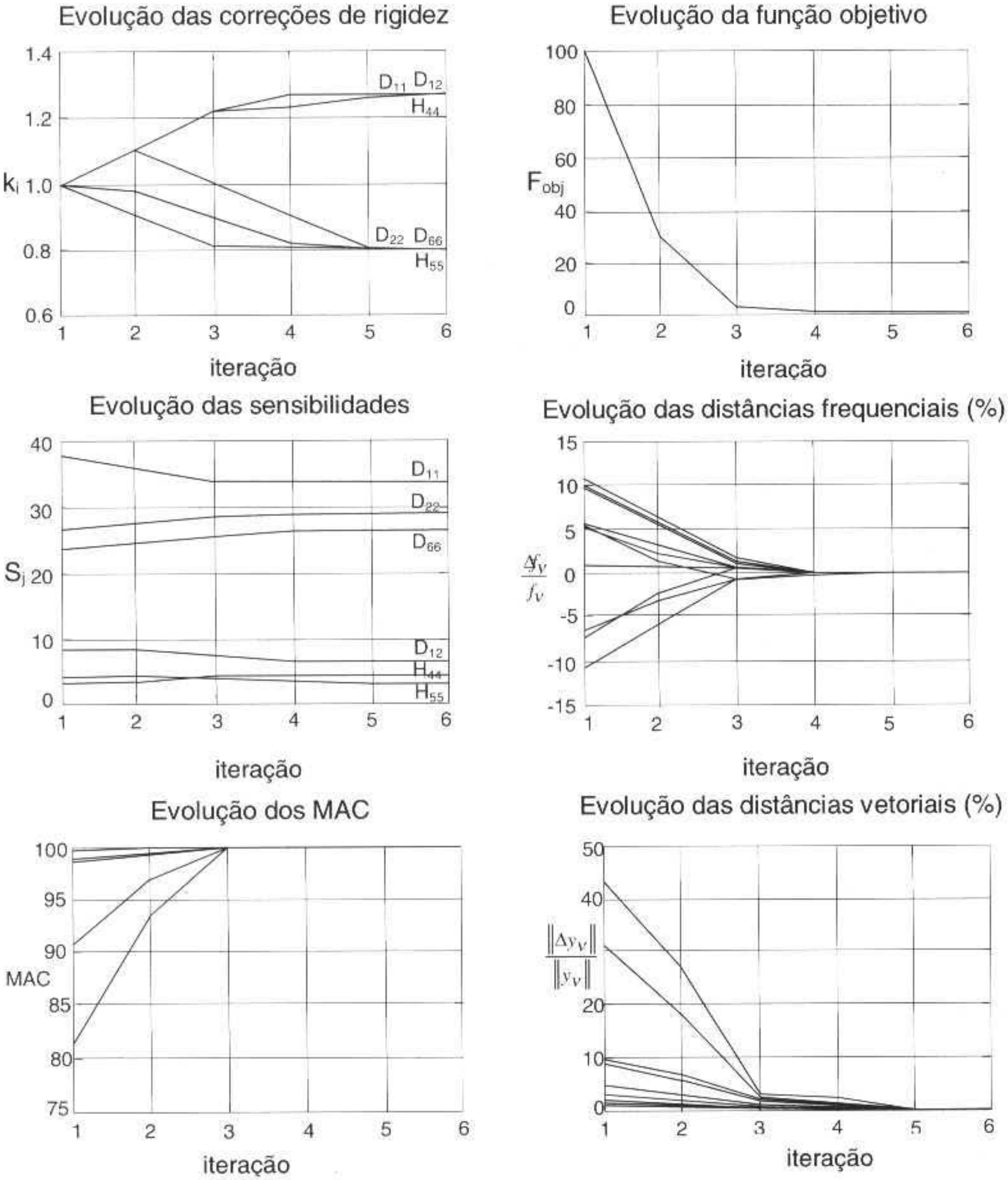

Fig. 4 Evolução dos parâmetros de ajuste ao longo das iterações

Tabela 1 - Resultado final do ajuste das constantes de rigidez

Constantes de rigidez	Modelo Inicial	Modelo Perturbado	Modelo Ajustado
D_{11} (N.m)	1719	2149 (25%)	1719 (0%)
D_{12} (N.m)	526	658 (25%)	526 (0%)
D_{22} (N.m)	1719	1376 (20%)	1719 (0%)
D_{66} (N.m)	594	475 (20%)	594 (0%)
H_{44} (N/m)	7.6×10^6	9.5×10^6 (25%)	7.6×10^6 (0%)
H_{55} (N/m)	8.0×10^6	6.4×10^6 (20%)	8.0×10^6 (0%)

Conclusão

A diversidade dos materiais e a complexidade das configurações estruturais faz com que a elaboração de modelos gerais de comportamento para os materiais compostos seja bastante difícil. Isto acontece igualmente para os métodos de identificação de propriedades mecânicas das estruturas estratificadas e sanduíches. Dentro deste contexto, a técnica de identificação à partir de ensaios dinâmicos é interessante pois pode ser aplicada em vários tipos de estruturas. O processo é do tipo não destrutivo e sua implementação é relativamente simples. A metodologia utilizada se mostra bem adaptada ao caráter de anisotropia dos materiais compostos. Em relação à outras técnicas de identificação, o método apresenta a vantagem de simplificar consideravelmente os testes pois pode-se identificar várias propriedades diferentes, de maneira simultânea. Uma outra vantagem é que se pode aplicar a técnica de identificação diretamente na estrutura (placas, cascas, tubos ou mesmo geometrias mais complexas), sem a necessidade de corpos de prova adaptados a cada ensaio, segundo o parâmetro a ser identificado. Por outro lado, as constantes de rigidez identificadas podem ser introduzidas diretamente como dado de entrada nos programas comerciais de elementos finitos.

Deve-se observar três aspectos importantes no processo de identificação : boa sensibilidade e independência linear das constantes a serem identificadas e uma boa base modal com um número suficiente de sensores. Existem várias fontes de erros possíveis na técnica de ajuste de modelos. Estes erros são (Cunha, 1997) : de modelização (malha elementos finitos, hipóteses simplificadoras de cálculo, etc) ; erros no processo de correção (método de sensibilidade) : má representatividade na função objetivo (linearização do problema, base modal experimental reduzida, ponderação dos parâmetros, etc.), não-unicidade e instabilidade da solução, etc ; erros de topologia do material : heterogeneidade das propriedades físicas, imperfeições geométricas (espessura, orientação das fibras, etc.), defeitos em geral ; erros de medidas : erros sistemáticos e aleatórios quando do ensaio dinâmico (posicionamento dos sensores, ruídos, etc.).

Concluindo, pode-se dizer que a qualidade dos resultados é, de uma maneira geral, ligada diretamente à qualidade do modelo de elementos finitos, à estratégia de ajuste utilizada e à precisão das medidas experimentais. É a associação destes três fatores que pode conduzir à uma identificação confiável.

Referências

Bert, C.W. A, 1984, "Critical Evaluation of New Plate Theories Applied to Laminated Composites", Composite Structures 2, pp.329-347.

Chou, T.W. , 1992, "Microstructural Design of Fiber Composites", Cambridge University Press.

Cunha, J. , 1997, "Application des Techniques de Recalage en Dynamique à l'Identification des Constantes Elastiques des Matériaux Composites", Thèse de Doctorat, Université de Franche-Comté, LMARC.

Dang, P. , 1976, "Théories des Plaques Sandwiches Élastiques Anisotropes", Thèse de Doctorat, Université de Technologie, Compiegne.

Deobald, L.R. and Gibson, R.F. , 1986, "Determination of Elastic Constants of Orthotropic Plates by a Modal Analysis/Rayleigh-Ritz Technique", Proceedings 4^{th} IMAC, pp. 682-690.

Donatus, N.O. , 1989, "Nouveau matériau sandwich pour circuits imprimés : analyse théorique, réalisation de prototypes et essais de validation", Thèse de Doctorat, Université de Franche-Comté, LMARC.

Dot Users Manual, Version 2.04, VMA Engineering, 1990.

Frederiksen, P. S., 1994, "Estimation of Elastic Moduli in Thick Composite Plates by Inversion of Vibrational Data", Proceedings of the Second Int. Symposium on Inverse Problems, Paris, pp. 111-118".

Link, M. and Zhiqing, Z., 1993, "Vibration Test of CFRP Sandwich Plate and Material Parameter Updating", Rapport Université de Kassel.

Pagano, N. J., 1970, "Exact Solution for Retangular Bidirectional Composites and Sandwich Plates", Journal of Composite Materials, vol. 4, 20-34.

Pedersen, P. Laminates, 1988, "Analysis, Sensitivity, Optimal Design, Identification of Material Parameters", Notes for Lectures.

Piranda, J., 1994, "Analyse Modale et Recalage de Modèle", Projet de Mémoire d'Habilitation à Diriger des Recherches, Université de Franche-Comté, LMARC.

Sol, H., 1986, "Identification of Anisotropic Plate Rigidities Using Free Vibration Data", PhD Thesis, Vrije Universiteit Brussel (V.U.B.), Belgium.

RBCM - J. of the Braz. Soc. Mechanical Sciences
Vol. XXI - No.2 - 1999 - pp. 322-331

ISSN 0100-7386
Printed in Brazil

Life Cycle Analysis as a Business Strategy for the Process Industry

A. Caldeira-Pires
P. Ferrão
J.N. Carranca
Instituto Superior Técnico
Technical University of Lisbon
Dept. of Mechanical Engineering
1049 Lisboa Codex Portugal
armando@dem.ist.utl.pt

Abstract

It has been observed throughout Europe that environmental policy has not necessarily had a negative economic impact. The integration of environmental technologies in industry can conduct to both economic and ecological advantages compared to usual technologies, whereas the use of resources is minimised and with them, the raw emissions, at all stages of the production process.

This paper analyses the environmental and the technological assessment associated with the implementation of a cogeneration power plant, using a high pressure boiler burning olive oil bagasse (as obtained after extraction) and a low-power steam turbine. It demonstrates the use of Linear Programming modelling as a tool for identifying and evaluating the best possible options for environmental performance of the system analysed, and extends this technique for the assessment of indirect eco-taxes, also called "Pigou taxes", associated with environmental regulations. It is shown in this study that a balance between environmental and economic performance in systems analysis lies in exploring a set of alternative options for system improvements. The results show that for a steam demand value lower than 80% of the maximum steam production capacity, the profit associated with the over-burning of bagasse should be associated with increasing values of the Pigou tax in order to prevent the consequent over emission of CO_2. The paper shows that the economical profitability of the system is correlated with the CO_2 emissions reductions, for this particular project, for different loading conditions of cogeneration plant in oil extraction plant. Although the extrapolation of this conclusion should be considered with caution, it can be assumed to be valid for many cogeneration systems in industry. The principles of the Life Cycle Assessment - LCA applied with Linear Programming techniques have allowed the quantification of side effects, associated with the use of technologies assessment, contributing for supporting decision making based on technical information in environmental policy.

Keywords: *Life Cycle Assessment, Linear Programming, Cogeneration Power-Plant, Technological Innovation, Environmental Management.*

Introduction

In the later decades of this remarkable century, the relationship of humans to the environment has become a prominent subject in our social dialogue. This social concern is leading nations for the use of the precautionary approach to protect the environment. Where there are threats of serious or irreversible damage, scientific uncertainty shall not be used to postpone cost-effective measures to prevent environmental degradation.

In the current debate on environmental policy and economic development two basic positions can be differentiated, which can be characterised as follows:

It is argued that a demanding environmental policy can be combined successfully with economic and employment policies.

It is claimed that taking the lead in environmental policy can endanger the economy.

As pointed out by Coenen and Klein-Vielhauer (1997), empirical evidence exists in support of the first position. At the same time, it can be observed throughout Europe that environmental policy has not necessarily had a negative economic impact. Moreover, according to the OECD, most macro-economic studies on the link between environmental expenditures and employment suggest that net employment effects are still positive, even if this linkage is weak.

It can be shown that integrating environmental technologies in industry results in both economic and ecological advantages compared to usual technologies. From the ecological point of view, the use of resources is reduced, as well as the raw emissions, not only at the stage of manufacturing but at the preceding stages of resource extraction and refining. Integrated environmental technology also offers solutions where others technologies fail. The application of integrated environmental technology is

Manuscript received: October 1997; revised: August 1998. Technical Editor: Leonardo Goldstein Jr.

connected with an improvement of the ecological and resource efficiency and can also lead to an increase in overall productivity.

In this paper, the emphasis is on the assessment of the environmental and economical benefits of the implementation of a cogeneration power plant in an olive bagasse oil extraction plant in the overall context of the olive bagasse oil life cycle. The paper analyses both the environmental and the economical assessment associated with the implementation of a cogeneration power plant, using a high pressure boiler burning olive oil bagasse (as obtained after extraction) and a low-power steam turbine, as described by Ferrão et al. (1997).

This paper demonstrate the use of Linear Programming modelling as a tool for identifying and evaluating the best possible options for environmental performance of the system analysed, as suggested by Azapazig and Clift (1995), and extends this technique for the assessment of indirect eco-taxes, also called "Pigou tax" (Pigou was an economist which first defended eco-taxes, about 50 years ago; see Pigou, 1952), associated with environmental regulations. Since sustainable improvements cannot be carried out on the basis of environmental analysis only, it is shown in this paper that a balance between environmental and economic performance in systems analysis lies in examining a set of alternative options for system improvements.

Background: The Evolution of Corporate Environmental Management

Historically, industry has played a minor role in setting broader environmental goals. Industrial firms' managers have traditionally held a short-term view towards environmental goal setting with problems downstream and upstream from the manufacturer often not being taken into account by corporations. This attitude was sustained by an environmental policy based on a notion of the environment as a public good whose protection and development lies beyond the individual concerns of private business.

However, in the last three decades, it as been observed a shift in corporate environmental goal-setting practices. Corporate behaviour has been changing as consumers express their preferences for environmentally-friendly products and practices and manufacturers are obliged to look "upstream" and inquire into their suppliers environmental practices due to liability and marketing concerns, and as company operating costs increase as a result of new environmental regulations. This shift encompasses a four stage evolution of corporate environmental management as described by Ehrenfeld and Howard (1996): Environmental Management as Problem-Solving, Environmental Management as Compliance, Proactive Environmental Management and Managing for the Environment.

At a first and most basic level environmental management is viewed as a case-by-case problem solving issue. Environmental protection is of little or no concern to corporate decision-making, which is patent in the lack of permanent staff or budget for dealing with environmental issues. At a second stage of evolution environmental management is viewed as a regulatory compliance issue. Environmental regulation is perceived as important enough to merit full-time attention but there is no concern about the environment itself, as a motive of new practices. The third stage is attained under the believe that environmental protection has certain strategic advantages and significant cost reductions opportunities.. At this stage the goals of the firm transcend mere compliance with government standards and encompass the voluntary establishment of stricter standards. At the fourth and last stage environmental concerns become a core strategic factor in corporate decision-making in a manner that leads rather than follows public policy. At this stage environmental management is considered as a key determinant to sustainable development, growing out of proactive practices to a new target for industrial environmental performance - Eco-Efficiency. Is at this level that wise resource use and product life cycle analysis become key instruments to firms and life-cycle thinking a basic concept to arising goal setting procedures like Industrial Ecology and Design for the Environment (Angel and Huber, 1996).

Life-Cycle Assessment as an Emerging Environmental Management Tool

Life-Cycle Assessment (LCA) is a technique that can be used to evaluate the environmental performance of a product, process or activity from "cradle to grave" as it follows it from extraction of raw materials to final disposal. Originating from "net energy analysis" studies first published in the 1970's (e.g. Boustead, 1972; Sundstrom, 1973) LCA use and importance has been increasing in the last twenty years. Most of the early LCA studies considered only packaging and only in the beginning of the 1990's LCA started to be applied to different consumer products like chemicals and agricultural products or activities like transports. Conceptual guidance was developed as a result of the need of a more standard approach of conducting LCA studies. In 1990 the Society for Environmental Toxicology and Chemistry (SETAC) initiated activities to define LCA and developed a general methodology for LCA. Soon afterwards the International Organisation for Standardisation (ISO) started similar work on developing principles and guidelines for the LCA methodology. These two organisations reached a general consensus on the methodological framework and final documents on the international standardised LCA methodology are expected by the end of this year.

Life-Cycle Assessment , as defined by SETAC, is "a process to evaluate the environmental burdens associated with a product, process or activity by identifying and quantifying energy and materials used and wastes released to the environment; to assess the impact of those energy and material uses and releases to the environment; and to identify and evaluate opportunities to effect environmental improvements" (Assies, 1991, Consoli, 1993, Curran, 1996). Figure 1 presents the methodological framework for LCA studies, which comprises four main stages: Goal Definition and Scoping, Inventory Analysis, Impact Assessment and Improvement Assessment.

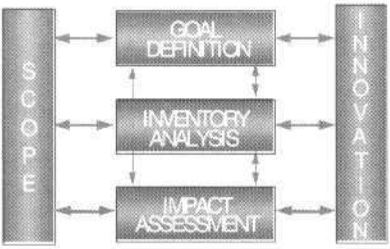

Fig. 1 LCA stages and the interaction between them

LCA is becoming an increasingly important decision making tool in environmental system management as it possesses among environmental management tools two unique attributes. First it considers the whole life cycle of a product or service from cradle to grave. This broad approach differs from other environmental management tools which consider specific parts of the life cycle, such as the releases of individual chemicals, the environmental balances of particular manufacturing sites, or the contributions to a single environmental problem. The life cycle approach can therefore help prevent "problem shifting", whereby a solution to one environmental problem leads to greater deterioration at another place or time in the life cycle. Second, the life-cycle approach allocates all the environmental burdens to the functional unit, i.e., to the value of the product or service to society. It is therefore possible to attempt a value/impact assessment whereby the value (performance and cost) of the product or "service to society" can be balanced against its environmental burden.

As an environmental management tool, LCA has two main objectives. The first is to quantify and evaluate the environmental performance of a product or a process and so help decision-makers to choose between alternative processes or products. Another objective is to provide basis for assessing potential improvements of the environmental performance of an existing or a new system. This is very important to engineers and environmental managers, because it can advice them on how to modify or design a system in order to decrease its overall environmental impacts. The first two stages of a full LCA, which together constitute the process of life cycle inventory (LCI), have been used as a tool for predicting environmental burdens associated with particular products or services. This approach, sustained by a large number of LCA experts, views LCA as one specific measuring technique, especially useful for assessing efficient resource use and waste management on a per-service basis and considered within an overall environmental management framework which encompasses the all range of environmental tools that are available. According to this view LCA can be most appropriately used as part of overall environmental management under its ultimate objective that should be environmentally and economically sustainable development (Berkhout, 1996).

Linear Programming

LCA provides for mathematical models of interaction between the human economic activities and the environment (e.g. Thompson and Thore, 1992). This representation, which relates the burdens and impacts of these activities to their outputs, is based on physical and technical relationships, including material and energy balances. Linear Programming (LP) is a simple systems modelling tool for LCA, and its value in the Inventory and Impact Assessment stages of LCA has already been demonstrated, e.g. Azapagic and Clift(1995) and Azapagic(1997).

LP problems can be stated as an optimisation problem to find a set of design parameters, $\mathbf{x} = \{x_1, x_2, x_n\}$, which can in some way be defined as optimal. In a simple case this may be the minimisation or maximisation of some system characteristic which is dependent of **x**, and subject to constraints. This original problem is called the primal linear problem, and is associated with its dual linear programming problem (e.g. Hiller and Lieberman, 1990). In this paper the relationships between the primal and the dual problem are stressed on the quantification of an excise tax to be imputed on the cost function due to pollutant emission, based on the identification of the optimal solution of the dual problem.

The study uses a commercial algorithm, General Algebraic Modelling System-GAMS, as described in Brooke *et al.*(1988), to perform the mathematical analysis.

Case Study

The Process Description

The interaction between business strategy, LCA and industrial costs is illustrated in this paper through an analysis of a technology improvement in a portuguese SME devoted to produce food oils.

The above mentioned company produces sunflower and olive bagasse oils and the impacts associated to the implementation of a cogeneration power-plant burning olive bagasse residuals is analysed in the broader context of the total life-cycle of the oil produced. The analysis is focused on the life-cycle of bagasse oil, which is obtained from olive bagasse, the sub-product of the production of olive oil.

The complete life cycle includes the olive farming and the olive oil primary extraction which is obtained by mechanical techniques as pressing and centrifuging the olives, together with water, resulting in three outputs: process oil, water and olive bagasse.

The olive oil is the main product of this cycle and has the largest economic value. The water must be treated after being released to the environment, and the olive bagasse is the major sub-product of the olive-oil production.

The evaluation of the environmental impacts associated with the olive oil and the olive-bagasse oil, resulting from the olive-oil extraction process, makes use of allocation techniques and criteria which, in this situation, could be based on their added value, although this discussion is beyond the scope of the present paper.

The olive bagasse has oil content of about 8% and is used to produce olive-oil bagasse. This product is transported to an oil extraction plant, where it is dried and the oil is chemically removed from the bagasse by a solvent, hexane, heated by low-pressure steam. This mixture of oil, water and solvent is separated in a distillation unit, allowing for the solvent re-utilisation. The remaining olive bagasse, after oil extraction, is used as fuel in the boiler.

The paper addresses the question of the economic and environment assessment of a technology improvement, the introduction of a cogeneration system in the oil extraction industry.

This assessment requires the comparison of two alternatives within the complete life-cycle:

- Steam production from a conventional boiler and purchase of electricity from the national grid;
- Steam production from a high-pressure boiler together with electricity generation in a steam turbine (cogeneration).

As this incremental step does only involve processes pertaining to the extraction industry, the main emphasis in this paper is given to this phase of the life cycle.

The costs involved in the energy utilisation throughout the industrial process depend on the consumption of exhausted olive bagasse (olive bagasse after oil extraction) and the electricity consumed. The hexane, fuel, steel and refractory production flows are similar in both situations, therefore they were not considered.

In the conventional solution, the steam demand of the oil production process is supplied by a steam generator burning exhausted bagasse, and the electrical energy consumed is supplied by the national grid. The technological improvement resulting from the integration of the cogeneration unit allows for the production of steam, and, simultaneously, the production of electricity, which can be sold to the national grid, whenever it exceeds the factory consumption.

The mass and energy flows characteristic of the olive bagasse oil extraction plant is illustrated in Fig. 2.

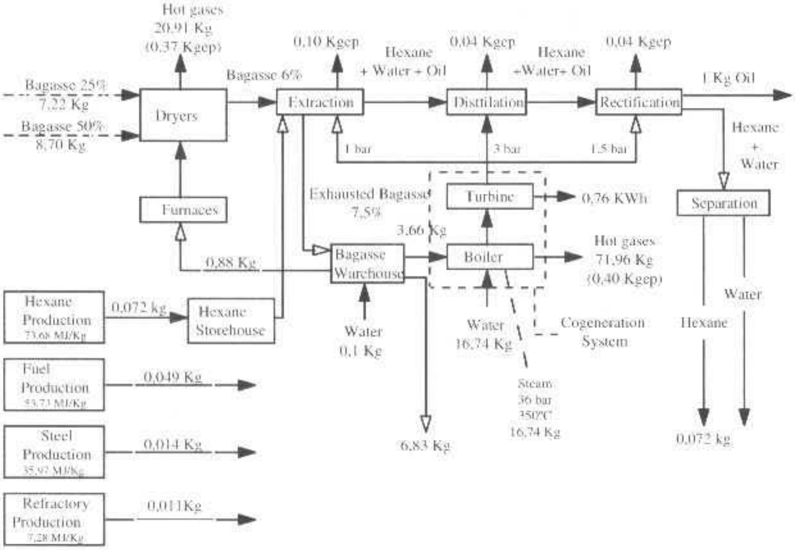

Fig. 2 Mass and energy flows characteristic of the extraction of 1Kg of olive bagasse oil

The economical and environmental assessment of the technological improvement related with the introduction of the cogeneration power plant in this industry can be evaluated taking into consideration two indicators:

The economic profit associated with the use of the cogeneration power plant.

The impact of the cogeneration power plant on the environmental burdens associated with the life-cycle of the olive-bagasse oil. As the major environmental intervention associated with the production of electricity in the cogeneration power plant consuming an industrial residual consist on the emission of CO_2, this was selected for the quantitative criteria for the environmental assessment of the technology improvement.

It should be noted that this industry is able to sell i) the surplus of steam generated, to a neighbour factory; ii) the surplus of electricity to the national grid; and iii) the surplus exhausted bagasse to the market. Therefore, the steam production, the electricity generation and the bagasse burning rate are variables that can be optimised.

The electrical power generation and steam production of the cogeneration power plant is depicted in Fig. 3 as a function of the exhausted bagasse burning rate. The lower and upper limits of the bagasse burning rate are technological limits of the cogeneration system.

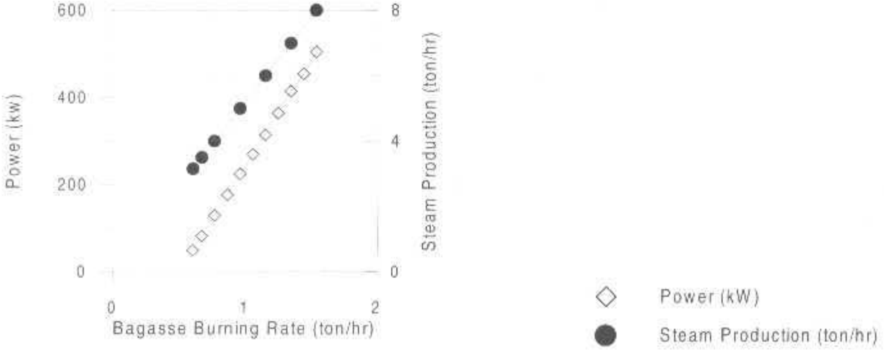

Fig. 3 Electrical power generation and steam production of the cogeneration power plant as a function of the exhausted bagasse burning rate

The Linear Programming Model

In the formulation of the environmental and economical assessment, the two indicators above mentioned can be merged, once a cost is associated to the release of CO_2.

This approach combines economic, technological and environmental assessment results in the optimisation of Eq. (1), that quantifies the economic benefit associated with the implementation of the cogeneration power-plant, F:

$$Max\ \mathbf{F} = K_{2min} \cdot \sum_{j=1}^{3} c_{2j} T_j + \sum_{i=1}^{5} \sum_{j=1}^{3} c_{ij} . T_j . \dot{x}_{ij} \tag{1}$$

In this equation C_{ij} accounts for the characteristic costs of the problem, where *i* is related with the five variables being optimised, as described below and, *j* is related with the values at different periods of the day, namely peak, full and empty, *j* = 1, 2, 3. In particular, in Portugal, these variables were quantified and are described elsewhere, Ferrão et al. (1997). The constraints of this linear programming model are described in Table 1.

Table 1 Constraints related with the Linear Programming Model

Constraint	Type
Total electrical energy produced at the cogeneration power-plant	Technological
Minimum amount of burned bagasse imposed by the cogeneration power-plant design parameters	Technological
Maximum amount of burned bagasse imposed by the cogeneration power-plant design parameters	Technological
Proportional relationship between the electrical energy bought and sold	Economical
Proportional relationship between the electrical energy bought and those produced and used within the process	Economical
Proportional relationship between the steam produced and the bagasse burned	Technological
Total CO_2 emissions [1]	Environmental

$$(CO_{BAG} - CO_{NAFTA} - CO_{GRID}) * \sum_{j=1}^{3} T_j\ (x_3 + x_5) \leq \sum_{j=1}^{3} T_j * (CO_{BAG} - \%pc * CO_{BAG} - CO_{NAFTA}) * (93.72 * SD - 245) \tag{2}$$

(1) – Sources of CO_2 emission are described in Table 2

This modelling approach generates "environmentally" optimum solutions, which are linked to their technological and economic performance, and, therefore, to the costs associated with them. The optimisation of the cost of the energy used within the life cycle of bagasse oil will contribute to identify acceptable solutions, which represent a balance between the objectives of economic and environmental performance.

This LP formulation is schematically represented in Fig. 4, which illustrates the main constraints and the solution domain, represented as a function of the exhausted bagasse burning rate.

The relations presented characterise the technology both in the conventional system and in the cogeneration power plant. Table 2 depicted the CO_2 sources related with the physical model studied, and used in Eq. (2).

Table 2 Sources of CO_2 Emission

Parameters	Definition	Value
CO_{GRID}	CO_2 emission rate at the national power-plant burning fuel-oil	0.641 kg CO_2 / kWh
CO_{NAFTA}	CO_2 emission rate at the neighbour factory boiler burning nafta	3.617 kg CO_2 / kWh
CO_{BAG}	CO_2 emission rate at the cogeneration plant burning exhausted bagasse	5.155 kg CO_2 /kWh
%pc	Loss of efficiency on the electricity generation process due to heat losses on the turbine	5 %
K_{2MIN}	Minimum burning rate necessary to supply process steam demand	SD/5.216 ton/h [2]

(2) - SD stands for the extraction process steam demand, which varies from 3.5 to 8 ton steam/hr, depending on the amount of bagasse to be extracted

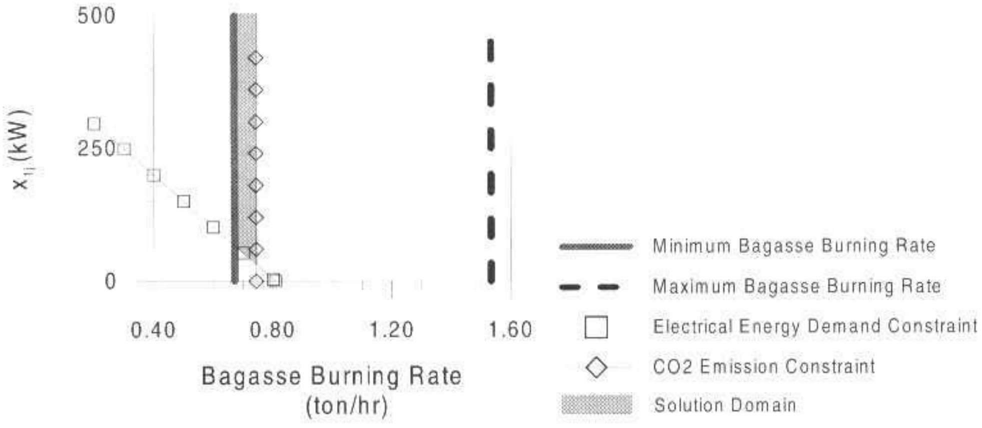

Fig. 4 Schematic Representation of the Linear Optimisation Problem

Results and Discussion

The simulation of the technological improvement associated with the cogeneration power-plant allowed for the quantification of the impact of the cogeneration system on the overall industrial efficiency, in terms of reduced pollutants emissions and energy consumption. The functional unit of the analysis consists on the service provided by the power plants, which is to say the amount of electricity, or its costs, supplied to the customer during one day.

The introduction of the cogeneration power plant has proved to have a positive environmental impact, contributing to significant air pollutant abatement, mainly by reducing CO_2, which would be emitted by the National power supplier plant along the complete processing of the olive bagasse oil.

The economical benefit associated with the electricity production in the cogeneration power-plant is a trade-off between the price of the energy as supplied by the national grid, the price of the fuel (exhausted olive bagasse) and the price of the steam which is sold to other industries. The daily net profit associated with the technological innovation is represented in Fig. 5, as a function of bagasse price (expressed in the Portuguese currency – Escudos) and SD.

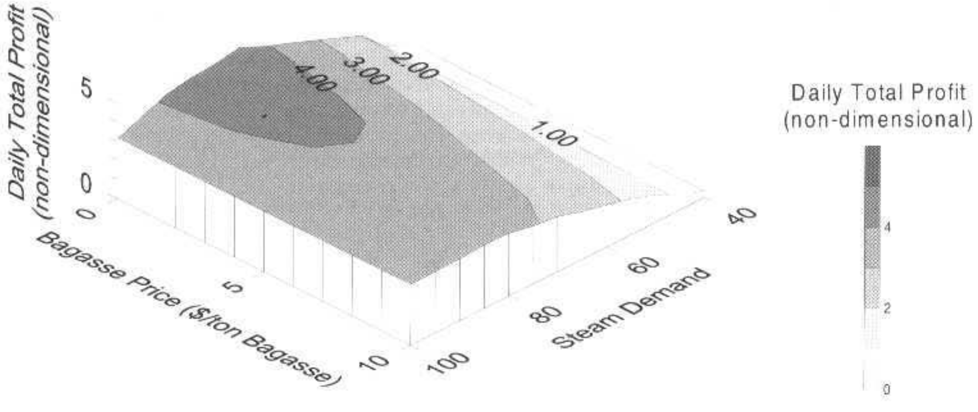

Fig. 5 Evolution of the Daily Total Profit (normalised by the original daily cost of electricity) as a function of the Bagasse price (Portuguese currency – Escudos) and of the Steam Demand (percentage of the maximum steam production capacity, 8 ton/hr)

It can be concluded that the maximum profit corresponds to the maximum steam demand value due to the over production of electricity, which is sold back to the national grid. It can be depicted in the same figure that the net profit is not dependent on the bagasse price, if the CO_2 emissions restriction is considered.

Pigou Tax

An important result of the LP analysis consists on the quantification of the so called Pigou tax, demonstrating the general proposition that, for a wide class of models, it is possible to combine environmental and economical concerns in the optimisation of an industrial process (e.g. Thore, 1991). A Pigou tax is an excise tax levied on the purchase of any good or service, based on the proposition that by suitable correction of the free prices it is possible to use the market to protect the environment.

The use of this methodology can be useful for a policy maker of a branch of local or central government for which the introduction of Pigou taxes or subsidies can constitute a viable alternative of actual implementation. In addition, it is felt that the results to follow are instructive in making clear the logical connection between optimised model and the price system. This connection rises even in cases where the policy maker does not contemplate any interference with the workings of the free markets or is in no position to make any such attempt. Moreover, it is demonstrated that, for a wide class of optimisation problems, the optimisation essentially modifies the existing price system.

The required value of this tax can be obtained as the optimal value of the dual variable (see Thore, 1991) related with the CO_2 emissions constraint. The cost structure associated with this new model will be derived from the constraint which has been artificially imposed to the CO_2 emissions, by stating that the CO_2 emissions from the cogeneration power plant shall not exceed the value corresponding to the same energy production in the national grid utility boilers. In the cogeneration power plant operation, the steam production is also taken into account by evaluating the CO_2 produced for generating that amount of steam in a conventional boiler.

The Pigou tax corresponds to the economic value associated with the loss of profit due to the limitation to the electricity generation in the cogeneration system imposed by the CO_2 emissions restrictions.

The results depicted in Fig. 6 clearly show that for a steam demand higher than 80% of the maximum steam production capacity, which corresponds to the isocontour region where the value of the Pigou tax equals the national grid electricity price, there is a weak dependence on the bagasse price as it will always be used to produce the steam required by a conventional system. For steam demand below this level the use of the cogeneration plant at its maximum steam production capacity results in net emissions of CO_2 higher than the conventional system and the profit associated with the over-burning of bagasse (resulting in a extra availability of electricity and steam), should be taxed with increasing values of the Pigou tax if the over emission of CO_2 is to be prevented.

In this context, the present European Commission's policy focus on the introduction of a Carbon Tax in order to stimulate energy savings and CO_2 emission reduction. The use of this tax will be performed as whole EC, however the tax design will be left to be evaluated by each country separately. This tax will be raised by Carbon content in energy (50%) and by the energy itself (50%), and it was rated at 1993 by 3US$/crude oil barrel with 1dollar/year increased until year 2000, reaching a maximum of 10US$/barrel. A company which has invested to save energy and to reduce CO_2 emission should be excluded with an except amount of (Carbon Tax Payment Total)- (Investment Cost), and if the previous calculation results in negative values, except the direct tax. These measures should neutralise the extra revenues due to over use of energy and over emission of CO_2.

Conclusions

The use of LCA approach is an important tool for assessing business competitiveness derived from integrating technology improvements with environmental performance. The paper shows that the economical profitability of the system is correlated with the CO_2 emissions reductions, for this particular project, for different loading conditions of cogeneration plant in the oil extraction plant.

Pollution taxes can contribute to internalise the externalities associated to the pollution damage costs caused by companies by restricting their pollution emissions to a sustainable optimal level. The accurate determination of an appropriate pollution tax level is dependent upon accurate information regarding the damage costs of that pollution and the benefits of its associated production of goods.

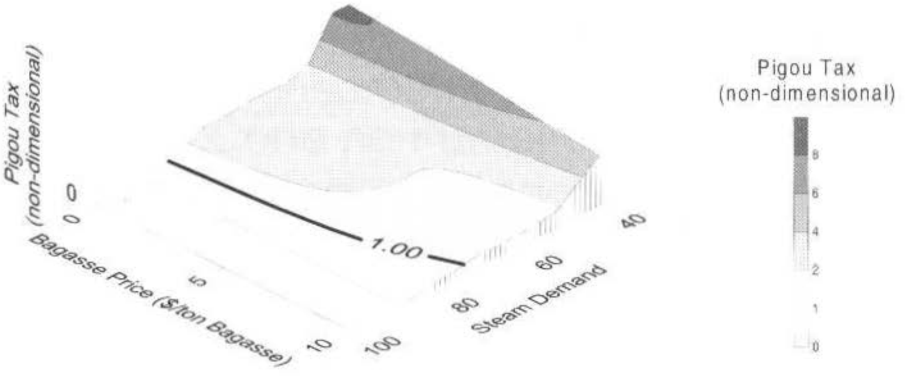

Fig. 6 **Evolution of the Pigou Tax (normalised by the mean hourly price of electricity) as a function of the Bagasse price (Portuguese Currency – Escudos) and of the Steam Demand (percentage of the maximum steam production capacity, 8ton/hr)**

The results show that in the study case evaluated for a steam demand value lower than 80% of the maximum steam production capacity, the profit associated with the over-burning of bagasse can be moderated with increasing values of the Pigou tax if the global over emission of CO_2 is to be minimised. Moreover, this study case also shows that the implementation of a cogeneration system is only environmentally and economically beneficial when it does correspond to the actual demands of the particular industry.

This correlation between economic profits and environmental benefits demonstrates that it pays to be green but an excise tax can be used to prevent the increasing of externalities costs. Although the extrapolation of this conclusion should be considered with precaution, it can be assumed to be valid for many cogeneration systems in industry.

The principles of the LCA analysis have thus allowed the quantification of side effects, associated with the use of technologies assessment, contributing for supporting decision making based on technical information in environmental policy.

Acknowledgements

Financial support for the implementation of the cogeneration project has been provided by DGXVII, through the THERMIE European program, and by Portuguese government, through the "PROGRAMA CIÊNCIA".

References

Angel, D. and Huber, J., 1996, "Building sustainable industries for sustainable societies", Business Strategy and the Environment, 5, pp.127-136.

Assies, J. A., 1991, "Life-cycle assessment - State of the art", Workshop Report from the Society of Environmental Toxicology and Chemistry - Europe, 2-3 December, Leiden, the Netherlands.

Azapagic, A., 1997, "Life Cycle Assessment: A Tool for Innovation and Improved Environmental Performance", in Proc. of 1st Intl. Conference on Technology , Policy and Innovation, Macau, pg 18.11- 18.19.

Azapagic, A. and Clift, R., 1995, "Life Cycle Assessment and Linear Programming - Environmental Optimisation of Product System", Computers Chem. Eng., 19, Suppl., pp.S229-S234.

Berkhout, F., 1996, "Life Cycle Assessment and Innovation in Large Firms. Business strategy and the Environment", 5, pp. 145-155

Boustead, I., 1972, "The Milk Bottle". Open University Press, Milton Keynes.

Brooke, A., Kendrick, D. and Meeraus, A., 1988, "GAMS: A User's Guide", The Scientific Press.

Coenen, R. and Klein-Vielhauer, S., 1997, "The Significance of Environmental Technology for Economically and Ecologically Sustainable Development", IPTS Report, 14, pp. 5-11.

Consoli et al., 1993, Guidelines for Life Cycle Assessment: A "Code of Practice" . SETAC, Brussels, Belgium.

Curran, M.A., 1996, "Environmental Life Cycle Assessment", McGraw-Hill, USA.

Ehrenfeld, J.R and Howard, J., 1996, "Setting Environmental Goals: The View from Industries - A Review of Practices from the 1960s to the Present". In Linking Science and Technology to Society's Environmental Goals", National Res. Council, Nat. Academy Press, pg. 281-325.

Ferrão, P., Caldeira-Pires, A., Carranca, J.N., 1997, "Life Cycle Analysis for technology Assessment in the Process Industry". In Proc. of 1st Intl. Conference on Technology, Policy and Innovation, Macau.

Hiller, F. S. and Lieberman, G.J., 1990, "Introduction to Operations Research", McGraw-Hill Book Co., 5th ed, Singapore.

Pigou, A.C., 1952, The Economics of Welfare, 4th ed: Macmillan, London.

Sundstrom, G., 1973, "Investigation of the Energy Requirements from Raw Materials to Garbage Treatment for Four Swedish Beer Packaging Alternatives". Report for Rigello Park AB, Sweden.

Thompson, G.L. and Thore, S. A. O., 1992, "Computational Economics: Economic Moddeling with Optimisation Software", Boyd & Fraser Pub. Com. , Massachusetts.

Thore, Sten A. O., 1991, "Economics logistics: the optimisation of spatial and sectoral resource, production and distribution systems", Quorum Books, New York.

RBCM - J. of the Braz. Soc. Mechanical Sciences
Vol. XXI - No.2 - 1999 - pp. 332-342

ISSN 0100-7386
Printed in Brazil

Projeto e Construção de um Protótipo de Transdutor Extensométrico para a Medição de Esforços de Corte na Furação

Design and Construction of a Prototype of a Strain-Gage Type Transducer for the Measurement of Drilling Forces

Volnei Andersson
Vitor José Frainer
Cláudio Cabrera Martins
Fundação Universidade Federal do Rio Grande
Departamento de Materiais e Construção
96201-900 Rio Grande, RS Brazil
metrolog@dmc.furg.br

Abstract

This work presents some considerations about design, construction and validation of a prototype of a strain-gage type transducer, developed to measure cutting forces produced in the drilling process of special geometric specimens. The validation tests showed that the analytical formulae employed can be used as a good design approach. When the prototype was used to measure cutting forces testing three steel specimens, the experimental values obtained nearly agree with the values analytically calculated using equations known from the bibliography. Therefore, the prototype utility in machinability testing of materials was proved.

Keywords: *Strain Gage Transducers, Drilling Forces, Design of Strain Gage Transducers, Drilling.*

Resumo

Neste trabalho são abordados conhecimentos de projeto, construção e validação de um protótipo de transdutor extensométrico, desenvolvido para a medição de esforços de corte na furação de corpos de teste. Os resultados de validação mostraram que a formulação analítica empregada tem boa aproximação para uso em projeto. Nos testes de uso, os esforços medidos foram comparados com esforços obtidos analiticamente de expressões conhecidas na bibliografia, comprovando-se a utilidade do protótipo em ensaios de usinagem de materiais.

Palavras chave : *Transdutor Extensométrico, Forças de Usinagem, Projeto de Transdutores Extensométricos, Furação.*

Introdução

A furação é um processo de fabricação com retirada de material, extremamente comum na produção de peças. A determinação experimental dos esforços de corte envolvidos nesse processo pode interessar no estudo de novos materiais, na avaliação do desempenho da máquina operatriz, no estudo da influência dos fluidos de corte e ângulos de corte das ferramentas, na determinação de parâmetros para o projeto de uma nova máquina ou no controle automatizado do processo de furação.

Segundo uma revisão bibliográfica apresentada por Levi (1966), em 1888 usava-se uma célula de carga para medir somente a força de avanço na furação. Em 1903, já se publicavam resultados experimentais de forças de corte, obtidos com dinamômetro mecânico, que empregava uma mola para medir forças de avanço, e alavancas, junto com dois dinamômetros mecânicos, para medir o torque. Para separar mecanicamente a força de avanço e o torque, empregava-se um rolamento de esferas ou simplesmente uma esfera. Nesse tipo de sistema de medição, foram introduzidas inovações tais como substituir o dinamômetro de mola por um hidráulico (Levi, 1966), ou por transdutores de força baseados em princípios elétricos (Cruz e Fonseca, 1987). Com o surgimento dos princípios elétricos, reconheceu-se que o uso de esferas ou rolamentos, para separar força e torque, introduzia histerese nas cargas baixas e ruído no sinal de saída, o qual é inerente às esferas (Levi, 1966). Então passou-se a usar transdutores com elemento elástico, em estruturas monobloco, com a separação dos esforços de corte ocorrendo eletricamente.

A medição dos esforços de corte na furação tem sido realizada principalmente com transdutores piezoelétricos e extensométricos. Os piezoelétricos têm a vantagem de apresentar elevadas rigidez e freqüências de ressonância. Em relação a eles, os extensométricos têm vantagens como menor influência da temperatura, mais fácil tecnologia de construção e menor custo. Devido também às freqüentes melhorias que têm ocorrido nas características de desempenho dos extensômetros resistivos,

Manuscript received: November 1997; revised version: September 1998. Technical Editor: Leonardo Goldstein Jr..

o uso deles predomina em transdutores com elemento elástico. Os usuários que necessitam transdutores específicos muitas vezes preferem projetar e construí-los, empregando geralmente o princípio dos extensômetros resistivos (Wevers e Mast, 1988).

O projeto de transdutores tem sido extensivamente divulgado na bibliografia e de um modo geral envolve aspectos metodológicos (Bosman, 1978; Doebelin, 1995; Finkelstein, 1983; Sydenham, 1989), modelagem matemática (Abdullah e Finkelstein, 1982; Finkelstein e Watts, 1978), dimensionamento e análise do elemento elástico (Abdullah e Erdem, 1978; Abdullah e Rahman, 1988; Anderson, 1975; Andersson e Lücke, 1988 e 1989; Bray, 1981; Bray et alli, 1990; Sydenham, 1984 e 1987), projeto dos componentes eletro-eletrônicos (Dorsey, 1977; Perry, 1984), uso da informática (Atkinsons, 1987; Brignell, 1985; Finkelstein, 1977; Sydenham, 1989; Woschni, 1977) e testes de validação (Doebelin, 1995; Levi, 1972; Lukas, 1982).

A construção de transdutores extensométricos envolve usinagem do elemento elástico e de componentes mecânicos, montagem dos extensômetros e dos demais componentes eletroeletrônicos, ajustagem do sinal de saída a valores padronizados, e calibração para o uso confiável (Andersson e Lücke, 1988; Dubois, 1981; Levi, 1972; Libertiny, 1975).

O objetivo deste artigo é mostrar alguns importantes conhecimentos de projeto, construção, testes de validação e de uso de um protótipo de transdutor extensométrico, desenvolvido para a medição da força de avanço e do torque, em corpos de teste submetidos ao processo de furação.

Projeto e Construção do Protótipo de Transdutor

Requisitos de Projeto

Quanto às características operacionais, o transdutor deverá atender aos seguintes requisitos:

- Transmitir os sinais de medição diretamente, usando fios elétricos, sem a necessidade de elementos de conexão girantes como escovas ou transmissão magnética;
- Ter espaço para acomodar um corpo de teste;
- Ser compacto e de fácil manutenção;
- Possuir vedação adequada para impedir contato do fluido de corte com elementos elétricos;
- Ter elemento elástico em estrutura monobloco;
- Sofrer um mínimo de influência de variações de temperatura no sinal de saída;
- Ter reduzido o sinal produzido por cada um dos dois esforços (força e torque) no canal do outro (efeito de sensibilidade transversal - Libertiny, 1975).

Quanto às características técnicas nominais, baseando-se em informações de bibliografia (Levi, 1966; Cruz e Fonseca, 1987; Wevers e Mast, 1975), foram estabelecidos os seguintes parâmetros:

- Faixa de forças de avanço de 0 até 10 kN;
- Faixa de torques de ± 140 Nm;
- Sinal de saída nominal, por canal, próximo de 2 mV/V.

O principal efeito da sensibilidade transversal é causado por componentes espúrias da força de avanço. Então, supondo uma força de avanço F aplicada com uma excentricidade ε, inclinada α em relação ao eixo vertical do transdutor e com as componentes radial, tangencial e axial sendo respectivamente $F_r = 0$, $F_t = F sen\alpha$ e $F_a = F cos\alpha$, o sinal adicional no canal do torque será causado por um torque T_F tal que

$$T_F = \varepsilon\, F\, sen\alpha \qquad (1)$$

onde $F sen\alpha$ representa a componente espúria. Assim, sendo F = 10kN e adotando valores especulativos de $\varepsilon = 0.001$m e $\alpha = 2°$, com base em valores práticos extremos, possíveis de ocorrer devido aos desvios geométricos de forma e posição das partes em contato, e também em conseqüência das deformações de contato, geradas em torno do ponto de aplicação da força F, resulta $T_F = 0.35$ Nm, que representa 0.25% da amplitude da faixa de medição do torque (140 Nm), ou seja, um valor de erro tolerável para transdutores extensométricos usuais. Portanto, sob tal aspecto, os valores máximos de força de avanço e torque foram estabelecidos convenientemente.

A forma escolhida do elemento elástico

Inicialmente aparece a questão de determinar em qual parte da furadeira deve ser montado o transdutor : junto ao cabeçote ou sobre a mesa? Wevers e Mast (1988) usaram um elemento elástico de forma básica cilíndrica que gira montado junto ao cabeçote. Levi (1966) desenvolveu um transdutor fixo à mesa e constituído de três elementos elásticos em forma de cruz, montados simetricamente em uma carcaça, constituindo um sistema estrutural onde foram colados doze extensômetros para detectar torque e outros doze para detectar força axial. Na montagem sobre a mesa, várias formas de elemento elástico podem ser usadas, com ausência de perturbações causadas por forças de inércia e sem a necessidade de transmitir sinais com elementos girantes.

Em geral, a escolha da forma do elemento elástico depende da carga máxima a ser aplicada, das possibilidades de arranjo (influências na compensação de temperatura e de componentes espúrias) e localização (influi na magnitude da sensibilidade) dos extensômetros sobre o elemento elástico, do material do elemento elástico, e de outras características de desempenho tais como resolução, não-linearidade, sinal de saída normalizado (Andersson e Lücke, 1991).

Formas de elementos elásticos derivadas de vigas apresentam amplas possibilidades de faixas de medição e, além disso, favorecem a simetria, característica geométrica importante para diminuir efeitos de temperatura e de componentes espúrias de cargas (Dubois, 1981). Assim, considerando esses fatores, escolheu-se o conhecido elemento elástico em forma de roda raiada (*spoked wheel*), representada na Fig. 1 e cujas quatro barras têm seção transversal retangular, para facilitar a colagem dos extensômetros resistivos e a usinagem.

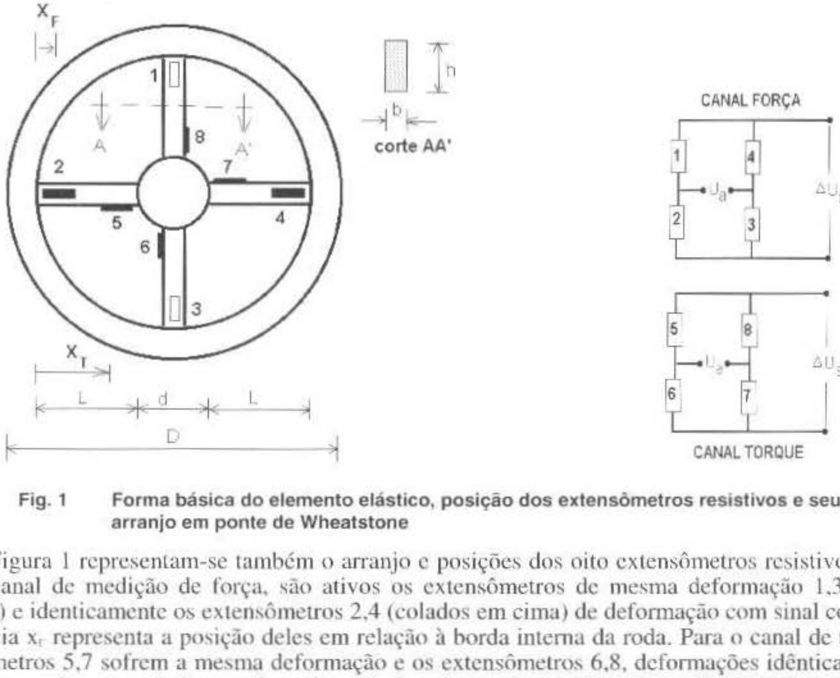

Fig. 1 **Forma básica do elemento elástico, posição dos extensômetros resistivos e seu arranjo em ponte de Wheatstone**

Na Figura 1 representam-se também o arranjo e posições dos oito extensômetros resistivos usados. Para o canal de medição de força, são ativos os extensômetros de mesma deformação 1,3 (colados embaixo) e identicamente os extensômetros 2,4 (colados em cima) de deformação com sinal contrário, e a distância x_F representa a posição deles em relação à borda interna da roda. Para o canal de torque, os extensômetros 5,7 sofrem a mesma deformação e os extensômetros 6,8, deformações idênticas de sinal contrário, e todos são colados nas faces laterais das vigas, a igual distância x_T da borda interna da roda. Idealmente os efeitos da força axial sobre os extensômetros do canal de torque são compensados pelo arranjo em ponte de Wheatstone usado e, da mesma forma, os efeitos do torque nos extensômetros do canal da força. Mas os efeitos de componentes espúrias e de desalinhamento dos extensômetros devem ser levados em conta na calibração. O arranjo simétrico dos extensômetros compensa o principal efeito de influência de temperatura no circuito ponte de Wheatstone, para cada canal, e os efeitos residuais são determinados na calibração.

Modelo Matemático

O elemento elástico escolhido foi modelado considerando que somente as quatro barras sejam deformáveis e tenham comportamento de vigas.

Para o caso da força de avanço, cada barra do elemento elástico foi modelada como uma viga em balanço com uma extremidade engastada na roda e a outra guiada verticalmente pelo corpo rígido central e sob a ação de um quarto da força de avanço aplicada. Na posição x_F, onde são colados os extensômetros 1,2,3 e 4 (Fig. 1), o momento fletor é

$$M = \frac{FL}{4}\left(\frac{1}{2} - \frac{x_F}{L}\right) \tag{2}$$

e as deformações específicas $\varepsilon_1 = \varepsilon_3 = \varepsilon_F$ e $\varepsilon_2 = \varepsilon_4 = -\varepsilon_F$, onde

$$\varepsilon_F = \frac{3FL}{2Ebh^2}\left(\frac{1}{2} - \frac{x_F}{L}\right) \tag{3}$$

O sinal de saída relativo y_F do canal da força de avanço F é determinado por

$$y_F = \left(\frac{\Delta U_S}{U_a}\right)_F \cong \frac{s_g}{4}\left(\varepsilon_1 - \varepsilon_2 + \varepsilon_3 - \varepsilon_4\right) = s_g \varepsilon_F \tag{4}$$

onde $s_g/4$ (V/V/m/m) é a sensibilidade de conversão e s_g (Ω/Ω/m/m) a sensibilidade de cada extensômetro resistivo.

Dentre as demais características de desempenho do transdutor, é importante para o controle do dimensionamento a não-linearidade η determinada aproximadamente por

$$\eta \cong \eta_e + \eta_m \tag{5}$$

onde η_e é a não-linearidade elétrica e η_m a não-linearidade mecânica definida como

$$\eta_m = \frac{v_r}{v_o} - 1 \tag{6}$$

e onde

$$v_o = \frac{F}{4Eb}\left(\frac{L}{h}\right)^3 \tag{7}$$

é o deslocamento clássico da extremidade guiada com rotação nula, e v_r é a melhor estimativa do deslocamento efetivo de tal extremidade, determinado através de (Andersson, 1990; Roark e Young, 1975)

$$v_r + \frac{\pi^3 bhEv_o}{32FL^3} v_r^3 - v_o = 0 \tag{8}$$

Essa expressão pode ser arranjada na forma

$$\frac{v_r}{v_o} - 1 = -\frac{\pi^3 bhE}{32FL^3} v_r^3 \tag{9}$$

Observa-se que $v_r < v_o$, mas também $v_r \cong v_o$. Então a não-linearidade mecânica pode ser estimada por

$$\eta_m \cong -\frac{\pi^3 bhE}{32FL^3} v_o^3 \tag{10}$$

Ao aplicar-se a força de avanço F no elemento elástico, devido à consideração de elemento rígido para a roda, em cada uma das quatro vigas gera-se uma força axial determinada por (Roark e Young, 1975)

$$F_a = \frac{\pi^2}{16} Ebh\left(\frac{v_r}{L}\right)^2 \cong \frac{\pi^2}{16} Ebh\left(\frac{v_o}{L}\right)^2 \tag{11}$$

que causa a deformação

$$\varepsilon_a = \frac{F_a}{Ebh} \qquad (12)$$

Esta deformação não aparece na estimativa do sinal determinada com a expressão (4). Mas provoca uma não-linearidade elétrica η_e em ponte de Wheatstone, determinada por (Andersson e Lücke, 1989)

$$\eta_e = -2 s_g \varepsilon_a \qquad (13)$$

Considerando a não-linearidade, a expressão de cálculo do valor previsto para o sinal de saída efetivo y_{Fr} passa a ter a forma

$$y_{Fr} = y_F(1+\eta_e) \qquad (14)$$

Quanto ao torque, deduziu-se uma expressão aproximada para estimar o sinal de saída, baseado no modelo de viga representado na Fig. 2, onde metade do corpo central do elemento elástico é suposta como uma barra prismática rígida de comprimento d sob ação da metade do torque. Observa-se que o plano de flexão dos dois elementos elásticos do modelo é o mesmo que contém as quatro barras do elemento elástico.

Em tal modelo, o momento fletor M vale

$$M = M_A + R_A x, \qquad para \quad 0 \le x \le L \qquad (15)$$

$$M = M_A + R_A x + \frac{T}{2}, \qquad para \quad (L+d) \le x \le (2L+d) \qquad (16)$$

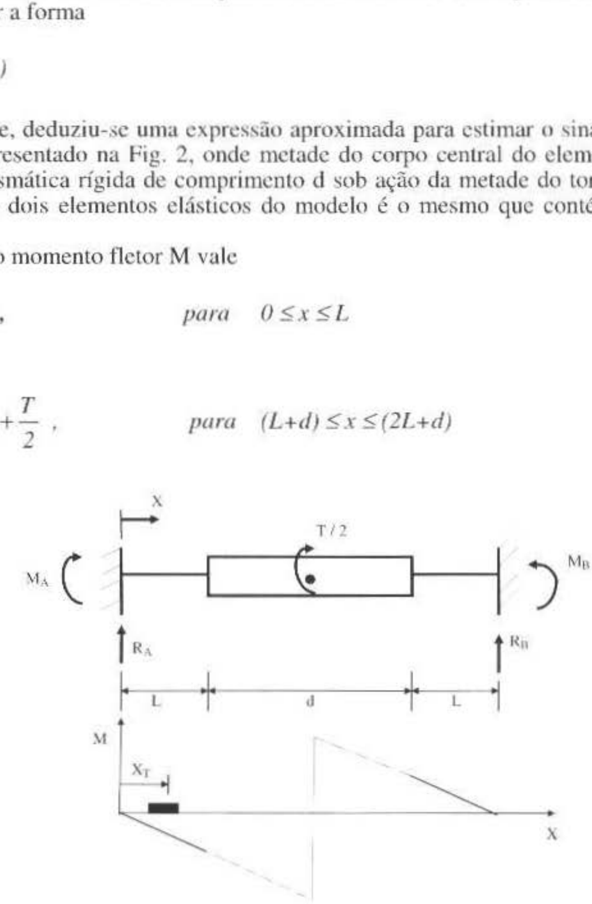

Fig. 2 Modelo de viga usado para estimar o sinal de saída no canal do torque

onde as reações M_A e R_A foram deduzidas empregando o teorema de Castigliano, para determinar o deslocamento e a rotação no engaste A (Fig. 2), os quais são nulos e, por isso, de suas expressões obtiveram-se

$$M_A = \frac{T}{4}\left[\frac{3\left(1+\frac{d}{L}\right)\left(2+\frac{d}{L}\right)}{4+6\left(\frac{d}{L}\right)+3\left(\frac{d}{L}\right)^2} - 1\right] \qquad (17)$$

$$R_A = -\frac{T}{2L}\left[\frac{3\left(1+\dfrac{d}{L}\right)}{4+6\left(\dfrac{d}{L}\right)+3\left(\dfrac{d}{L}\right)^2}\right] \tag{18}$$

A deformação específica ε_T, na superfície lateral de cada viga (Figs. 1 e 2) e na posição x_T, é

$$\varepsilon_T = \frac{6(M_A + R_A x_T)}{Ehb^2} \tag{19}$$

O sinal de saída relativo y_T no canal do torque é determinado aproximadamente por

$$y_T = \left(\frac{\Delta U_S}{U_a}\right)_T \cong \frac{s_g}{4}(\varepsilon_5 - \varepsilon_6 + \varepsilon_7 - \varepsilon_8) = s_g \varepsilon_T \tag{20}$$

O deslocamento clássico w_o das extremidades guiadas é obtido integrando duas vezes a equação geral da linha elástica, usando o momento expresso por (15), com as constantes de integração sendo determinadas para as condições de contorno $w_{,x}=0$ e $w=0$, em $x=0$. Assim, resulta

$$w_o = \frac{6}{Eh}\left(\frac{L}{b}\right)^3\left(\frac{M_A}{L} + \frac{R_A}{3}\right) \tag{21}$$

A não-linearidade mecânica é determinada usando (10), onde v_o e F são substituídos respectivamente por w_o e $T/(2d)$. Identicamente, a não-linearidade elétrica é determinada usando (11), (12) e (13) com v_o substituído por w_o.

Dimensionamento do Elemento Elástico

Geralmente o dimensionamento do elemento elástico é realizado usando expressões algébricas de características de desempenho, deduzidas em função de parâmetros geométricos e de propriedades elásticas do elemento e dos conversores elétricos, sob determinadas condições de projeto. Essas condições podem ser valores fixos, limites máximos, ou mínimos, concernentes às características consideradas. Freqüentemente empregam-se as condições : sinal de saída fixo, máxima tensão normal limitada a um valor máximo admissível, limite mínimo de freqüência natural, maior deslocamento limitado a um valor máximo, resolução e não-linearidade com limites máximos. Tal metodologia é fácil de aplicar e eficiente, quando se consideram transdutores com um único canal (Andersson e Lücke, 1991) e se dispõe de um aplicativo específico de auxílio ao projeto (Andersson e Lücke, 1988 e 1989). Para este caso de transdutor com dois canais, desejavelmente independentes, o dimensionamento torna-se mais complexo devido à dificuldade de obter dimensões que proporcionem sinais de saída aproximadamente iguais a 2 mV/V em ambos canais.

A sistemática de projeto consistiu então em interativamente dimensionar o elemento elástico como um transdutor de força, usando um aplicativo disponível e específico para auxiliar o projeto de transdutores de força uniaxial, que contém as expressões (2) até (13), aqui apresentadas (Andersson, 1990), e substituir os parâmetros geométricos obtidos na expressão de cálculo do sinal de saída relativo do canal de torque, repetidamente, até que resultassem sinais de saída próximos do valor de 2 mV/V, requerido inicialmente para os dois canais, e valores aceitáveis de outras características (como mínima não-linearidade) para o canal de força e não-linearidade mínima para o canal de torque.

Ao utilizar o aplicativo para o dimensionamento como transdutor de força, adotou-se o aço ABNT D6 (E = 207 GPa), disponível para o máximo diâmetro D = 115 mm, e foram usados os extensômetros resistivos existentes de designação KFC-2- C1-11 da KYOWA (120 Ω, s_g = 2 e comprimento da grade ativa de 2 mm). As dimensões das vigas e características de interesse para este trabalho, obtidas com o aplicativo, constam na Tabela 1.

No dimensionamento como transdutor de torque, considerando que o diâmetro do corpo central do elemento elástico seja o maior possível, para poder acomodar corpos de teste relativamente grandes, estabeleceu-se d = 0.060 m. Sendo conhecida a geometria básica e o módulo de elasticidade do elemento elástico, o fator s_g e a posição x_T dos extensômetros, com T = 140 Nm, usando as expressões

(15) até (21) e (10) até (13), resultaram o valor estimado do sinal de saída e as não-linearidades indicadas na Tabela 1.

Portanto, usando extensômetros resistivos disponíveis, montados sobre um elemento elástico em forma de roda raiada e de aço ABNT D6, e uma metodologia de dimensionamento baseada em uma formulação analítica modelada como viga, obtiveram-se as dimensões básicas do elemento elástico e sinais de saída relativos próximos do valor nominal de 2 mV/V inicialmente requerido para ambos canais. Nota-se que o valor do sinal de saída para o canal do torque não está tão próximo de 2 mV/V quanto o valor nominal do sinal de saída do canal de força. A igualdade de tais valores poderia ser obtida igualando as expressões (3) e (19) de onde resultaria uma expressão inter-relacionando os elementos geométricos básicos, posições dos extensômetros e cargas aplicadas. Isso implicaria em outra sistemática de projeto, com possibilidade de alteração dos valores nominais das cargas inicialmente requeridas.

Tabela 1 Dimensões básicas do elemento elástico e características previstas

Dimensões e características	Canal força	Canal torque
Comprimento das vigas	$L = 17.5$ mm	
Largura das vigas	$b = 4.6$ mm	
Altura das vigas	$h = 8.0$ mm	
Diâmetro do Corpo rígido central	$d = 60.0$ mm	
Diâmetro externo da roda	$D = 115$ mm	
Deslocamento para 10 kN	$v_o = 0.027$ mm	--
Deslocamento para 140 Nm	--	$w_o = 0.023$ mm
Posição da linha média da grade ativa dos extensômetros	$x_F = 4.5$ mm	$x_T = 13$ mm
Sinal de saída relativo	$y_F = 2.09$ mV/V	$y_T = 1.49$ mV/V
Não-linearidade mecânica	$\eta_m = -0.0003\%$	$\eta_m = -0.0014\%$
Não-linearidade elétrica	$\eta_e = -0.0012\%$	$\eta_e = -0.0004\%$
Não-linearidade	$\eta = -0.0015\%$	$\eta = -0.0018\%$

Construção do Protótipo

Na Figura 3, apresenta-se uma fotografia que mostra os elementos mecânicos e elétricos do protótipo construído. Nota-se que o recesso do corpo rígido central admite corpos de teste quadrados, com 38 mm de lado e 20 mm de espessura, e podem ser usadas brocas com até 20 mm de diâmetro.

O elemento elástico foi temperado a uma temperatura de austenitização de 850 °C, durante duas horas, e resfriado em óleo. Após, procedeu-se um duplo revenido a 210 °C, durante duas horas.

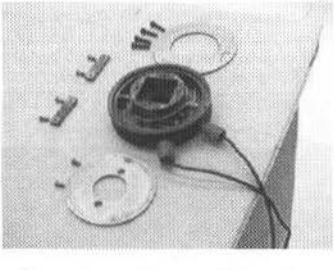

Fig. 3 Elementos eletro-mecânicos do protótipo

Os cabos elétricos para alimentação e saída de sinal contêm quatro fios, têm a blindagem ligada ao elemento elástico, e são fixados por um sistema tipo pinça (prensa-fio).

A proteção dos extensômetros e das ligações internas, contra a ação direta do fluído de corte, é conseguida usando dois anéis de aço, vedados com borracha de silicone.

Validação do Projeto

Na validação de projeto de transdutores com elemento elástico, devem ser realizados testes experimentais visando comparar o desempenho previsto com o efetivo e, se necessário, corrigir a formulação empregada. Basicamente, isso pode ser conseguido efetuando calibrações onde se procura determinar:

- A relação entre o sinal de saída de cada canal e as possíveis forças e momentos atuantes;

- A influência de variações de temperatura em cada canal;
- As respostas em freqüência para excitações nas direções das cargas nominais.

Além disso, outro item de fundamental importância a considerar nas calibrações é a estimativa das incertezas dos resultados de medição (GUIDE, 1993).

Neste artigo, apresenta-se a validação do modelo matemático através da determinação experimental da relação entre o sinal de saída de cada canal e a força e torque aplicados, o que representa o principal objetivo de uma calibração estática. A determinação criteriosa das incertezas, envolvendo tais relações estímulo-resposta e também as flutuações nos zeros e nas sensibilidades, não se apresentam.

A expressão de calibração estática usual, para relacionar o sinal y_k de cada canal e as forças x_i atuantes, é (Levi, 1972)

$$y_k = a_{ko} + \sum_{i=1}^{6} a_{ki} x_i \sum_{i=1}^{6} \sum_{j=1}^{6} a_{kji} x_i x_j \tag{22}$$

onde k=1,...,6 e a_{ko}, a_{ki}, a_{kji} são constantes determinadas por regressão. Os métodos para aplicar as forças x_i são discutidos em (Bray, 1981).

A expressão de uso tem a forma inversa

$$x_k = b_{ko} + \sum_{i=1}^{6} b_{ki} y_i + \sum_{i=1}^{6} \sum_{j=1}^{6} b_{kji} y_i y_j \tag{23}$$

onde b_{ko}, b_{ki}, b_{kji} também podem ser determinados por regressão.

A calibração estática do protótipo construído foi realizada medindo simultaneamente os sinais em cada um dos dois canais, primeiro para aplicações unicamente de forças de avanço (tabela 2) e depois só para torque (Tabela 3). Assim, ao empregar a expressão (22), o sinal y_F no canal de força é a soma dos dois sinais medidos ao aplicar primeiro só a força de avanço e depois só o torque. O sinal y_T no canal do torque é obtido identicamente.

Para relacionar sinais e esforços, optou-se pela forma linear da expressão (22), devido às insignificantes não-linearidades previstas e também para simplificar a obtenção de valores inversos, e que se representa matricialmente como

$$\begin{Bmatrix} y_F \\ y_T \end{Bmatrix} = \begin{Bmatrix} a_o \\ b_o \end{Bmatrix} + \begin{bmatrix} a_1 & a_2 \\ b_1 & b_2 \end{bmatrix} \begin{Bmatrix} F \\ T \end{Bmatrix} \tag{24}$$

Tabela 2 Sinais médios medidos ao aplicar somente força axial

Número de ordem	Força aplicada F (N)	Sinal no canal F (mV/V)	Sinal no canal T (mV/V)
1	0	0	0
2	1177.2	0.287	0.010
3	2954.4	0.570	0.020
4	3531.6	0.852	0.028
5	4708.8	1.134	0.035
6	5886.0	1.418	0.044
7	7063.2	1.691	0.061
8	8240.4	1.967	0.063
9	10000.0	2.404	0.079

Obs.: a maior incerteza padrão estimada dos resultados de medição foi ± 0.007 mV/V.

Usando regressão múltipla em nove pontos de medição (F_i,T_i,y_{Fi},y_{Ti}) obteve-se:

$a_o = 0.0016$	mV/V;
$a_1 = 2.413 \times 10^{-4}$	mV/V/N;
$a_2 = 6.325 \times 10^{-4}$	mV/V/Nm;
$b_0 = -0.0028$	m/VV;
$b_1 = 2.531 \times 10^{-6}$	mV/V/N;
$b_2 = 0.0101$	mV/V/Nm.

Tabela 3 Sinais médios medidos ao aplicar somente torque

Número de ordem	Torque aplicada T (Nm)	Sinal no canal T (mV/V)	Sinal no canal F (mV/V)
1	0	0	0
2	5.89	0.047	0.004
3	14.72	0.125	0.011
4	19.62	0.172	0.015
5	29.43	0.270	0.023
6	39.24	0.361	0.032
7	53.96	0.503	0.044
8	70.00	0.660	0.059
9	88.29	0.833	0.074
10	117.72	1.118	0.098
11	140.00	1.333	0.114

Obs.: a maior incerteza padrão estimada dos resultados de medição foi ± 0.006 mV/V.

Nas medições de sinais de cargas individuais, constatou-se que o sinal previsto para $F = 10000$ N está 13% abaixo do correspondente sinal medido. Para o torque $T = 140$ Nm, o sinal previsto supera o medido em 12%. Além disso, representando os sinais medidos como função polinomial do segundo grau de uma única variável independente, determinou-se a não linearidade terminal extrema em 0.06% para o canal da força de 0.4% para o torque. O efeito do torque representa aproximadamente 3% do sinal medido no canal da força e o efeito desta, 8% no canal do torque.

Observa-se que os valores previstos dos sinais de saída, obtidos analiticamente, diferem dos respectivos valores experimentais em quantidades aceitáveis para cálculos preliminares de projeto e, portanto, são válidos ao propósito de dimensionamento. Diferenças menores podem ser obtidas determinando as deformações específicas com o uso de aplicativos baseados no método dos elementos finitos. Da mesma forma, a previsão da não-linearidade, em termos do sinal de saída (expressão (10)), também é melhorada usando elementos finitos com formulação não-linear. Mas, mesmo assim, seriam obtidas diferenças consideráveis entre os valores previsto e experimental, como ocorreu com a formulação analítica usada. A principal causa disso deve-se ao atrito entre dispositivos de aplicação de carga e o elemento elástico, e à presença de componentes espúrias não identificadas no teste experimental de validação. Mas o uso das expressões analíticas deduzidas para o cálculo da não linearidade é útil ao controle do dimensionamento do elemento elástico. Os efeitos de sensibilidade transversal nos canais do torque e força não foram previstos analiticamente, mas eram esperados e foram levados em conta na expressão (24) de calibração.

Testes de Uso do Protótipo de Transdutor

Foram ensaiados três corpos de teste de aço ABNT 1020, usando fluído de corte e broca de 20 mm de diâmetro tendo ângulo de ponta de 120°. Escolheram-se um avanço de 0.25 mm/volta e rotação de 236 rpm na furadeira radial disponível (Fig. 4).

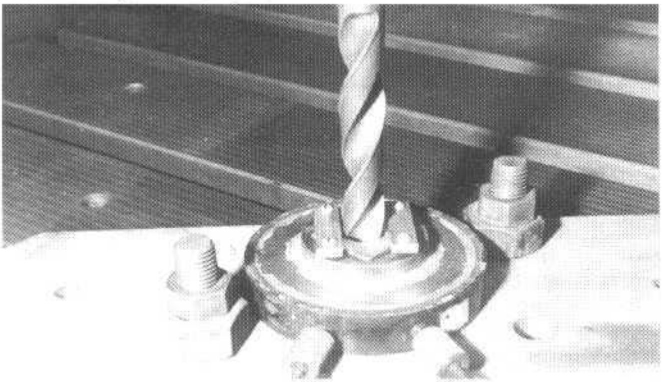

Fig. 4 Protótipo montado sobre a mesa da furadeira radial, tendo um corpo de teste ensaiado em seu recesso

Utilizando um sistema de aquisição de dados controlado por computador, mediram-se os sinais de cada canal, obtendo-se valores médios de y_F = 1.698 mV/V e y_T = 0.414 mV/V. Substituindo estes valores em (24), resultaram os esforços apresentados na Tabela 4 que são comparados com valores determinados de fórmulas conhecidas (Ferraresi, 1970), empregando as mesmas condições dos ensaios. Observa-se que as diferenças entre os valores medidos e os determinados analiticamente estão aproximadamente entre -1.0% e 2.5%.

Tabela 4 Esforços medidos com o protótipo de transdutor e determinados analiticamente

Esforços	Valor Medido	Valor Determinado Analiticamente	
Força de avanço		Spur	H. Daar
F (N)	6925 ± 50	6819	6754
Torque		Kienzle	Kronemberg
T (Nm)	39.5 ± 1.9	39.8	39.9

Conclusões

Apresentaram-se alguns conhecimentos importantes do desenvolvimento de um protótipo de transdutor extensométrico, que tem elemento elástico da conhecida forma de roda raiada e serve para ser utilizado na medição da força de avanço e torque, em ensaios de corpos de teste submetidos ao processo de furação com brocas de até 20 mm de diâmetro.

Quanto ao projeto, o trabalho contribui com uma metodologia baseada numa formulação analítica de vigas, que se mostrou aceitável na avaliação do sinal de saída relativo, e também com expressões aproximadas de não-linearidades, úteis para o controle do dimensionamento do elemento elástico.

O protótipo foi construído com a mais simples tecnologia de extensômetros resistivos e os efeitos de sensibilidade transversal podem ser levados em conta, ao usar o transdutor, empregando apropriadamente as expressões de calibração em sistemas de medição computadorizados. A sua caracterização metrológica (estática e dinâmica), envolvendo também a determinação experimental das influências de variações de temperaturas e das correspondentes incertezas de medição, serão objetivo de um futuro artigo.

Os testes de uso do protótipo mostraram resultados que têm uma boa aproximação com a formulação conhecida, ao medir esforços de corte na furação de corpos de teste de aço ABNT 1020.

Assim, pelos resultados de validação e testes de uso realizados, mostrou-se que o protótipo pode ser usado em ensaios de furação, onde se requer a medição de força e torque de usinagem, em condições semelhantes às apresentadas neste artigo. Além disso, considerando cada canal isoladamente, pode-se empregá-lo como um transdutor de força estática uniaxial ou torquímetro estático de reação.

Referências

Abdullah, F. e Erdem, U., 1978, "Mathematical modelling and design of a shear force load cell transducer", VDI-Berichte, Nr. 312, pp 149 - 155.

Abdullah, F. and Finkelstein, L., 1982, "Review of Mathematical Modelling of Instrument Transducers", IMEKO 9th World Congress, Pre-print Vol. V/I, pp 24 - 28, Berlin (west), May.

Abdullah, F. and Rahman, M. N., 1988, "Computer Aided Design of Elastic Elements in Instrumentation", IMEKO 11th World Congress, Vol. plenaries, Invited papers, Computers and Intelligent Systems, pp 143 - 158, Houston, Texas, USA, Oct.

Anderson, P. G., 1975, "Techniques for the Design of Integral-component Load Sensors", Experimental Mechanics, pp 282 - 288, July.

Andersson, V. 1990, "Uma Sistemática para o Projeto de Elementos Elásticos de Transdutores de Grandezas Mecânicas", Tese de doutorado, PG Eng. Mec., UFSC, Florianópolis, SC.

Andersson, V. e Lücke, H. A. H., 1988, "CAD in Transducers Design", IMEKO 11th World Congress, Vol. Applications, pp 601 - 608, Houston, Texas, USA, Oct.

Andersson, V. e Lücke, H. A. H., 1989, "Critérios Adequados para Projetar Elementos Elásticos de Transdutores Elétricos em Microcomputadores", Anais do X COBEM, pp 197 - 200, Rio de Janeiro, RJ, dez.

Andersson, V. e Lücke, H. A. H., 1991, "Recomendações de Escolha da Forma do Elemento Elástico em Projetos de Transdutores de Força Uniaxial", Anais do XI COBEM, pp 85 - 88, dez.

Atkinson, J. K., 1987, "Review article : Communication protocols in instrumentation", J. Phys. E. : Sci. Instrum. Vol. 20, pp 484 - 491.

Bray, A., 1981, "The Role of Stress Analysis in the Design of Force-standard Transducers", Experimental mechanics, pp 1 - 20, Jan.

Bray, A., Barbato, G. and Levi, R., 1990, "Theory and Practice of Force Measurement", Academic Press, London.

Brignell, J. E., 1985, "Invited Paper : Sensors within systems", J. Phys. E. : Sci. Instrum., Vol. 17, pp 759 - 765.

Bosman, D., 1978, "Instrument Science : Systematic design of instrumentation systems", J. Phys. E. : Sci. Instrum., Vol. 11, pp 97 - 105.

Cruz, C. e Fonseca, E. M., 1987, "Instrumentação de uma Furadeira Radial para Medição de Esforços de Furação", anais do IX COBEM, Florianópolis, SC, dez.

Doebelin, E. O., 1985, "Engineering Experimentation : Planning, Execution, Reporting", McGraw-Hill, Inc.

Dorsey, J., 1977, "Homegrow Strain-gauge Transducers", Experimental Mechanics, pp 255 - 260, July.

Dubois, M., 1981, "Six-component Strain-gage Balances for Large Wind Tunnels", Experimental Mechanics, pp 401 - 407, Nov.

Ferraresi, D., 1970, "Fundamentos de Usinagem dos Metais", Editora Edgar Blucher Ltda, Vol. I.

Finkelstein, L., 1977, "Instrument Science : Introductory article", J. Phys. E. : Sci. Instrum., Vol. 10, pp 566 - 572.

Finkelstein, L. and Finkelstein, A. C. W., 1983, "Review of design methodology", IEE Proceedings, Vol. 130, Pt. A, Nr. 4, pp 213- 222.

Finkelstein, L. and Watts, R. D., 1978, "Mathematical models of instruments - fundamental principles", J. Phys. E. : Sci. Instrum., Vol. 11, pp 841 - 855.

GUIDE to the expression of uncertainty in measurement, 1993, First Ed., International Organisation for Standardisation, Switzerland.

Levi, R., 1966, "Drill Press Dynamometers", Int. J. Mach. Tools Des. Res., Vol. 7, pp 269.

Levi, R., 1972, "Multicomponent Calibration of Machine Tool Dynamometers", J. of Eng. for Industry, pp 1067 - 1072.

Libertiny, G., 1975, "The Design of Multiaxial force/Moment Transducers with Particular Emphasis on the Problem of Cross-talk", Experimental Mechanics, pp 403 - 408, Oct.

Lukas, J., 1982, "Multicomponent Strain Gauge Measurement of Forces", IMEKO 9th World Congress, Berlin (west), Pre-print Vol. V/III, pp 358 - 371, May.

Perry, C. C., 1984, "Modern Strain Gage Transducers : Their Design and Construction", Epsilonics, parts I to IX, Oct. 1981 to Oct. 1984.

Roark, R. J. e Young, W. C., 1975, "Formulas for stress and strain", International Student Edition, McGraw-Hill, 5th ed.

Sydenham, P. H., 1984, "Elastic Design of fine Mechanism in Instruments", J. Phys. E. : Sci. Instrum., Vol. 17, pp 922 - 930.

Sydenham, P. H., 1987, "Computer-aided engineering of measuring instrument systems", CAE Journal, Vol. 4, Nr. 3, pp 117 - 123.

Sydenham, P. H., Hancock, N. H. and Thorn, R., 1989, "Introduction to Measurement Science and Engineering", John Wiley e sons.

Wevers, L. J. and Mast, J. P., 1988, "Development of a Multicomponent Torque and Force Transducer for Downwhole Drilling Research", IMEKO 11th World Congress, Vol. Sensors, pp 653 - 661, Houston, Texas, USA, Oct.

Woschni, E. G., 1977, "Instrument Science : Dynamics an information theory", J. Phys. E. : Sci. Instrum., Vol. 10, pp 1081 - 1092.

RBCM - J. of the Braz. Soc. Mechanical Sciences ISSN 0100-7386
Vol. XXI - No.2 - 1999 - pp. 343-354 Printed in Brazil

Evaluating The Quality Of Turned Hardened Steel Workpieces

Hide Kasu Matsumoto
Anselmo Eduardo Diniz
Departamento de Engenharia de Fabricação
Faculdade de Engenharia Mecânica
Universidade Estadual de Campinas
13083-970 Campinas, SP Brazil
anselmo@fem.unicamp.br

Abstract

Recently many works have been done in order to study the turning process of hardened steels, mainly concerning the lives of ceramic and PCBN tools. However, just few works deal with the problem of turning accuracy, comparing it with grinding accuracy, mainly when the lathe used has a conventional mechanical design. Therefore, it is important to evaluate the capability of these conventional machines to replace the grinding operation by turning and still maintain workpiece quality typical of grinding operations. This work tries to contribute to fill this gap. Several AISI E52100 hardened steel workpieces (60 HRc) were turned using mixed ceramic and PCBN tool materials and different cutting speeds in a lathe of conventional design. Workpiece surface roughness and diameter variation were measured throughout the tool life test, in order to evaluate the quality of the workpiece. The length of the workpieces was also varied to analyze the influence of workpiece shape on its quality. The main conclusion of this work was that the turning process is able to replace grinding in hardened steel finishing operations. Moreover, it is able to achieve a surface and dimensional quality similar to that of ground components, even when the machine used has a conventional mechanical design.

Keywords: *Turning Hardened Steels, Accuracy, Surface Roughness*

Introduction

This century is marked by serious attempts to achieve higher productivity and quality in industrial processes. In the metal cutting field, improvement in the processes has been considerable, mainly in the last decades, when tool materials and machine tools have been extensively improved. Besides these improvements, a lot has been done to replace or eliminate manufacturing operations (Bossom, 1994; König, Berktold and Koch, 1993). Turning hardened steel workpieces, instead of grinding, is a good example of the replacement and elimination of operations. Steel components, such as gears and bearings, need a high degree of hardness to increase their wear resistance. Conventionally, these components have attained their final dimensions by a grinding operation often using Al_2O_3 wheels, although this is a low productivity process, since it consumes large amounts of energy and time. With the development of very hard and thermally resistant cutting tool materials, such as ceramics and policrystalline cubic boron nitride (PCBN), that are able to cut hard materials, together with the development of more rigid and precise lathes, turning became a good alternative to grinding. The main advantages of turning over grinding are higher flexibility and productivity and lower costs (König, Berktold and Koch, 1993).

This work attempts to contribute to the use of turning instead of grinding in finishing operations, when the surface roughness desired is usually lower than $R_a = 0.6$ µm and the dimensional tolerance is within the ISO IT5 range. Most of the lathes used for this purpose today have a conventional design, i.e., they do not have some of the requisites important for increasing their accuracy, such as hydrostatic bearings and slideways, or even linear slideways. Therefore, it is important to discover the capability of these conventional machines to replace the grinding operation by turning and still maintain the workpiece quality typical of grinding operations. Several AISI E52100 hardened steel workpieces (60 HRc) were turned using mixed ceramic and PCBN tool materials and different cutting speeds in a lathe of conventional design. Workpiece surface roughness and diameter were measured throughout the tool life, in order to evaluate the quality of the workpiece. The length of the workpieces was also varied to analyze the influence of workpiece shape on its quality. The main conclusion of this work was that the turning process is able to replace grinding in hardened steel finishing operations. It is able to achieve a surface and dimensional quality similar to that of the grinding operation, even when the machine used has a conventional mechanical design.

Before continuing, it is important to mention that the comparison of turning and grinding made in this work is concerned to conventional grinding only (that one made with Al_2O_3 wheel) and it does not apply to grinding with superabrasive wheels.

Manuscript received: July 1998; revision received: March 1999.Technical Editor: Alisson Rocha Machado.

Some Aspects Of The Accuracy of Hardened Steel Turning

In order to use the turning process to replace grinding, it is important to know how to maintain all aspects related to the process in such a way to minimize errors. Firstly, it is important to understand the cutting forces involved, because they are responsible for the deflection of the workpiece, the workpiece fixture device, the machine and the tool. In cylindrical turning operations, it is specially important to know the radial force behavior. This component of the cutting force is responsible for the workpiece and tool deflection and, therefore, it is important to maintain it at its minimum value in order to improve the accuracy of the operation.

Two important parameters of influence on the radial force are tool nose radius and cutting edge angle. In order to decrease the radial force, it is necessary to decrease the tool nose radius and to increase the cutting edge angle (to keep it close to 90°) (Ferraresi, 1978). Otherwise, if the tool nose radius is decreased, it is more difficult to achieve a good surface finish, since its growth contributes geometrically to the decrease in surface roughness. Therefore, it is necessary to have an intermediate value for tool nose radius to obtain dimensional accuracy on one hand and to have a good surface finish on the other.

Abrão and Aspinwall (1995) turned AISI E52100 steel (62 HRC) with PCBN and mixed ceramic tools and concluded that, in finishing operations, the radial force is greater than the other components of total force, because the depth of cutting is smaller than the tool nose radius. Therefore, most of the cutting is done inside the curved region of the tool edge (inside the tool nose radius region), which causes the effective cutting edge angle to decrease. All the components of the cutting force decreased slightly with the increase in cutting speed and increased linearly with the increase in feed and depth of cut.

In this work, the tool nose radius was $r_\varepsilon = 0.8$ mm in all the experiments. This value is smaller than usually recommended for turning hardened steels (where very low surface roughness is desirable) in order to maintain a low radial force, but higher than those usually used in finish turning of soft steels, in order to achieve a good surface quality. The cutting edge angle used were 90° for triangular inserts and 75° for square inserts.

Abrão and Aspinwall (1996) carried out several turning experiments, machining AISI H13 (52 HRC) and AISI E52100 (62 HRC) steels, using PCBN and ceramic tools and a rigid lathe. They obtained surface roughness values of $R_a = 0.18$ µm for the H13 steel and $R_a = 0.14$ µm for the AISI E52100 steel. Costa (1993) achieved R_a values between 0.2 and 0.3 µm by turning the AISI 52100 and M2 steels with PCBN and ceramic tools, using the same CNC lathe that was used in this work.

In hard turning, a significant increase in the cutting forces demands both, strength of the cutting tool and stiffness of the machine tool system. The high values of cutting forces together with the high ratio of radial to tangential forces, can cause large deflections of the tool and workpiece, which can cause chipping of the cutting edge of brittle tool material like those used in hard turning (Chou and Barash, 1995). Konig, Klinger, and Link (1990) indicated that the segmented type of chip formation typical of hard turning is associated with large amplitude dynamic forces causing forced excitation of the machine tool-workpiece-tool system what can result in rapid tool wear. For a less stiff system, cracks on the cutting edge are observed since the beginning of cutting. Crater depth and flank wear land also become larger (Chryssolouris, 1982). Machine tool stiffness is also an important factor for the surface roughness of turned steels, which is very important when turning has to replace grinding process.

The risk to damage the surface metallurgical properties is higher in grinding than in turning. König, Berktold and Koch (1993) studied the progression of the residual stress depth distribution during tool life, after turning hardened 16MnCr5 steel (62 HRc) using PCBN tool material. They showed that, when the tool is fresh, low compression residual stresses occur in the workpiece surface. Residual tensile stress (that is harmful to the workpiece strength) does not show up until considerable cutting time has elapsed. This result suggests that residual tensile stress is attributable to wear land friction. The value of tensile stress on the turned surface after 200 minutes of cutting time is easily reached in grinding operations (Shaw and Vyas, 1994).

König, Berktold and Koch (1993) suggested that the following two basic improvements be made in the turning process, in order to make its quality even better than what is achieved today:

a. Optimization of PCBN and ceramic inserts - one problem of these tool materials that limits the improvement of surface quality is the rounding and the formation of rough regions on the cutting edge. It is impossible to obtain a very sharp edge due to the crystalline structure of the materials. The values of tool edge rounding and roughness are more than one hundred times larger than the monocrystalline materials used in ultrahigh precision turning. Therefore, it is necessary to improve the insert quality through polishing and grinding of the rake and clearance tool faces with diamond micrograins. To select a suitable PCBN grade is very important. PCBN types containing low amounts of CBN and ceramic components as a secondary phase present low thermal conductivity and, therefore, are suitable for finishing operations, where less heat is generated. Under this circumstance, a lower amount of heat will flow through the tool, increasing the cutting temperature and helping to reduce the shear strength of the workpiece material. Consequently, cutting forces are reduced (Bossom, 1994). Cutting speeds up to 550 m/min do not influence very much surface quality and cutting forces. However, influence tool wear, mainly when the chip cross section is very small. The temperature in the cutting zone, which depends on cutting speed, is very important. Unlike the machining of soft steels, for low cutting speeds (and low temperatures) the low plasticity of the hardened workpiece material shortens the tool life and results in a bad surface quality. High cutting speeds (and, consequently, high temperatures) on the other hand, may cause problems related to metallurgical damage in the external layer of the workpiece. Another limitation related to cutting speed is the rigidity of the machine tool-workpiece-tool system. Depending on this rigidity, the increase in cutting speed may cause an increase in system vibration, which may damage the tool and the workpiece surface finish.

b. Another way to improve the quality of turned hardened steel workpieces is the use of high precision machining technology, by the use of more rigid machine tools which contain hydrostatic bearings and slideways.

Tools For Hard Turning

The tool materials recommended for hard turning are mainly PCBN and ceramics, because only these materials have the necessary hardness and chemical stability to cut a very hard material like hardened steel (Sandvik, 1994), (Tönshoff, Wobker and Brandt, 1995), (Buschmole, 1995). There are several ceramic materials used in machining, although the kind recommended for hard turning is the one based on aluminum oxide, that is classified in three main groups:

- Pure ceramics - composed only by oxides, mainly Al_2O_3. They can also have small amounts of MgO and ZrO_2;
- Mixed ceramics - composed of Al_2O_3 and titanium carbide (TiC) or titanium nitride (TiN);
- Whiskers reinforced alumina - composed by an Al_2O_3 matrix reinforced with monocrystals of SiC.

Among these groups, the most used in hard turning is the mixed ceramic, due to its higher thermal shock resistance and hot hardness in high temperatures compared with pure ceramics. Ceramic tools, in general, have high chemical stability when compared with other tool materials and, therefore, are resistant to diffusion wear, that happens mainly due to the friction between long chips and tool rake face.

PCBN tool material is another alternative for hardened steel turning. Compared with aluminium based ceramic, it has higher hardness and toughness, but smaller chemical stability in the presence of iron. High chemical stability is a very important tool property in hard turning, because the tool edge reaches very high temperature and diffusion between tool material and chip may wear the tool quickly (crater wear). PCBN tool material is classified into two main groups:

- PCBN for rough operations - in this kind of operations, besides hardness, the tool have to have high toughness. Therefore, this PCBN grade is basically cubic boron nitride (90% in volume);
- PCBN for finishing - in this kind of operation, the cutting speed is higher and, therefore, the tool is required to have high chemical stability obtained by adding a ceramic phase to PCBN.

Materials, Equipment And Experimental Procedure

Two sets of turning experiments were carried out cutting AISI E52100 steel hardened to 60 HRC. In order to vary the stiffness of the workpiece, two kinds of workpieces were used: long ones and short ones. Figure 1 shows a scheme of these workpieces.

A CNC lathe with a 30 HP main motor and conventional roller bearings was used. The inserts used were Sandvik Coromant CC 650 (Al_2O_3 + TiC) ISO coded TNGA 120408 T01020 (triangular) and SNGN 120408 T01020 (square) and GE BZN 8000 (55% PCBN) code TNMG 120408 (triangular).

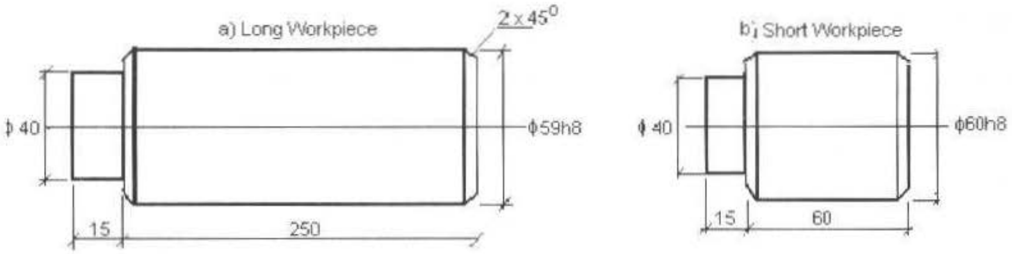

Dimensions before the cut --- Units im mm

Fig. 1 Workpiece Dimensions

All experiments were done with a feedrate of $f = 0.08$ mm/rev and a depth of cut of $a_p = 0.4$ mm. Table 1 shows the cutting speeds (v_c), tools and workpiece geometry used in the experiments. Each experiment was repeated several times (Table 1 also shows the number of times each experiment was conducted), to increase the reliability of the results.

Table 1 Tool Materials, Cutting Speeds, Number of Replications and Kind of Workpieces Used in the Experiments

Tool	Cutting speed v_c (m/min)	Number of replicates	Workpiece geometry
Triangular PCBN	108	4	long
	130	7	long
	150	3	long
Triangular Ceramic	108	4	long
	108	3	short
	130	4	long
	130	4	short
	150	1	long
Square Ceramic	130	4	short

After cutting some of the workpieces, the experiment was interrupted and the surface roughness, the diameter and the circularity error of each workpiece were measured. This procedure was repeated till the workpiece average surface roughness reached $R_a = 0.6$ µm. At this time, the tool was considered to have reached the end of its life and the experiment was ended. This value of R_a was chosen because it is frequently desired in precision grinding (Agostinho, Rodrigues and Lirani, 1977). As the purpose of hard turning is to replace the grinding process, the surface roughness obtained must have the same value as that obtained by grinding. Another objective of the work was to keep the diameter tolerance range similar to that typical of the grinding process, but the workpiece diameter was not used as a criteria to replace the tool. Roughness and diameter were measured in three positions of the long workpieces, as it can be seen in Fig. 2. For the short workpieces, these measurements were taken only at the middle of the workpiece.

Fig. 2 Positions Where Surface Roughness and Diameter Were Measured

Results Obtained For Long Workpieces

PCBN Tools

Figure 3 shows the dimensional variation in the workpiece diameter versus cutting length, using PCBN tools at a cutting speed of 150 m/min. The experiment done with this cutting speed was chosen for this analysis because it presented the longest tool life for PCBN tools. As said before, the circularity errors of the workpieces were also measured, but will not be analyzed because their values were always below 2 μm. Several things can be seen in this Figure:

- The first three measurements in the three positions of the first workpiece showed smaller diameters than the other measurements. This occurred due to an error in the position of the tool as frequently occurs in the first workpiece machined by a cutting edge. After this first workpiece, the tool position was corrected and the other diameters were within the same range;
- The diameters measured at position 1 were always the largest, followed by those at position 2 and, finally, position 3. Therefore, the workpieces presented a larger conicity, which reached 0.170 mm in the worst case and was always higher than 0.130 mm. This conicity is not related to the process itself, but occurred due to the inaccuracy of the machine tool. The center line of the chuck and the center line of the tailstock of the machine used presented a misalignment that generated the conicity;

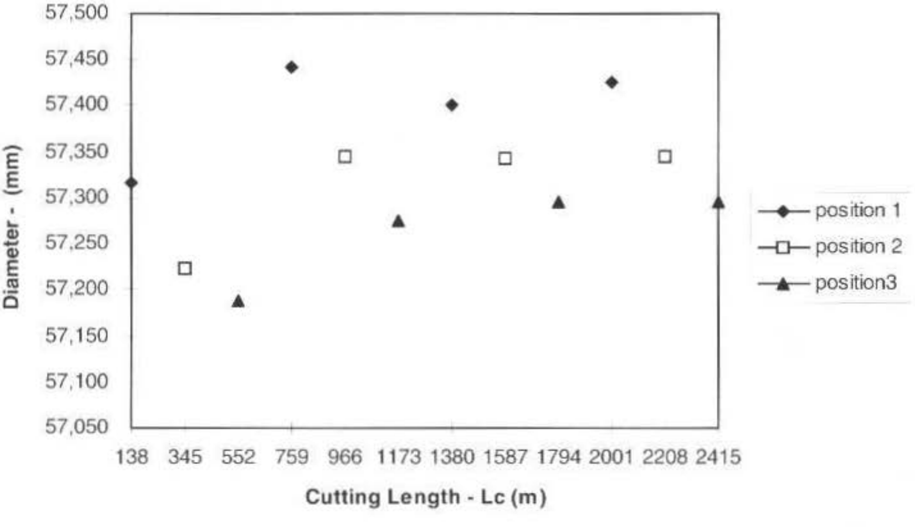

Fig. 3 Workpiece Diameter Variation Versus Cutting Length - PCBN Tool

- The difference between the measurements made at the same position in different workpieces was not excessive. The difference between the maximum and the minimum diameters at position 2 (where this difference was the smallest) was of 0.003 mm (quality ISO IT5), and at position 3 (where this difference was the largest) it was of 0.021 mm (close to quality ISO IT6). It is worth of noting that the position with the largest deviation was close to the chuck (which was supposed to be the most rigid) and the position with the smallest deviation was the central position, far from both chuck and tailstock (which was supposed to be the least rigid position). This dimensional variation was supposedly caused by the inaccuracy of the center hole. It was not possible to maintain a narrow tolerance range during the machining of these holes. So, each hole had a different dimension, which caused differences in the fixtures of the workpieces and the difference in workpiece dimensions.

Figure 4 shows the values of the average surface roughness versus cutting length for the same experiment as that shown on Figure 3. It can be seen in this Figure that surface roughness varied during the tool life, but almost always within the range regularly obtained by the grinding process, i.e., below 0.6 μm. Surface roughness increased and decreased depending on the variation in tool nose shape moulded by tool wear. After some cutting time had elapsed, the tool wear was such that surface roughness increased up to $R_a = 0.7$ µm.

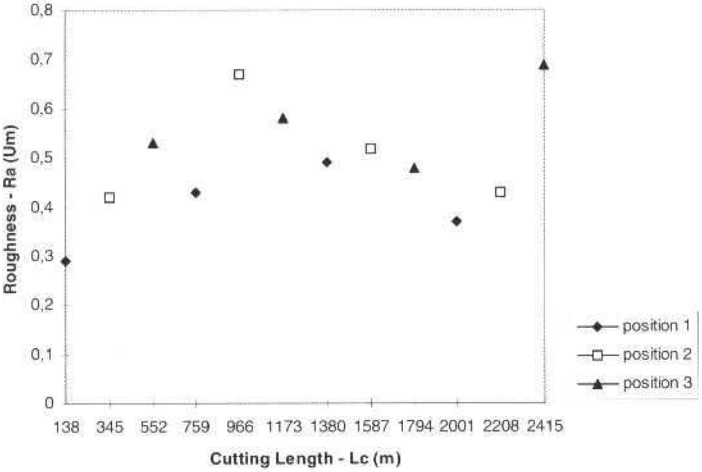

Fig. 4 Surface Roughness Variation Versus Cutting Length - PCBN Tool

In most of the workpieces, the smallest value for surface roughness was found close to the tailstock (position 1), which indicates that this is the most rigid position. In addition, the hardest part of the workpiece was always close to position 1, where hardness reached 62 HRC, while the other positions showed values of 58 to 60 HRC. Costa (1993) affirmed that an increase in hardness would make chip formation easier due to the lower strain needed to cause chip fracture, what should cause a decrease in the surface roughness of the workpiece. The value of hardness close to position 1 was higher because in this position, the workpiece received heat in both radial and axial directions during heat treatment. The other positions received heat just only in the radial direction.

The value of roughness at positions 2 and 3 in each workpiece were similar, i.e., the value of roughness close to the chuck was not lower than that at the center of the workpiece, as expected. This fact demonstrates that the rigidity of the machine tool chuck is not as high as assumed before beginning the experiments. At the end of the tool life, a sudden increase in surface roughness occurred (position 3 with Lc = 2415 m) due to the chipping of the cutting edge, which occurred between positions 2 and 3 (close to Lc = 2400 m).

Figure 5 shows the average value of R_a using new cutting edges for different cutting speeds. Each value is the average of several experiments, as shown previously in this work. Therefore, the surface roughness values shown in this figure were not influenced by the tool wear.

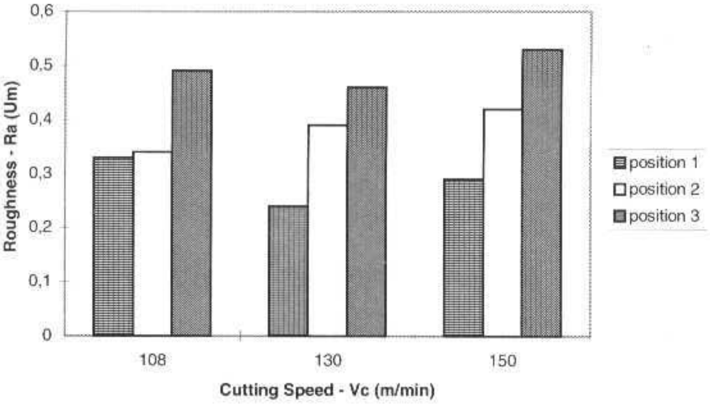

Fig. 5 Average Surface Roughness at the Beginning of Tool Life for Different Cutting Speeds - PCBN Tools

Here again, it can be seen that the lowest value of roughness was obtained at the position 1 (close to the tailstock). But, in contrast with what was shown in Figure 4, the roughness values at position 2 were consistently smaller than those at position 3, which demonstrates that the machine chuck used was not rigid enough. It can also be seen in this figure that there was no systematic influence of cutting speed on surface roughness. R_a increased slightly with cutting speed at position 2, but increased and decreased at the other positions. This result agrees with Bonifácio (1993) who affirms that when there is no formation of built up edge, the influence of the cutting speed on surface roughness is not direct and depends on its influence on system vibration, which strongly influences the surface roughness.

Ceramic Tools

Figure 6 shows the behavior of workpiece diameter versus cutting length, using ceramic tool and cutting speed v_c = 108 m/min. Of all the experiments carried out with ceramic tools, only this experiment is shown because it was the longest and represents quite well the results obtained in the other experiments. The cutting speed shown in this figure was not 150 m/min like in Fig. 3, because with ceramic tools, differently of PCBN, this speed presented the shortest tool life. Also here, the circularity errors of the workpieces were measured, but will not be analyzed because their values were always below 2 μm. It can be seen in this figure that, when the analysis was continued up to Lc = 5000 m, dimensional tolerance was maintained at IT 5 (13 μm) for position 1 and at IT6 (19 μm) for positions 2 and 3, as had already occurred for PCBN tools. After Lc = 5000 m, the variation in diameter increased due to tool wear and chipping. For the same reasons cited previously, conicity remained high, with the diameter values close to the tailstock (position 3) always larger than those close to the chuck (position 1). The influence of tool wear and chipping on workpiece dimension can be observed, since the tool position was not corrected during the experiment. It can be seen that after Lc = 5000 m the tool nose moved more than 0.1 mm, which caused a variation in diameter bigger than 0.2 mm. It is interesting to note that, despite this large variation in tool nose position, surface roughness did not increase beyond Lc = 5000 m, as can be seen in Fig. 7. Therefore, it can be concluded that the tool nose moved backwards due to tool wear, but maintained a shape close to the original one and thus, the values obtained with the fresh tool for surface roughness remained almost the same. Only when the tool became very worn (above Lc = 6500 m) surface roughness increased and fall outside the range suitable for finishing operations.

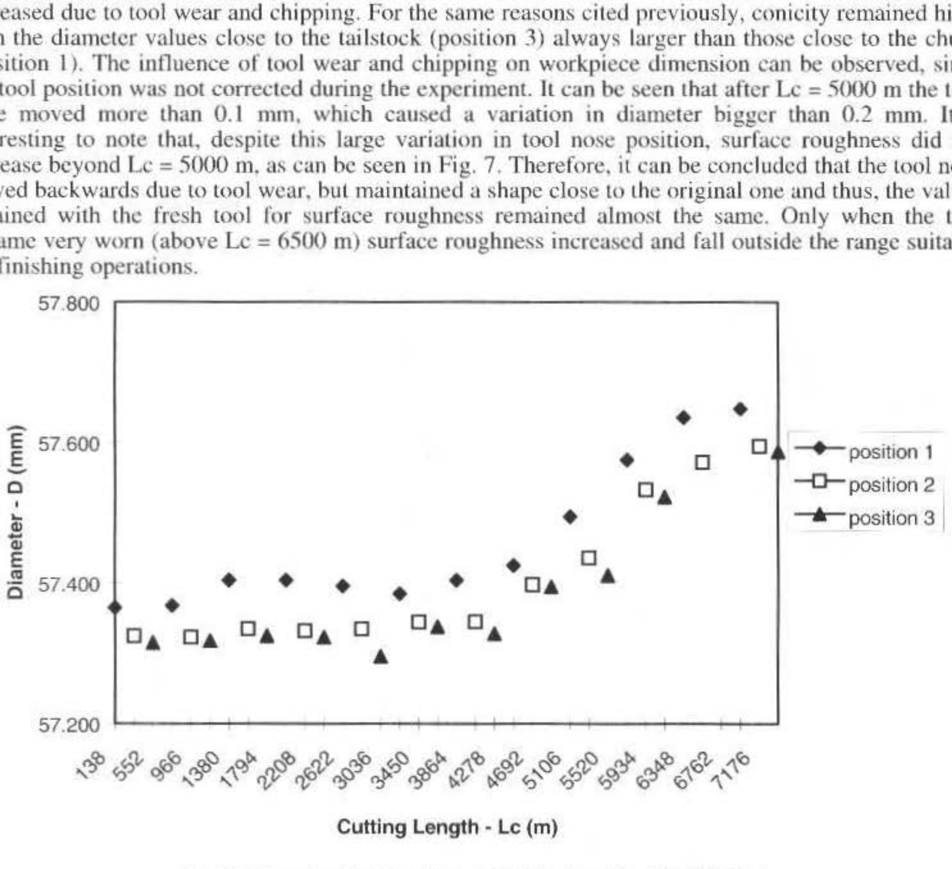

Fig. 6 Diameter Variation Versus Cutting Length - Ceramic Tool

An analysis of Fig. 7 shows that surface roughness increases and decreases as the cutting length increases due to the variation in tool nose shape, caused by tool wear and chipping. It can be noted that the surface roughness increased up to Lc = 3200 m. After that it decreased up Lc = 5100 m, and then increased again. This behavior is due to the variation in tool nose shape. After a certain level of chipping, the tool nose shape may become similar to the original shape and so, roughness approximates the values obtained with the fresh tool. Of course, when this occurs the position of the tool nose is not the same and, consequently, the workpiece dimension is far from the original one, as can be seen in Fig. 6. After that, the chipping process continues and roughness once again increases.

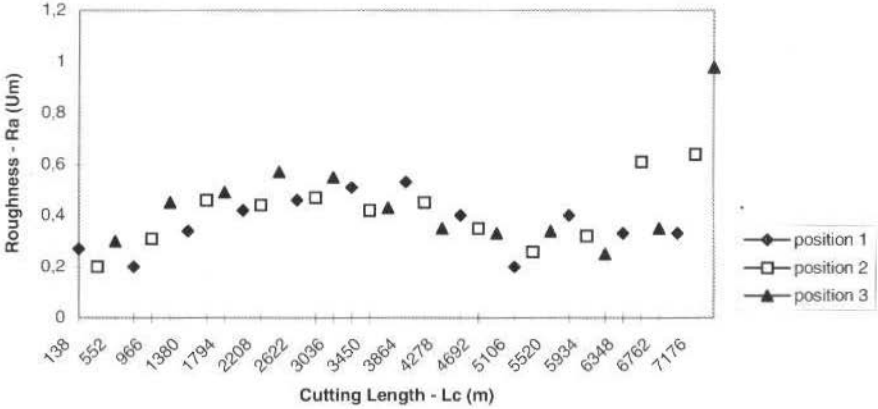

Fig. 7 Workpiece Surface Roughness Versus Cutting Length - Ceramic Tool - v_c = 108 m/min

The variation in roughness between the three positions is not as visible as when the PCBN tool is used. Up to Lc = 2500 m, the smallest value of roughness is found at position 1 and the largest at position 3, but after this point it behaves at random. This may have occurred due to the greater instability of the tool nose, since the ceramic tool chips more than PCBN (PCBN tool wear is higher than the ceramic). Therefore, the roughness behavior of the workpiece machined with a ceramic tool is similar to that machined with a PCBN tool up to a certain level of wear, where the chipping level is still low. After this point, the increase in chipping causes surface roughness to behave at random.

Again in this case, the surface roughness obtained was within the range of those typical of grinding operations.

Figure 8 shows the average workpiece roughness (R_a) machined with fresh tools for all the experiments done at different cutting speeds. Again, no straight forward relationship between R_a and cutting speed can be seen.

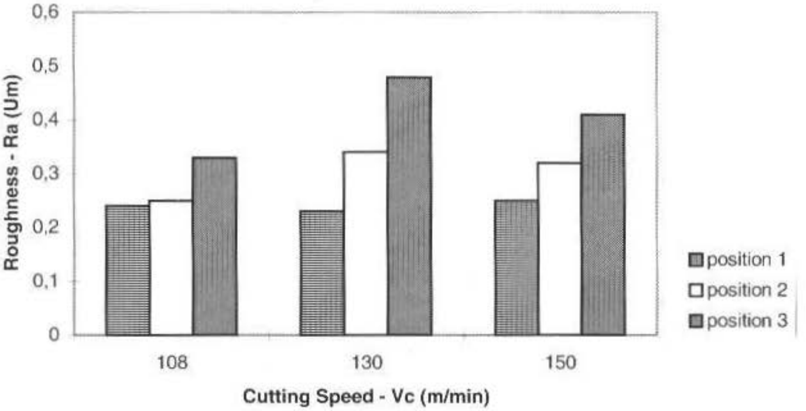

Fig. 8 Surface Roughness (R_a) versus Cutting Speed - Long Workpieces - Ceramic Tools

Another interesting point to be noted is that, in contrast to what happened at v_c = 108 m/min (shown in Fig. 7), for the other cutting speeds, the difference between roughness at the three positions was larger. This can be explained by the fact that, besides the greater rigidity of position 1 previously cited, tool wear during the cutting between positions 1 and 2 and positions 2 and 3 is what caused the roughness increase greatly between these positions. At v_c = 108 m/min, the ceramic tool did not wear as quickly and, therefore, the difference in roughness between the three positions was not as high.

When comparing Fig. 5 with Fig. 8, it can be seen that the ceramic tool usually generated a lower roughness value than the PCBN tool. This fact probably occurred due to the cutting edge finishing. It was not possible to maintain a high quality in the sharpening and resharpening of the PCBN cutting edges. Otherwise, the ceramic cutting edges were not sharpened, because the inserts were used as received from the supplier and when they were worn, they were discarded. This fact made the quality of the ceramic tool flank and rake faces much better than that of the PCBN inserts.

Results Obtained For Short Workpieces

When short workpieces were turned, only ceramic tools were used because they showed longer tool lives than PCBN in the tests with long workpieces. Here, not only triangular inserts were used, but also square, because the triangular inserts had chipped several times in the experiments with long workpieces. Therefore, with the larger included plan angle of a square tool, the tool nose was supposed to be more resistant and, thus, to chip less frequently. Because of this, the cutting edge angle decreased (in the triangular tool it was 90^0, while in the square tool it was 75^0) and, consequently, the radial force may have increased, which may have negatively affected the workpiece surface finish and tolerances, due to deflection of the workpiece. However, because the workpiece is shorter, it is more rigid and, so it is believed that this growth of radial force may not have negatively influenced the workpiece quality.

Figure 9 shows the variation in diameter when short workpieces were turned. Only the Figure related to the experiment at v_c = 130 m/min is shown, because both insert shapes were tested at this cutting speed. However, the results at v_c = 108 m/min are similar. Again, the values of circularity errors will not be analyzed due to the same reasons cited before. It can be seen that after the first workpiece (after the machining of this workpiece, the tool position was corrected), the variation in diameter was very low, and it was possible to maintain the tolerances within the IT5 range (13 μm) for both insert shapes. At the end of the tool life the workpiece diameter increased slightly for both triangular and square inserts but even in this case the diameters were within that tolerance range. Therefore, the tool wear and chipping that occurred during the tool life were not great enough to negatively influence the workpiece dimension.

a) triangular inserts

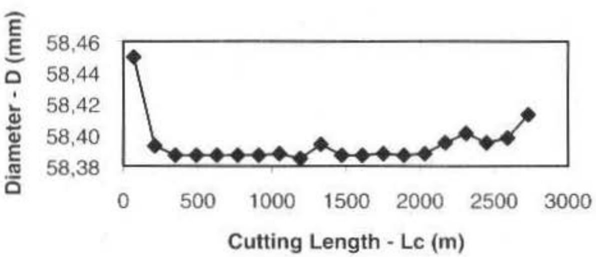

b) square insert

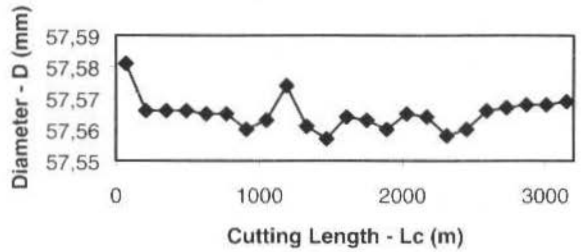

Fig. 9 Workpiece Diameter versus Cutting Length - v_c = 108 m/min

Figure 10 shows surface roughness behavior versus cutting length (Lc) for both square and triangular inserts. In this figure it can be seen that roughness continued to vary during tool life, but still within the typical range of roughness for the grinding operation. The square insert, which was supposed to be more resistant to chipping and breakage, showed the same behavior as the ceramic insert, i.e., roughness varied due to edge chipping. In other words, due to irregular chipping of the tool edge, sometimes the tool nose shape differed from the original one and the roughness increased and at other times the shape was similar to the original one and the roughness decreased. After a period of cutting, edge chipping is so high that the tool must be replaced due to the high degree of workpiece roughness. In addition, if the operation continues after this point, the edge can break off, which brings undesirable consequences to the process. But one point that is interesting to note, not observed when long workpieces were machined with ceramic tools, is that the growth of surface roughness was not accompanied by an increase of workpiece dimension (Fig. 9). Therefore, the size of the particles lost due to the chipping, was not big enough to negatively affect the diameter of the workpiece, but did affect surface roughness.

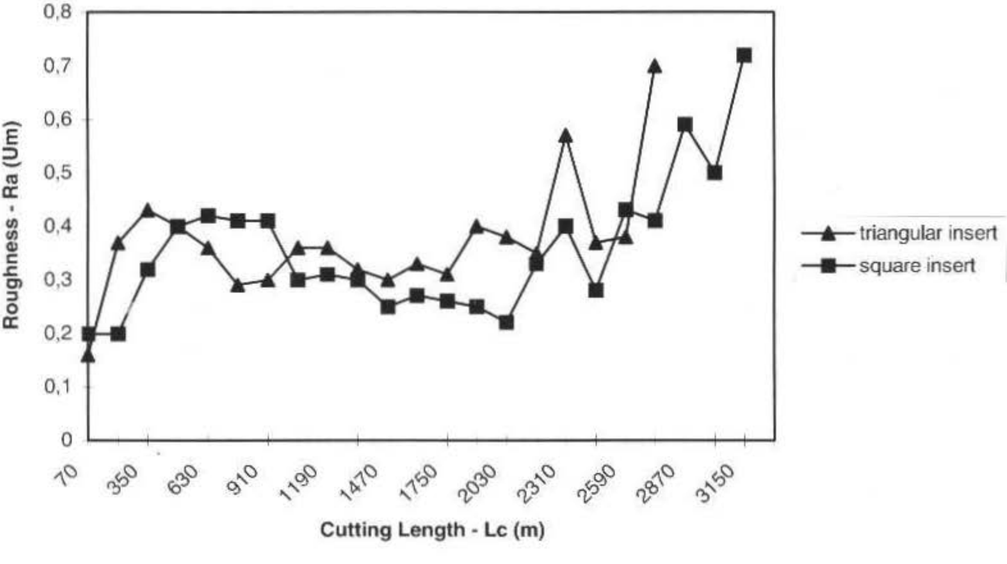

Fig. 10 Surface Roughness (R_a) versus Cutting Length for Ceramic Tools - v_c = 108 m/min

Therefore, it can be concluded that, at least for short workpieces, the hardened steel turning process is able to achieve a dimensional and surface quality typical of that of the grinding process, even when the machine used is a lathe of conventional design (no hydrostatic bearings and slideways). It is worth remembering that, for long workpieces, the same quality was not obtained due to specific factors related to the machine used (misalignment of chuck and tailstock center line) and to errors during the machining of the center holes. These factors are not directly related to the turning process so it can not be said that the turning process is unable to achieve sufficient quality, even with long workpieces.

Cutting speed did not significantly influence workpiece roughness when the speed was changed from 108 to 130 m/min, with triangular ceramic insert, as can be seen in Fig. 11. Changing the entering angle from 90^0 (triangular insert) to 75^0 (square insert) did not have a substantial influence on the roughness values either. It can be seen in the figure that roughness dropped by around 10% when the triangular insert was replaced by the square one, which is not to much, since roughness values regularly present a high scatter. Based on this, it can be concluded that the supposed increase in radial force due to the decrease in cutting edge angle, did not cause the system vibration to increase and, thus, did not cause an increase in workpiece roughness.

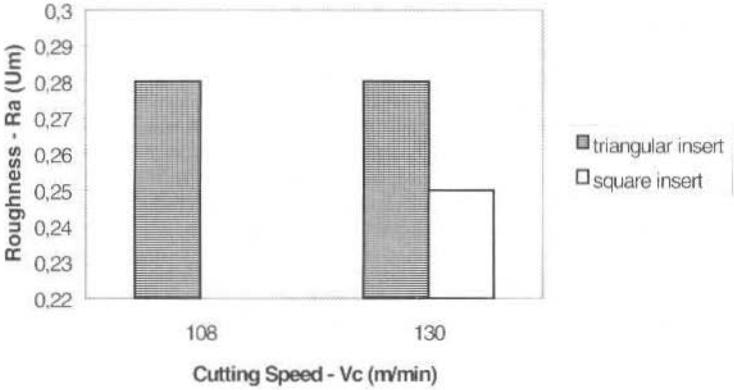

Fig. 11 Initial Values of Surface Roughness for Different Cutting Speeds

Comparing Fig. 11 with Fig. 8, it can be seen that there was not a big difference between the initial roughness values for long and short workpieces for either v_c = 130 m/min or v_c = 108 m/min (for triangular inserts, of course, because only these were used in both workpieces). The only exception was position 3 of the long workpiece, where the tool wear effect was added to the lack of rigidity of the chuck. The rigidity of the long workpiece close to the tailstock and in the middle was very high, similar to that obtained with short workpieces, since the roughness values obtained were also similar.

Conclusions

- It was difficult to maintain tighter tolerances than ISO IT6 during the machining of long workpieces, due to the misalignment of the machine and to the machining of the center holes, resulting in workpiece conicity;
- In short workpieces it was possible to maintain the ISO IT5 tolerance during the whole tool life;
- Surface roughness behavior throughout the tool life was unstable, but was always below the value considered the limit for grinding operations ($R_a < 0,6$ μm);
- For long workpieces the position close to the chuck was the one that showed the highest roughness value;
- PCBN tools showed higher surface roughness values than ceramic tools;
- Neither cutting speed nor cutting edge angle substantially influenced roughness values;
- The turning process is able to replace grinding in hardened steel finishing operations, particularly for short workpieces. It is able to achieve surface and dimensional quality similar to that of the grinding operation, even when the machine used has a conventional mechanical design.

References

Abrão, A. M.; Aspinwall, D. K., 1995, "Cutting forces assesment when turning hardened bearing steel". Journal of the Brazilian Soc. Mechanical Science, v. XVII - nº.4, pp. 353 - 359.

Abrão, A. M.; Aspinwall, D. K., 1996, "The surface integrity of turned and ground hardened bearing steel". Wear, Vol. 196, pp. 279 - 284.

Agostinho, O.L.; Rodrigues, A. C. S.; Lirani, J., 1977, "Tolerâncias, ajustes, desvios e análise de dimensões". Edgard Blücher Ltda, São Paulo, Brazil

Bonifácio, M. E. R. 1993, "Monitoramento do Processo de Torneamento de Acabamento Via Sinais de Vibração", Dissertação de mestrado, Faculdade de Engenharia Mecânica, UNICAMP, Campinas, SP, Brazil.

Bossom, P.K., 1994, "Usinagem de acabamento de ligas ferrosas duras". *De Beers Industrial Diamond Division.*

Buschmole, N., 1995, "Hard Turning With Ceramics", Proceedings of the 1st International Machining and Grinding Conference, Dearborn, USA, pp. 979-987.

Chou, Y. S.; Barash, M. M., 1995, "Review on Hard Turning and CBN Cutting Tools", Proceedings of the 1st Int. Machining and Grinding Conference, Dearborn, USA, pp. 949 – 962.

Chryssolouris, G., 1982, "Effects of Machine-Tool-Workpiece Stiffness on the Wear Behavior of Superhard Cutting Materials", Annals of the CIRP, Vol. 31/1, pp. 65-69

Costa, D. D. 1993, "Análise dos Parâmetros de torneamento de aços endurecidos", Dissertação de mestrado, Faculdade de Engenharia Mecânica, UNICAMP, Campinas, SP, Brazil

Ferraresi, D., 1978, "Fundamentos da Usinagem dos Metais", Editora Edgard Blücher, São Paulo, Brazil

König, W.; Berktold, A.; Koch, K. F., 1993, "Turning versus grinding - a comparison of surface integrity aspects and attainable accuracies", Annals of the CIRP, Vol. 42/1, pp. 39-43.

König, W., Klinger, M. and Link, R., 1990, "Machining Hard Materials With Geometrically Defined Cutting Edges – Field of Applications and Limitations", Annals of the CIRP, Vol. 39/1, pp. 61-64

Sandvik Coromant, 1994, "Modern Metal Cutting", AB Sandvik Coromant, Sandviken, Sweden.

Shaw, M. C. and Vyas, A., 1994, "Heat Affected Zones in Grinding Steel", Annals of the CIRP, Vol. 43/1, pp. 279-282

Tönshoff, H. K. Wobker, H. G. and Brandt, D., 1995, "Potential and Limitation of Hard Turning", Proceedings of the 1st Int. Machining and Grinding Conference, Dearborn, USA, pp.963-978.

RBCM - J. of the Braz. Soc. Mechanical Sciences
Vol. XXI - No.2 - 1999 - pp. 355-363

ISSN 0100-7386
Printed in Brazil

Estudo do Processo de Embutimento Profundo de Copo Pelo Método dos Elementos Finitos

Finite Element Analysis of a Cup Deep Drawing Process

Sérgio Tonini Button
Roberto Bortolussi
Departamento de Engenharia de Materiais
Faculdade de Engenharia Mecânica
Universidade Estadual de Campinas
13083-970 Campinas, SP Brazil
sergiot@fem.unicamp.br

Abstract

Deep drawing processes have an important role in manufacturing, mainly in the automotive industry. The increasing competition requires that design and manufacture of dies be fast and without errors. New forms to develop the dies have been used. The finite element method has helped engineers to reduce errors during die development. In this paper an elasto-plastic element was used to simulate the cylindrical deep drawing of an ABNT 1006 steel cup. The simulation made possible the determination of the forces, thickness and circumferential strains ocurring during the deep drawing process, which were compared to experimental results.

Keywords: *Deep Drawing, Finite Elements.*

Introdução

A estampagem profunda tem por finalidade a fabricação de peças a partir de chapas planas. Este processo tem como um dos seus maiores usuários a indústria automobilística em que a competitividade existente tem provocado grandes transformações na forma de execução dos projetos dos ferramentais para a redução de tempo e custo deste desenvolvimento.

A complexidade da transformação da forma durante o processo, o grande número de variáveis envolvidas, como velocidade do equipamento, rigidez das matrizes e o atrito durante o processo, limitam a aplicação de métodos analíticos, pois a capacidade de relacionar muitas variáveis é limitada nesses métodos (Bathe, 1982; Cook et al., 1989).

Com o aumento na velocidade de processamento e na capacidade dos computadores, a possibilidade de relacionar um grande número de variáveis vem ampliando o campo de utilização de métodos numéricos, principalmente o Método dos Elementos Finitos (MEF), para a simulação de processos de conformação (Rowe et al., 1991), incluindo os de estampagem profunda (Chou e Pan, 1994; Gontier, 1994; Keck et al., 1990 e Lee et al, 1989).

Neste trabalho foi realizada a simulação, empregando-se o programa comercial ANSYS 5.0A (Ansys, 1993), do processo de embutimento de copo cilíndrico de aço ABNT 1006 classe EEP, com o objetivo de prever as deformações atuantes na conformação antes da construção das ferramentas. Esta simulação utilizou elementos de formulação elasto-plástica axissimétrica para a discretização da chapa que será embutida, e para o contato entre a chapa e a ferramenta, utilizou-se elementos que simulam o atrito segundo a lei de Coulomb e com os quais foi possível verificar a influência do coeficiente de atrito sobre as deformações.

Utilizou-se o modelo de material denominado multilinear isotrópico, desprezando-se o efeito da anisotropia sobre as propriedades de estampagem (Borst e Feenstra, 1990, Oñate e Zienkiewicz, 1983 e Darendeliler e Altan, 1996).

Para a solução do sistema de equações foi empregado o método iterativo de Newton-Raphson, um dos mais utilizados para a solução de problemas que apresentam não-linearidade (Bathe, 1982).

A validação da simulação foi feita pela comparação de seus resultados com os de ensaios experimentais nos quais efetuou-se o embutimento de copos, medindo-se a força de embutimento, a deformação da espessura e a deformação circunferencial.

Processo de Estampagem Profunda de Peças Cilíndricas

O processo de estampagem profunda submete a chapa plana a um estado complexo de tensões e deformações que alteram sua espessura durante o processo. O estado típico de tensão varia conforme a

Manuscript received: August 1997; revision received: July 1998. Technical Editor: Leonardo Goldstein Jr.

posição da retirada do elemento de análise na peça que está sendo conformada. Para peças cilíndricas existem três diferentes estados de tensão: um na flange, um na lateral e um no fundo do copo, como pode ser visto na Fig. 1.

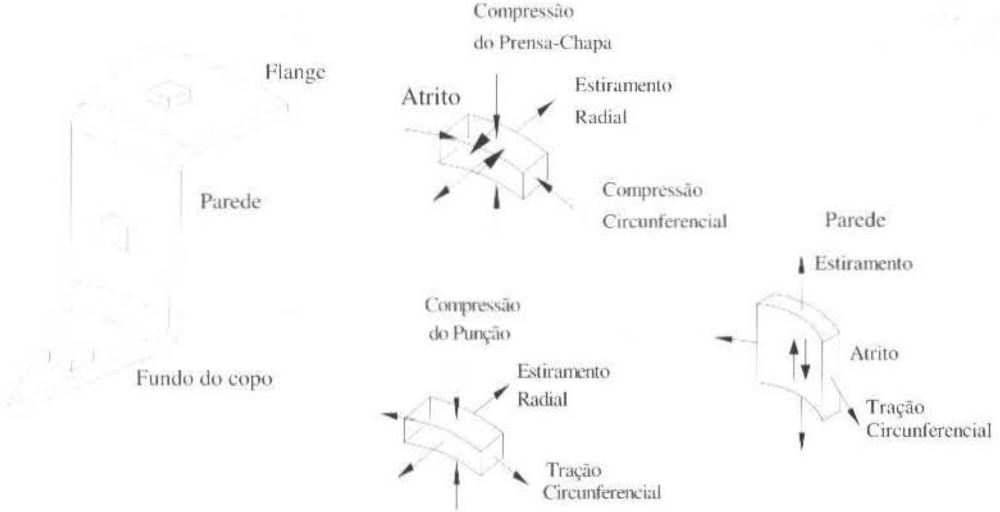

Fig. 1 Estado de deformações atuantes no copo durante o embutimento profundo (Bresciani et al., 1997)

As variações de espessura devida a esses estados de tensão fazem com que a parede do copo fique com o aspecto mostrado na Fig. 2.

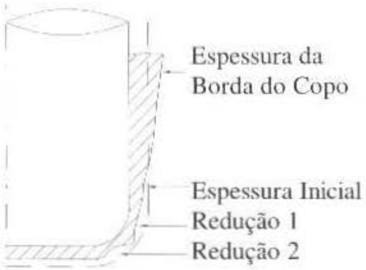

Fig. 2 Variação da espessura ao longo do copo embutido (Slater, 1977)

Quando as variações de espessura na redução 1 são muito intensas ocorre a ruptura do fundo do copo, que é a principal causa de falha de processo no embutimento cilíndrico.

O grande número de variáveis existentes no processo inviabiliza que um modelo analítico tenha condições de determinar precisamente as variações de espessura e sua distribuição, principalmente as duas reduções de espessura na região de curvatura do fundo do copo (Mahdavian e He, 1995).

Método dos Elementos Finitos.

Elemento para grandes deformações

Em processos de conformação plástica, o material que está sendo conformado passa por grandes deformações. Isto faz com que os elementos que são utilizados para modelar estes problemas, tenham a capacidade de suportar grandes deformações.

Para a modelagem da chapa a ser embutida será utilizado o elemento VISCO106. Este elemento possui a formulação para trabalhar com grandes deformações, apresenta volume constante durante o processamento e pode ser viscoplástico (os esforços dependem da taxa de deformação) ou então elastoplástico (os esforços não dependem da taxa de deformação), este elemento apresenta 4 nós e 3 graus de liberdade por nó (deslocamentos nas direções X, Y, Z).

O conceito teórico básico deste tipo de elemento é Lagrangeano, as deformações são logarítmicas (ou de Hencky) e as tensões são as verdadeiras (ou de Cauchy).

O material utilizado nas modelagens com este tipo de elemento deve ser isotrópico e as deformações elásticas devem ser desprezíveis em comparação às deformações plásticas.

Por suas características, este elemento possui formulação altamente não-linear, o que torna necessário trabalhar com o Método de Newton-Raphson.

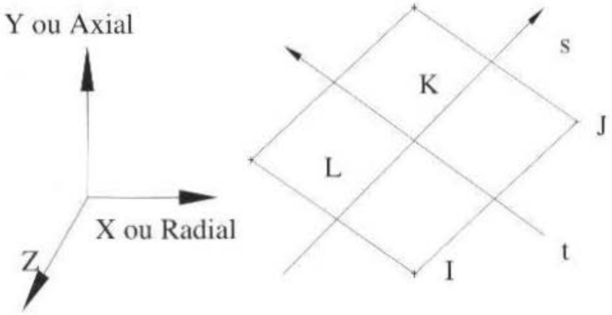

Fig. 3 Elemento VISCO106

Elementos de Contato

Os elementos de contato descrevem basicamente duas condições:

- Aberto, ou seja, não ocorre o contato ou
- Fechado, ocorre o contato.

Para a modelagem será utilizado o elemento de contato com 3 nós chamado CONTAC48. Nesse elemento, para que seja estabelecido o contato, o nó que está na superfície de saída (nó K) deve penetrar na linha definida pelos nós na superfície "alvo" (nós I e J), como mostrado na Fig. 4. Esse tipo de definição de contato é denominado algoritmo "Pinball".

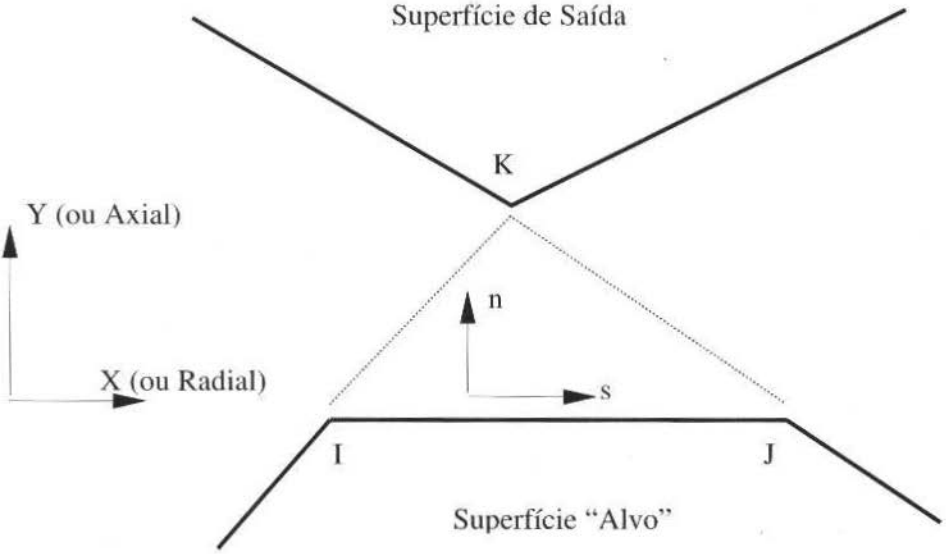

Fig.4 Elemento de contato - CONTAC48

Após assumir o contato, começa a ocorrer a transmissão da força entre as duas superfícies. Este elemento utiliza o modelo de atrito de Coulomb.

Modelo de Elementos Finitos

Para a modelagem do embutimento profundo foi discretizado o ferramental mostrado na Fig. 5 com um "blank" de diâmetro igual a 101,28 mm e espessura igual a 1,0 mm. Esse é o ferramental utilizado para o ensaio de Swift, que determina o máximo diâmetro de disco que pode ser embutido em relação ao diâmetro do punção (Dieter, 1984).

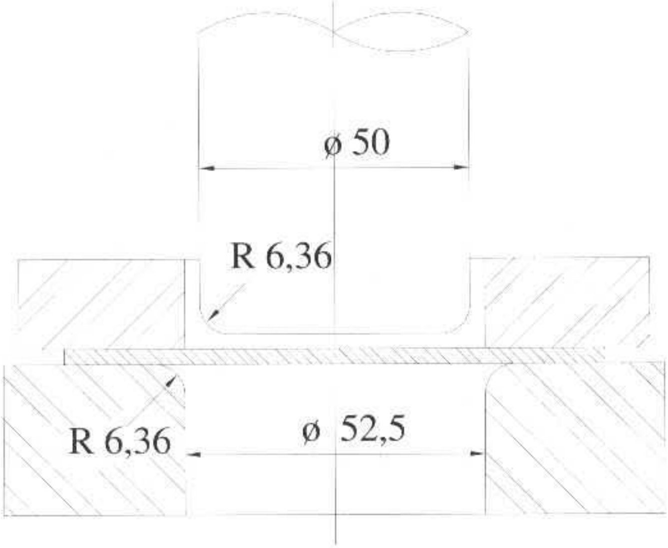

Fig. 5 Ferrametal utilizado na simulação

Para a modelagem do ferramental utilizou-se o elemento chamado PLANE 42, que possui dois graus de liberdade por nó e características axissimétricas; para modelagem da chapa foi utilizado o elemento VISCO106 (Ansys, 1993)

A composição química e as características mecânicas do aço ABNT 1006 – EEP, utilizado na parte experimental e na simulação, estão relacionadas nas Tabelas 1 e 2, respectivamente

Tabela 1 Composição química do aço ABNT 1006 EEP

Elemento Químico	Teor
Carbono	0,051
Silício	0,001
Enxofre	0,024
Manganês	0,320
Fósforo	0,014
Alumínio	0,062

Tabela 2 Resultados obtidos no ensaio de tração

Corpo de Prova [°]	σ_0 [MPa]	Desvio Padrão	σ_l [MPa]	Desvio Padrão	Alongamento Uniforme (%)	Desvio Padrão	Alongamento Total (%)	Desvio Padrão
0	153,00	16,81	300,00	29,19	24,60	1,35	42,00	1,15
90	150,00	16,32	289,00	38,92	23,40	2,17	42,00	1,34

Partindo-se dos resultados obtidos no ensaio de tração, foi levantada a curva tensão verdadeira por deformação verdadeira, através do Método dos Mínimos Quadrados.

Tabela 3 Índices para a curva real ($\sigma = K.\varepsilon^n$)

Corpo de Prova [°]	K [MPa]	Coeficiente de Encruamento (n)
0	510,10	0,22
90	472,08	0,21

Os índices de anisotropia planar e normal foram determinados utilizando-se corpos de prova retirados a 0°, 45° e 90° em relação ao sentido de laminação, conforme Tabela 4.

Tabela 4 Razão de deformação plástica

Corpo de Prova	R	Desvio Padrão
0^0	2,15	0,07
45^0	1,54	0,10
90^0	2,47	0,07

Com os dados acima encontram-se os índices de anisotropia normal e o índice de anisotropia planar:

$$\overline{R} = 1{,}93$$

$$\Delta R = 0{,}77$$

Os valores encontrados de índices de anisotropia são típicos de aços aplicados a estampagem profunda., garantindo bons limites de embutimento.

O tipo de elemento utilizado na simulação da chapa, como dito anteriormente, admite somente a modelagem de material isotrópico; dessa forma utilizou-se os valores da curva de escoamento obtida na direção paralela à direção de laminação para construção do modelo multilinear (Tabela 5). O ponto inicial da curva corresponde à deformação e tensão iguais a zero.

Tabela 5 Relação de pontos para a montagem da curva tensão x deformação multilinear

Ponto	Deformação	Tensão [MPa]
1	$3{,}96\times10^{-4}$	82,00
2	$2{,}00\times10^{-3}$	127,03
3	$1{,}00\times10^{-2}$	181,08
4	$2{,}00\times10^{-2}$	212,61
5	$4{,}00\times10^{-2}$	248,27
6	$7{,}00\times10^{-2}$	281,38
7	$12{,}00\times10^{-2}$	317,44
8	$18{,}00\times10^{-2}$	347,58
9	$27{,}70\times10^{-2}$	382,96

Foram adotados dois carregamentos diferentes para a simulação do processo:

1. Deslocamento de 26 mm do punção, para a geração do copo, 1 mm de deslocamento de aproximação e 25 mm de contato efetivo.

2. Pressão do prensa-chapa de 2,07 MPa, constante durante durante a descida do punção.

Como condições de contorno foram impedidos os deslocamentos nodais do punção e do prensa-chapa na direção do eixo X e da matriz na direção dos eixos X e Y.

Foram realizadas simulações com quatro coeficientes diferentes de atrito (0; 0,05; 0,10 e 0,15) a fim de verificar sua influência sobre os esforços, as deformações e a variação da espessura (Schey, 1983).

Apresentação e Análise dos Resultados

A Figura 6 apresenta o modelo de elementos finitos, após a conformação, com deslocamento de 26 mm. Como se pode observar na Fig. 2, a partir dos resultados da simulação, a espessura apresentou duas reduções ao longo do raio, provocadas pela mudança no sentido das tensões, conforme Guo et al. (1990).

Fig. 6 Modelo de elementos finitos deformado

Como pode ser observado na Fig. 7, a simulação do processo comprovou o comportamento da espessura do copo embutido. O fundo do copo apresentou deformação constante; a redução 2, uma deformação acentuada, seguida de um aumento de espessura; a redução 1, ruptura, quando os limites de embutimento são ultrapassados, e aumento contínuo da espessura até a borda do copo. Também pode ser visto que a deformação da espessura cresceu com o aumento do coeficiente de atrito.

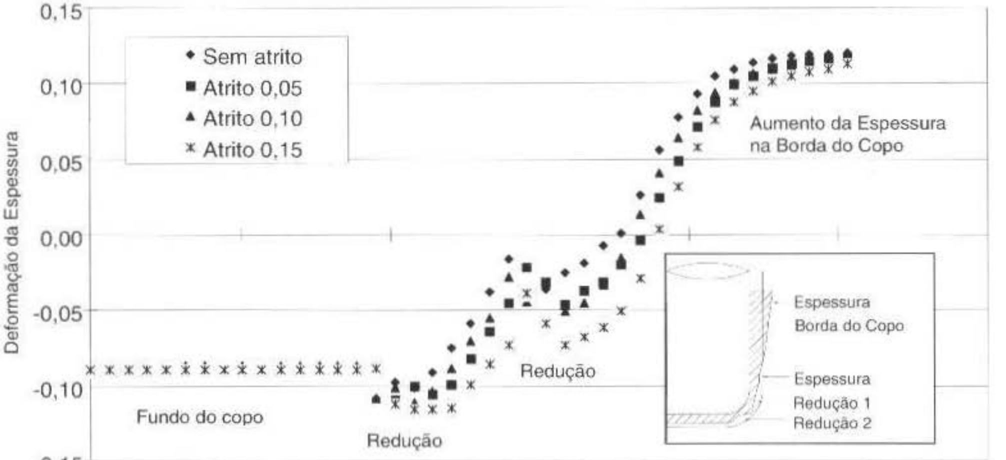

Fig. 7 Simulação da deformação na espessura para o "blank" de diâmetro 101,28 mm, em função da posição radial

A Figura 8 apresenta as deformações circunferenciais encontradas para os vários coeficientes de atrito utilizados na simulação. Com o aumento do atrito ocorre uma pequena redução na deformação circunferencial provocada no final da chapa pelo aumento da deformação da espessura.

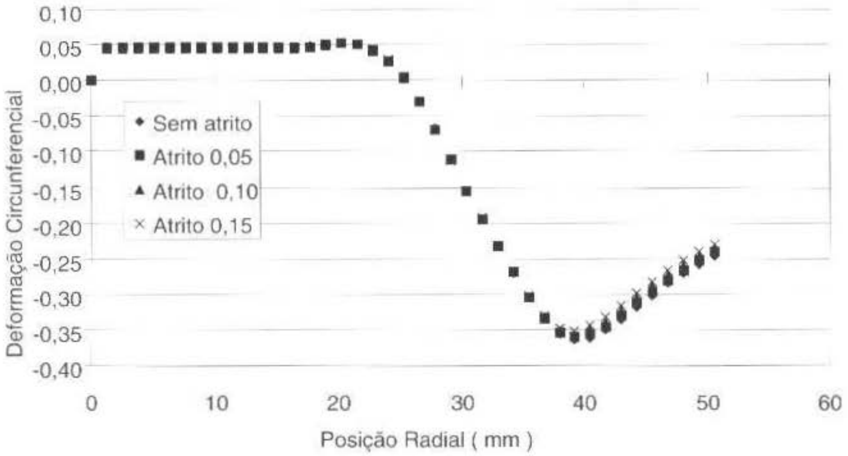

Fig. 8 **Simulação da deformação circunferencial para o "blank" de diâmetro 101,28 mm, em função da posição radial**

Para validação da simulação foram realizados ensaios de embutimento com o material modelado em uma máquina de ensaio Roel & Korthaus KG - Mod. BP 612, com o ferramental mostrado na Fig. 5 (Bortolussi, 1996). Foram realizados três embutimentos de discos com diâmetro de 101,28 mm utilizando como lubrificante uma pasta de bissulfeto de molibdênio sobre a superfície destes discos.

A deformação na espessura foi obtida medindo-se oito pontos diferentes ao longo de um "grid" de circunferências concêntricas que variavam em 5 mm no diâmetro de uma para outra em três copos embutidos, tendo-se assim 24 pontos em cada diâmetro de circunferência do "grid".

A Figura 9 apresenta os resultados experimentais para a deformação da espessura juntamente com os resultados do modelo matemático obtidos com coeficiente de atrito igual a 0,15.

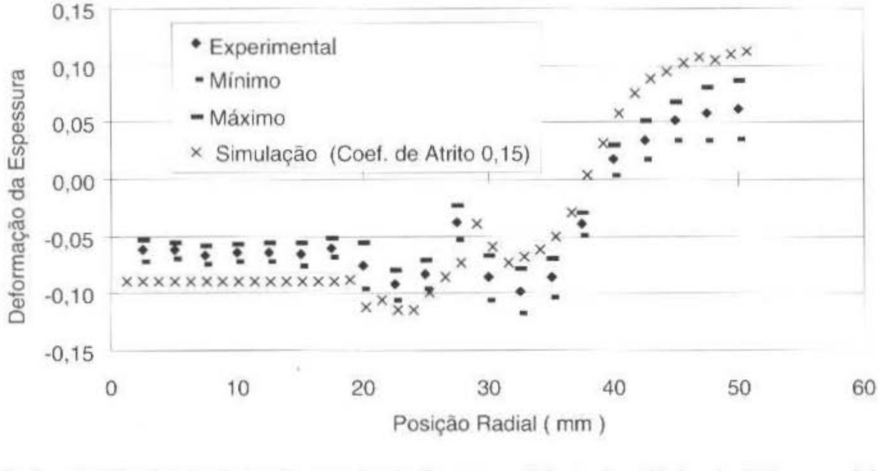

Fig. 9 **Resultados experimentais e de simulação com coeficiente de atrito igual a 0,15 para a deformação da espessura do disco de diâmetro 101,28 mm, em função da posição radial**

Observa-se que para a redução 1, onde ocorre a fratura por excesso de deformação, os valores obtidos no modelo foram menores que nos experimentos e o contrário é observado na redução 2. Já o aumento da espessura na borda do copo para o modelo foi maior que o obtido nos experimentos. Essas diferenças podem ser explicadas pela influência da anisotropia do material, observada nos experimentos pela formação de orelhas. Outro fator é a variação das condições de lubrificação ao longo do processo, variando o coeficiente de atrito nas diferentes regiões da ferramenta, principalmente nos raios, condição que não é considerada no modelo, pois adotou-se um coeficiente de atrito constante.

A utilização de um alto valor de rigidez para a modelagem do contato, em sistema inicialmente com baixa rigidez e a condição de deslocamento imposto em todos os nós do punção, deixando totalmente rígido, também contribuíram para as diferenças observadas.

Na Figura 10 apresenta-se os resultados experimentais e do modelo matemático para a deformação circunferencial, utilizando-se coeficiente de atrito igual a 0,15.

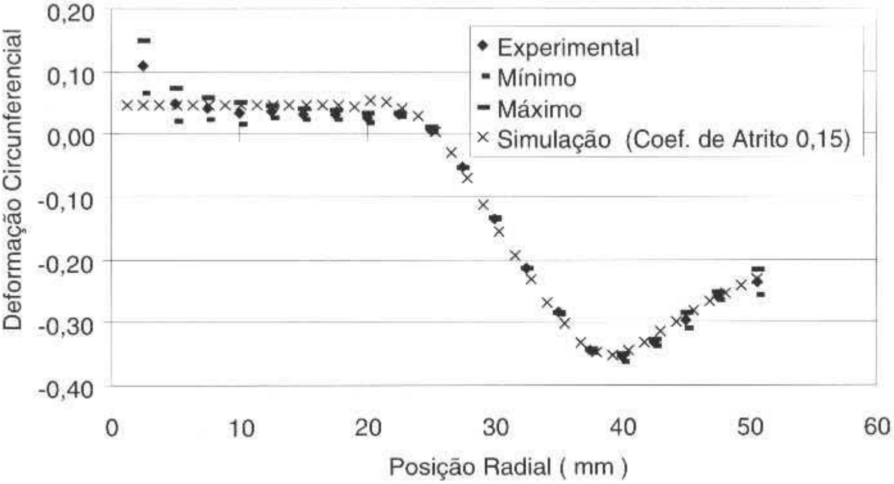

Fig. 10 **Resultados experimentais e de simulação com coeficiente de atrito igual a 0,15 para a deformação circunferencial do disco de diâmetro 101,28 mm, em função da posição radial**

Observa-se que a deformação circunferencial é pouco influenciada pelas condições de atrito e pela resistência mecânica da chapa. Essa deformação é importante para a verificação geométrica do copo embutido, pois variações nos diâmetros das circunferências do "grid" na região da parede do copo, independentemente do diâmetro inicial do disco, indicam que estão ocorrendo deformações excessivas na ferramenta ou que o valor da folga entre a matriz e o punção está inadequado.

A utilização de modelo axissimétrico e o emprego de um modelo de material isotrópico eliminou a possibilidade de verificação da formação das orelhas que ocorre durante a estampagem devido a anisotropia planar da chapa metálica, observadas nos ensaios pela alteração da geometria das circunferências do "grid", causando um aumento do desvio padrão na região da flange e, conseqüentemente, a diferença observada em relação aos resultados da simulação.

A força de embutimento encontrada no modelo de simulação empregando-se um coeficiente de atrito de 0,15, foi de 44753 N, sendo que experimentalmente foi encontrada uma força média igual a 50333 N com um desvio padrão de 1154 N. Utilizou-se uma célula de carga com capacidade nominal de 120000 N. A diferença média de 10% encontrada entre os resultados do modelo e os experimentais pode ser considerada satisfatória, considerando as diversas hipóteses simplificadoras assumidas na simulação.

Conclusões

A aplicação do método dos elementos finitos para análise do processo de estampagem apresentou-se viável para a determinação das deformações na chapa embutida, pois permitiu verificar o comportamento das deformações com o aumento do atrito e determinar os valores atingidos nas reduções 1 e 2, próximas do fundo do copo.

As diferenças observadas entre os resultados do modelo matemático e os experimentos devem-se principalmente aos seguintes fatores:

- Aplicação de um material isotrópico no modelo, que despreza o aumento da resistência ao estiramento que ocorre devido a anisotropia da chapa;

- Variações que ocorrem durante o processamento no coeficiente de atrito devido a alterações na camada de lubrificante, que vão desde a lubrificação hidrodinâmica em algumas condições, a atrito seco em outras posições da ferramenta, principalmente no raio da matriz. No modelo essas variações não são consideradas;
- Uso de um modelo axissimétrico reduz consideravelmente o tempo de processamento mas dificulta a interpretação dos resultados, e limita o tipo de produto embutido que pode ser modelado;
- Dificuldade de definir-se valores adequados para o número de elementos de contato, para a rigidez imposta a esses elementos e, finalmente, para o próprio coeficiente de atrito.

Referências

Ansys, 1993, ANSYS User's Manuals, Vols. 1 (Procedures), 2 (Commands), 3 (Elements) and 4 (Theory), Swanson Analysis Systems Inc.

Bathe, K. J., 1982, "Finite Elements Procedure in Engineering Analysis", Prentice-Hall, Englewood Cliffs.

Borst, R. and Feenstra, P.H., 1990, "Studies in Anisotropic Plasticity With Reference to the Hill Criterion", International Journal of Numerical Methods in Engineering, Vol. 29, pp. 315-336.

Bortolussi, R., 1.996, "Simulação do Processo de Estampagem Profunda de Corpos Cilíndricos Através do Método dos Elementos Finitos", Dissertação de Mestrado, UNICAMP, cap. 5, pp. 81-88.

Bresciani, Fo., E., Button, S.T., Gomes, E., Nery, F.A.C., Zavaglia, C.A.C., 1.996, "Conformação Plástica dos Metais", Ed. UNICAMP, p. 127.

Chou, C.H. and Pan,J. , 1990, "Analysis of Sheet Metal Forming Operations by a Stress Resultant Constitutive Law" , International Journal of Numerical Methods in Engineering, Vol. 29, pp. 315-336.

Cook, R. D., Malkus, D. S., Plesha, M. E., 1989, "Concepts and Applications of Finite Element Analysis", John Willey & Sons, 3ª Edição.

Darendeliler, H., Altan, T., 1996, "Analysis of axisymmetric cup drawing in relation to friction ", Journal of Materials Processing Technology, Vol 58, pp 293-301.

Dieter, G. E, 1984, "Workability Testing Techniques", ASM International.

Gontier, C. , 1994, "About The Numerical Simulation of the Sheet Metal Stamping Process", International Journal of Numerical Methods in Engineering, Vol. 37, pp. 669-692.

Guo, Y.Q., Batoz, J. L., Detraux, J. M., Duroux, P., 1990, "Finite Elements Procedures for Strain Estimations of Sheet Metal Forming Parts", International Journal of Numerical Methods in Engineering, Vol. 30, pp. 1385-1401.

Mahdavian, S. M., He, D., 1995, "Product Thickness Analysis in Pure Cup Drawing", Journal of Materials Processing Technology, Vol. 51, pp. 387-406.

Keck, P., Wilhelm, M., Lange, K., 1990, "Application of the Finite Element Method to the Simulation of Sheet Forming Processes: Comparison of Calculations and Experiments", International Journal of Numerical Methods in Engineering, Vol. 30, pp. 1415-1430.

Lee, D., Majlessi, S. A., Vogel, J. H., 1989, "Process Modeling and Simulation for Sheet Metal", Metals Handbook, Vol. 14, 9th Edition, pp. 911-927, ASM International.

Oñate, E. and Zienkiewicz, O. C., 1983, "A Viscous Shell Formulation for The Analysis of Thin Sheet Metal Forming" , International Journal of Mechanical Science, Vol. 25, nº 5, pp. 305-335.

Rowe, G. W., Strugess, C. E. N., Hartley, P., Pillinger, I., 1991, "Finite Element Plasticity and Metal Forming Analysis", Cambridge University Press, 1ª Edição.

Schey, J. A., 1983, " Tribology in Metalworking", ASM International.

Slater, R. A. C. , 1977, " Engineering Plasticity", The Macmillian Press.

RBCM - J. of the Braz. Soc. Mechanical Sciences
Vol. XXI - No.2 - 1999 - pp. 364-368

ISSN 0100-7386
Printed in Brazil

Abstracts

Simões, M. G., Franceschetti, N. N. and Adamowski, J. C., 1999 "Interdisciplinary Control Design for a Solar Car Implementation", J. of the Braz. Soc. Mechanical Sciences, Vol. 21, No. 2, pp. 164-174.

The paper describes an advanced drive system control for a solar powered vehicle. The drive system control extracts the maximum electrical power from a distributed solar array that covers the surface of the vehicle, with distributed RISC based peak power tracker controllers for each individual solar panel. The vehicle propulsion has two steering wheels and one propulsion wheel based on a brushless dc machine drive control. The system is capable to sequence from start-up to shutdown, it is torque or speed controlled and a on-board computer for system monitoring and communication for energy management in the race strategy which optimizes the energy management. The drive system has been fully implemented in a two seat carbon fiber prototype with satisfactory performance and can be easily translated to other types of electrical vehicles.
***Keywords**:Solar Car, Electric Vehicle, Control Drive.*

Nenchev, D.N., Yoshida, K. and Uchiyama, M., 1999, "Reaction Null Space Control of Free-Floating and Elastic Base Robots Abstract", J. of the Braz. Soc. Mechanical Sciences, Vol. 21, No. 2, pp. 175-184.

The equations of motion of both free-flying and elastic base robots have a similar structure. Particularly, we show that a so-called inertia coupling matrix plays a significant role for the dynamics. We derive necessary conditions for the existence of the null space of this matrix. The nult space aims in decoupling manipulator motions from base motion. Decoupling means that fast motions can be performed without disturbing the base. Also, efficient inertial coupling can be achieved, which is helpful for controlling base motion through manipulator-induced reactions.
***Keywords:** Reaction Null Space Control, Robots*

Jardim, C. M. and Yoneyama, T., 1999, "Integrated Design of Flight/Propulsion Control Systems for Helicopters Using μ-Synthesis", J. of the Braz. Soc. Mechanical Sciences, Vol. 21, No. 2, pp. 185-199.

This work concerns the application of μ-synthesis to the integrated design of a flight/propulsion control system for a typical high performance single-main-rotor helicopter. In order to improve the handling qualities, the controllers are designed to yield accurate control of vertical velocity, yaw rate, pitch and roll attitude. Multivariable robust control theory is required in view of the presence of un-modelled rotor dynamics and parameter uncertainty as well as exogenous disturbances such as wind gusts. Performance and stability tests are carried out both in frequency-domain and time-domain. The end result is a flight/propulsion control system that is stable, robust and ensures good closed loop tracking, disturbance rejection and decoupling properties.
***Keywords:** Helicopter, Robust Control, Multivariable, μ-Synthesis.*

Veras, C. A. G., Carvalho Jr., J. A. and Saatamoinen, J., 1999, "The Influence of Gas Pressure on Single Solid Fuel Combustion", J. of the Braz. Soc. Mechanical Sciences, Vol. 21, No. 2, pp. 200-210.

A model designed for the prediction of heat and mass transfer effects in the boundary layer of a reacting coal particle was extended to analyze the trends as the pressure is increased well above atmospheric conditions. The oxidation of volatile species in the boundary layer is based on a two step mechanism where the dependence of the flame speed on pressure is accounted for. The model was able to particle temperature in a broad range of gas composition and pressure as well as fuel type.
***Keywords**: Coal Combustion, Char Combustion, Pressurized Combustion, Combustion Modeling.*

Parise, J. A. R. and Saboya, F. E. M., 1999, "Transport Coefficients for Developing Laminar Flow in Isosceles Triangular Ducts", J. of the Braz. Soc. Mechanical Sciences, Vol. 21, No. 2, pp. 211-221.

Experiments were performed to determine overall heat transfer coefficients in the laminar entrance region of 30, 45, 60 and 90 degrees isosceles triangular ducts. The results were obtained by application of the analogy between heat and mass transfer in conjunction with the naphthalene sublimation technique. In accordance with the analogy, the experimental conditions simulated a heat transfer situation characterized by simultaneous developing of velocity and *temperature fields in an isosceles triangular duct with isothermal lateral walls and adiabatic base. The measurements were performed for Reynolds numbers ranging from 100 to 1800 and a duct length to hydraulic diameter ratio from 2 to 40. In this manner, a long range of the dimensionless streamwise coordinate values was covered, including the neighborhood of entrance region. Curve-fitting equations were produced, providing the Sherwood number as a function of the Graetz number. Extension of the results for other apex angles, within the 20-100 degrees range, was also possible.*

With the analogy between heat and mass transfer, similar correlations were provided for the corresponding Nusselt number. The triangular duct geometry finds application in the compact heat exchanger design such as solar collectors with triangular cavities for direct air heating.

***Keywords**: Heat and Mass Transfer Analogy, Duct Flow, Laminar Entrance Region.*

Bortolus, M. V. and Giovannini, A., 1999, "Heat Transfer in Complex Turbulent Flow: Wall functions and Sensibility to Inlet Conditions", J. of the Braz. Soc. Mechanical Sciences, Vol. 21, No. 2, pp. 222-232 (In Portuguese).

First, different wall treatments based in wall functions are tested together with the Standard k - ε turbulence model. These models are tested in the case of wall heat transfer prediction in complex turbulent flow. Then, the sensibility of these models to inlet conditions are analysed. Variations in the Nusselt distribution due to Reynolds number and initial boundary layer thickness are discussed. The incompressible flow over a backward facing step has been elected as a test case for which na extensive data base exists. Comparison between numerical results and experimental measurements is presented and discussed.

***Keywords:** Turbulence, Recirculating Flows, Heat Transfer, Wall Functions, Numerical Simulation.*

Bannwart, A. C., 1999, "A Simple Model for Pressure Drop in Horizontal Core Annular Flow", J. of the Braz. Soc. Mechanical Sciences, Vol. 21, No. 2, pp. 233-244.

Based upon experimental data for heavy oil-water flow inside steel (26.7 mm ID) and cemented (23.9 mm ID) horizontal tubes, a very simple model for pressure drop in the core annular flow pattern was developed. The experiments were run at room temperature and the fluids used were a fuel oil ($\mu = 2.7$ Pa.s, $\rho = 989$ kg/m^3) and tap water, both drawn from a separator tank. First, it is shown that for both tubes the so-callled "perfect core annular flow" approach (shortly PCAF) poorly correlates the data. This is due to the waviness of the interface and turbulence in the annulus flow. These effects are taken into account in the model proposed in this paper and justify the assumption of no-slip, which was earlier concluded by the author from wavespeed measurements for the same flow (Bannwart, 1998). As a result, a very simple correlation model for the pressure gradient is derived. The model was adjusted to fit the data and generalized to other tube sizes and fluids. Different correlations for oleophilic and oleophobic pipe walls are provided. Calculations using the correlation for oleophobic pipe behavior are in very good agreement with data from another source.

***Keywords:** Multiphase Flow, Liquid-Liquid flow, Core Annular Flow, Pressure Drop, Modeling.*

Jabardo, J. M. S., Bandarra Filho, E. P. and Lima, C. U. S., 1999, "New Correlation for Convective Boiling of Pure Halocarbon Refrigerants Flowing in Horizontal Tubes", J. of the Braz. Soc. Mechanical Sciences, Vol. 21, No. 2, pp. 245-258.

An extensive literature survey of convective boiling has been performed in this study. Published correlations have been divided into three main groups: strictly convective, those based on the superposition rule, and strictly empirical. An empirical correlation has been developed from an experimental data bank obtained elsewhere through an optimized curve fitting procedure. Average deviations of results from the proposed correlation with respect to experimental data are significantly low compared to deviations from other correlations. Comparisons between local heat transfer coefficients from correlations and those obtained experimentally, though qualitatively sound, have shown distinct deviations. Improved physical models are needed to adequately correlate local heat transfer coefficients.

***Keywords**: Convective Boiling, Refrigerants, Horizontal Flow.*

Braga, S. L. and Nóbrega, C. E. L., 1999, "A Numerical Study of Thermal Storage on Encapsulated Phase Change Materials", J. of the Braz. Soc. Mechanical Sciences, Vol. 21, No. 2, pp. 259-270.

The role of thermal energy storage in the energetic scene has been continuously increasing over the last years, since electrical utilities started to adopt different rates for "peak" and "off-peak" power consumption periods. As a result, several works have been devoted to modeling and predicting the transient response of both sensible and latent heat storage devices, over a variety of geometric forms. Following the current trend, latent heat storage on encapsulated *phase change material (PCM) was chosen as the object of the present work. Since the main feature is to take advantage of the high storage capacity offered by the latent heat, this work only deals with situations with small values of the Stefan number (Ste) which allow the solidification to be predicted by a quasi-stationary model. To obtain more general results, all the physical variables are arranged in non-dimensional groups, the influence of which on the response of the storage unit is evaluated in order to provide guidelines to the design and operation of those devices. Several assumptions are made with a view to maintain the model as simple as possible, without disregarding a careful reflection about its accuracy and impact on the reliability of the solution. The transient behavior of the storage unit is described by the evolution of the outlet temperature, as well as the thermal resistance ratio (TRR) through the discharge process. To ratify the model, some comparisons with previously published works are provided, showing not only qualitative but quantitative concurrency as well.*

Keywords: *Thermal Storage, Phase Change.*

Moraes Jr., Paulo, 1999, "A Wind-Tunnel Investigation of Ground-Wind Steady Loads on a Strap-on Launch Vehicle", J. of the Braz. Soc. Mechanical Sciences, Vol. 21, No. 2, pp. 271-278.

The effect of wind loads on slender bodies has been observed and investigated for many years by many authors. The present paper deals with an experimental investigation of wind induced loads on strap-on launch vehicle configurations. The work is firstly restricted to the observation of steady global loads acting on a configuration based on an arrangement of four cylinder shaped boosters around a cylindrical central core of equal diameter. The paper discusses the results obtained for the transversal or drag force, the rolling moment, and the longitudinal position of center of pressure, as function of several parameters.

Keywords: *Aerodynamics, Wind-Loads, Wind-Tunnel, Launch Vehicle.*

Fico Jr., N. G. C. R., Azevedo, J. L. F. and Ortega, M. A., 1999, "On the Use of CFD Methods in the Design of Transonic Wind Tunnel Nozzles", J. of the Braz. Soc. Mechanical Sciences, Vol. 21, No. 2, pp. 279-293.

A numerical investigation of the flowfield in three proposed geometries for the nozzle and contraction of a transonic wind tunnel facility is performed. The primary objective was to understand details of the flow in the tunnel in order to try to maximize test section flow quality. The calculations presented here include preliminary 2-D simulations and full 3-D computations. The codes used for the present calculations were previously validated by the authors and co-workers, and these validation studies are available in the literature. The primary flow solvers implement an Euler formulation, and use the Beam and Warming implicit approximate factorization algorithm for the solution of the discretized equations. A boundary layer code was typically run at a post-processing stage in order to estimate boundary layer growth and its impact on flow quality. Results obtained for a sonic nozzle and for two Laval nozzles are presented, and they were instrumental in the selection process which led to the transonic facility which is currently being built.

Keywords: *Transonic Nozzle Flow, Transonic Wind Tunnel, CFD Methods, Tunnel Design.*

Castro, J. T. P. and Meggiolaro, M. A., 1999, "Some Comments on the Automation of the εN Method for Fatigue Design under Complex Loading", J. of the Braz. Soc. Mechanical Sciences, Vol. 21, No. 2, pp. 294-312 (In Portuguese).

The εN fatigue design method is non-linear and depends on the loading order and on the initial state of the piece. Therefore, the traditional procedure based on rain-flow counting of the loading followed by Neuber, Ramberg-Osgood, Coffin-Manson and Miner rules does ***not*** *guarantee the prediction of physically admissible hysteresis loops at the notches in the complex loading case. Solutions for this problem are proposed, and their implementation in a powerful language named* **ViDa***, developed to automatize the fatigue design process, is discussed.*

Keywords: *εN Method, Fatigue Design Automation, Complex Loading.*

Cunha, J. and Piranda, J., 1999, "The use of Model Updating Techniques in Dynamics for Identification of Stiffness Properties of Sandwich Composite Structures", J. of the Braz. Soc. Mechanical Sciences, Vol. 21, No. 2, pp. 313-321 (In Portuguese).

The present paper consists of the identification of the stiffness properties of sandwich composite structures by using vibration measurement's data. The coefficients are identified by a model updating technique. The used formulation is based on the minimization of the eigensolution residuals (sensitivity method). This technique allows the simultaneous identification of several properties from a single test. Stiffness properties of extension, bending, twisting and transverse shear effects are identified, what is not evident from classical identification tests of sandwich structures. Results obtained by numerical simulations show the efficiency of the proposed methodology.

***Keywords** : Composite Materials, Sandwich Structures, Elastic Constants, Identification, Model Updating, Vibration.*

Pires, A. C., Ferrão, P. and Carranca, J.N., 1999, "Life Cycle Analysis as a Business Strategy for the Process Industry", J. of the Braz. Soc. Mechanical Sciences, Vol. 21, No. 2, pp. 322-331.

It has been observed throughout Europe that environmental policy has not necessarily had a negative economic impact. The integration of environmental technologies in industry can conduct to both economic and ecological advantages compared to usual technologies, whereas the use of resources is minimised and with them, the raw emissions, at all stages of the production process.

This paper analyses the environmental and the technological assessment associated with the implementation of a cogeneration power plant, using a high pressure boiler burning olive oil bagasse (as obtained after extraction) and a low-power steam turbine. It demonstrates the use of Linear Programming modelling as a tool for identifying and evaluating the best possible options for environmental performance of the system analysed, and extends this technique for the assessment of indirect eco-taxes, also called "Pigou taxes", associated with environmental regulations. It is shown in this study that a balance between environmental and economic performance in systems analysis lies in exploring a set of alternative options for system improvements. The results show that for a steam demand value lower than 80% of the maximum steam production capacity, the profit associated with the over-burning of bagasse should be associated with increasing values of the Pigou tax in order to prevent the consequent over emission of CO_2*. The paper shows that the economical profitability of the system is correlated with the* CO_2 *emissions reductions, for this particular project, for different loading conditions of cogeneration plant in oil extraction plant. Although the extrapolation of this conclusion should be considered with caution, it can be assumed to be valid for many cogeneration systems in industry. The principles of the Life Cycle Assessment - LCA applied with Linear Programming techniques have allowed the quantification of side effects, associated with the use of technologies assessment, contributing for supporting decision making based on technical information in environmental policy.*

***Keywords**: Life Cycle Assessment, Linear Programming, Cogeneration Power-Plant, Technological Innovation, Environmental Management.*

Andersson, V., Frainer, V. J. and Martins, C. C., 1999, "Design and Construction of a Prototype of a Strain-Gage Type Transducer for the Measurement of Drilling Forces", J. of the Braz. Soc. Mechanical Sciences, Vol. 21, No. 2, pp. 332-342 (In Portuguese).

This work presents some considerations about design, construction and validation of a prototype of a strain-gage type transducer, developed to measure cutting forces produced in the drilling process of special geometric specimens. The validation tests showed that the analytical formulae employed can be used as a good design approach. When the prototype was used to measure cutting forces testing three steel specimens, the experimental values obtained nearly agree with the values analytically calculated using equations known from the bibliography. Therefore, the prototype utility in machinability testing of materials was proved.

***Keywords:** Strain Gage Transducers, Drilling Forces, Design of Strain Gage Transducers, Drilling.*

Matsumoto, H. K. and Diniz, A. E., 1999, "Evaluating The Quality Of Turned Hardened Steel Workpieces", J. of the Braz. Soc. Mechanical Sciences, Vol. 21, No. 2, pp. 343-354.

Recently many works have been done in order to study the turning process of hardened steels, mainly concerning the lives of ceramic and PCBN tools. However, just few works deal with the problem of turning accuracy, comparing it with grinding accuracy, mainly when the lathe used has a conventional mechanical design. Therefore, it is important to evaluate the capability of these conventional machines to replace the grinding operation by turning and still maintain workpiece quality typical of grinding operations. This work tries to contribute to fill this gap. Several AISI E52100 hardened steel workpieces (60 HRc) were turned using mixed ceramic and PCBN tool materials and different cutting speeds in a lathe of conventional design. Workpiece surface roughness and diameter variation were measured throughout the tool life test, in order to evaluate the quality of the workpiece. The length of the workpieces was also varied to analyze the influence of workpiece shape on its quality. The main conclusion of this work was that the turning process is able to replace grinding in hardened steel finishing operations. Moreover, it is able to achieve a surface and dimensional quality similar to that of ground components, even when the machine used has a conventional mechanical design.

***Keywords:** Turning Hardened Steels, Accuracy, Surface Roughness.*

Button, S. T. and Bortolussi, R., 1999, "Finite Element Analysis of a Cup Deep Drawing Process", J. of the Braz. Soc. Mechanical Sciences, Vol. 21, No. 2, pp. 355-363 (In Portuguese).

Deep drawing processes have an important role in manufacturing, mainly in the automotive industry. The increasing competition requires that design and manufacture of dies be fast and without errors. New forms to develop the dies have been used. The finite element method has helped engineers to reduce errors during die development. In this paper an elasto-plastic element was used to simulate the cylindrical deep drawing of an ABNT 1006 steel cup. The simulation made possible the determination of the forces, thickness and circumferential strains ocurring during the deep drawing process, which were compared to experimental results.

Keywords: *Deep Drawing, Finite Elements.*

Diagramação:
M&M Computação Gráfica e Publicidade Ltda
13044-260 Campinas SP Brasil
mmcompgr@uol.com.br
Fone: 2300977

Journal of the Brazilian Society of Mechanical Sciences

Information for Authors

SCOPE AND POLICY

- The purpose of the Journal of the Brazilian Society of Mechanical Sciences is to publish papers of permanent interest dealing with research, development and design related to science and technology in Mechanical Engineering, encompassing interfaces with Civil, Electrical, Chemical, Naval, Nuclear, Materials, Aerospace, Petroleum, System Engineering, Food, Agriculture, etc., as well as with Physics and Applied Mathematics.
- The Journal publishes Full Length Papers, Review Papers, Book Reviews and Letters to the Editor. Authors must agree not to publish elsewhere a paper submitted and accepted by the Journal. Papers previously published in proceedings of conferences can also be considered for publication; this event should be cited as a footnote on the title page. Copies of the conference referees' reviews should be included. Review articles should constitute a critical appraisal of the published information.
- The decision of acceptance for publication lies with the Editors and is based on the recommendations of at least two ad hoc reviewers, and of the Editorial Board, if necessary.

SUBMISSION

- Manuscripts and correspondence should be sent to the Editor or, alternatively, to the nearest Associate Editor.
- Five (5) copies of the paper are required. The Author should retain the manuscript disk until the end of the review process.
- Manuscripts should be submitted only in **English**.
- A manuscript submitted for publication should be accompanied by a cover page containing the full name of the Author(s), the Author for contact, institution address, phone number, e-mail address and, if the Authors so wish, the names of up to five (5) possible referees, with respective addresses.

FORMAT

- Manuscripts should begin with the title, followed by an Abstract and from three to five Keywords. The manuscript should not contain the Authors' names. The Abstract should state the objectives, methodology used and main conclusions, in no more than 200 words.
- In research papers sufficient information should be provided in the text, or by referring to papers in generally available Journals, to permit the work to be repeated.
- The paper must begin with an Introduction that is written for the general reader of the Journal, not for the specialist. This section should describe the problem statement, its relevance, significant results and conclusions from prior work, and objectives of the present work.
- Uncertainties should be specified for experimental and numerical results.
- Manuscripts should be typed double-spaced, on one side of the page, using A4 sized paper, with 2 cm margins. The pages should be numbered and not to excess 24, including tables and figures. Avoid footnotes.
- All symbols should be defined in the text. A separate nomenclature section should list, in alphabetical order, the symbols used and their definitions. The Greek symbols follow the English symbols, and are followed by the subscripts and superscripts. Each dimensional symbol must have SI (metric) units mentioned; in addition, English units may be included parenthetically. Dimensionless groups and coefficients must be so defined and indicated.

MATHEMATICAL EQUATIONS

- All mathematical expressions should be typewritten using only letters and symbols available on the keyboard.
- Equations that extend beyond the text width should be restated to go in two or more lines, as necessary to fit within the page width.
- Fractional powers should be used instead of root signs.
- A solidus (/) should be used instead of an horizontal line for fractions, whenever possible; for example, use 2/3 for two-thirds.

- Mathematical expressions should not be introduced along the text itself, as part of a sentence line, but typed on individual lines.
- Numbers that identify mathematical expressions should be enclosed in parenthesis. Refer to equations in the text as " Eq.(1)" or, if at the beginning of a sentence, as " Equation (1)".
- Vectors should be typed **boldface**. Do not use arrows, wavy-line underscoring,etc.

FIGURES AND TABLES

- Figures and Tables should be referred in consecutive Arabic numerals. They should have a caption and be placed as close as possible to their first reference in the text. Refer to figures in the text with the abbreviation "Fig. 1", except at the beginning of a sentence, where " Figure 1" should be used.
- The figures presenting technical data/results should have a boundary on all four sides, with scale indicators (tick marks) on all sides.
- The legend for the data symbols should be put inside the figure, as well as the labels for each curve. Lettering should be large enough to be clearly legible (1.5-2.0 mm).
- Laser print output line drawings are preferred. Drawings prepared on tracing paper or vellum, using black india ink, are acceptable.
- Photographs must be glossy prints.

REFERENCES

- References should be cited in the text by giving the last name of the author(s) and the year of publication. Either use "Recent work (Smith and Farias, 1997) or " Recently Smith and Farias (1997). With four (4) or more names, use the form " Smith et al. (1997)". If two or more references would have the same identification, distinguish them by appending "a","b", etc., to the year of publication.
- Acceptable references include journal articles, numbered papers, dissertations, thesis, published conference proceedings, preprints from conferences, books, submitted articles, if the journal is identified, and private communications.
- References should be listed in alphabetical order, according to the last name of the first author, at the end of the paper. Some sample references follow:
- Soviero, P.A.O. and Lavagna, L.G.M.,1997, "A Numerical Model for Thin Airfoils in Unsteady Motion", RBCM- J. of the Brazilian Soc. Mechanical Sciences, Vol.19, No. 3, pp. 332-340.
- Bordalo, S.N., Ferziger,J.H. and Kline, S.J.,1989, "The Development of Zonal Models for Turbulence", Proceedings of the 10th Brazilian Congress of Mechanical Engineering, Vol.1, Rio de Janeiro, Brazil, pp. 41-44.
- Sparrow, E.M., 1980a, "Forced Convection Heat Transfer in a Duct Having Spanwise-Periodic Rectangular Protuberances", Numerical Heat Transfer, Vol.3, pp. 149-167.
- Sparrow, E.M., 1980b, "Fluid-to-Fluid Conjugate Heat Transfer for a Vertical Pipe-Internal and External Natural Convection", ASME Journal of Heat Transfer, Vol.102, pp. 402-407.
- Silva, L.H.M.,1988, "New Integral Formulation for Problems in Mechanics" (In Portuguese), Ph.D. Thesis, Federal University of Santa Catarina, Florianópolis, S.C., Brazil, 223 p.
- Coimbra, A.L., 1978, "Lessons of Continuum Mechanics", Ed. Edgard Blücher, S.Paulo, Brazil, 428 p.
- Clark, J.A.,1986, Private Communication, University of Michigan, Ann Harbor.

FINAL VERSION OF THE MANUSCRIPT

- Upon notification of acceptance, Authors should submit two copies of the final version and the manuscript disk, in Windows or Macintosh, Word or WordPerfect , thus avoiding retyping, with subsequent reduction of errors.

(Contents Continued)

Fatigue

Sandwich Composite Structures

Life Cycle Analysis

Machining

Metal Drawing Process

ISSN 0100 - 7386

JOURNAL OF THE BRAZILIAN SOCIETY OF MECHANICAL SCIENCES
REVISTA BRASILEIRA DE CIÊNCIAS MECÂNICAS

VOL. XXI - No. 2 - JUNE 1999

Control Systems

Combustion

Convection Heat Transfer

Two-Phase Flow

Phase-Change Heat Transfer

Thermal Storage

Aerodynamics

(Continued on Inside Back Cover)